The Faint Intergalactic Redshifted Emission Balloon and the Cosmic Web Imager: Two Integral Field Spectrographs Designed to Study Emission from the Intergalactic Medium

Thesis by

Mateusz Konrad Matuszewski

In Partial Fulfillment of the Requirements

for the Degree of

Doctor of Philosophy

California Institute of Technology

Pasadena, California

2012

(Defended June 30, 2011)

To Bolek, Ewa, Meg, and Zbigniew

Acknowledgments

The work presented in this volume would not have been possible without the care and support of my family, friends, and colleagues. It is next to impossible to mention everyone who has contributed to the projects or helped me along the way, and I am sure I will have omitted someone unintentionally. I humbly apologize to anyone that I have left out and I promise I will sneak into the library and staple an appropriate addendum to this page.

I would like to thank my adviser, Chris Martin, for giving me a chance to work on some really neat experiments and to interact with very talented, friendly, and amazing people. I have benefited from Chris' insights and from his understanding that people do err and need to be pointed the right direction.

Bruno Milliard and David Schiminovich have been amazing resources, as well as being patient with their help and explanations. I can only hope that at least a tiny bit of their experience and ingenuity has rubbed off on me during the two FIREBall campaigns.

Collaborating with Jean Evrard, Frederi Mirc, and the CNES team was a joy. I am grateful for their hospitality during my stay in Toulouse. I hope they develop taste for better beer than that which they exhibited while choosing between red and green sauce in Fort Sumner, New Mexico.

I want to thank Robert Grange, Stephan Frank and the talented and energetic scientists and engineers from LAM. Despite their own busy project schedules and deadlines, they always seemed to find time to help and point me in the right direction.

Ryan McLean, Anna Moore, and Patrick Morrissey managed to strike just the right balance of oversight, guidance, support, and humor. Their perspective and attitude have made many stressful and tense situations bearable; their knowledge and insights have been invaluable in my work.

Marty Crabill, Stephen Kaye, and John Klemic have always been willing to share their experience, happy to lend a hand or a kind word. They have taught me numerous skills and tricks, many of which I have found useful in my work and away from it.

It has been a pleasure working with the dedicated staff at Mount Palomar. Thanks to Steve Kunsman, Gregord van Idsinga, and Mike Doyle for helping us not break CWI; Jean Muller and Kajsa Pfeffer for preventing us from breaking the 200", and to Dipali Crosse for making sure we did not break ourselves.

The balloon project would not have been possible without the experience and hard work of the staff of the Columbia Scientific Balloon Facility. Their eagerness to help and effectiveness in doing so are greatly appreciated.

I thank the skilled people at the physics machine shop, and at central engineering for their careful work. It is amazing how many times Mark, Terry, Isaac, José, Bovan, and Rick managed to make the right parts when looking at the scribbles that I handed them. I acknowledge the contributions to FIREBall of Robert Chave.

Thanks to Michele Yeater, who has been fantastic at helping me cut through bureaucratic red tape and who has always been fun to talk to whenever I needed a break from the office grind.

I have met many terrific people through bridge and ultimate. They have provided me with a distraction and an outlet whenever I was in need of one.

Working and sharing an office with Thiago Gonçalves, Shahinur Rahman, Daphne Chang, and Nicole Lingner has been a lot of fun and has led to lots of amusing, interesting, and useful discussions.

I have had the distinct pleasure of breaking things in the company, and with the help, of Daphne Chang, Shahin Rahman, and Sarah Tuttle. We somehow always managed to find enough duct tape and staples to put the things back together. I find it amazing (and a little shocking) that the things we have built actually ended up working and doing what they were supposed to. It has been over a year since Daphne left us; her contributions to the work described in this thesis have been immense. She was hard-working, brilliant, and funny. I miss her.

I thank Stephan, Sarah, and Meg for reading through drafts of this thesis, making helpful suggestions, pointing out egregious errors

Thanks to Meg, Micol, Chin and Tim for checking up on me periodically and making sure I have some down time away from the lab and office. I am very lucky to have you as friends.

Bolek, Ewa, Meg, and Zbigniew are people without whose love, care, support, and understanding I would not have been able to accomplish anything. My parents, Ewa and Zbigniew, gave me the best opportunity and foundation I could imagine; they have always encouraged my endeavours, giving me a gentle nudge or a swift kick whenever I needed one. My brother has never shied away from helping me, and I can hope he can say the same of me; he has grown up to be an incredibly talented, interesting, and intelligent person. I am very proud of him. Meg has been amazingly patient with me; somehow, she has stuck with me through the years I have spent in graduate school. I look forward to us spending a very long time together.

FIREBall was generously supported by NASA and CNRS, while CWI research and development efforts were enabled by funding from NSF and Caltech Optical Observatories. This research has made use of NASA's Astrophysics Data System.

Abstract

Gas in the intergalactic medium serves as the fuel for galaxies. It carries signatures of galactic feedback, including matter and energy outflows. Understanding the morphology, thermodynamics, chemistry, and kinematics of this gas is key to understanding galaxy formation and evolution. The principal method of characterizing this gas has been the study of the Lyman α forest and associated metal systems. While this work has yielded deep insights into the nature of intergalactic matter, the scarcity of suitable background sources does allow for a full three-dimensional picture. Numerical simulations and theoretical work indicate that this gas produces faint and extended recombinant line emission. Its signatures in Lyα (1216 Å), OVI(1033 Å), CIV(1550 Å) are expected to be the strongest. Recent advances in technology and fresh ideas in instrumentation are allowing access to the predicted surface brightness of intergalactic emission. The Faint Intergalactic Redshifted Emission Balloon (FIREBall) and the Cosmic Web Imager (CWI) are two integral field spectrographs probing different redshift regimes, which have been designed for the specific purpose of detecting and mapping emission from the intergalactic medium. FIREBall, operating in the balloon ultraviolet window around 2000 Å, probes the redshift range $0.3 < z < 1$, while CWI, a ground-based optical instrument, studies the Universe at $2.5 < z < 7.0$. Both instruments collected their first science data in mid-2009. This manuscript discusses the science case for the spectrographs, focuses on their designs, construction, testing, first light, target selection, observations, data reduction, and analysis. Initial results are presented and discussed.

Contents

List of Tables

List of Figures

Chapter 1

Introduction

1.1 Overview

A century of theoretical and observational work in cosmology, including a series of clever and careful measurements driven forward by technological advances, has led us to a model of the Universe that we have dryly termed the ΛCDM concordance cosmology (Einstein & de Sitter 1932; Hubble 1929; Netterfield et al. 2002; Smoot & Murdin 2002; Komatsu et al. 2011; Bennett et al. 2003; Perlmutter et al. 1997; Riess et al. 1998).

We believe that the observable Universe began with a Big Bang. It underwent a series of transitions during which the fundamental forces—the strong, weak, electromagnetic and gravitational—decoupled from one another. Space expanded during an exceedingly short period of rapid inflation (Guth 1981), by at least 78 orders of magnitude, effectively erasing any nonzero curvature the Universe was imparted with. It left behind a hot, nearly spatially uniform soup of quarks, gluons, leptons, and, it appears, dark matter particles. A much less rapid cosmological expansion followed and the plasma began to cool. Baryogenesis occurred, leaving the world dominated by matter (in preference to antimatter) via a yet-to-be fully understood symmetry-breaking process. Nucleosynthesis formed light elements, the building blocks of stars and galaxies, with the photon-to-baryon ratio at that time imprinted into the relative abundances of light elements and a characteristic deuterium-to-hydrogen D/H ratio (Burles et al. 2001). Dark mater particles, then neutrinos, then photons, decoupled from the cooling baryonic matter. The latter left a (very informative) fingerprint on the sky, the so-called surface of last scattering, detected in the form of the cosmic microwave background radiation (CMBR) (Komatsu et al. 2011; Bennett et al. 2003; Lee et al. 2001; Netterfield et al. 2002; Bennett et al. 1996; Smoot & Murdin 2002). After this epoch, near $z \sim 1100$, atoms recombined and the Universe became opaque to light at ultraviolet and visible wavelengths. As the plasma continued to cool and expand, gravitational interactions continued to amplify small primordial density perturbations, causing dark and baryonic matter to slowly coalesce into a network of interconnected sheets and filaments: a cosmic web (Bond et al. 1996). The material continued

its collapse, with progressively larger overdensity regions breaking away from the bulk expansion, contracting by many orders of magnitude to form stars, galaxies, galaxy groups, and, most recently, galaxy clusters.

Statistical analysis of the distribution of matter can reveal how much different components and species contribute to the closure density of the Universe. Locations of the peaks in the baryonic matter power spectrum obtained from CMB measurements, combined with distance measurements to standard-candle supernovae Ia, and matter power spectra derived from galaxy surveys and line-of-sight Lyman α forest observations, indicate that we appear to live in a world that has $73.4 \pm 2.9\%$ of its energy density locked in the form of enigmatic dark energy, $22.2 \pm 2.6\%$ confined in mysterious dark matter, and $4.49 \pm 0.28\%$ stowed in pedestrian baryons[1]. There is a natural sequence of questions that may be asked about each of these components: What are they? Where are they? How do they interact with each other? How do they change over cosmic time? How can we detect them? Have we detected them? An immense effort is under way to answer these queries for the three chief components of the energy budget of our Universe.

Dark energy. This component is responsible for the acceleration of our Universe, and is the likely culprit responsible for the epoch of inflation. It is unclear whether it is a manifestation of vacuum energy, some new form of energy, or simply a term that covers up a flaw in our understanding of general relativity. The state of knowledge about dark energy is reviewed in Frieman et al. (2008).

Dark matter. The essence of dark matter is also uncertain. The case has been mounting for a (thus far) invisible, pressureless matter component, that interacts almost exclusively gravitationally. Its presence has been argued since Zwicky's observation of motions of galaxies in the Coma cluster (Zwicky 1933), through Rubin's study of rotation curves of galaxies (Rubin et al. 1985), with strong evidence emerging from recent observations of the Bullet cluster (Clowe et al. 2006). The properties of particles that constitute this matter are being constrained by particle physicists and astronomers, with various candidates, including WIMPs, sterile neutrinos, and axions, coming under consideration. A summary of the physics involved, and the efforts to advance the understanding of dark matter, is given in Feng (2010).

Baryons. The final major contributor to the cosmic energy density, baryonic matter, couples readily to electromagnetic radiation, which our eyes, and the technology we have been able to develop, are suited to detect. Consequently, this is the best studied fraction of the cosmic energy budget; data has been gathered about its state 380,000 years after the Big Bang to our current

[1]Various residual radiation fields and particles add to the Universe's energy density, but their contributions are small (see Fukugita & Peebles 2004). Additionally, observations of the CMBR indicate that the Universe is flat, with the energy density associated with the curvature term negligibly small.

epoch, when the Universe is 13.7 billion years old. Despite this, our knowledge of baryonic matter is far from complete. For instance, a census of material at redshift $z \approx 3$ accounts for all of the baryonic matter in collapsed components (stars, galaxies) and diffuse components (Lyman α forest), although the latter is based on extrapolation from line-of-sight absorption measurements. The same bookkeeping exercise for the current epoch, $z \approx 0$, reveals that we do not see roughly 40% of these particles (Fukugita & Peebles 2004; Prochaska & Tumlinson 2009). Constraints from the CMB derived from WMAP (Komatsu et al. 2011; Bennett et al. 2003) and the presence of the Gunn-Peterson trough in the spectra of high-redshift quasars (Gunn & Peterson 1965; Becker et al. 2001) imply that the normal matter in the Universe, which became neutral soon after having decoupled from the radiation field ($z \sim 1100$), was later reionized. The vast majority of HI was all but obliterated in the redshift interval $6 < z < 14$, leaving behind a trace fraction, $n_{\rm HI}/n_{\rm H} \sim 10^{-5}$, that is detected through the presence of the Lyman α forest. He II reionization appears to have followed suit at $z \sim 3$ (recently reviewed in Loeb & Barkana 2001; Fan et al. 2006). Neither the nature of the objects responsible, nor the specifics of the process, are well understood. QSO, AGN, and star-forming galaxies are listed as the potential ionizing sources, but the mechanisms by which ionizing radiation escapes these, the amount that escapes, and the ways in which this radiation affects the surrounding diffuse gas, are areas of active research.

Stars and galaxies are among the brightest, and therefore best studied, systems in our skies, yet the processes which control the formation of galaxies, the details of galactic inflows and outflows, the factors that trigger and quench star formation episodes within those galaxies, and the nature of the first sources that turned on, are not well-known.

A major key to understanding these issues concerning normal matter lies in characterizing the morphology, kinematics, chemistry, and thermodynamics of baryons that lie outside and at the boundaries of collapsed structures—the intergalactic medium (IGM); in figuring out how this matter contributes to the formation of galaxies, how it exchanges mass and energy with the galaxies and stars; how the gas evolves over cosmic time in changing gravitational and radiation fields; how, and when, it becomes enriched in heavier elements. Tremendous inroads have been made into this topic over the last 50 years via an intensive observational effort, predominantly using line-of-sight absorption system studies of the spectra of distant quasars, and theoretical work, supplemented by progressively more sophisticated numerical simulation techniques. The model that has emerged from this work and accounts well for the observable quantities is presented in section 1.2.2.

The author has participated in the design, development, construction, and first observations of two instruments dedicated to detecting, and beginning the process of mapping emission from the

IGM: FIREBall and CWI. FIREBall is a balloon-borne telescope coupled to a fiber-fed integral field spectrograph operating in a narrow atmospheric transmission window around 2100 Å probing hydrogen, oxygen, and carbon line emission from the IGM in the redshift range $0.3 > z > 1.2$.

CWI is a ground-based optical slicer-based integral field spectrograph mounted to the 5 m Hale telescope at Mt. Palomar, covering the visible wavelengths, aimed at mapping extended low surface brightness emission from gas at redshifts $2 > z > 7$.

Section 1.2.1 discusses the observational signatures of the intergalactic medium in absorption and emission, and outlines the techniques used to exploit them. Section 1.2.2 describes the current model of the IGM, focusing on the supporting observational evidence, and theoretical models and predictions. Section 1.2.3 presents the case for, and feasibility of, mapping the IGM, highlighting the new perspectives it offers on old problems. Sections 1.5.1 and 1.5.2 discuss the two instruments in the context of the goal of mapping the IGM, including science design drivers. The subsequent chapters detail the design, manufacture, integration, calibration, commissioning, and initial observations with the two spectrographs. Each chapter ends with a brief summary and a short description of planned future work.

Throughout this manuscript Λ-CDM concordance cosmology is assumed, with parameters based based on the WMAP 7 year data (Komatsu et al. 2011): $h = 0.7$, $\Omega_m = 0.27$, $\Omega_\Lambda = 0.73$, $\Omega_b = 0.046$.

The choice has been made use physical surface brightness units throughout this work, namely the Line Unit (LU) for radiative line emission and the related Continuum Unit (CU) for continuum fluxes. These are defined by

$$1\,\mathrm{LU} = 1\,\mathrm{photon\,s^{-1}\,cm^{-2}\,sr^{-1}}, \tag{1.1}$$

$$1\,\mathrm{CU} = 1\,\mathrm{photon\,s^{-1}\,cm^{-2}\,sr^{-1}\,\text{Å}^{-1}}. \tag{1.2}$$

These are related to the more frequently encountered surface brightness units by

$$1\,\mathrm{LU} \approx 1.16 \times \left(\frac{\lambda}{4000\,\text{Å}}\right)^{-1} \times 10^{-22}\,\mathrm{ergs\,s^{-1}\,cm^{-2}\,arcsec^{-2}}, \tag{1.3}$$

with a corresponding expression for CU.

1.2 Structure Formation and Intergalactic Matter

1.2.1 IGM Observational Signatures and Detection Techniques

Observational astronomy relies on the detection of an excess or a deficit of electromagnetic radiation from celestial objects as compared to their surroundings, although efforts are ongoing to detect other signatures, notably neutrinos (MINOS Collaboration 2006; IceCube Collaboration 2007), cos-

mic rays (Auger Collaboration 2004; Belz 2009), and gravitational waves (Barish 1995; Sigg & the LIGO Scientific Collaboration 2008; Acernese & the VIRGO Scientific Collaboration 2008; Prince 2009). The challenge is always to select, or build, an observational tool that is well matched to the expected characteristics of the phenomenon being studied. The process is usually iterative: increased understanding of the physics involved refines the requirements placed on instrumentation; the application of this new knowledge, coupled with advancements in technology, reveal more about the underlying science, closing the loop. This has been the case with observations of the intergalactic and circumgalactic gas.

Detection thresholds for absorption and emission measurements are dependent on the effective collecting area of the telescope (its physical size, its throughput, and the throughput of the atmosphere), the nature of the object being observed (its physical size, spectral width) with additional constraints from the limited sizes of available detectors. Expressions for the limiting sensitivities of spectrographs aimed at diffuse emission are discussed in appendix A.

1.2.1.1 Absorption: Line-of-Sight Spectroscopy

The IGM was first observed as a decrement in the spectra of high redshift QSOs blueward of their Lyman α emission peak (Gunn & Peterson 1965). This detection foreshadowed the primary method that has been used for studying the diffuse intergalactic matter since, starting with Lynds (1971): line-of-sight absorption spectroscopy.

Intervening matter lying between the observer and a distant continuum source leaves an imprint on the spectrum of that object in the form of absorption lines. It is preferable that the object spectrum be fairly featureless, or at least well constrained; furthermore, the object needs to be at a sufficiently high redshift and bright enough to allow us to probe matter over a useful fraction of cosmological time. The primary type of objects used have been high redshift quasars, with gamma-ray burst (GRB) afterglows (Fiore et al. 2000; Vreeswijk et al. 2004; Chen et al. 2005) and galaxies (Steidel et al. 2010) employed recently.

The technique relies on the rich spectrum of atomic transitions of the most abundant cosmic elements that resonantly scatter or absorb incident light. As almost 90% of all atoms in the Universe are hydrogen, Lyman α, the strongest of the HI transitions in the UV, is most frequently encountered. Useful reviews of the physics of the the IGM, and the absorption signatures its neutral hydrogen fraction imprints on background continuum spectra, the Lyman α forest, can be found in Rauch (1998) and Meiksin (2009); the discussion here draws substantially on the latter manuscript. The wavelengths associated with the studied transitions lie predominantly in the ultraviolet and visible regimes of the electromagnetic spectrum, with some notable lines corresponding to inner shell transitions of heavier elements occurring in the x-ray range. The primary lines used in this technique are listed in table 1.1. The observed wavelengths of these transitions depend on the redshifts of

the scattering material being probed, which can cause confusion in line identification, complicating data analysis. Absorption line studies in our Universe are further complicated by an increase in the number of line-of-sight scatterers per unit redshift, with redshift; $dN/dz \propto (1+z)^{\gamma}$, with γ evolving from $\gamma \approx 0.13$ at $z < 1$ to $\gamma \approx 2.47$ for $z > 1.5$ (Janknecht et al. 2006). Thus the neutral hydrogen lines become dense in wavelength, often blending and masking one another and the signatures of other elements. The characterization of metal lines that fall within the Lyman α forest relies on identification, fitting, and removal of HI lines, combined with association of these lines with those of other species tracing the same physical systems. Absorption lines from transitions that have redshifted wavelengths longer than the observed Lyman α wavelength of the background source (e.g., MgII, CIV, SiIV) are more easily accessible.

The absorption lines can be fitted with Voigt profiles, with the optical depth at line center given by

$$\tau_0 = \frac{\sqrt{\pi}e^2}{m_e c}\left[\frac{1}{4\pi\varepsilon_0}\right]\frac{N}{b}\lambda_{lu}f_{lu}, \tag{1.4}$$

$$b = \left(b_{\rm th}^2 + b_{\rm kin}^2\right)^{1/2}, \tag{1.5}$$

$$b_{\rm th} = \left(\frac{2k_B T}{m_a}\right)^{1/2}, \tag{1.6}$$

where N is the line-of-sight column density of the scattering species; b is the Doppler parameter, which has contributions both from the thermal motions of the atoms ($b_{\rm th}$) and from microturbulence within the cloud ($b_{\rm kin}$); λ_{lu} the transition wavelength,; f_{lu} the transition oscillator strength; m_a the mass of the scatterer. Other quantities have their usual meanings. The product $\lambda_{lu}f_{lu}$ has been tabulated for the species relevant to radiative processes within the IGM (Morton 1991, 2000, 2003).

The characterization of a single absorption line does not reveal much about the matter responsible for it. There are degeneracies between column density and temperature, thermal and kinematic Doppler widths, as well as some ambiguity about what element is responsible for the absorption. A combination of several lines or multiline complexes can resolve these degeneracies, though the amount of information that can be extracted depends on the nature of the lines and the quality of the spectrum. Absorption lines imprinted by optically thin absorbers ($\tau_0 \ll 1$) allow for the line profile to be fitted, revealing information about both b and τ_0, provided instrument broadening effects can be removed. For opaque (saturated) lines, and for instances where instrument broadening cannot be canceled, the total amount of flux removed by the absorber is measured, and tabulated as an equivalent width w_λ; this quantity is converted into τ_0 by referring to a so-called curve of growth for the ionized species in question. The opacity of the line determines the parameter that is directly extracted; optically thin ($\tau_0 \ll 1$) and very opaque ($\tau_0 > 10^4$) lines yield the column density N of the absorber, while an intermediate optical depth provides a measurement of the Doppler parameter

b, with very loose constraints on N. The latter has been the root cause in the difficulty pinning down the HI column densities of Lyman limit systems, with metal lines required to estimate $N_{\rm HI}$ (O'Meara et al. 2007).

The relative locations of the lines within the rest-frame electromagnetic spectrum can disentangle the elements responsible for the absorption. Lines corresponding to the different ionization states of the same element — provided the column ratios of the species are well constrained — coupled with radiative transfer models (e.g., `CLOUDY`; Ferland et al. 1998) that include relevant ionizing sources (background or local point source radiation), indicate the temperature. Lines originating from different elements can decouple thermal from kinetic broadening and constrain the metallicity of the scattering medium.

Determining the lineshape to extract physical parameters is difficult when spectral resolution of the instrument is insufficient, or when absorption lines blend together, especially in ranges of the continuum where the line density is high (as for the Lyman α forest at $z \sim 3$). In such cases, the mean optical depth along the line-of-sight as a function of redshift is computed and compared to a theoretically derived expression in an attempt to learn something about the statistical nature of the absorbers. Such a formula was derived by Gunn & Peterson (1965):

$$\tau_{GP} = 1.8 h^{-1} \Omega_{\rm M}^{-\frac{1}{2}} \left(\frac{\Omega_{\rm b} h^2}{0.02} \right) \left(\frac{1+z}{7} \right)^{\frac{3}{2}} \left(\frac{n_{\rm HI}}{n_{\rm H}} \right). \tag{1.7}$$

This may be inverted to yield the hydrogen neutral fraction whenever τ can be measured. Statistical methods are also used when comparing measured absorption spectra with those generated by numerical methods, as they are computationally faster and more robust than automated fitting of absorption lines.

The workhorse instruments of this technique have been the Faint Object Spectrograph (FOS; Harms et al. 1979), Space Telescope Imaging Spectrograph (STIS; Woodgate et al. 1998), and now Cosmic Origins Spectrograph (COS; Froning & Green 2009; Green 2000), aboard the Hubble Space Telescope, and Far Ultraviolet Spectroscopic Explorer in the ultraviolet; Chandra X-Ray Observatory and XMM-Newton in the x-ray regime; and instruments on 5 and 10 m class ground telescopes in the optical and near-infrared, including HIRES at Keck (Vogt et al. 1994) and UVES at the VLT (Dekker et al. 2000) . The latter have deployed a variety of technologies, including basic long-slit, multislit mask (e.g., DEIMOS at Keck; Faber et al. 2003), and multiobject fiber-fed (e.g., SDSS; Owen et al. 1994). The spectral resolution of the observations with the above instrumentation ranged from $R \equiv \lambda/\delta\lambda$ of a few thousand to a few tens of thousands (equivalently, Δv from 100 down to 10 km/s), the latter sufficient to resolve some of the narrowest metal and hydrogen lines within the Lyman α forest.

Table 1.1. Partial list of atomic transitions used for study in the IGM, including the physical conditions their presence traces

Species	Wavelength(Å)		CIE	Redshift Range						Notes
				CWI				FIREBall		
				Full		Current				
	Prim	Sec	Temp (K)	Min	Max	Min	Max	Min	Max	
HI	1216	var.	—	2.1	7.2	2.8	3.5	0.6	0.9	Lyα and other Lyman transitions (down to the Lyman limit at 912 Å) are ubiqutous in emission and absorption. Spectral profiles depend on the optical depth of the emitting/absorbing gas and its environment.
CIII	977	—	7.0×10^4	2.9	9.2	3.7	4.6	1.0	1.3	Present in moderately shocked gas in the CGM at low redshift
CIV	1548	1551	1.0×10^5	1.5	5.5	2.0	2.5	0.3	0.5	At higher redshifts, is predominantly detected in the Lyα forest in a photoionized state; at lower redshifts the species continiues to be present in the low temperature Lyα forest, but is also present in shock-heated, collisionally ionized gas in the CGM and WHIM, in both absorption and emission.
NV	1239	1243	1.8×10^5	2.1	7.1	2.7	3.4	0.6	0.8	Traces WHIM+CGM, present in photoinonized gas at high redshift.
OVI	1032	1038	2.8×10^6	2.7	8.7	3.4	4.3	0.9	1.2	Mostly photoionized at high redshifts, collisionally ionized at later times, tracing somewhat warmer gas in the WHIM and CGM than CIV, detectable in both absorption and emission.
NeVIII	770	780	5.6×10^6	3.9	11.9	4.9	6.1	1.6	1.9	Strong tracer of WHIM and CGM in CIE.
MgII	2796	2803	1.0×10^4	0.4	2.6	0.6	1.0	—	—	One of the major tracers of the cool, photionized gas in the Lyα forest.
SiIV	1394	1403	8.0×10^4	1.7	6.2	2.3	2.9	0.4	0.6	Strong tracer of the cool Lyα forest in absorption, might be detectable in emission from the collisionally ionized WHIM and CGM.

Reliance on sparse point sources is the primary weakness of the powerful line-of-sight absorption technique. The method probes line-of-sight distribution of matter but carries little information about the transverse structure it pierces. The on-sky densities of sufficiently bright high redshift QSOs that yield high quality absorption spectra are on the order of one per square degree (Richards et al. 2002), with a modest number of closely spaced or multiply lensed QSOs that can probe the the same foreground cosmic structures. Another class of objects, GRB afterglows, although they have excellent spectral characteristics, do not provide improved spatial coverage over that of QSOs. Galaxies, as they are more extended and have a larger covering fraction, give a much higher resolution view of the foreground matter. Their spectra are fainter and more complex than those of quasars, and while pioneering observations using them as the continuum background source are being conducted (Steidel et al. 2010), large-scale statistically significant surveys employing them will require the next generation of 30 m ground-based telescopes and large aperture UV-Vis space missions.

1.2.1.2 Emission from the IGM

The diffuse matter of the intergalactic medium is at temperature $T > 10^4\,\mathrm{K}$, as inferred from absorption linewidths, and radiates as it cools. The strength and spectrum of the radiation depends on the temperature, density, geometry, and metallicity of the gas; those quantities are affected by the local ionizing background, mechanical energy input, and chemical enrichment from the surroundings. A parcel of hot gas, such as that in the IGM or CGM,[2] will lose energy, with the dominant cooling pathways involving radiation. The principal ones are free-free emission (Bremsstrahlung), inverse Compton scattering, and line radiation, including the two-photon process. Depending on the composition, density, temperature, and environment of the gas, any of the three mechanisms may be significant. The top panel of figure 1.1, borrowed from Sutherland & Dopita (1993), shows the contributions of various cooling mechanisms (with the exception of IC) to the overall cooling of a parcel of gas.

Free-free emission. Also known as thermal Bremsstrahlung, or braking radiation, this is the result of thermal electrons scattering in the electric fields of ionized nuclei. The emissivity depends on the abundance and charge of at least partially ionized nuclei (n_i, Z_i), free electrons (n_e), and the plasma temperature (T):

$$\epsilon_{ff} \propto T^{\frac{1}{2}} n_e \sum_i n_i Z_i^2, \tag{1.8}$$

[2]While the term intergalactic medium typically refers to all matter present outside of galaxies, in this volume the material lying in the immediate neighborhood of galaxies, that with which the galaxies interact through inflows, outflows, or radiation is referred to as the circumgalactic medium (CGM).

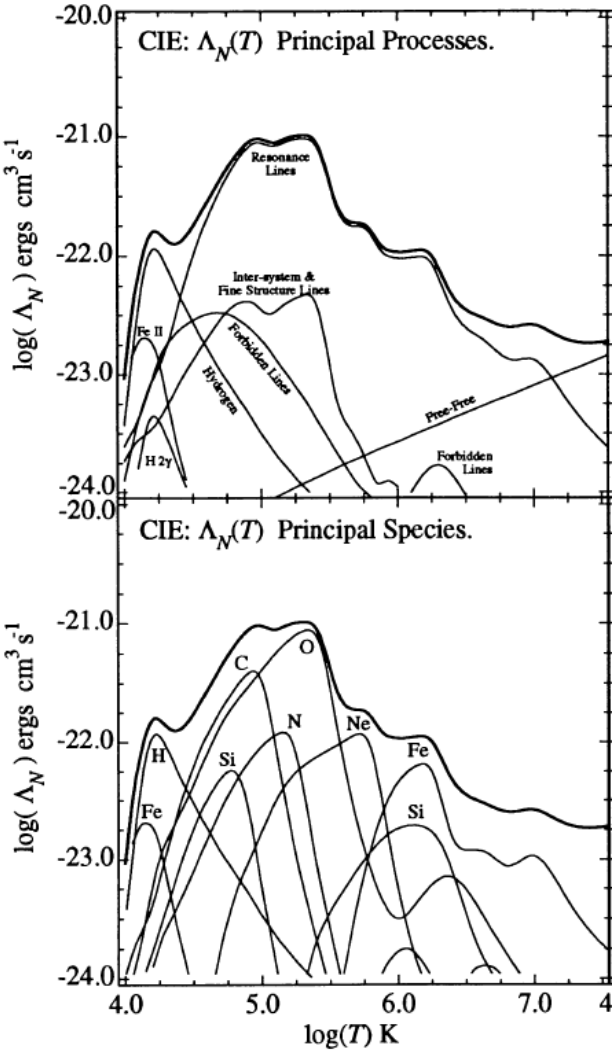

Figure 1.1. Cooling function for solar abundance gas in collisional ionization equilibrium. Much of the gas in the CGM and in the warm-hot intergalactic medium (WHIM) is expected to be in this state. The top panel shows the contribution of different processes to the overall cooling as a function of temperature. Recombinant radiation from metals and hydrogen dominates the curve. The bottom panel indicates the contributions of different elements. Hydrogen, carbon, and oxygen recombinant radiation dominate the cooling curve; this is the principal reason why emission mapping focuses on strong lines of those three elements. The contribution of metals to radiative energy dissipation changes proportionally with the metallicity of the gas, since they do not have an appreciable impact on the free electron population, regardless of their ionization state. At temperatures $T \sim 10^4$ K, hydrogen is the main cooling pathway for intergalactic plasma. Figure reproduced form Sutherland & Dopita (1993) with permission of the authors and AAS.

where the summation takes into account contributions from different species. In the context of the intergalactic matter, free-free emission may become significant in regions that are at high temperature, especially if they contain substantial metal abundances. Notably, this implies that this effect needs to be considered when observing the warm-hot gas within the IGM (WHIM) and around galaxies (CGM), where temperatures may reach as high as $T \sim 10^7\,\mathrm{K}$ with substantial metal enrichment. Bremsstrahlung is also a major cooling mode for $T \sim 10^8\,\mathrm{K}$ gas in cluster cores, and allows for the estimation of the gas's contribution to the energy budget (Reiprich & Böhringer 2002).

Inverse Compton scattering. A plasma can lose energy when its electrons Compton scatter off of a low energy background radiation field. The formalism was worked out by Weymann (1965), with the energy lost by gas at temperature T to a radiation field at temperature T_R given by

$$\epsilon_{IC} = \left[4c\frac{\sigma_T}{m_e c^2}\right] n_e\, a T_R^4\, k_b (T - T_R), \tag{1.9}$$

where the physical constants have their usual meanings. In the context of IGM cooling, the radiation field of most interest is the CMBR, which at the present epoch has a temperature $T_{CMB} = 2.735\,\mathrm{K}$ (Mather et al. 1990), contributing only negligibly to the cooling. The effect was much more relevant at earlier epochs, given the strong redshift dependence of $T_{CMB} \propto (1+z)^4$. This mechanism is responsible for intracluster gas up-scattering CMB photons, the Sunyaev-Zeldovich effect, noted in CMB observations.

Line radiation. Ions in a plasma recapture electrons, which cascade down the energy levels of the atom, emitting photons, which may escape the gas, carrying away energy. The energy loss is a function of temperature and ionization species; the rate is proportional to the density of the ion in question, and the density of unbound electrons: $\epsilon_{LR} \approx n_i n_e \beta(T)$, where $\beta(T)$ encodes the temperature dependence of the emission process. Although the simplest case of pure H can be investigated analytically (see Meiksin 2009), the ionization balance and energy transfer of multispecies plasmas are solved using self-consistent radiative transfer computer programs. These take into account excitation and deexcitation mechanisms affecting each species and ionization state, including collisional ionization, autoionization, photoionization, radiative recombination, dielectronic-recombination, charge transfer ionization with HII and HeII, charge transfer ionization with He I, and photoionization with Auger electron ejection. Furthermore, the emergent spectrum of the radiation depends on the geometry and optical depth of the parcel of gas.

Photons emitted in optically thin environments escape the gas, and the emission spectrum typically has a Voigt profile, shaped by the nature of the transition, thermal, and kinematic broadening. This is the case with line emission from metals within the IGM and CGM.

If the opacity of the gas is high, the full mechanism of radiative transfer needs to be employed. In the context of the IGM, this happens almost exclusively in the case of neutral hydrogen in the densest regions. Energy imparted on the gas — either radiation from a UV background, a strong internal or external ionizing source, or energy dissipated via gravitational infall converted into thermal motions of particles — ionizes hydrogen atoms. Recombinative reionization cascades lead to production of various hydrogen series photons: ∼40% of recombinations bypass the $n = 2$ hydrogen level, while one-third of those that do not bypass it go through the $l = 0$ rather than the $l = 1$ state, resulting in two-photon decay. Thus ∼40% of individual recombinations terminate in the emission of a Lyα photon. However, a high opacity gas will recapture the vast majority of the photons that bypassed $n = 2$, and reprocess ∼2/3 of those into Lyα. Monte Carlo simulations of the emergent spectrum of ionizing radiation incident on an optically thick gas predict that nearly 70% is recovered in Lyα radiation (Gould & Weinberg 1996); an additional few percent are expected to be lost to dust absorption. Furthermore, as the gas is optically too thick to allow these photons to escape, they undergo a random walk within the cloud, both spatially and spectrally. They remain trapped until their energy shifts sufficiently toward the wings of the resonance line for the optical depth they experience to become small, $\tau < 1$, at which point the photons escape. The resultant spectral profile has a characteristic double peak, with the wavelength separation of the two peaks proportional to $\tau_0^{1/3}$, the optical depth of the emitting gas at the center of the line. The details of the spectra for different cases have been studied analytically, and evaluated computationally by various authors, e.g., (Neufeld 1990; Gould & Weinberg 1996; Verhamme et al. 2006; Kollmeier et al. 2010). While the profile is symmetric and double peaked in an idealized case, observed spectra are expected to show asymmetry, mainly due to reabsorption of the blue-side peak within the emitter's environment. This emission mode is often referred to as Lyman α fluorescence.

The intensity of emission depends on the conditions of the gas. Cosmological numerical simulations (see section 1.2.1.10), follow the evolution of baryonic matter density, temperature, and metallicity; they include galactic feedback, outflows, inflows, and shocks. A radiative transfer code, typically `CLOUDY` (Ferland et al. 1998), is used to compute the surface brightness, size, and spectra of emission from the simulated baryons. The typical characteristics of IGM emission emerging from this method are shown in table 1.2, while figure 1.2 shows some of the generated emission maps relevant to IGM/CGM mapping. It should be noted that these computations usually assume single phase gas in thermal equilibrium. This assumption need not be accurate, and models are being developed to understand emission from multiphase or shocked media (Cen & Fang 2006; Gnat & Sternberg 2007).

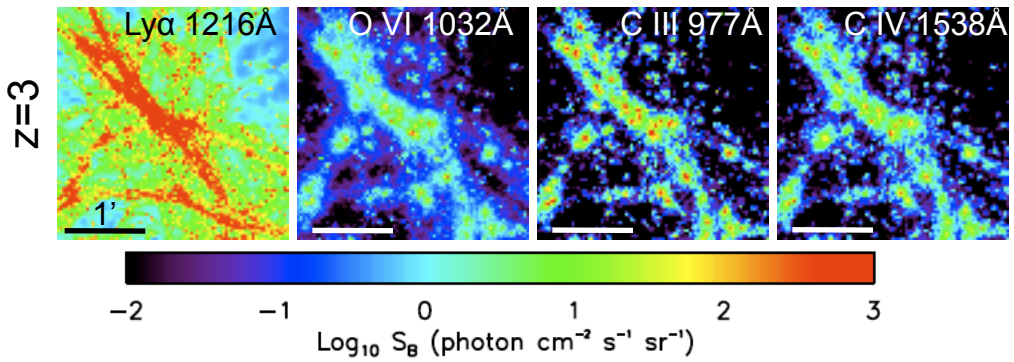

Figure 1.2. Modeled emission maps for four UV ionization species, as indicated, for gas at redshift $z = 3$. Each image is marked with a 1' bar, roughly the size of the field of view of CWI (and KCWI). Lyman α and O VI emission appear more diffuse and delineate the overall filamentary structure of the overdense region, whereas the two carbon transitions exhibit clumpier morphology, more concentrated at the densest regions of the field, presumably in the immediate vicinity of galaxies. The color bar encodes the surface brightness in line units (LU); red and possibly yellow regions are accessible with CWI in direct imaging, while green might be detectable with cross-correlation analysis (see text). Figures adapted, with permission, from Bertone & Schaye (2010) who generated them based on simulations from the OWLS project (Schaye et al. 2010) using `CLOUDY`.

1.2.1.3 Emission: Line-of-Sight Spectroscopy

Line-of-sight spectroscopy is not limited to absorption measurements. A well-informed, or serendipitous, placement of the spectrograph slit on the sky can lead to a detection of emission from diffuse matter. As the format of the field of view is not well matched to the typical emitting region shapes and sizes, the method is mostly sensitive to small objects (approximately the size of the slit-width), and, in principle, to very extended objects, such as filaments. Slit-size effects are a concern for slit spectroscopy. If the seeing disk or the targeted object is larger than the size of the spectrograph aperture, the measurement may underestimate the flux from the source. This effect must be accounted for in data analysis, although using multiple pointings with adjacent, or overlapping, slit position can help. Deep long-slit spectroscopic imaging has been utilized, and has revealed emission regions of a few kiloparsecs around galaxies (Rauch et al. 2008).

1.2.1.4 Emission : Narrowband Imaging

The strength of narrowband imaging is combining a large field of view with good efficiency (limited number of optics compared to a spectrograph), and a spectrally narrow filter (usually a few nanometers). These characteristics make narrowband imaging a prime tool for survey-oriented observations, recording emission from a single line, typically Lyα in the case of structure and galaxy formation searches. Typical observations involve long-integration-time narrowband imaging of a

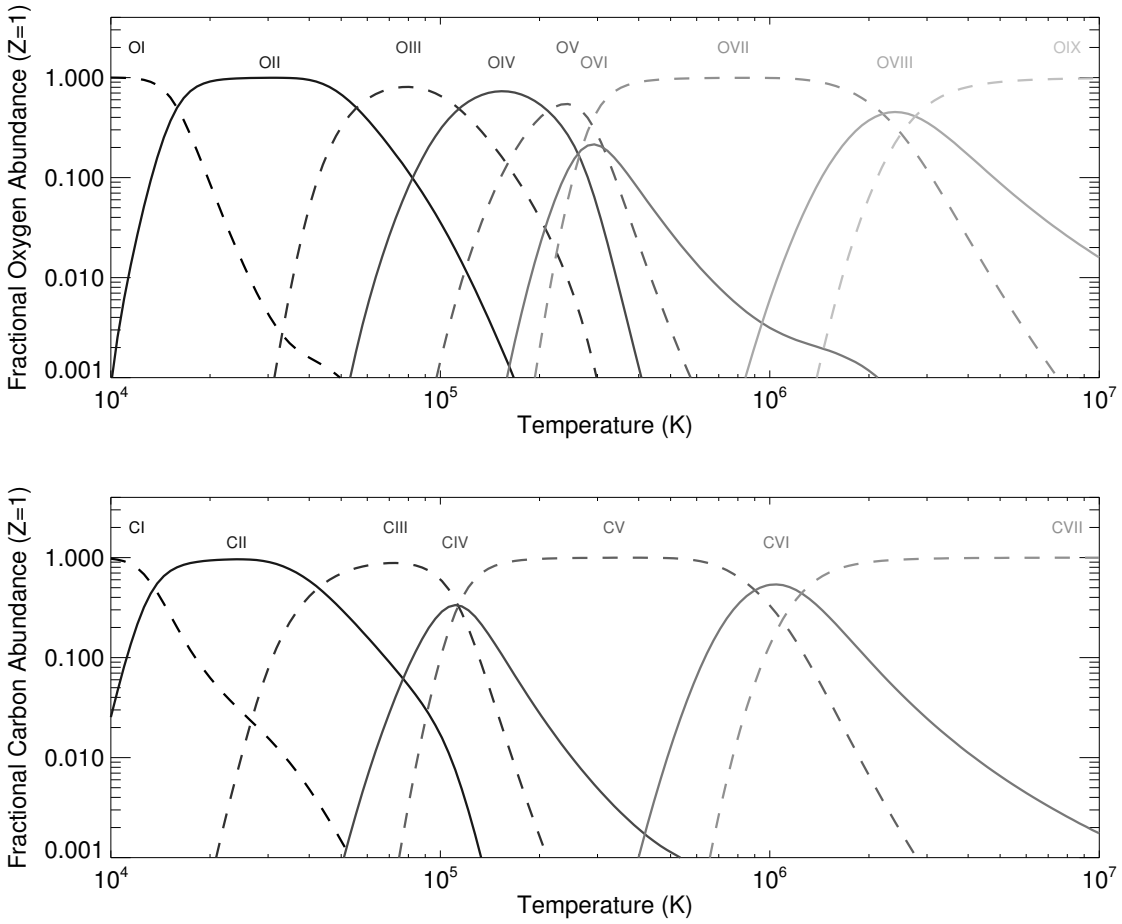

Figure 1.3. Fractional abundances of various states of ionization of carbon and oxygen for a solar composition gas in collisional ionization equilibrium. The species primarily responsible for emission from the IGM around galaxies and from the WHIM are C IV, O VI, and O VII. C IV and O VI have high oscillator strengths and dominate emission around their peak abundances. The values were computed using CLOUDY (Ferland et al. 1998) by Gnat & Sternberg (2007) and made available on the web (`http://wise-obs.tau.ac.il/~orlyg/cooling/`).

field and shorter broadband images of the same target. The broadband data is used for identification of continuum sources and combined to form a background image, which includes sky and instrument backgrounds, subsequently subtracted from the narrowband image. The primary factors that limit the sensitivity of narrowband imaging are detector noise, system efficiency, and spatial sky background variation. A wekness of the technique, when it comes to understanding the processes governing the targets being observed, is that it carries limited velocity information. While a 50 – 100 Å bandpass is sufficient to detect and flag the locations of major features of the emitting gas, any velocity information on scales of $\Delta v \sim 1500$ km/s in the visible part of the spectrum is lost.

1.2.1.5 Technique: Integral Field Spectroscopy

The concept of integral field spectroscopy (IFS), also known as imaging spectroscopy, is simple: reformat a low aspect ratio patch of a telescope's focal plane into a long-slit configuration that serves as the entrance to the optics of a classical spectrograph. There are multiple ways this reformatting can be achieved; the methods are discussed in more detailed in section 1.3 and reviewed in Bershady (2009). The technique is a hybrid between classical spectroscopy and narrowband imaging. Typical applications do not offer the giant field-of-view of narrowband imaging, nor do they provide a very high spectral resolution that classical spectrographs do, they do offer a compromise, and instrument parameters may be chosen to optimize the resolution field-of-view product to the target science. This was the intent of employing IFS on CWI and FIREBall, the two instruments designed and built to observe dim and diffuse emission from intergalactic matter. The IGM, CGM, and WHIM structures have low aspect ratios, with characteristic sizes varying from a few to a few tens of arcseconds (with the exception of the longest filamentary structures which may span a few tens of arcminutes). IFS is well suited to observing these structures, provided sufficiently high spectral resolution is achieved. The spectral and spatial requirements for integral field spectrographs in the context of observing low surface-brightness emission from diffuse sources are discussed in section 1.4.

1.2.1.6 Detection Method: Direct Observation

Direct detection of emission from the IGM, or CGM, requires long integrations (either spectroscopically or via narrow-band imaging) on a target region, and on a sky-background patch. The expected emission levels are expected to be faint; sky brightness and subtraction accuracy, detector background, instrument efficiency and resolution, and several other factors limit instrument sensitivity. These factors are discussed in the context of integral field spectroscopy in appendix A. Idealized noise-free observations are considered here, to investigate the dependence of the sensitivity limit on salient observational parameters. The sensitivity limit for an emitting region of size Ω, drowned out by a sky of surface brightness I_B being observed with an instrument with collecting area A,

efficiency η, through a filter of width $\Delta\lambda$ for a time T, with a signal-to-noise ratio requirement Σ is

$$I_S \geq \Sigma \left(\frac{2 I_B \Delta\lambda}{A \Omega \eta T} \right)^{\frac{1}{2}}, \tag{1.10}$$

$$\begin{aligned} I_S^{NB} \geq 5.2 \times 10^3 \left(\frac{\Sigma}{5} \right) \left(\frac{I_B}{10^5\,\mathrm{CU}} \right)^{\frac{1}{2}} \left(\frac{\Delta\lambda}{30\,\text{Å}} \right)^{\frac{1}{2}} \left(\frac{A}{5 \times 10^5\,\mathrm{cm}^2} \right)^{-\frac{1}{2}} \\ \left(\frac{\Omega}{100\,\mathrm{arcsec}^2} \right)^{-\frac{1}{2}} \left(\frac{\eta}{40\%} \right)^{-\frac{1}{2}} \left(\frac{T}{100\,\mathrm{ks}} \right)^{-\frac{1}{2}} \mathrm{LU} \end{aligned} \tag{1.11}$$

$$\begin{aligned} I_S^{IFS} \geq 3.7 \times 10^3 \left(\frac{\Sigma}{5} \right) \left(\frac{I_B}{10^5\,\mathrm{CU}} \right)^{\frac{1}{2}} \left(\frac{\Delta\lambda}{10\,\text{Å}} \right)^{\frac{1}{2}} \left(\frac{A}{2 \times 10^5\,\mathrm{cm}^2} \right)^{-\frac{1}{2}} \\ \left(\frac{\Omega}{100\,\mathrm{arcsec}^2} \right)^{-\frac{1}{2}} \left(\frac{\eta}{30\%} \right)^{-\frac{1}{2}} \left(\frac{T}{50\,\mathrm{ks}} \right)^{-\frac{1}{2}} \mathrm{LU}, \end{aligned} \tag{1.12}$$

where the second expression has been calculated for a deep narrowband exposure for a 5 m telescope, and the bottom expression for an integral field spectrograph exposure on the same class telescope for half the on-target integration time (the other half being used for obtaining sky background data). The quantities chosen reflect the typical parameters for narrowband and spectroscopic observations seeking dim and diffuse emission. The sensitivity limits are comparable, and both approaches have advantages (large field vs. good velocity resolution) and specific uses (survey vs. object study). It is worth noting that the narrower the emission line, or the broader the narrowband filter, the more pronounced the advantage of IFS (provided it can be resolved), since the limiting sensitivities scale as

$$\frac{I_S^{IFS}}{I_S^{NB}} \propto \left(\frac{\Delta\lambda_{IFS}}{\Delta\lambda_{NB}} \right)^{\frac{1}{2}}. \tag{1.13}$$

1.2.1.7 Detection Method: Stacking

Emission (or absorption) that is too faint to detect directly with a significant signal-to-noise ratio that is associated with brighter objects within the same physical structure can be characterized by stacking images (spectra) based on the location of those objects (or their spectral features), or, to a similar effect, coadding data, losing some spatial information. The gain of stacking data is increasing the effective integration time for a class of objects, especially when multiple instances of those objects are present in a single pointing.

This technique has been employed, for instance, in analysis of line-of-sight spectroscopic data to coax out information about metallicities of various classes of absorbers (Norris et al. 1983; Lu 1991; Pieri et al. 2010), or searching for ionizing emission leaking out of galaxies shortward of the Lyα

limit (Steidel et al. 2003; Shapley et al. 2003, 2006; Bridge et al. 2010; Steidel et al. 2010). Stacking has also been used in conjunction with narrowband imaging, making coadded images of galaxies to investigate emission from surrounding Lyman α halos (Hayashino et al. 2004; Steidel et al. 2011; Matuszewski & Martin in prep.).

Stacking and coadding can be used to characterize the strength and extent of emission from faint IGM in the context of integral field spectroscopy. As with narrowband imaging, stacks can be generated based on locations and redshifts of galaxies or QSOs. It is also possible to stack on anticipated large-scale structure filaments, as inferred from segments connecting known galaxy, quasar, or Lyα blob locations. The technique applied to imaging or integral field spectroscopy sacrifices finer morphological details of the signal to generate a higher signal-to-noise ratio detection. The method offers insight into the general properties of the stacked ensemble, rather than characteristics of the individual features.

1.2.1.8 Detection Method: Absorption Cross-Correlation Analysis

The surface brightness of the emitting region might be below the sensitivity limit for direct detection of a given spectrograph. In cases where the targeted volume is pierced by a bright background continuum source, the surface brightness of the region of the sky around the bright source can be cross-correlated with absorption features in the continuum spectrum. As the gas that is emitting is also the matter responsible for absorption, a simple product of the spectra of the background source and region surrounding it should reveal a signal. Figure 1.4 demonstrates the functionality of this method. The morphology of emitting gas can be mapped with the cross-correlation signal strength serving as a proxy, with computer modeling used to disentangle the geometry.

1.2.1.9 Detection Method: Pixel Luminosity Distribution Function

Emission from the IGM and CGM can be characterized in a statistical sense by considering the distribution of pixel surface brightnesses for emission from a single emission line. A trio of predictions based on numerical simulations is shown in figure 1.5. The simulations indicate that some of the processes governing the energetics of the IGM (AGN feedback, supernova feedback, IMF) can be constrained by looking at the high surface brightness tail of the PDF (Furlanetto et al. 2003; Bertone & Schaye 2010; Bertone et al. 2010b).

1.2.1.10 Numerical Simulations

As processing power has followed Moore's law (Moore 1965), access to more powerful and cheaper computers has become more common, and their use in cosmological, and astrophysical, simulations is now an industry in astronomy. Numerical modeling is, obviously, not a method of observation of the IGM, CGM or any other astrophysical phenomenon. It is, however, a predictive tool that

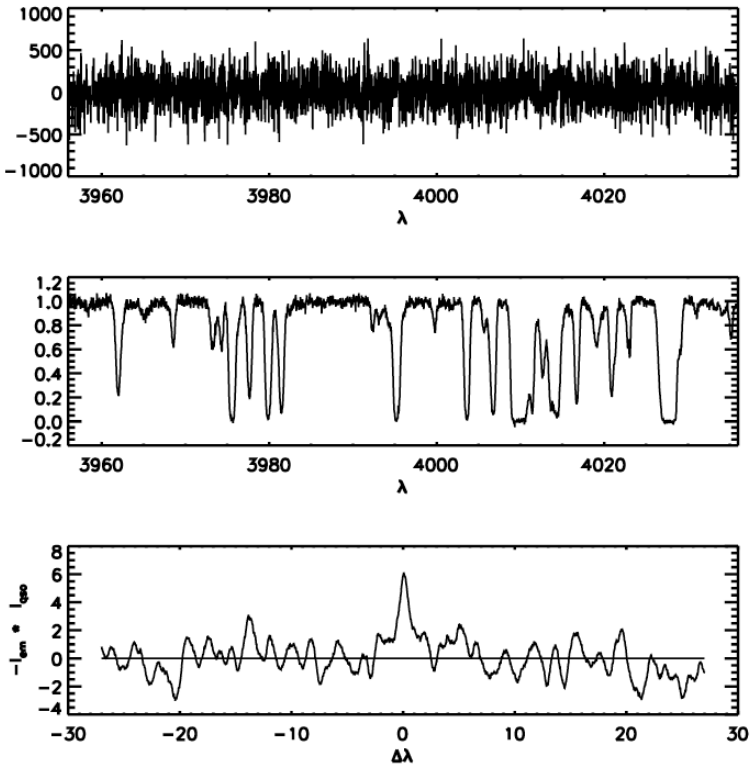

Figure 1.4. Dim emission from the IGM may be detectable by cross-correlation with a compact background source piercing the observed matter. The top panel shows a simulated weak ($\sim$10 LU) emission signal at $\lambda \approx 3995$ Å measured with a signal-to-noise ratio $S/N \sim 0.5$. The middle panel displays a spectrum of a QSO whose light passes through the emitting matter on the way to us (a HIRES spectrum of QSO 1122+30 courtesy of Tom Barlow). The bottom panel presents the cross-correlation signal obtained by multiplying the two spectra shown above, exhibiting a noticeable signal.

synthesizes our knowledge of initial conditions, current observations, and our understanding of underlying physics, to generate comparisons of theory with observations, and predictions of observable quantities. These predictions serve as drivers for the design and development of dedicated instrumentation. Comparison of simulation outputs with observations can lead to improvement of the models and refinement of our understanding.

Cosmological simulations follow dark and baryonic matter inside a fixed comoving size simulation box from high redshift, with their initial distribution drawn from a distribution consistent with the cosmological model being studied, typically computed using `CMBFAST` (Seljak & Zaldarriaga 1996). The primordial perturbations are then evolved, either on a grid (Bryan et al. 2001; Cen 1992), or as distinct particles (Springel 2010; Schaye et al. 2010), taking into account gravitational, thermodynamic, and radiative interactions, to redshift $z = 0$. A review of the approaches of the methods can be found in Bertschinger (1998), while a comparison of some of the specific implementations is

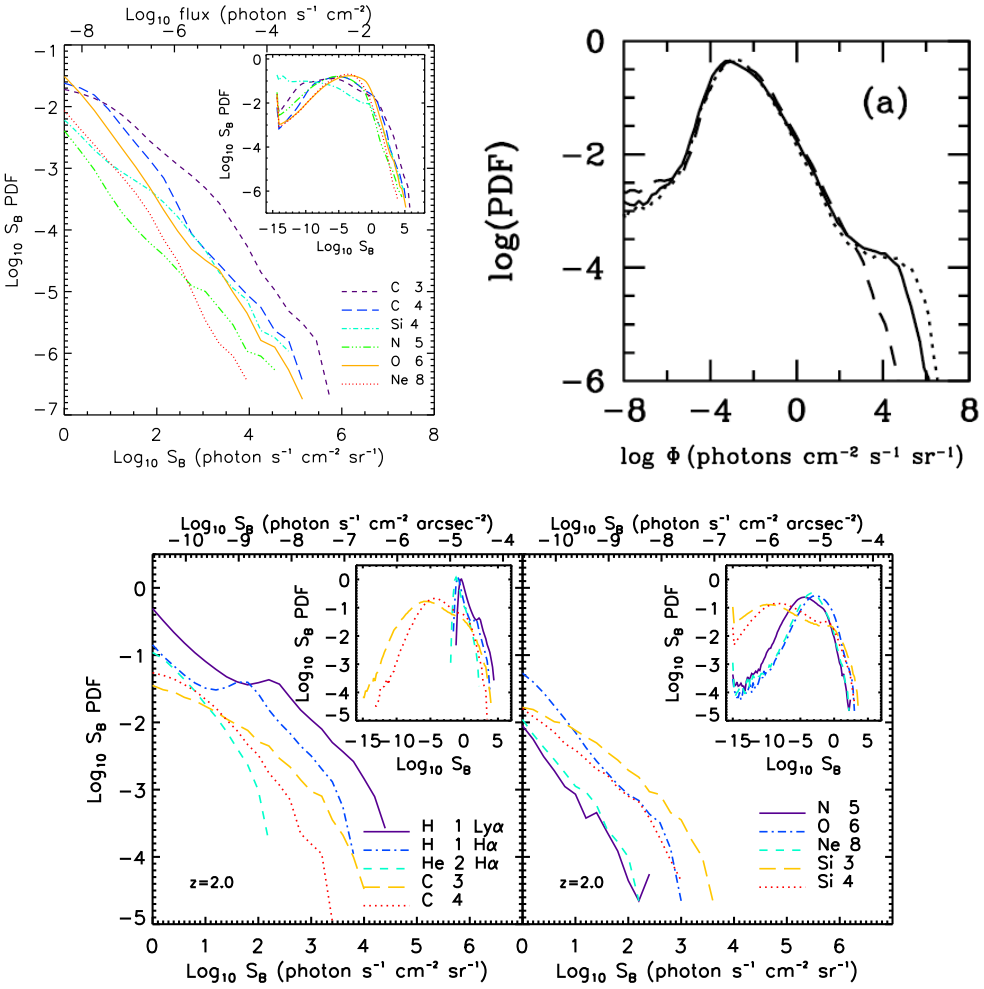

Figure 1.5. Example pixel luminosity distribution functions (PDF) from numerical simulations. The top left panel, taken from Bertone et al. (2010b) shows the PDF for metals at low redshift ($z = 0.25$) for a slice $\Delta z = 7.4 \times 10^{-3}$ thick. The top right panel is from Furlanetto et al. (2003). The curves represent different assumptions about the opacity of the emitting gas. The plot is based on a $\Delta z = 10^{-3}$ slice at $z = 0.15$. The bottom pair of plots are from Bertone & Schaye (2010). They display a PDF for structure at $z = 2$ and thickness $\Delta z = 0.025$. The top right panel reproduced with permission from S. Furlanetto and the AAS, remaining panels with permission from S. Bertone and the publisher of the top left panel, John WIley and Sons.

in O'Shea et al. (2005). Despite advances in computing, a choice has to be made between the size of the simulation volume and the spatial resolution in the resulting output. Consequently, processes that probe physics below the resolution scale of the simulations, or ones that would be prohibitively expensive in terms of computer time, are applied to the models via a so-called semianalytic approach, where heuristic physical expressions adjust the model variables. Simulations that concern themselves with large-scale structure evolution track mechanisms such as star formation episodes, galactic feedback effects (metallicity enhancement, energy and mass ejection), accretion shocks, and radiative transport this way. Smaller volumes, with finer mass and spatial resolution, allow for more detailed studies of inflow of gas onto galaxies (Kereš et al. 2005; Dekel et al. 2009), star formation, and galactic winds. Observed quantities, such as absorption spectra or surface brightness maps in individual emission lines, are generated postmodeling based on the known distribution and physical properties of simulated matter using radiative transfer software, typically `CLOUDY` (Ferland et al. 1998).

In the context of the IGM, these simulations have led to a better understanding of the gas's correlation with dark matter structure, its power spectrum, metallicity, thermal and kinematic distribution. Based on this foundation, simulations are giving us predictions of the sizes, temperatures, compositions, metallicities, kinematics, and morphology of the IGM and CGM, generating maps of expected emission (Furlanetto et al. 2005, 2004; Cantalupo et al. 2005; Bertone & Schaye 2010; Bertone et al. 2010b,a; Kollmeier et al. 2010; Cen & Ostriker 1999; Bryan 2008).

1.2.2 The Cosmic Web of Baryons

Our model of structure in the Universe arises from observations of its very early stages, coupled with a large-scale surveys of bright objects at later epochs, such as galaxies, quasars, and clusters, combined with observations of the diffuse baryonic component through QSO sightlines. This information serves as both an input and a check on numerical cosmological simulations, which combine our understanding of the physical processes involved to allow us to construct a consistent model of where matter (dark and baryonic) is, and what it is doing.

The epoch of inflation left the universe remarkably homogeneous. Observations of the CMBR tell us that random variations in temperature at $z \sim 1100$ were on the order of $\delta T/T \sim 10^{-5}$ (Banday et al. 1997); the corresponding density anisotropy was $\delta\rho/\rho \sim 10^{-3}$. These perturbations grew via gravitational attraction, with their expansion starting to decouple from the Hubble flow when their density contrast only exceeded unity by a few percent: $\delta \approx 1.06$, where $\delta \equiv (\rho - \bar{\rho})/\bar{\rho}$, and $\bar{\rho} = \frac{3H^2}{8\pi G}$ is the critical matter density, H the Hubble parameter. Volumes of slight overdensity formed sheets and filaments, with their intersections delineating more massive regions. The matter in these areas contracted further, with baryons virializing once their density contrast δ rose to $\sim$200, the characteristic overdensity beyond which the underlying dark matter structure cannot collapse,

as it lacks a dissipative mechanism. The baryons, however, as they can radiate away their energy, continue to inflow, cool, and begin to form galaxies and stars.

A cartoon schematic of the current understanding of the interplay of galaxies and the intergalactic medium is shown in figure 1.6, while the core physical properties of the various components are summarized in table 1.2. The broad characteristics of this model do not change much from $z = 4$ to $z = 0$, though there is significant evolution in the details, which is touched on in figure 1.7, and discussed below.

Most of the baryons reside in a cosmic web of filaments, outside of collapsed objects, such as galaxies. This matter is slightly overdense, $1 < \delta < 100$, and ionized by the pervasive metagalactic UV background (see section 1.2.3.3), maintaining a temperature 10^4 K $< T < 10^5$ K. The residual HI fraction, responsible for the absorption features in QSO spectra, decreases quickly after $z \approx 6$. A systematic study of the systems, beginning with Weymann et al. (1979) and Sargent et al. (1980), revealed three types of objects classified by the column density of neutral hydrogen:

Lyman α forest lines (LαF). These systems have imprint unsaturated absorption lines in continuum spectra at the Lyα wavelength at the redshift of the absorbing matter, $\lambda = 1216(1 + z_{abs})$ Å. They exhibit modest column densities, $N_{\rm HI} < 10^{17}\,{\rm cm}^{-2}$, showing characteristic temperatures $10^4\,{\rm K} < T < 10^5\,{\rm K}$. The troughs generally show Doppler profiles, and their equivalent widths lie on the linear part of the curve of growth, meaning their Doppler parameter and column density can be recovered. A review of these systems can be found in Rauch (1998).

Lyman limit systems (LLS). In addition to an absorption feature at the Lyα wavelength, these systems are sufficiently opaque to block the background continuum below the Lyman α limit at 912 Å. The Doppler parameter is nearly proportional to the equivalent width of the line, while the column density is nearly independent of the EW, making it difficult to extract. Column densities lie in the range $10^{17}\,{\rm cm}^{-2} < N_{\rm HI} < 2 \times 10^{20}\,{\rm cm}^{-2}$ with the estimates resulting from observations of absorption lines of other elements associated with the system. LLS have typical temperatures on the order of $\times 10^4$ K.

Damped Lyman absorbers (DLA). These systems have typical column densities $N_{\rm HI} > 2 \times 10^{20}\,{\rm cm}^{-2}$ and cut off the background continua below the Lyman limit. DLA lines are saturated in quasar spectra with Lorentz wings of the Voigt profile clearly visible. These can be fit allowing for the recovery of the absorber's column density. DLAs are predominantly neutral systems at low temperatures, $10^2\,{\rm K} < T < 10^4\,{\rm K}$. They are the dominant reservoirs of neutral hydrogen in the universe. Wolfe et al. (2005) summarizes the theory and observations of DLA systems.

The wealth of HI absorber data available allows for the construction of statistical properties of the population, including tabulation of the number counts of various types of systems as a function of redshift. These statistics can be used to estimate the contribution of this material to the cosmic closure density. The computation relies on the integral over all LαF column densities of

$$\rho_{\mathrm{L}\alpha\mathrm{F}} = m_p \int dN_{HI} \, \frac{\partial^2 \mathcal{N}}{\partial N_{\mathrm{HI}} \partial z} \frac{N_{HI}}{x_{HI}} \left(\frac{dl_p}{dz} \right)^{-1}, \tag{1.14}$$

where m_p is the mean molecular weight within the gas (slightly larger than unity due to the presence of He in the mix); the double derivative denotes the number of absorbers per unit redshift, per unit absorber column density; the ratio N_{HI}/x_{HI} relates the neutral column density to the total hydrogen column density, as x_{HI} is the ionized fraction; dl_p is the proper distance path corresponding to a redshift interval dz. Application of this expression for redshifts $z > 3$ implies that nearly all matter outside of collapsed objects, nearly 90% of the baryons, lies within the different components of the Lyα forest. There are a couple of uncertainties in the computation, however. The ionization fraction, x_{HI}, depends on the temperature of the gas, on the strength of the ionizing UV background, and on assumptions about the transverse sizes of the absorbing gas; the latter typically assumed to be the same in extent as the radial value.

Significant effort has been extended to estimate the metallicity of the IGM and determine the spatial characteristics of the pollution. The work has mainly focused on some of the stronger absorption lines, MgII, CIV, and OVI, though signatures of other elements, (Si, B, Ne, S), have also been studied (a summary of the cumulative observational work and a thorough list of references is given in Meiksin 2009). Heavier element content typically ranges from $\sim 10^{-3}$ within the LαF (Simcoe et al. 2004) to $\sim 10^{-1} \mathrm{Z}_{\odot}$ in DLAs, showing a factor of two increase from $z = 4$ to $z = 1$ (Wolfe et al. 2005). The data indicates an early, and continuing, enrichment mechanism, although Stocke et al. (2007), who focused on absorbers within cosmic voids at low redshift, did not detect a strong presence of metals. This nondetection is not conclusive, however, as their upper bound was $\sim 1\% \, Z_{\odot}$. The metal enrichment mechanism is not well understood. Galactic superwinds and outflows are the likely culprits. Evidence for this includes correlations of line-of-sight absorbers with foreground galaxies (e.g., Adelberger et al. 2005) that indicate metal enrichment out to a few hundred kiloparsecs; studies of QSO environments (Simcoe et al. 2006) that show significant metal enrichment at similar distances; outflows on the order of several hundred kilometers per second typically seen in star-forming galaxies (Shapley et al. 2003; Weiner et al. 2009).

Baryonic matter continues to accrete onto the progressively heavier filamentary structure. It heats as it dissipates gravitational energy and encounters shocks reaching temperatures ($10^5 \, \mathrm{K} < T < 10^7 \, \mathrm{K}$) at which collisional ionization becomes significant, even at low densities. By the current

epoch, $z = 0$, about 50% of normal matter is expected to have been converted into this warm-hot phase of the IGM (WHIM). Nearly half of that material not been observed. This gas cools radiatively via Lyα and metal lines, and the spectrum of emission changes with temperature. The dominant rest-frame UV cooling lines are Lyα at $10^{4.5}$ K, CIV near 10^5 K, OVI at 3×10^5 K, with some contributions from NV and NeVIII at 2×10^5 and 6×10^5 K, respectively. Higher metal ionization states contribute at $T > 10^6$ K, their emission wavelengths lying in the soft x-ray band.

Absorption signatures of this warm plasma imprinted on quasar spectra are thermally broadened lines with Doppler widths on the order of 100 km/s. These include hydrogen Lyα, various ionization states of oxygen (OVI, OVII, OVIII), nitrogen (NV), and neon (NeVIII), with lower ionization state transitions lying in the UV while higher ones reside in the x-ray band. There has been a focused effort to detect these species within the WHIM both at high redshift (Simcoe et al. 2002), and at low redshift, for which space-borne (HST/STIS, FUSE, HST/COS, XMM-Newton, Chandra) and balloon-borne (FIREBall; Milliard et al. 2010) have been used. A review of the search for baryons within the WHIM can be found in Bregman (2007). Searches for broad Lyα (BLA; Richter et al. 2006; Danforth et al. 2010), and metal lines in the UV (Tripp et al. 2008; Thom & Chen 2008a,b; Danforth & Shull 2008) have revealed the presence of WHIM gas and can account for ∼22% of the matter density at $z = 0$, while ∼30% remains in the cooler Lyα forest; collapsed objects contribute another 10%. Four-tenths of the normal matter remain undetected at low redshift.

Work in the x-ray has led to some mixed initial results; including an observation of an OVII system toward the Sculptor wall (Fang et al. 2010), disputed absorption detections (Nicastro et al. 2005; Kaastra et al. 2006; Rasmussen et al. 2007); emission from a filament joining two clusters has also been reported (Werner et al. 2008). The difficulty in the x-ray part of the spectrum lies in having to rely on individual absorption features for species identification rather than multiplets and multiple species, and less-than-ideal spatial and spectral resolution.

Galaxies and groups form in dark matter halos in the densest ($\delta \gtrsim 100$) regions of the filamentary structure, most notably at the intersections of these structures. The interface between a galaxy and the filamentary IGM, the circumgalactic medium (CGM), is a complex mix of matter and energy. These halos, which may extend a few hundred kiloparsecs, experience inflows from the IGM, outflows and energy ejection from the galaxies within them, and mergers with other halos and galaxies.

Galaxies require an influx and a subsequent replenishment of gas to continuously form stars; the existing reservoirs of cold HI and molecular gas would be exhausted on timescales of ∼1 Gyr, while star formation rates remain high over the range of observable redshifts, until $z \sim 1$ (Kennicutt 1998; Hopkins 2007; Daddi et al. 2010). Three main mechanisms are suggested for how this gas is delivered. The first has gas accreting into the dark matter halo surrounding the galaxy; the gas virializes near the virial radius of the halo, increasing in temperature by as much as a factor

of 100. This hot ($T \sim 10^6$ K), collisionally ionized gas cools via line radiation as it continues to descend onto the galaxy. The cooling time for gas at the relevant temperatures is long; an alternate mechanism has recently emerged from theoretical considerations and numerical study whereby cold material ejected from the galactic disk by winds pierces the halo, cooling and condensing the coronal material (Marinacci et al. 2010; Fraternali 2010).

The second mechanism relies on mergers, which may result in stripping of the gas from the smaller consumed galaxy into the CGM of the larger host. The third path involves gas lying in the cooler ($T \sim 10^{4.5}$ K) cores of IGM filaments streaming deep into the CGM halos, possibly to the very outskirts of the galaxy. This matter is heated modestly as it descends into the gravitational potential well, and is expected to release a bulk of its energy through Lyα (Fardal et al. 2001). Recent simulations of galaxy formation (Kereš et al. 2005, 2009a,b; Dijkstra & Loeb 2009; Dekel et al. 2009) indicate that the influx of unvirialized matter into galaxies occurs via both the hot and cold modes described above. The hot mode is predicted to dominate in high mass halos and at low redshifts, while the cold mode is more efficient at delivering gas at higher redshifts and for smaller halos. This duality may explain the dichotomy in the galaxy population, in which blue, actively star-forming galaxies and red, passively evolving galaxies are observed (Dekel & Birnboim 2006). The transition to hot-mode accretion at low redshifts $z < 1$ coincides with a steep decline in the global star formation rate (Hopkins 2007), for which the change in method of gas delivery may be responsible. There have been no direct observations of the resupply of galaxies with IGM gas.

The galaxies within the CGM do not just acquire gas. The processes that occur within them eject matter and energy into the halos. Spectroscopy of Lyman break galaxies at $z \sim 3$, for instance, finds lines typically associated with interstellar matter separated from hotter gas, traced by Lyα, by several hundred kilometers per second (Steidel et al. 2010; Shapley et al. 2003). At these redshifts, star formation is inefficient in retaining matter; roughly the same amount of gas that becomes trapped in stars is blown off by supernova driven winds into the CGM. A galaxy that is forming a few solar masses of stars a year, for a typical starburst lifetime of 10^8 years, will deposit $\sim 10^{59}$ ergs into its surroundings, while driving metal-infused matter hundreds of kiloparsecs into the CGM. Observations based on line-of-sight emission do show enhanced metallicity on these scales outside of galaxies (Adelberger et al. 2005; Simcoe et al. 2006), with more recent work showing a correlation between the strength of MgII absorption and star-formation tracing [OII] emission (Ménard et al. 2009). These outflows may also be strong enough to temporarily halt the inflow of star-forming fuel, quenching star formation. Galactic outflows will generate shocks within the CGM, heat up ambient matter at larger radii, and sweep up dust as they propagate outward. The metal-enriched shock-heated matter will be collisionally ionized, and will cool radiatively through resonance lines, typically, OVI, CIII, CIV, and Lyα; He II (1640 Å) will be a strong signature in cases of metal-poor gas being shocked. A fraction of the ionizing radiation from a central AGN and from young O and

B stars, which is not absorbed by the interstellar medium, will escape the galaxy and photoionize gas within the CGM; a portion of that ionizing radiation will escape the halo altogether. The escape fraction of Lyman continuum radiation has an impact on the pervasive UV ionizing background, and is of importance to understanding the epoch of reionization; it is an active topic of interest that is being studied spectroscopically, and through imaging. The effect of superwind outflows likely remains important until the end of the star-formation epoch near $z \sim 1$, as the number density of rest-frame UV galaxies remains high through that time (Schiminovich et al. 2005; Madau et al. 1996).

Circumgalactic halos are predicted to have sizes similar to the dimensions of Lyman limit systems, as inferred from line-of-sight cross-correlations and are likely responsible for LLS and some DLA features observed in QSO spectra. With so many processes taking place within the halos, it is not surprising that the gas they contain is expected to be multiphase; temperature is predicted to span the range from cool $T \sim 10^4\,\mathrm{K}$ to warm $T \sim 10^6\,\mathrm{K}$; metallicities likely range from close to primordial, to as high as a few tens percent solar. Overdensity may be as low as $\delta \sim 10^2$ along cold flows and at the edges of the CGM halos, as high as $\delta \sim 10^5$ near the cores. High-resolution spectra of metal lines associated LLS and DLA reveal complex multiphase structure consistent with the picture outlined above; spectra of high-redshift Lyman break galaxies also reveal complex morphological and kinematic structure. Furthermore, stacked narrowband images show extended diffuse emission zones around these galaxies (Steidel et al. 2011; Hayashino et al. 2004) having surface brightnesses on the order of a few tens of thousands of LU, extending out to radii close to 100 kpc. A similar study of low redshift, $0.2 < z < 0.5$, of WiggleZ (Glazebrook et al. 2007) selected GALEX sources indicates a possible detection at a similar level (Matuszewski & Martin in prep.). Stacking techniques preserve the radial emission profile, but average over any azimuthal and random variations within it. The spectrum of the emergent radiation depends on the scattering characteristics of the medium, as does the amount of escaping ionizing radiation.

1.2.3 Motivation for IGM Mapping

The observational methods used for detecting the IGM were discussed in section 1.2.1. Absorption line measurements have proven to be an excellent tool for probing the IGM and its interplay with galaxies, they also have probed the correlation of the IGM with dark matter. These observations have been complemented by deep narrowband imaging. A combination of these methods is informative, but does not provide a fully comprehensive picture of the structures being observed that includes three-dimensional location and velocity distribution. Mapping the IGM will provide a new perspective on key topics in galaxy formation and evolution, the life cycle of quasars, dark matter distribution, and the location, chemistry, and morphology of the diffuse baryonic component. The

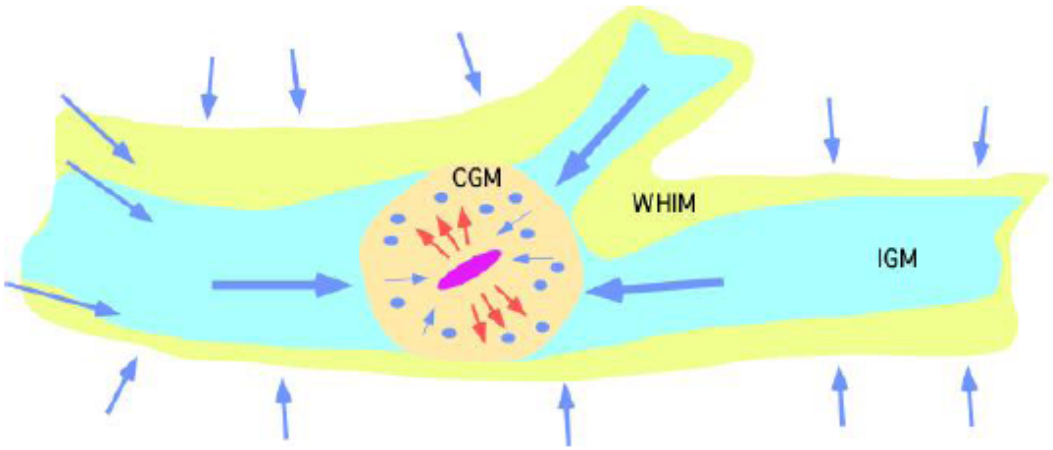

Figure 1.6. A cartoon depicting our current understanding of the IGM, as gleaned from large scale structure, absorption spectra observation, and cosmological simulations. The schematic does not depict the densest environments, such as galaxy clusters and their hot $T > 10^7$ K gas. See section 1.2.2 for a discussion. Image reproduced with permission from Martin (2009).

Table 1.2. A tabular view of the components of the IGM discussed in section 1.2.2. The rows identify the nature of the four phases of gas listed in the columns, their characteristic overdensities, sizes, temperatures; what features they imprint on quasar spectra, their emission characteristics and expected emission levels.

Property	**Component**			
	Cosmic Web	**Web Halos**	**Dark Halos**	**Galaxies**
Baryon and Structure tracer	IGM Fuel	WHIM Baryons & Metals	CGM Infall Winds Metals	XUV Disk Galactic Winds Star Formation
δ	$1-100$	$1-100$	10^2-10^3	$>10^6$
Size (Mpc)	$0.3-30$	$1-30$	$0.1-0.3$	$0.03-0.1$
T (K)	10^4-10^5	10^5-10^7	10^4-10^6	
QSO Absorption	Lyα Forest	OVI Broad Lyα	LLS Metal Lines	Damped Lyα
Emission	Photon Pumping (PP)	Collisional Excitation (CE), PP	CE, PP, Lyα Fluorescence	UV Continuum CE from feedback
Intensity (LU)	$1-100$	$1-100$	10^2-10^4	

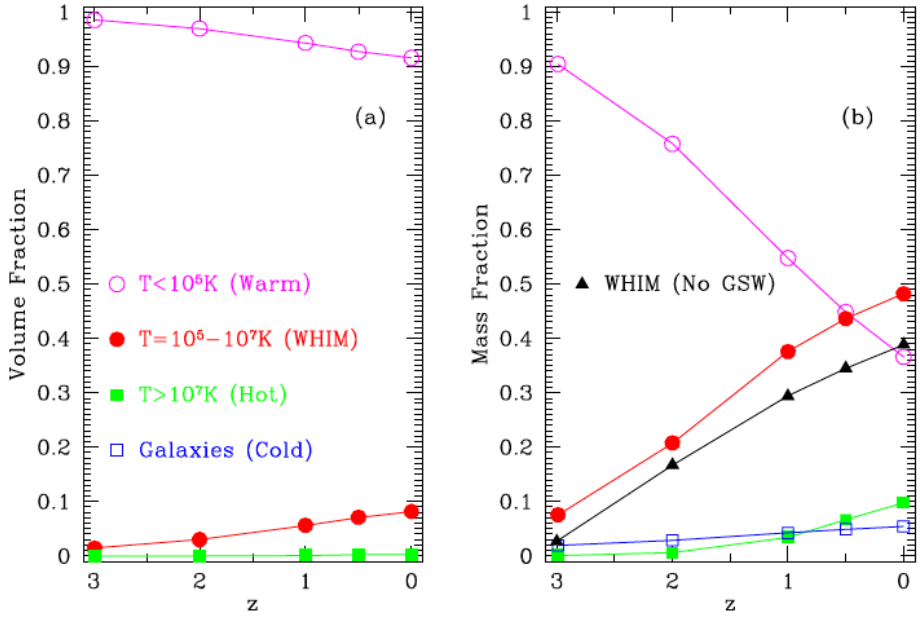

Figure 1.7. Fractional distribution of baryonic components as a function of cosmic time, based on a cosmological simulation by Cen & Ostriker (2006). The figure emphasizes the continued structure formation; increase in the fraction of baryons within galaxies, hot cluster gas, and WHIM that shocks and heats as it accretes onto denser structure. Reproduced with permission of the author and the AAS. A discussion of the weighing of various baryonic fractions, and a census at two different redshifts, $z \sim 3$ and $z \sim 0$ can be found in Fukugita & Peebles (2004) and Prochaska & Tumlinson (2009).

paragraphs below outline what we have learned about these techniques and what new, or improved, information emission mapping will yield.

1.2.3.1 IGM Mapping Traces Baryons

The picture of the IGM that has been built up through decades of observation and numerical modeling was discussed in section 1.2.2. The chief observational technique used thus far in the study of diffuse baryons was described in section 1.2.1.1. While this data has allowed us to estimate the mass of gas within the diffuse IGM, WHIM and CGM, its metallicity, temperature, correlation with bright objects, and has constrained how these qualities evolve with redshift, it has not yielded a three-dimensional morphological and kinematic picture of this gas. In fact, while the method accounts for all extragalactic matter at redshift $z \gtrsim 3$, at lower redshift four-tenths of this matter remains undetected. Furthermore, some of the quantities derived from QSO spectra ($\Omega_{\rm L\alpha F}$, LαF power spectrum) depend on assumptions about transverse sizes of the absorbing matter (typically based on its LOS depth or extrapolated from neighboring sight lines), and about the shape, strength, and uniformity of the UV background.

Emission lines from diffuse matter within large-scale structure can not only be used to detect and chart the missing component, but also to understand its morphology and kinematic structure. Imaging spectroscopy has the power not only to detect this gas, but also to weigh it more directly than LOS methods, characterize its metallicity, determine its motions, and to place constraints on the UV background.

Mass. The transverse extent, L, of an emitting region is a direct observable of integral field spectroscopy, while the column density N of hydrogen can be evaluated from the emission spectral profile similarly to LOS methods. Some caveats do exist: care will need to be taken to understand the opacity of the emitting gas and any energy within or outside of it that may contribute to the emission. Computational radiative transfer methods will have to be employed to deconvolve expected asymmetrical double-peaked profiles, for instance. The mass is estimated by $M \sim m_p N L^2$, where m_p is the mean molecular weight of intergalactic matter, approximately 1.4 proton masses. The density of this gas follows from directly from the mass end size estimates.

Metallicity. Maps focused on emission lines of different species yield a direct measurement of line ratios, while the linewidths constrain the temperature. These two pieces of data combined with the density estimate above are sufficient to constrain metallicity ratios within collisionally ionized matter using a standard modelling approach (Sutherland & Dopita 1993; Gnat & Sternberg 2007). Determination of the metallicity from photoionized gas requires knowledge of the ionizing source; once that is available, radiative transfer models can estimate metal abundances. As will be discussed in section 1.2.3.3, the UV background can be constrained through observation of Lyα fluorescence regions, while star formation and AGN activity can be inferred from IR and x-ray data. Maps of metal distribution will help understand the mechanisms responsible for the enrichment of the IGM with those elements.

Motion. Spectroscopic mapping allows for the determination of bulk motions of diffuse gas. The maps give direct measurements of inflow and outflow velocities of matter, and pinpoint locations of shocks (through collisionally excited CIV and OVI lines). The observed mass and velocity information may combine to constrain the flux of matter within the IGM and to characterize any angular momentum that might be present. Martin et al. (2011) used the Cosmic Web Imager to detect mass inflow and measure the associated angular momentum of the infalling gas of forming galaxy at $z \approx 3$.

Although mapping is a powerful tool that holds a lot of promise, and should be a major contributor to our knowledge of the diffuse gas in the Universe, it is not an easy task. The emission from the baryons in the IGM is dim; the majority of the glowing matter resides in modest overdensity regions with $\delta < 100$, and surface brightnesses dimmer than 1% of the sky background. The technology,

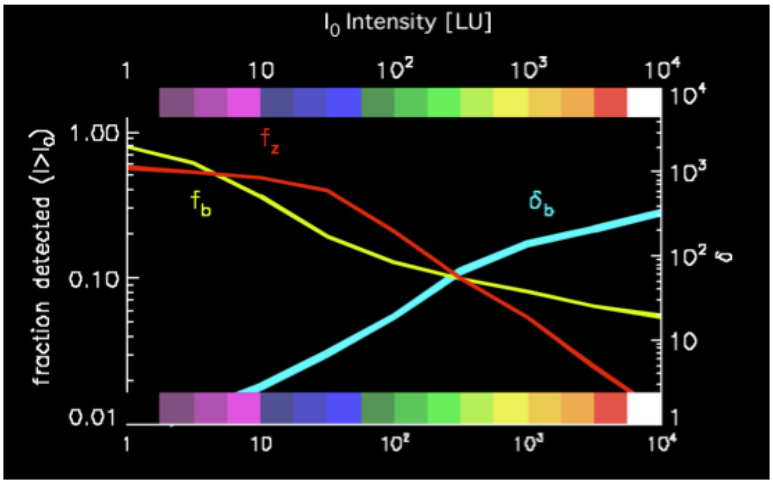

Figure 1.8. The mass fraction of baryons f_b and metals f_z in the IGM that emit above a given level (in LU) at redshift $z \approx 0.5$ (left vertical axis) and the intensity of emission. Based on simulations by R. Cen (Cen & Fang 2006; Cen & Ostriker 2006)

instrumentation, observational and data reduction techniques necessary to obtain a significant direct detection of emission from the cosmic web are now at a level that should allow us to do so. The sensitivity of a given instrument ultimately determines the fraction of baryons that it has a chance of detecting. Figure 1.8 shows the cumulative mass fractions at $z \sim 0.5$ of baryons (f_b) and metals (f_z), as a function of surface brightness (in line units) obtained from a cosmological simulation (Cen & Fang 2006; Cen & Ostriker 2006). As a reference, a state-of-the-art δ-doped CCD (Nikzad et al. 2011) coupled to a space-borne spectrograph tailored to IGM mapping should directly detect approximately 20% of the brightest baryons ($I > 20\,\mathrm{LU}$) in a reasonable deep integration time. Dimmer regions are accessible, as discussed in section 1.2.1, by cross-correlation observations with line-of-sight absorption spectra, and stacking on known galaxies or expected large-scale-structure locations.

1.2.3.2 IGM Mapping Traces Galaxy Formation and Evolution

Galaxies trace the highest overdensity regions in the Universe. They form within, and at the intersections of, IGM filaments and sheets. Observations and logic indicate that galaxies are not isolated entities but are surrounded by halos that are the interfaces between the diffuse baryons in the large scale structure and the dense matter within the galaxies. This circumgalactic medium is a complex volume of inflows, outflows, shocks, and multiphase gas. Some of the evidence for the interaction between the galaxies and their surrounding matter was mentioned in section 1.2.2. Emission mapping of regions around galaxies will present us with data about their formation and evolution.

One question mapping can address is how do galaxies get their gas? Section 1.2.2 discussed the two major modes of accretion, the cold and the hot. Dekel et al. (2009) argue that the signatures of

cold accretion are objects like the observed Lyα blobs, though caution needs to be exercised, as these may shield star-forming regions or a central AGN that contribute to the luminosity. The temperature regimes for the two modes of accretion are different; thus their spectral signatures will differ. The hot mode, with virialized gas at $T \sim 10^{5.5}\,\mathrm{K}$, will exhibit emission similar to that of the filamentary WHIM, showing strong lines from collisionally ionized carbon and oxygen. The gas accreting through the cold mode is predicted to stream along filaments, will have modest temperature, $T \sim 10^{4.5}\,\mathrm{K}$. This matter will glow in CIII, CIV, OVI, and Lyα lines (Furlanetto et al. 2004; Bertone et al. 2010a). The geometry of the emitting regions will provide an additional clue to the nature of the inflows. The hot mode leads to virialization at the outskirts of the dark matter halos surrounding the interior galaxies; cold gas streaming along filaments should trace these structures into the CGM halos.

The second question that mapping can tackle is how do galaxies affect their environment? Star formation episodes and AGN activity drive matter and energy out of a galaxy into its surroundings. The discussion in section 1.2.2 touched on some of the observational evidence of the scales, velocities, and energetics involved in these processes. Spectral imaging of extended regions around galaxies may resolve the shape and velocity structure of these outflows, figure 1.9 gives an idea of the extent of this emission; the CGM regions extend few tens to hundreds proper kiloparsecs from the galaxy they surround, subtending up to a few tens of arcseconds on the sky. For instance, if 1% of the energy carried by galactic superwinds is released through the Lyα emission line within a CGM halo, the gas should glow at a level of $I \sim 10^3\,\mathrm{LU}$.

Deep spectroscopic and stacked narrowband observations (Rauch et al. 2008; Steidel et al. 2011) show extended Lyα emission halos around galaxies. The observed emission regions near $z \sim 3$ have radii $r \sim 10\,\mathrm{arcseconds}$ from the central source and surface brightnesses $I \sim 10^{-18}\,\mathrm{erg\,cm^2\,s\,arcsec}$ ($\approx 8\times10^3\,\mathrm{LU}$). Steidel et al. (2011) model the emission as a central radiation source being resonantly scattered into the observer's line of sight by HI within the galaxy halo. The signal is commensurate with that anticipated from shock heating, and, within uncertainties, with that expected from gas accreting onto galaxies and quasars (Fardal et al. 2001; Barkana & Loeb 2003; Furlanetto et al. 2005; Kollmeier et al. 2010).

1.2.3.3 IGM Mapping Constrains the UV Background

A metagalactic UV background is known to permeate the Universe, maintaining the high level of ionization observed within the IGM. If this radiation were lacking, intergalactic matter would appear opaque to UV radiation, as it begins to do in the spectra of high redshift ($z \sim 6$) quasars (Gunn & Peterson 1965; Becker et al. 2001). Star-forming galaxies and QSOs are believed to be the primary contributors to the UV background, with recombination emission from the IGM playing a minor role (Haardt & Madau 1996, 2001; Bechtold et al. 1987). The background is of primary importance to the ionization and energetics of the IGM; it carries information about the ionizing sources, including

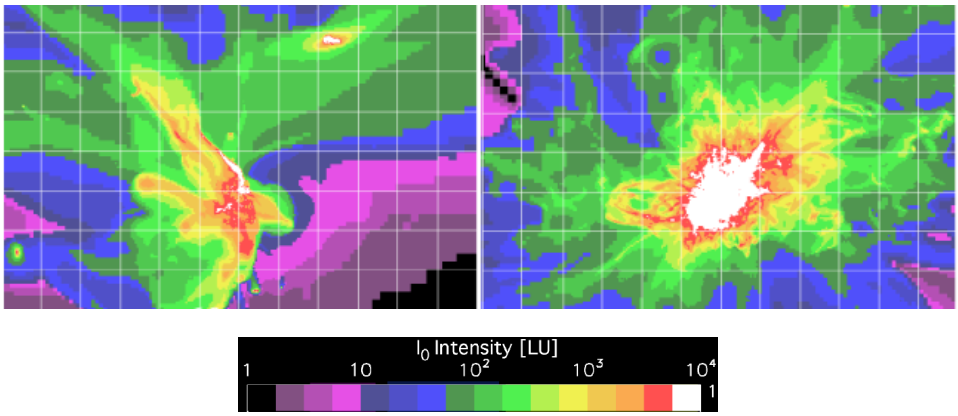

Figure 1.9. A snapshot of a galaxy at $z \sim 0.5$ from galaxy evolution simulations (Bryan 1999; O'Shea et al. 2004). The colors indicate surface brightness, as encoded by the color bar. The gridmarks correspond to 5 arcseconds, or ∼30 kpc. The left panel shows a Lyα emission profile from a galaxy in a simulation that did not include galactic feedback effects, while the right panel shows the same structure for a model that did include such effects. Azimuthal and radial profiles of galaxies constructed from emission maps using various emitting species (though especially Lyα) carry information about the extent and isotropy of the outflows. The signal is expected to be on the order of a few thousand LU; somewhat brighter emission is expected at higher redshift, as star-formation rates are higher. Figure reproduced with permission from G. Bryan.

those responsible for reionization of hydrogen and helium. The radiation may also suppress cooling and star formation in dwarf galaxies (Doroshkevich et al. 1967; Couchman & Rees 1986; Efstathiou 1992). Observations of the absorption features in the spectra of quasars have been used in several ways to constrain the strength and spectral shape of this background radiation:

Proximity effect. The nature of the Lyα forest changes in the neighborhood of a strong photo-ionizing source, such as a QSO. The source obliterates a portion of the residual neutral hydrogen within the surrounding matter, in addition to that already ionized by the ubiquitous UV background. The decrease in the HI fraction around the quasar is quantified by noting the change in the column densities of line-of-sight absorption systems in comparison with the expected number of absorbers at the same redshift lacking the energy source, effectively a decrease in optical depth of the surrounding gas. This value, coupled with a measurement of the source luminosity obtained directly from its spectrum, can be inverted using analytical methods or computer simulations to yield the energy density of the UV radiation field (Bajtlik et al. 1988; Carswell et al. 1982; Murdoch et al. 1986; Liske & Williger 2001; Dall'Aglio et al. 2008; Scott et al. 2002). The influence of the central source extends to a few comoving Mpc. The principal errors in this method originate from the uncertainty of the quasar redshift (as strong outflows can affect that measurement), from uncertainties in the local overdensity enhancement around the source, and from possible quasar activity variability.

Flux decrement. Advancements in cosmological simulations have made it possible to model the Lyman α forest and study the UV background's effect on the optical depth of the gas as a function of redshift. The intensity of the radiation in the model is adjusted to match the mean observed decrement in the continuum flux as a function of redshift (Rauch et al. 1997; Songaila et al. 1999; Tytler et al. 2004). There is some uncertainty in the resultant UV background estimate due to degeneracy with gas temperature.

Transverse proximity effect. The nature of this effect is akin to the the proximity effect discussed above. Sight lines to background continuum sources that pass near a foreground quasar are surveyed to detect a change in the HI absorption signature (Crotts 1989; Crotts & Fang 1998; Schirber et al. 2004; Croft 2004) as compared to unobstructed light paths. Observations of this effect have not yielded a detection (e.g., Crotts & Fang 1998; Schirber et al. 2004; Kirkman & Tytler 2008).

Ionization ratios. Measurements of the relative abundances of ionization states of H, He, C, O, N, and Si in absorption spectra, in conjunction with radiative transfer models, reveal the species' column densities and constrain the ratios of the UV background at the ionization energy thresholds of the species (Agafonova et al. 2007, 2005; Reimers et al. 2006; Chaffee et al. 1986; Bergeron & Stasińska 1986).

Adding emission map data to what has been learned from absorption using the techniques outlined above will yield a finer understanding of the UV background, with Lyman α fluorescence being, at least initially, the key signature. Measuring the luminosity of this emission will give an indication of the localized UV background intensity, as it reprocesses ionizing radiation from QSOs, galaxies, protogalaxies, or AGN. The bright candidate fluorescence emitters, such as Lyman limit systems (LLS), and damped Lyman absorbers (DLA), lie in overdense regions. Their characteristic sizes, as inferred from QSO line-of-sight impact parameters, are 1 to 100 kpc (0.4 to 13 arcseconds on the sky). Probable emission from DLA has been detected in QSO absorption spectra (Adelberger et al. 2006; Hennawi et al. 2009) at a level of I $\sim 10^6$ LU. Another class of emission sources that form in overdense regions, which should also carry information about the UV background, are Lyα blobs. These are of comparable size to the LLS, at a few tens of arcseconds (Steidel et al. 2000; Matsuda et al. 2004; Nilsson et al. 2006), with observed surface brightness range 10^3 to 10^6 LU. Care must be taken when studying these objects to rule out energy sources that do not add to the ionizing background, such as gravitational potential energy dissipation. Emission from less dense regions of the cosmic web is expected to be dimmer, originating predominantly in filaments. It is expected to glow via the Lyα line at a level of 1-100 LU, with characteristic sizes of 0.1 to $\sim$ 10 Mpc.

1.2.3.4 IGM Emission Traces QSO Activity

Gas in the vicinity of a QSO experiences radiation and outflows originating from the source. Line-of-sight observations of that quasar, and sight lines from background quasars with small impact parameters, reveal a population of absorption systems slightly distinct from the intervening absorbers further removed from a QSO. These so-called associate systems show increased metallicities, sometimes supersolar, higher abundances of high-ionization species, and some evidence for changes in optical depth. They are typically few thousands of kilometers per second removed from the systemic redshift of the quasar, indicating that they are part of the same large-scale structure.

Line-of-sight spectra also reveal double-peaked emission features characteristic of Lyα fluorescence coincident with documented damped Lyman absorbers, implying a residual presence of extended HI structures. These are thought to be either adjacent gas concentrations illuminated by the quasar, or part of an outflow (Adelberger et al. 2006; Hennawi et al. 2006, 2009). Additionally, there appears to be a general decrease in the line-of-sight number of absorbers in the immediate vicinity of the quasar, related to increased ionization of the neighborhood gas — more succinctly, the proximity effect discussed above.

Radiation from the source will illuminate the surrounding gas, boosting Lyα fluorescence by as much as four orders of magnitude (Cantalupo et al. 2005). A spectroscopic mapping of the circum-QSO medium (CQM) in Lyα and metal lines (particularly C IV and O VI) will characterize the environment surrounding the source, allowing for the determination of the overdensity, and excess metal enrichment. A map of gas surrounding the QSO may also reveal the radiation history of the object; mapping ionization fronts, including any anisotropy, would constrain the age, geometry, and evolution of the source, including its age and lifetime (Kirkman & Tytler 2008).

1.2.3.5 IGM Traces Dark Matter Overdensities

Simulations show that unvirialized baryonic matter is closely coupled with the underlying dark matter structure, whereas the currently used tracers, galaxies, are biased, forming and conglomerating in regions of highest overdensities. The simulation-derived distribution of baryonic matter is consistent with line-of-sight absorption observations. This conclusion is enforced by comparing computer-generated Lyman α forest spectra with observed ones, with consideration for both individual absorber characteristics and bulk optical depths. Methods have been developed to recover the one-dimensional matter fluctuation power spectrum from Lyα forest lines in QSO sight lines, and to convert that to a three-dimensional power spectrum (Hui et al. 1999; McDonald & Miralda-Escudé 1999). Mapping the IGM present in cosmic structure filaments will yield a direct measurement of the three-dimensional power spectrum, removing many uncertainties present in the current mechanism. Additionally, a tightened estimate of the UV background and better understanding of the geome-

try of the emitting IGM will yield more accurate expressions for transforming observed absorption spectra into density fields, improving the existing technique.

1.2.3.6 IGM Constrains Dark Energy

Alcock & Paczyński (1979) introduced a method to distinguish between differing cosmologies by comparing the transverse and radial sizes of isotropic objects as a function of redshift. The ratio of the two measured lengths is sensitive to cosmological parameters, yielding an independent test of the Λ-CDM model, with the added benefit of not being dependent on the evolution of the objects used, provided they are isotropic in nature. Sizes of galaxy clusters (Alcock & Paczyński 1979; Kim & Croft 2007), distribution of quasars (Phillipps 1994; Popowski et al. 1998), large scale galaxy clustering (e.g., Ballinger et al. 1996; Peacock et al. 2001; Glazebrook et al. 2007; Blake et al. 2011), galaxy pairs, (Marinoni & Buzzi 2010), and Lyα forest auto- and cross-correlation scales (Hui et al. 1999; McDonald & Miralda-Escudé 1999) have been considered test subjects. The methods relying on collapsed objects probe matter that has decoupled from the bulk Hubble flow and is in the process of collapse, necessitating the introduction of a bias parameter characterizing into the computations. The Lyα method probes the linear regime of cosmic structure, but suffers from modest statistics due to a small number of neighboring quasar pairs.

IGM, as observed in emission, could be used as input to the Alcock-Paczyński test, with the transverse sizes being a direct product of the maps, and with line-of-sight depths coming either from complementary QSO absorption spectra, or derived from three-dimensional emission mapping data cubes.

1.3 The Integral Field Spectroscopy Zoo

Integral field spectroscopy (IFS) allows simultaneous study of the spatial and spectral characteristics of extended astronomical objects. An excellent description of the various techniques of achieving this goal, and the parameter space available, can be found in Bershady (2009). This section draws on that manuscript, focusing on the aspects of IFS relevant to deep observations of the IGM.

An IFS is used for reformatting a compact region of the focal plane into a geometry that is fed into a subsequent spectrograph, a long or fragmented slit. The standard methods used to achieve this make use of optical fibers, optical fibers with microlens arrays, mircolens arrays, and image slicers. A cartoon depicting these schemes is shown in figure 1.10; the characteristics, advantages and drawbacks of these are shown in table 1.3.

Fiber bundle. An optical fiber bundle is conceptually the simplest method for rearranging a two-dimensional telescope focal plane into a spectrograph entrance slit. A fiber bundle offers

instrument design flexibility in terms of location of the spectrograph with respect to the telescope. The surfaces at the two ends of the fiber bundle can be matched to the curvatures of the focal plane of the telescope or entrance slit of the spectrograph, optimizing optical performance. As the fibers require cladding to function, are often surrounded by jacketing material, and have circular cross sections, it is not possible to achieve total coverage of the focal plane. The telescope must dither to fully observe a contiguous patch of sky. The size of the fiber, combined with the telescope plate scale, constrains the spatial resolution of the instrument. The fibers need to be adequately spaced from one another at the spectrograph slit end; otherwise the fiber spectrum images can overlap on the detector, resulting in loss of spatial resolution, or cross talk. Bare fibers do suffer from focal ratio degradation (FRD) (Ramsey 1988; Wynne 1993; Schmoll et al. 2003; Carrasco & Parry 1994), necessitating faster spectrograph optics, thus making optical design more involved and expensive. Fibers are not well suited to work in the far UV, as they have low throughput at those wavelengths.

Fiber bundle with lenslets. This arrangement inherits most of the advantages and disadvantages of the bare fiber bundle. Using lenslets at the entrance to the bundle improves the focal plane coverage and coupling of the telescope input beam to the typical fast acceptance angles of fibers. Employing lenslets at the outlet of the bundle can slow down the output beam, counteracting FRD and reducing requirements on the spectrograph that follows. The lenslets introduce several more material interfaces, leading to scattering and reflective losses; material choice is key to minimize transmissive losses, especially in the UV and the blue part of the visible spectrum. Finally, lenslet arrays make it difficult to match the slit curvature to improve the instrument's optical performance.

Lenslet array. A lenslet array in the (possibly reimaged) focal plane of the telescope creates an array of telescope pupil images in a single plane that serves as the entrance to the spectrograph. This focal plane coverage is very high, close to 100%. The spatial resolution is limited by the size of the lenslets. The spectral bandpass needs to be restricted to prevent overlap of spectra on the detector. The lenslets are a scattering source; Fresnel losses at interfaces and absorptive losses within the lenslet material are concerns. The primary example of this technology is SAURON (Bacon et al. 2001).

Image slicer. An image slicer uses two sets of mirrors to rearrange a two-dimensional area of the telescope focal plane, forming a virtual slitlike image that serves as the entrance to the spectrograph optics that follow. The first mirror array is in the focal plane of the telescope, redirecting light toward a second mirror array that reimages the first set of mirrors into a staggered slit. The image slicer has complete coverage of the focal plane. The spatial resolution of a spectrograph equipped with an image slicer is diffraction, seeing, or instrument limited

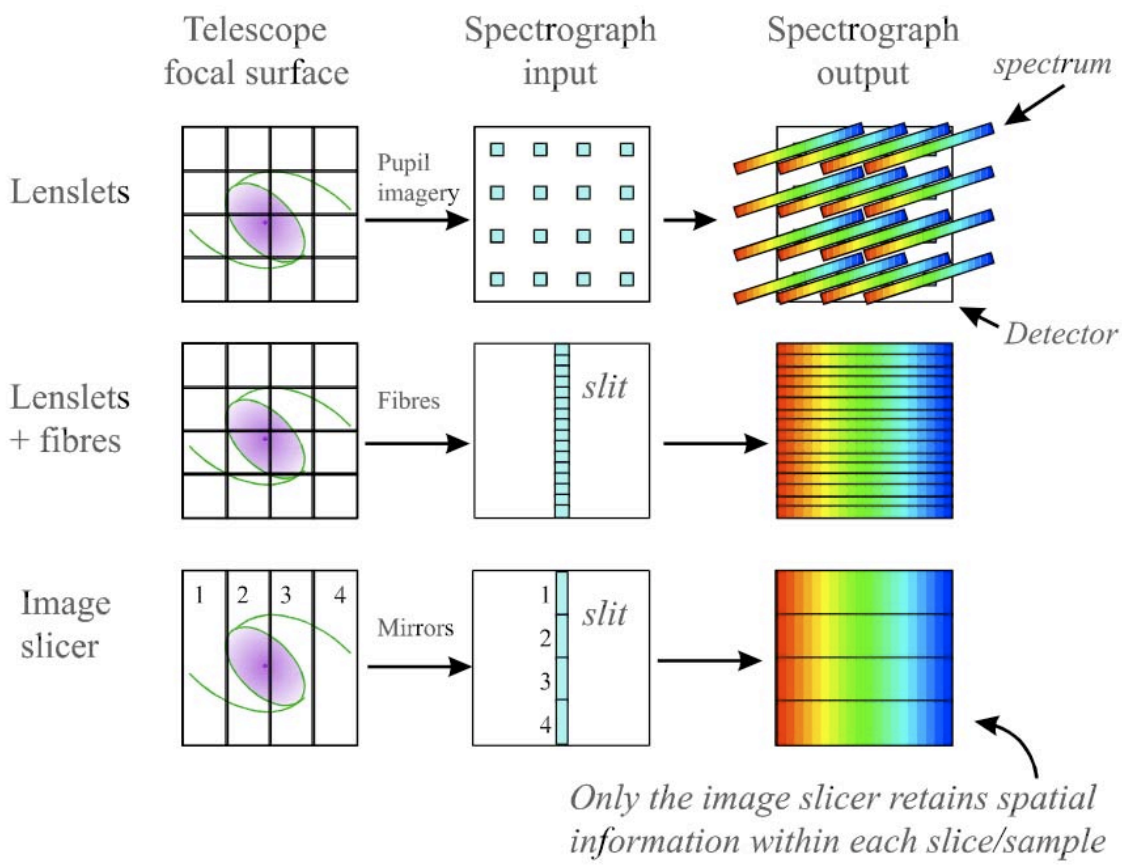

Figure 1.10. The principles behind the three basic types of integral field units. The method shown in the top row differs fundamentally from the other two displayed. A lenslet array reimages the telescope pupil into a two-dimensional grid; this grid then serves as an entrance to the spectrograph. Fiber and image slicer methods (shown in the subsequent two rows) reprocess the image plane of the instrument instead. Figure created by and reproduced with the permission of J. Allington-Smith.

along a slice, and limited by the width of the slice in the other dimension. The efficiency is limited by the quality of reflective coatings, which can be made near perfect for specific wavebands and ranges of angles, and by vignetting losses within the focal plane unit due to the fanned-out nature of the thin mirrors. Due to this geometry, image slicers are most efficient at telescopes with small focal ratios. Currently existing instruments of this kind are ESI (Sheinis 2006), CWI (Matuszewski et al. 2010), and OSWIFT (Thatte et al. 2006), with KCWI (Martin et al. 2010) and MUSE (Laurent et al. 2008; Bacon et al. 2006) in development.

There are various figures of merit that can be constructed to reflect the performance of a spectrograph. The figure of merit (FOM) applicable to deep observations of diffuse and dim structures is

$$\text{F.O.M} = R \times \Omega \times \eta A, \tag{1.15}$$

Property	**Image slicer**	**Fiber bundle**	**Fiber bundle + microlens**	**Microlens array**
Spatial coverage	Continuous field, nearly 100% coverage	Sparse. Focal plane area lost to fiber-packing, cladding, and jacket.	Good, close to 100%	Good, close to 100%
Spatial resolution	Seeing or instrument-optics limited in one dimension, slice-width limited in the other	Fiber-size limited	Lenslet-size limited	Lenslet-size limited, often requires re-imaging of the focal plane.
Detector coverage	Good. Small gaps betwen slice images	Sparse. Fiber images must be spaced to prevent cross-contamination.	Sparse. Fiber images must be spaced to prevent cross-contamination.	Sparse. Requires band-limiting filter to prevent spectral overlap.
Spectral performance	All-reflective design, dependent on coatings, can be typically optimized to a given spectral band	Poor tranmission in the UV	Poor transmission in the UV	Good; limited by internal transmission of the lenslet material and reflective losses.
Beam-speed restrictions	Slow beam to prevent vignetting within the image slicer mirror-fan	Spectrograph optics matched to the degraded focal ratio of light exiting the fibers		
Optical performance	Low scatter	Moderate scatter, transmissive losses	High scatter, transmissive losses	Moderate scatter

Table 1.3. A comparison of the characteristics, advantages, and drawbacks of the four integral field spectroscopy techniques.

where η is the instrument efficiency, including sky and telescope, R is the spectral resolving power, Ω the instrument field of view, and A the telescope area. The emphasis of the FOM is on spectral resolution (as that is key to sky background subtraction), field of view sufficient to encompass the structure being observed, and the telescope-instrument effective area. Much less of a concern are spatial resolution, which can be coarse given the characteristic sizes of IGM structures, on the order of a few to a few tens of arcseconds at redshifts $2 < z < 4$; and wavelength coverage, given the small Δz of even the largest cosmological structures of interest. A comparison of the figure of merit for various ground-based IFS is given in table 1.4.

1.4 Instrument Requirements

The instrument parameters are driven by the specifics of the scientific targets, and constrained by mechanical, technological, environmental, and fiscal factors.

The goal of three-dimensional mapping and characterizing the IGM requires that both spatial and spectral information about the material be collected; wavelength information serves as a proxy for the line-of-sight distance, keeping in mind the usual caveat of disentangling line-of-sight proper motions from cosmological distance.

Optimally, an instrument intended for integral field spectroscopy would have a giant field of view Ω with arbitrarily small spatial resolution $\delta\omega$, spectral bandpass Λ, and would cover all relevant parts of the electromagnetic spectrum with negligibly small spectral resolution $\delta\lambda$. This, of course, is not possible. Detectors have finite sizes and finite resolution; thus the number of spectral and spatial resolution elements that can be recorded is limited. In the usual case where one of the axes of the detector lies along the spectral direction, the other along the spatial, any attempt to increase the spectral resolving power of the instrument will result in a decrease in the field of view of the instrument. In a simple case of an instrument with resolving power $R \equiv \lambda/\delta\lambda$, detector of area D_A, camera focal length f, operating at wavelength λ, the product of the field-of-view and bandpass can be approximated by: $\Omega\Lambda \approx \lambda D_A f^{-2} R^{-1}$.

For observations at a fixed wavelength λ, the product is maximized by selecting a camera with the shortest possible focal length, focusing spectra onto the largest available detector, and observing at the smallest acceptable spectral resolution. Once these parameters have been determined, the product $\Omega\Lambda$ is fixed, and any increase in one will be at a corresponding loss in the other.

Conservation of the so-called grasp through the instrument (see, e.g., Schroeder 1987), $A \times \Omega$, where A is the area of the telescope and Ω the sky solid angle observed, constrains the field of view of the camera.

Inst. name	**Field of view** Ω **(arcsec^2)**	**Spatial res.** $\Delta\theta$ **(arcsec)**	**Instant bandpass** Λ **(Å)**	**Spectral res.** $R \equiv \lambda/\Delta\lambda$	**Wav. Low** λ_{min} **(Å)**	**Range High** λ_{max} **(Å)**	**Eff.** η **%**	**Tel. diam.** D **(m)**	**Fig. of merit FOM**	**Notes**
VIRUS	29,000	1.0	2300	1000	3400	5700	16	9.2	900	HET, fibers, survey oriented. Expected 2013
MUSE	3600	0.3	4650	2000	4650	9300	20	8.2	450	VLT, slicer, facility-class. Expected 2013.
KCWI	2400	1.0	450	5000	3700	10,000	25	10	135	Keck, slicer, Expected 2013
VIMOS	729	0.7	2050	2500	3600	10,200	20	8.2	50	VLT, fibers+microlenses, Operational
CWI	2400	1.0	450	5000	4400	5600	20	5	27	Palomar, slicer, blue optimized Operational
OSWIFT	220	0.4	3500	3500	6500	11,000	15	5	10	image slicer, red-optimized
ESI	24	1.0	6300	3500	3700	10,000	20	10	10	Keck, image slicer Operational
GMOS IFU	35	0.4	1400	3700	3800	9500	25	8	3	Gemini, fibers+microlenses Operational
SAURON	1350	0.9	590	1250	4810	5400	15	4.2	3	WHT, lens array Operational
FIREBall	20,000	10	300	5000	1985	2250	0.05	1.0	1.5	UV Balloon telescope, fibers Operational

Table 1.4. Comparison of CWI (and KCWI, currently in development) with other existing IFUs. The figure of merit is computed via $FOM = \Omega \times \Lambda \times R \times \eta \times D^2/10^9$.

Several instruments have been omitted from the table as their FOMs were small compared with those included. These were: SPARSEPAK and Hydra on the Bench spectrograph at the WIYN telescope, AAΩ Spiral, the WIFES spectrograph, and SIFS at SOAR. Although the FOM is a useful single parametrization of an IFU, it is not ideal, and the merits of the individual instruments have to be evaluated based on their applicability to their intended science and scope. A more telling figure is the minimum flux directly detectable and characterizable from a fixed-size, fixed-spectral-width diffuse region observed for a fixed time. The advantage of a large instrument field of view is negated by the fixed size of the emitter, though it is tough to argue that maximizing the FOV should not be an instrument goal. The details of a sensitivity calculation are discussed in Appendix A.

1.4.1 Field-of-View and Spatial Resolution

Lyman α forest absorption observations, galaxy surveys, and simulations indicate that typical sizes of the IGM filaments are 100 ckpc across, and ∼300 cMpc in length; WHIM has similar dimensions. Gas in the CGM extends over radii of a few hundred kiloparsecs away from the central galaxy. Given that the angular diameter distance for the concordance Λ-CDM cosmology varies from 4 ckpc/arcsec at $z \approx 0.3$ to 8.5 ckpc/arcsec at $z \approx 1.5$, falling off at higher redshifts, the characteristic sizes listed above correspond to on-sky angles from 25 arcsec to 20 degrees at $z \approx 0.3$, and from 12 arcsec to 10 degrees at $z \approx 1.5$. As the number of spatial elements is limited in a detector, a choice needs to be made whether to observe a very wide field with coarse resolution, a smaller field with fine resolution, or some middle-of-the road approach.

If the intended targets are large structures in the IGM or WHIM, i.e., filaments, spatial resolution can be sacrificed at the cost of field of view. This approach has the benefit of improving the signal-to-noise ratio of the observation, since a larger solid on the angle corresponds to a single pixel on the detector, diminishing the significance of detector noise. The principal drawback is that point sources (stars, AGN, QSOs, and also — effectively — galaxies) are not resolved, resulting in the need to mask multiple spatial pixels. Additionally, information about the immediate environments of these sources is lost. A resolution element needs to be small enough to resolve the transverse size of the filaments, on the order of 10 arcseconds.

An instrument aimed to study the CGM needs to have a field of view large to encompass these structures, which are predicted to subtend a few tens of arcseconds on the sky. That is also the characteristic size of Lyman α blobs. Spatial resolution must be sufficiently fine to observe the substructure within these objects, and to resolve any central sources. The pixel size cannot be arbitrarily small, with spatial resolution limited either by atmospheric seeing, instrument optics, or diffraction. As typical sizes of galaxies are on the order of a few kiloparsecs, resolution of 1 arcsecond is sufficiently fine to allow for their subtraction or masking.

1.4.2 Spectral Bandpass

Galaxies appear to have outflows with velocities on the order of $\Delta v \sim 1000$ km/s, while associated absorption systems lie within $\Delta v \sim 5000$ km/s of QSOs. A mapping of the morphology and kinematics of these systems requires redshift coverage $\Delta z/(1+z) \geq \Delta v/c$. For observations of the Lyα line, this corresponds to $\Delta\lambda \geq 66$ Å at $z = 0.7$ and $\Delta\lambda \geq 170$ Å at $z = 3$. Ideally, the spectral bandpass would be large enough to accommodate significant neighboring transitions that originate from the same structures, such as Hβ and the OIII multiplet, or Hα and SII, for instance.

1.4.3 Spectral Resolution

The instrument spectral resolution $R \equiv \lambda/\delta\lambda$ is driven by several considerations, notably spectral characteristics of anticipated targets and background, and instrument systematics. These factors are highlighted below.

Resolve emission multiplets. R must be sufficient to resolve the key emission multiplets from the IGM, namely CIV (1548.2 Å, 1550.8 Å), and O VI (1031.9 Å, 1037.6 Å); this is not a particularly demanding restriction, as $R \approx 600$ is sufficient.

Resolve gas kinematics. Characteristic velocities of galactic outflows, and typical rotational velocities of protodisks, are $v \approx 100\,\mathrm{km/s}$. Resolving these motions requires $R \geq 3000$.

Resolve gas temperature. Intergalactic gas temperatures vary from 10^4 to $10^7\,\mathrm{K}$. Constraining the mass and composition of the gas requires an accurate estimate of the temperature using linewidths of observed features. Assuming purely thermal Doppler broadening of the lines, (ignoring any kinematic motions of the gas), the linewidth is $\Delta\lambda/\lambda \approx \sqrt{(8kT\ln 2)/(mc^2)}$. Equating this to the instrument resolution, $\Delta\lambda/\lambda \approx 1/R$, implies that at a temperature $T \approx 10^5\,\mathrm{K}$ the resolving power needs to be $R \approx 4500$ to well constrain the gas temperature.

Sky spectrum subtraction. The night sky is rich in emission and absorption lines, especially at the red end of the visible spectrum and into the IR. In an instrument that does not have sufficiently high resolution to tell these lines apart, they will be smeared out, forming a continuum background, degrading the signal-to-noise ratio. Analysis of high resolution spectra degraded to lower resolutions appears to indicate that R of a few thousand is an acceptable value (Bershady 2009).

Control of systematics. In the case of a balloon borne telescope (such as FIREBall), or a Cassegrain mounted instrument (CWI), the hardware flexes; the optical path, alignment, or focus will change. Higher spectral (and spatial) resolution allows for these effects to be corrected.

Avoiding detector noise. While high resolving power is desirable for the reasons mentioned above, it is possible for R to be too large; in particular, it is not desirable to oversample an emission or absorption line when the detector being used is noisy. The net effect of smearing out a feature over a larger area of the detector is increasing the total detector noise for a fixed strength signal, degrading the observed signal-to-noise ratio. The impact depends on the signal being sought, and the relative values of the sky and detector backgrounds; in the case of detector background limited observations, the weakest detectable flux for a fixed signal-to-noise ratio scales as $R^{\frac{1}{2}}$.

1.4.4 Noise Characteristics and Control

Detecting a signal that has surface brightness several orders of magnitude below the glow of the night sky requires that the sources of noise, both from the instrument and from the sky, be characterized. The paragraphs below discuss the various sources of error.

Detector noise. Detectors typically introduce noise into the obtained spectra or images. It is desirable, if possible, to use a detector where the noise is small enough such that its contribution is small compared to the shot noise due to the sky. Following the notation of appendix A, we require $B \gg \sigma_D^2$. Terms depending on the observation time, spectral width, and observing time cancel out, leaving the expression: $(I_B\eta)/(DR) \gg 1$, where I_B is the sky background in CU, η the total throughput, including atmosphere, D the detector noise rate per unit area, R the instrument spectral resolution. Inverting this yields a constraint on the detector noise rate, per unit detector area. That is a natural unit of noise measurement for photon-counting devices like microchannel plates. For CCDs, the constraint pertains to read-noise, where the rate is understood to take into account any pixel binning and readout cadence. Naturally, detectors with inherently low noise characteristics need to be chosen to minimize their impact on the error budget.

Sky background. The chief sources of sky background light are zodiacal light, unresolved stellar populations, atmospheric airglow, diffuse galactic light, and scattered Terrestrial light. Spatial, spectral, and temporal variabilities of these are discussed in Leinert et al. (1998).

Zodiacal light. This component increases in intensity from $\sim$1000 CU at 1000 Å to $\sim 10^5$ CU at 5000 Å. The intensity decreases away from the ecliptic plane; selecting observational targets away from this plane will reduce the observed background.

Unresolved stellar sources. Dim, unresolved stars could contribute as much to the background as zodiacal light. IGM observations typically avoid the galactic plane, whereby reducing this contribution substantially.

Diffuse galactic light. This pollutant contributes on par with zodiacal light at 1000 Å, though is several orders of magnitude weaker at visible wavelengths. This component does not vary with time, though it does exhibit spatial variation on the scale of a few arcminutes. The spatial structure of this emission can be fitted using IR dust emission maps (Schlegel et al. 1998; Schiminovich et al. 2001), or GALEX imaging information, where available. Observations aimed at detecting the IGM will select nearby background fields lying close to the target field having similar observed levels of diffuse galactic light.

Atmospheric airglow. Various chemical species in the upper atmosphere excited by solar radiation, thermal, and chemical processes produce emission lines, often in bands. This

background varies on short timescales (minutes) and with position (arcminutes). The strategy to reduce its impact on IGM observations is multifold. Targets are selected, if possible, to avoid strong airglow lines, utilizing high instrument spectral resolution to isolate the desired signal from the background. Background sky fields are chosen near the science objects in an attempt to sample the same patch of sky; this is either accomplished by having a field of view large enough to image both the diffuse signal science field and the sky-background field simultaneously, or by alternating exposures on sky and background fields, possibly employing the nod-and-shuffle technique on CCD detectors which allows for interleaving target and sky observation within a single integration. This increases the frequency of switching between the two fields, improving the sampling of any temporal changes in sky brightness.

Terrestrial scattered light. Light pollution is a problem for ground-based observing. Minimizing its contribution to the sky background requires observing in directions away from local municipalities, and avoiding strong characteristic lines, such as the sodium complex at 589 nm. Spectroscopic observations with moderately high resolution are well suited to eliminate individual spectral features; frequent chopping between science target and nearby sky background field can remove this background signal identically to atmospheric airglow.

Stray and scattered light. Stray and scattered light within the instrument raises the background level at the detector, effectively increasing the overall uncertainties within the collected data. The contribution of this factor must be much smaller than the dominant source of background in the system, whether it be sky or detector noise. In the event of observation of dim fields, which all of the IGM observations will be, the amount of stray and scattered light within the instrument for both the target and sky background frames should be identical, provided there are no bright sources near either field. The mechanics of subtracting this component will be the same, with errors of the same nature, as those resulting from the process of sky background subtraction. The effects of stray and scattered light are curbed by ensuring the instrument enclosure is light tight, carefully baffling light paths, obtaining optics with constraints on surface characteristics (scratch/dig), coating them with good quality optical films, and fastidiously eliminating any random light sources within the instrument (LEDs on controllers or other electronics).

Out-of-band light. Light at wavelengths outside of the bandpass of the instrument needs to be limited, as it represents a source of noise. This concern is particularly valid for observations at ultraviolet and blue wavelengths, as the sky background in those ranges is faint, as are the desired signals, compared to the sky background in the red. The situation is alleviated for a

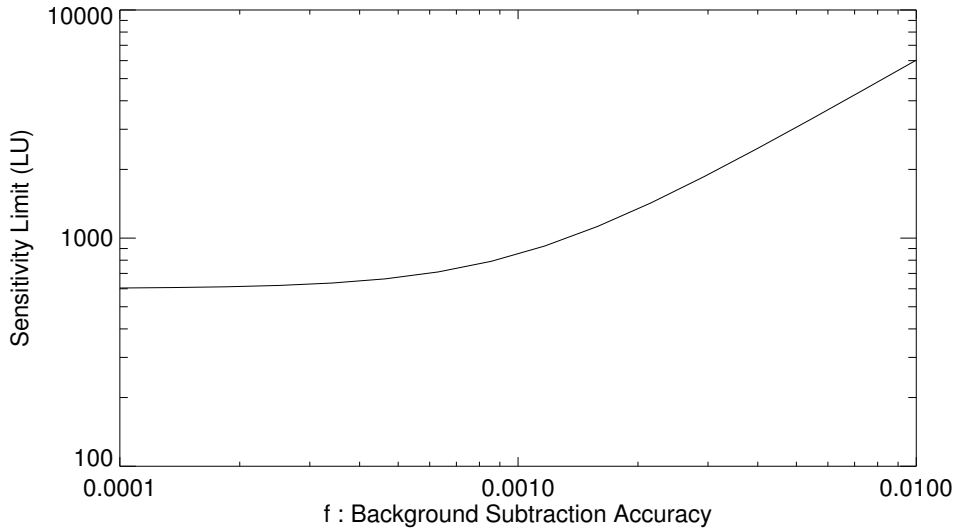

Figure 1.11. The nstrument sensitivity limit as a function of fractional background subtraction accuracy. This calculation was performed for CWI. It assumed an that extended emission line source subtended 100 arcsec^2 on the sky with spectral width of 3 Å. It was assumed to be drowned by a combined sky and instrument background equivalent to 200000 CU (twice the expected sky surface brightness). The source is assumed to be observed for a total of 24 hours (12 hours on target, 12 hours on the background field). Improved background subtraction is important, until the residual fraction, f, is comparable with the associated shot noise. This occurs when $f \sim 1/\sqrt{N}$, where N is the expected number of collected photoelectrons. For the values assumed in for this plot, $f \approx 9 \times 10^{-4}$. This is where the break in the plot occurs, and where improving sky subtraction accuracy does not lead to improved sensitivity.

spectrograph, as opposed to a simple imager, as out-of-band light is diffracted away from the detector, and careful baffling and blackening of the spectrograph interior diminishes the effect. Instruments are equipped with optical filters that reject out-of-band light, with the rejection ratio anywhere from 10:1 to 10^4:1, the lower ratios typically for the UV. Additionally, the chosen detector might be insensitive to light longward of some wavelength; this is the case with microchannel plates equipped with CsTe cathodes (∼350 Å), standard CCDs (∼1100 Å), or the still-in-development GaAlN semiconducting detectors with a foundry-tunable red cutoff wavelength.

Accurate background subtraction is key to detecting diffuse emission. The required subtraction precision depends on the level of sky and instrument background present. Figure 1.11 shows the dependence of instrument sensitivity on background subtraction accuracy.

1.4.5 Effective Instrument Area

Ideally, the instrument effective area would be equal to the light-collecting area of the telescope minus atmospheric attenuation losses. This is not a feasible requirement, especially for a spectrograph aimed at ultraviolet wavelengths. The requirement on the instrument effective area (in reality simply instrument and atmosphere throughput, as the telescope collecting area is usually fixed) is determined by requiring that a particular level signal I_s subtending an angle Ω on the sky, with a linewidth Λ, be detectable with a signal-to-noise ratio Σ during an observation lasting a time T. The specifics of this computation are given in appendix A. For simplicity, detector background limited and sky background limited observations are considered here.

1.5 FIREBall and CWI

FIREBall and CWI were designed and constructed with the specific aim of detecting and characterizing emission from diffuse intergalactic matter. They are both high resolution integral-field spectrographs, though their details are tailored to more specialized observations. Their similarities and differences are summarized in table 1.5, with more detailed comments below, and a full description of instrument design, implementation and usage in the following chapters.

1.5.1 FIREBall

FIREBall, the Faint Intergalactic Redshifted Emission Balloon, probes part of the epoch during which roughly half of the baryons in the Lyman α forest are expected to have transformed into the WHIM, $0.3 > z > 1.2$. The instrument was intended as a path-finding experiment to demonstrate the feasibility of IGM mapping in the ultraviolet; it is the first integral field spectrograph to operate in that regime. FIREBall is a stratospheric balloon-borne 1 m class F/2.5 focal ratio telescope coupled to an integral field spectrograph. It exploits a narrow, $\sim$350 Å, transmission window around 2100 Å accessible at stratospheric altitudes (see section 3.2.1). The large collecting area is chosen to maximize sky signal, while the fast focal ratio allows for a large telescope field of view. At 180 arcseconds in diameter, this is sufficient to encompass emission from WHIM gas around spectroscopically identified associations of galaxies tracing large scale structure nodes and filaments. It is also large enough to collect the bulk of the emission from the vicinity of a quasar. The spatial resolution (8") is somewhat coarse; it is limited by the size of the detector given the field of view, and by the physical size of fibers (100 µm) in an F/2.5 telescope. The spectral bandpass is fixed by atmospheric transmission, while the resolution $R \sim 4800$ was mandated for reasons outlined in section 1.4.3. The detector used is a spare GALEX NUV microchannel-plate photon-counting device, which, despite good noise performance at $1\,\mathrm{count\,cm^{-2}\,s^{-1}}$, is the dominant source of noise in the system. Dark time during flight is limited to several hours, and the choice was made to rely on GALEX data for

Quantity	FIREBall	CWI	Notes
Primary target	WHIM emission from large scale structure, Circum QSO medium	Circum-galatic medium, Lyα blobs, QSO neighborhoods	
Field of view	180" diameter	60" × 40"	
Spatial res.	8"	2.4" × 0.8"	CWI spatial resolution is seeing limited along the 40" long slice and slit-width limited perpendicular to them.
Spectral coverage	1985 Å to 2300 Å	3800 Å to 9500 Å	
Spectral bandpass	315 Å	150 Å	FIREBall: Narrow stratospheric balloon window CWI: 450Å observable in non nod-and-shuffle mode.
Spectral res.	5000	5000	For a discussion of the selection of spectral resolution see section 1.4.3.
Throughput (incl. atm)	0.3%	10%	The FIREBall throughput is strongly dependent on the achieved balloon altitude (see section 3.3.3.10).
Telescope Diam.	1 m	5 m	FIREBall is a standalone telescope, while CWI makes use of the Hale telescope at Mt. Palomar.
Observing Time	6 h	Unlimited	Balloon-borne FIREBall observes for a single flight. CWI observations are are limited by the time allotted to the instrument at Mt. Palomar.
Sky background	10^3 CU	10^5 CU	The sky is dimmer in the ultraviolet than at visible wavelenghts. Even across that band the blue part of the spectrum is quieter than the red.
Platform	Balloon	Ground-Based	
IFU Design	Fibers	Optical Slicer	
Detector	Microchannel plate	CCD	
Detector Noise	1 count/cm^2/s	3 e$^-$	
First light	July 2009	November 2009	

Table 1.5. A comparison of the FIREBall and CWI instrument parameters. See discussion in sections 1.5.1 and 1.5.2.

the target fields to provide information about the sky background, and to dither the fiber bundle on the sky during observations to alleviate differential instrument response across the field of view. As explained in appendix A, the sensitivity of the FIREBall spectrograph is limited by the detector and depends on the size of the emitting region. A 2500 arcsec^2 area on the sky must glow in a single 2 Å wide emission line at more than 20×10^4 LU to be detected with a signal-to-noise ratio of 5. This corresponds to the brightest and most compact regions in the circumgalactic medium.

1.5.2 Cosmic Web Imager

CWI, the cosmic web imager, is designed to detect C IV, OVI, and Lyα emission from diffuse sources at high redshifts, $2 < z < 7$. The instrument mounts at the F/16 Cassegrain focus on the 200" telescope at Mt. Palomar. CWI's primary objectives are to map matter in the so-called circumgalactic medium during the peak epoch of galaxy and star formation, $2 < z < 4$, study the nature of the Lyman α blob population, and investigate regions around quasars. These targets have characteristic sizes of under 300 kpc, subtending less than ∼40 arcseconds on the sky; the CWI field of view was chosen accordingly, at $40 \times 60\,\mathrm{arcsec}^2$. The spatial resolution is seeing limited (∼0.7 arcsec) along the field short dimension, and slit limited (∼2.5 arcsec) perpendicular to it. It might be possible to use pointing dithering or field-of-view rotation between integrations, in combination with tomographic image processing, to obtain more uniform and improved resolution in both axes, though this has not yet been attempted with CWI. The instrument is built with spectral resolution $R \sim 5000$ to satisfy the requirements discussed in section 1.4.3. Instantaneous bandpass depends on the detector and observing configuration. When the full CCD utilized, CWI covers ∼450 Å, probing $\pm 1.3 \times 10^4$ km/s around the selected target; in the nominal nod-and-shuffle configuration, intended to improve sky-subtraction accuracy, only the central one-third of the detector is exposed to light, limiting the bandpass to ∼140 Å, or $\pm 4 \times 10^3$ km/s. As mentioned in section 1.4.2, this is sufficient to probe the characteristic velocities within the CGM, and gas inflows during galaxy formation, and adequate to characterize emission from QSO associated absorbers.

CWI employs an *e2v* $60 \times 60\,\mathrm{mm}^2$ CCD with 15 µm pixels. The manufacturer reported read noise at $2\,\mathrm{e}^-$ level for this device, with measured CWI value being closer to $3\,\mathrm{e}^-$. Binning (currently 2×2) reduces the impact of read noise on system performance. CWI becomes sky-background dominated for diffuse target observations in roughly 20-minute integrations. The sensitivity of CWI is dependent on the background subtraction accuracy and the size of the emitting region. A three night observation of a 100 arcsec^2 object with 0.1% sky subtraction can reach down to ∼1000 LU, sampling brighter regions of the circumgalactic medium, warm-hot intergalactic medium, regions around quasars, and brighter Lyα blobs.

Chapter 2

CWI: The Cosmic Web Imager

2.1 Instrument Overview

The Cosmic Web Imager (CWI) is an integral field spectrograph for the 200" Hale telescope at Palomar Mountain. It is intended for observations of the dim and diffuse universe. It combines a sizable field of view, at 60"×40", with spectral bandpass of ∼450 Å, chosen from the available wavelength range. The spectral resolution for the current configuration is $R = \lambda/\Delta\lambda \sim 5000$. The spatial resolution is seeing limited (1") along the short dimension of the field of view, and instrument limited (2.5") along the longer dimension. The instrument background is kept low by careful baffling and a custom built enclosure, coupled with a detector CCD with excellent noise characteristics. CWI is designed to make use of the nod-and-shuffle observation technique (Cuillandre et al. 1994; Sembach & Tonry 1996), to improve sky subtraction. The scientific drivers and requirements behind the instrument are discussed in Chapter 1.

Design and integration of the instrument began at the California Institute of Technology in 2006. It was designed, constructed, tested, and commissioned by members of professor Chris Martin's research group. The bulk of the work was done by three graduate students: Daphne Chang, Shahinur Rahman, and the author. The detector subsystem was built by staff scientist Patrick Morrissey and another graduate student Nicole Lingner. Chris Martin, Anna Moore, and Ryan McLean provided guidance, support, and helping hands, whenever one was needed.

The details of the instrument design, integration, and commissioning are given in section 2.2, with the key instrument parameters summarized in table 2.1. CWI is put in context of existing instruments and those in development in table 1.4. The Cosmic Web Imager saw first light during an engineering run in July 2009, with subsequent scientific observations in November 2009, March, May, September, October 2010, April and June 2011. The targets, observing procedure, and some of the results for those runs are discussed in section 2.4.

Table 2.1. Key CWI instrument parameters

Parameter	Value	Notes
Field of View	40" × 60"	Composed of twenty-four 1 mm × 16 mm slices, each corresponding to 2.5"×40" on the sky.
Spatial Resolution	1" × 2.5"	The instrument is seeing limited along the IFU slices and slit-width limited along the other dimension. The slit-width limit can be overcome via an observing strategy of dithering the FOV on the sky by subslice lengths, or rotating the FOV.
Instantaneous Bandwidth	450 Å	The grating choice, combined with grating and camera angles can be adjusted to pick out a 450 Å wide subinterval of the available spectrum. In the nod-and-shuffle configuration, only a third of the detector is available, limiting the bandwidth to 150 Å.
Spectral Coverage	3800 − 9500 Å	As of this writing CWI is equipped with a single grating that covers 4450 to 5500 Å.
Spectral Resolution	$R \sim 5000$	A lower resolution configuration with a larger instantaneous bandwidth is possible, and is described in section 2.2.3.2.
Instrument Efficiency	10%	That is the peak instrument efficiency including the effects of the atmosphere and telescope.
Sensitivity Limit	3500 LU	This value depends on the sky brightness during the observation, sky subtraction efficiency, instrument parameters and nature of the source being observed. The given value is calculated for detection of a 3 Å wide emission line at 5000 Å eminating from a 100 arcsec^2 region assuming instrument instrument parameters above and detector readnoise of 2.5 e^-.

2.2 Instrument Design, Construction, and Integration

2.2.1 Optical Design

The CWI optical layout was arrived at by combining the moderate resolution requirement ($R \sim 5000$), and a sizable 150 mm beam, with the spatial constraints of the Cassegrain focus cage. A two-sided optical bench was used to allow for the total necessary 4800 mm light path. The optical layout is shown in figure 2.1. All optical elements are installed to machine tolerances, using the regular hole pattern of the bench as a reference. As CWI is a seeing limited instrument, and uses a slow (F/16) telescope beam, the tolerances on optical alignment are not very tight for the large optics. Small errors in positioning and angle can be overcome using the available degrees of freedom built into the instrument. The CWI optical elements, their optical properties, and available adjustments are outlined in the paragraphs below.

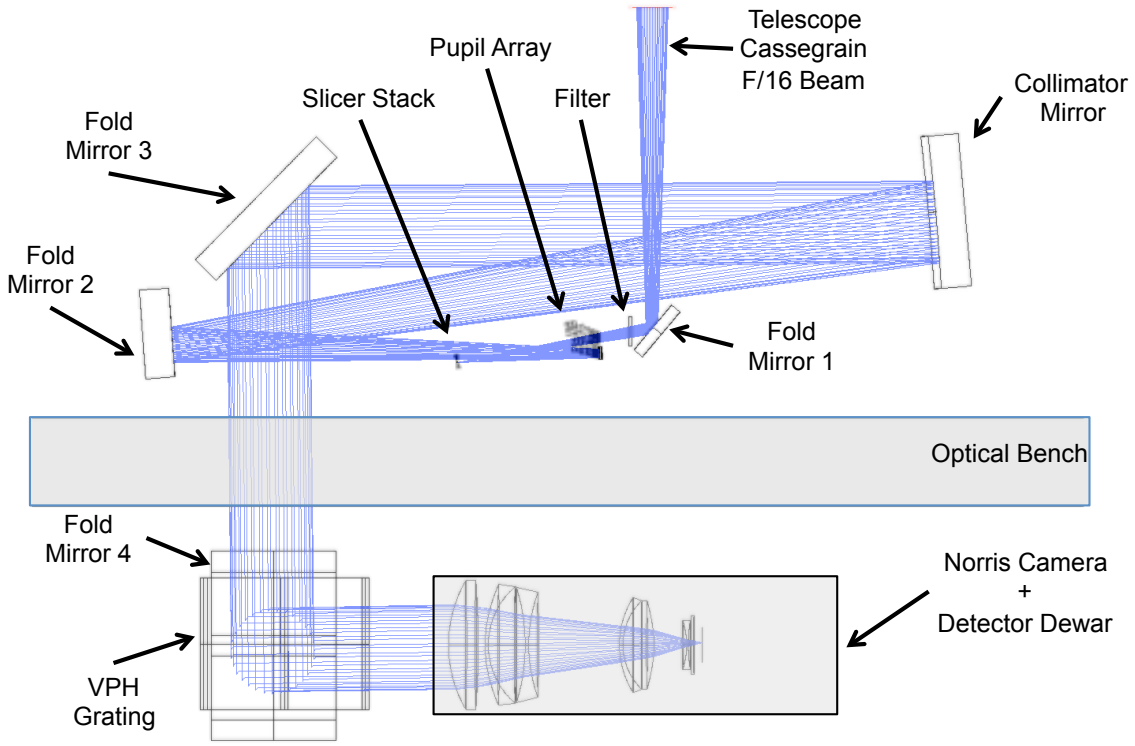

Figure 2.1. Ray trace of the full CWI Instrument. The telescope beam enters the instrument from above and is reflected by a fold mirror (FM1), through an astronomical filter, and brought to a focus at the slicer mirror stack. The beam coming off FM1 is at a 10 degree angle with respect to the optical bench. CWI does not reimage the focal plane, and the beam geometry of the full system near the IFU is crowded. Had the IFU been in the plane of the optical bench, baffling of the portion of the telescope beam focusing next to the slicer would have been impossible without vignetting the science beams, the unbaffled light would propagate through the spectrograph and be reimaged, slightly out of focus, at the center of the detector. The slight tilt brings this light out of the operating path of the instrument. The science beam continues into the integral field unit (IFU) were the slicer fans out the field of view into twenty-four separate beams. These are directed by an array of pupil mirrors toward a folding flat (FM2). The light then travels to a spherical collimator mirror. The now-collimated beams are reflected by a pair of actuated folding flats (FM3, FM4) to the underside of the optical bench, where they are dispersed by a volume phase holographic grating (VPH), and focused by the Norris lens onto an 4k×4k e2v CCD.

Fold mirror 1 (FM1) is a 4" diameter mirror. It is mounted in a commercial mount attached to a custom stand fixed to an 8" linear actuator that also holds the calibration system periscope. The mirror height above the optical bench is fixed. The mirror angle is controlled using a pair of fine threaded screws within a Newport U400-AC2K mirror mount. The nominal FM1 orientation sends the telescope chief ray at a 10 degree angle to the optical bench. This is done to avoid fields that were missing the IFU from being reimaged onto the detector by the remaining CWI optics (see Fig. 2.2). The mirror was adjusted only once. At the start of the CWI engineering observing run in July 2009, the telescope was slewed to move and center the beam from a bright star (Vega) onto FM1. The mirror tip-tilt angle was set to place the focused star image at the center of the slicer stack. A rectangular mask was mounted on the face of the mirror to partially baffle beams that are not directed at the slicer. Figure 2.3 shows FM1 mounted and installed into the system.

The filter is a 2" square, thin (3-5 mm) optical interference or absorption glass element mounted on the back side of the pupil mirror array block. It is encased in an aluminum clamshell that can be moved along the direction perpendicular to the bench to ensure the optic is in the telescope beam. Transmission curves for the two CWI filters are shown in figure 2.4

The slicer mirror stack is constructed of twenty-four 1 mm tall, 16 mm wide slicer mirrors. The angles of the individual slices were machined to a tight tolerance and are given in table 2.2. There is some freedom in mounting the slicer stack assembly to the IFU base plate by way of shimming. The IFU base plate can be adjusted several millimeters along the beam direction, and a millimeter perpendicular to it.

The pupil mirror array consists of twenty-four small mirrors, of which half are $21\times32\,\mathrm{mm}^2$, the others $23\times36\,\mathrm{mm}^2$. The mirrors are fixed to a pair of backing plates using special mounting blocks. The backing plates are attached to the same interface plate as the slicer mirror stack. The position of the mirrors is fixed by the block mounting locations, though shims can be used to move them along the beam. The blocks have a flexure design that allows the individual pupil mirror tip-tilt angles to be adjusted in situ. This adjustment is necessary to evenly space the individual slitlet images on the detector to correct for any slight errors in the slicer mirror compound angle, pupil mounting block angles, or pupil mirror substrate wedge. Figure 2.3 shows the slicer stack and pupil mirror array.

Fold mirror 2 (FM2) is a flat $550\times140\,\mathrm{mm}^2$ mirror angled away from the bench by 5 degrees. The mirror is mounted on an linear actuator and can move along the beam arriving from the pupil array. It has a range of motion of 50 mm. This motion allows FM2 to be used as an internal focusing mechanism for the instrument. This is necessary as the location focus of the system changes slightly with grating setting and wavelength.

The collimator is a spherical 650×240 mm mirror with an as-built radius of curvature of 4760 mm. It has no built-in automated degrees of freedom, though the angle of the mirror can be adjusted during the initial installation.

Fold mirror 3 (FM3) is a 425×290 mm^2 flat folding mirror. Its function is to direct the spectrograph beams to the underside of the bench. The mirror has an actuated tip mechanism that allows rotation by ±1° around the mirror axis parallel to the bench. This motion is used to compensate for any slight alignment errors in the direction transverse to the virtual slit. The rotation of this mirror is also suited to negating any motion of the spectra on the detector along the spectral direction due to flexure.

Fold mirror 4 (FM4) is a 370×190 mm folding mirror. It redirects the spectrograph beam along the underside of the optical bench. It is actuated around the mirror axis parallel to the bench and has a range of motion of ±1°. This motion can be used to compensate for any misalignment along the spectrograph slit, and can correct for the effects of flexure along that direction as well. Furthermore, there is play in the detector dewar mounting mechanism, and the CCD is typically shifted slightly whenever the dewar is removed and reattached. The actuated mechanism of FM4 corrects for this misalignment.

The grating is a 350×250 mm transmissive element that is mounted near the beam pupil. It is attached to a rotary stage that turns it about an axis in the grating plane, near its center, perpendicular to the optical bench. The slight offset, ∼19 mm, is built in to account for the refracted light paths within the grating, ensuring that the beam footprint is not vignetted by the grating. The rotation sets the beam angles of incidence and diffraction, controlling spectrograph bandpass and grating efficiency.

The system lens is the heritage Norris lens from the Norris Spectrograph (Epps 1990; Hamilton et al. 1993; Cohen et al. 1988). It is attached to a custom curved track that rotates the optic through a 30 degree arc around the same pivot point as the grating. The angle selects the wavelength range falling on the detector.

The detector is installed in a dewar that is bolted onto the back of the Norris lens. It inherits the rotational degree of motion around the grating axis. The spacing between the dewar and the camera is controlled by a set of standoffs. These can be changed to adjust the detector position to the lens focus location. The thickness of these pads is configured so that the nominal focus for the instrument is when FM2 is at the center of its range.

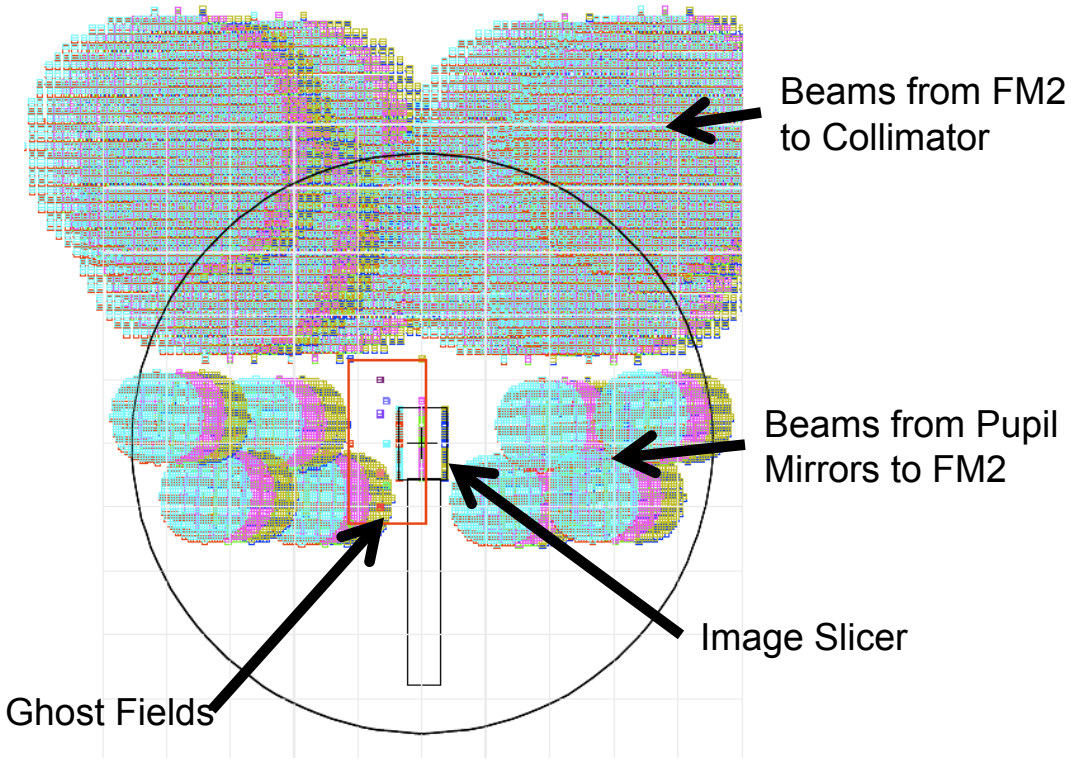

Figure 2.2. A composite footprint of several sets of beams in the focal plane of CWI prior to the addition of a 10 degree tilt between the IFU axis and the bench. The perspective is that of looking at the image slicer face-on from the direction of FM1. The image slicer is small black rectangle at the center of the image. Light is reflected from the slicer toward the reader, is incident on the array of pupil mirrors and then crosses the focal plane on its way toward FM2. FM2 redirects the beams at the collimator mirror, during this traverse the beams cross the focal plane once more. Fields points that miss the IFU are marked as "Ghost Fields" and bounded by a red rectangle in the image (there is a matching set on the other side of the image slicer). In the initial CWI designs, the chief rays of the beams from the pupil mirrors to FM2 were nearly colinear with the incoming beams from the telescope. In such a configuration, the ghost fields were reimaged by the spectrograph optics near the center of the CCD. Two solutions were considered. The first was to add large baffles next to the slicer; unfortunately, due to the other beams crossing the slicer plane, this was not possible without also partially vignetting the science field. The second solution was to introduce a tilt to remove the beam coincidence; this solution was adapted.

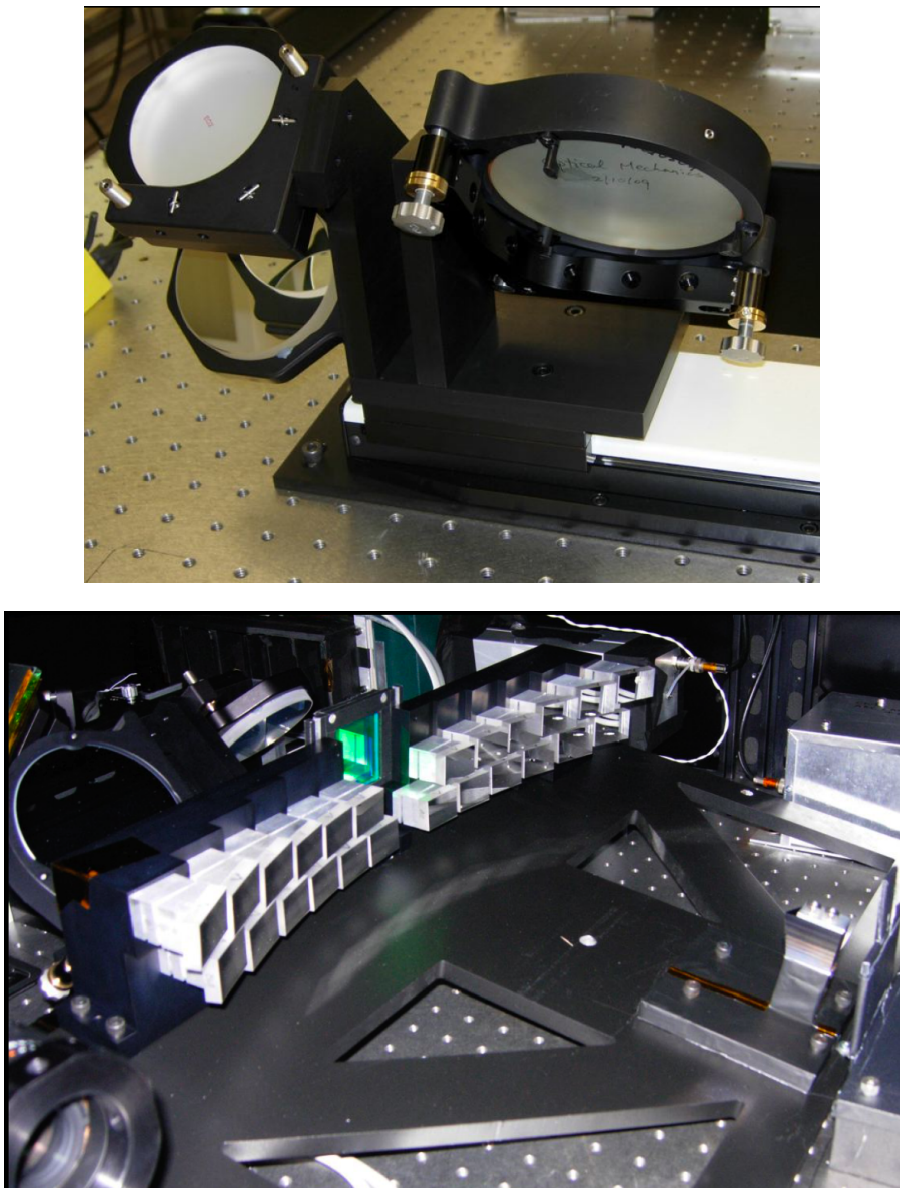

Figure 2.3. Fold mirror 1. The left panel shows FM1 installed in a commercial mount, attached to a linear stage next to the calibration system periscope mirrors. The right panel depicts the CWI slicer unit, pupil, mirrors, filter, FM1, and periscope mirrors. FM1 and the periscope are installed behind the pupil mirror array. In the image the instrument is configured for calibration mode. The band-pass filter is visible in the gap between the two sides of the pupil mirror array. The slicer stack is at the right of the photograph.

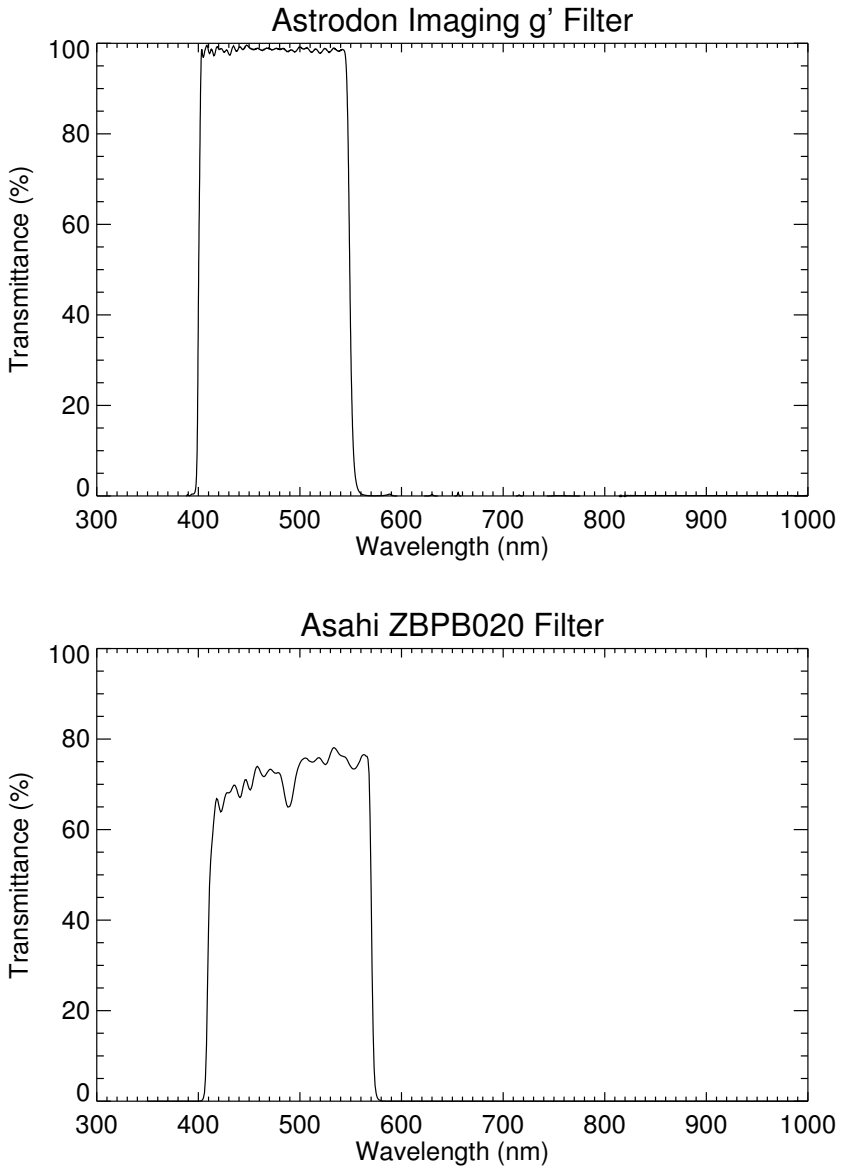

Figure 2.4. Throughput of two filters used in CWI. The top panel shows the transmission curve for an Astrodon g'S50 Sloan-like filter that was installed prior to the May 2011 observing run. The bottom panel is the transmittance of an Asahi ZBPB020 filter that was used up to that time. The relative transmission of the two filters was measured in lab, the Astrodon filter was found to have transmission ∼1.2 times higher than the Asahi optic within the pass-band of the g' filter. Transmission data for the g' filter courtesy of Astrodon Imaging. Asahi ZBPB020 data taken from the product website.

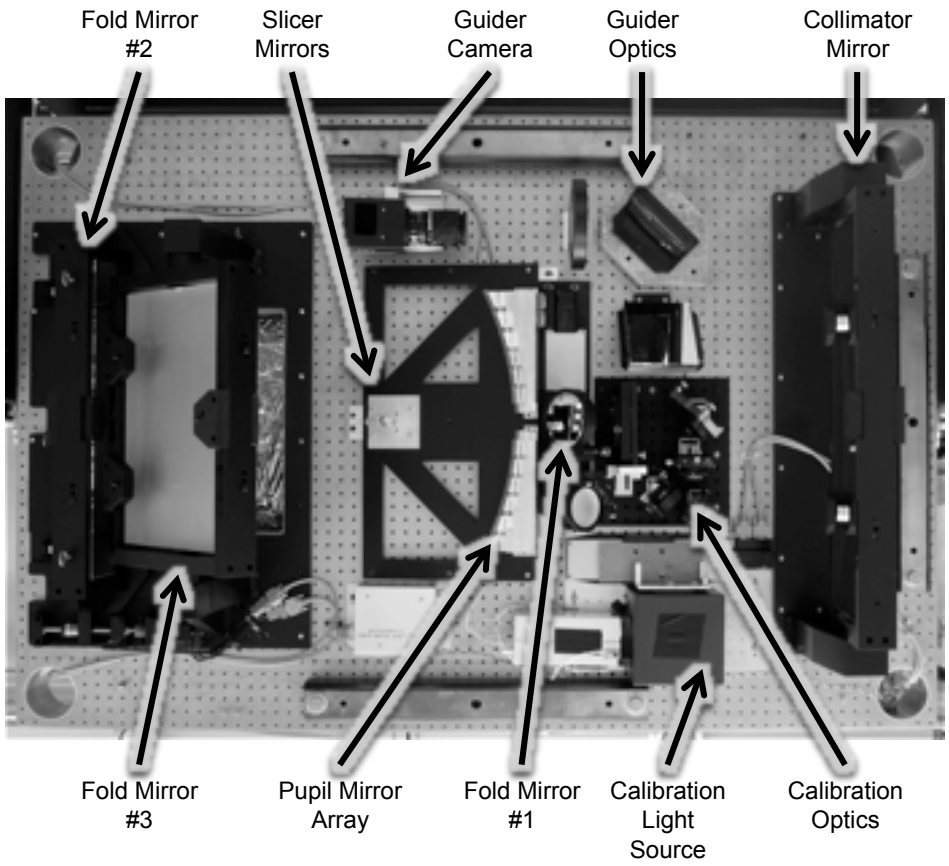

Figure 2.5. Instrument layout on the top side of the two-sided optical bench. The picture is taken from the direction the telescope beam enters the instrument. The beam is reflected by fold mirror 1 (FM1), through a filter (not pictured) into the IFU. The instrument field of view is carved into twenty-four slitlets by the slicer and pupil mirror pairs. It is then directed by FM2 onto a spherical collimator, and sent through the opening in the bench by fold mirror 3 (FM3). The calibration unit is positioned to the right of FM1, and is described in more detail in section 2.2.6. The offset guider and associated optics, which include a pair of folding mirrors and a field lens, are to the right of FM1 in the image. Three (unlabeled) mounting bars can be seen at the top, bottom, and right of the bench. These are used to attach the instrument to the telescope using a specially designed mounting structure.

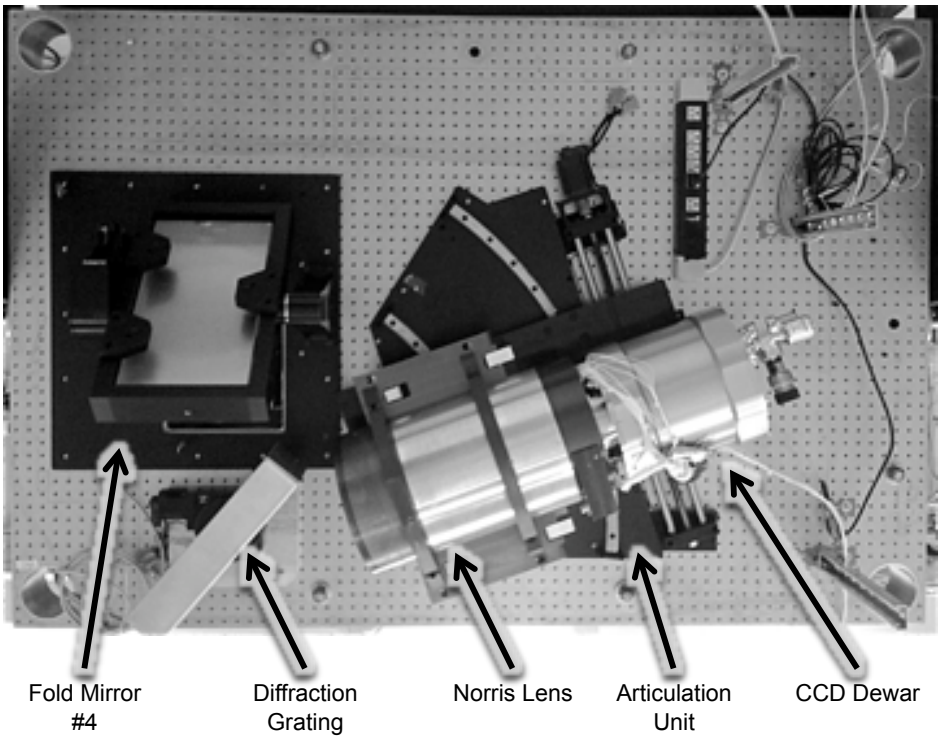

Figure 2.6. Instrument layout on the bottom side of the two-sided optical bench. The beam from the top side is reflected by FM4 toward a VPH diffraction grating, where it is diffracted at the articulated lens, and focused onto the detector. The grating can rotate around its center point; the camera system is mounted on a circular track that rotates it around the same axis. Though not pictured, this surface also houses the motor controllers, lens shutter controller, power strips, and CCD readout electronics.

2.2.2 Integral Field Unit

The CWI IFU design was chosen for its simplicity, functionality, and cost considerations. It is a stack of twenty-four flat slicer mirrors placed in the telescope focal plane to redirect parts of the field of view to twenty-four individually adjustable pupil mirrors. The virtual images of the slicer mirrors in the pupil mirrors form a staggered virtual slit that acts as the entrance aperture to the more classical spectrograph that follows. Ray traces of the IFU and virtual slit is shown in figure 2.8.

The IFU optical design was converged on by Daphne Chang and the author. Daphne oversaw manufacture of the slicer stack and performed integration of the IFU system, with mechanical design input from Shahinur Rahman. The final testing, calibration, and alignment was performed by all three persons mentioned above.

2.2.2.1 Optical Design

The 60"×40" instrument field of view requires a 24 mm×16 mm focal plane integral field unit. Both a fiber array and a reflective image slicer were considered in preliminary designs. Concerns regarding focal plane filling factor, focal ratio degradation, and throughput variations due to flexure steered the preferred design toward an all-reflective slicer stack. An image slicer was also considered a proof-of-concept design for a future vacuum-UV IFU instrument where reflective optics are preferred to refractive designs on efficiency.

The thicknesses of the individual slicer mirrors in the slicer stack needed to be larger than the typical seeing disk size at Palomar, so a minimum of 1" $\sim 400\,\mu$m, but also needed to be large enough that the virtual slit has length of no more than $\sim$0.5 m, to constrain the sizes of the instrument optics. This led to a slit width of 1 mm. The choice was made to orient the slices along the shorter dimension of the 24 mm × 16 mm stack. Although this entails more optical elements, the tilt angles of the individual slices would lead the edges of the slices to be further from the telescope focal plane than when they are oriented along the other dimension.

The design draws on the work of Weitzel et al. (1996). It starts with modeling the slicer as a single point in the focal plane of the telescope. Pupil mirrors are then placed on a paraboloid surface with a focus at the slicer and its axis coincident with the telescope axis. The distance from the vertex to the focus of the paraboloid is chosen to be 250 mm. This allows the IFU assembly to fit in the allotted space on the optical bench, maintains the total length of the virtual slit below $\sim$0.5 m, spaces out the individual 16 mm wide slitlets by 2 mm and counteracts overlap of beam footprints at the pupil mirror array. The pupil mirrors are arranged in a brick-wall pattern to ensure that this vignetting does not occur. These mirrors are also arranged in a slightly upward-curving set of locations (a "smile") to offset the effect of conic diffraction at the grating. The pupil mirrors are tilted by an extra 5 degrees away from the IFU base plate to bring the exiting beams parallel to the bench surface. The locations and angles of the slicer and pupil mirrors were entered into ray-tracing software (ZEMAX). The angles of the pupil mirrors and their positions along the beam were allowed to vary to optimize the resultant imaging performance. The final angles, without the additional 5 degree tilt, are listed in table 2.2, and the change from an early design to the final version is emphasized in figure 2.7.

2.2.2.2 Slicer Assembly

The slicer assembly was designed primarily by Daphne Chang with input from other members of the group and engineers at the Kugler Corporation.

The slicer assembly is constructed of AlMgSi alloy. Each 1 mm thick, 16 mm wide slicer mirror was manufactured independently. The compound angles were machined to a $\pm 0.05^\circ$ tolerance, with the reflective surface diamond turned, to rms surface finish better than 7 nm, as evidenced by the

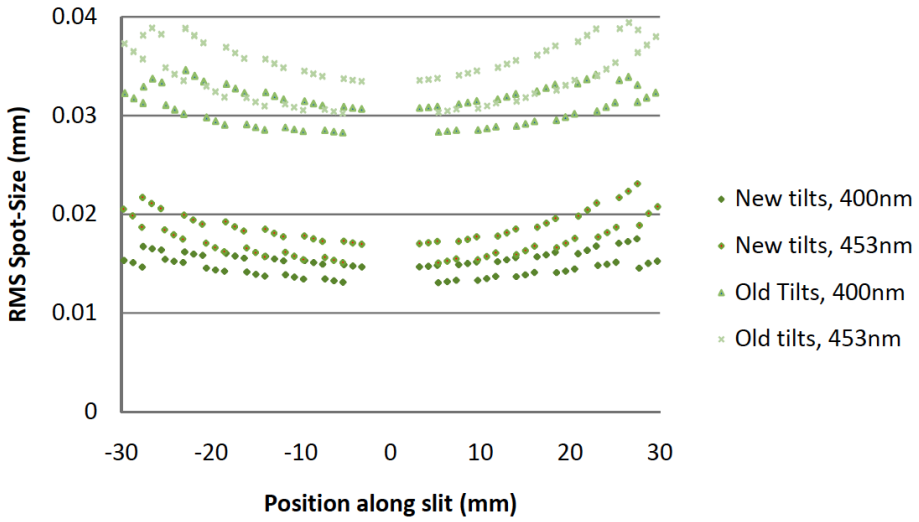

Figure 2.7. Imaged rms spot radii for CWI as a function of position on the detector. The two bottom sets of points are for two different wavelengths in the final IFU configuration. The top two sets are for the same wavelengths, prior to optimization of the mirror angles and pupil mirror positions.

Table 2.2. Listing of the design angles, in degrees, for the IFU mirrors. Some of the angles differ between the slicer and pupil mirrors; this is a result of ray-trace (ZEMAX) optimization.

Slit	**Slicer**		**Pupil**	
	Tip	**Tilt**	**Tip**	**Tilt**
1	-24.0	-3.6	-24.1	-2.8
2	-22.4	-0.3	-22.4	0.6
3	-20.6	-2.6	-20.6	-2.0
4	-18.9	0.6	-18.9	1.3
5	-17.0	-1.7	-17.1	-1.2
6	-15.2	1.47	-15.3	2.0
7	-13.3	-1.1	-13.4	-0.7
8	-11.5	2.1	-11.5	2.4
9	-9.6	-0.5	-9.6	-0.3
10	-7.7	2.7	-7.7	2.9
11	-5.7	0.0	-5.7	0.1
12	-3.8	3.1	-3.7	3.2
13	3.8	3.3	3.7	3.4
14	5.7	0.4	5.7	0.5
15	7.7	3.3	7.7	3.5
16	9.6	0.3	9.6	0.6
17	11.5	3.1	11.5	3.5
18	13.3	0.2	13.3	0.6
19	15.2	2.9	15.2	3.5
20	17.0	0.0	17.1	0.6
21	18.9	2.4	18.8	3.2
22	20.6	-0.5	20.6	0.3
23	22.4	1.9	22.3	3.0
24	24.0	-1.1	24.1	0.0

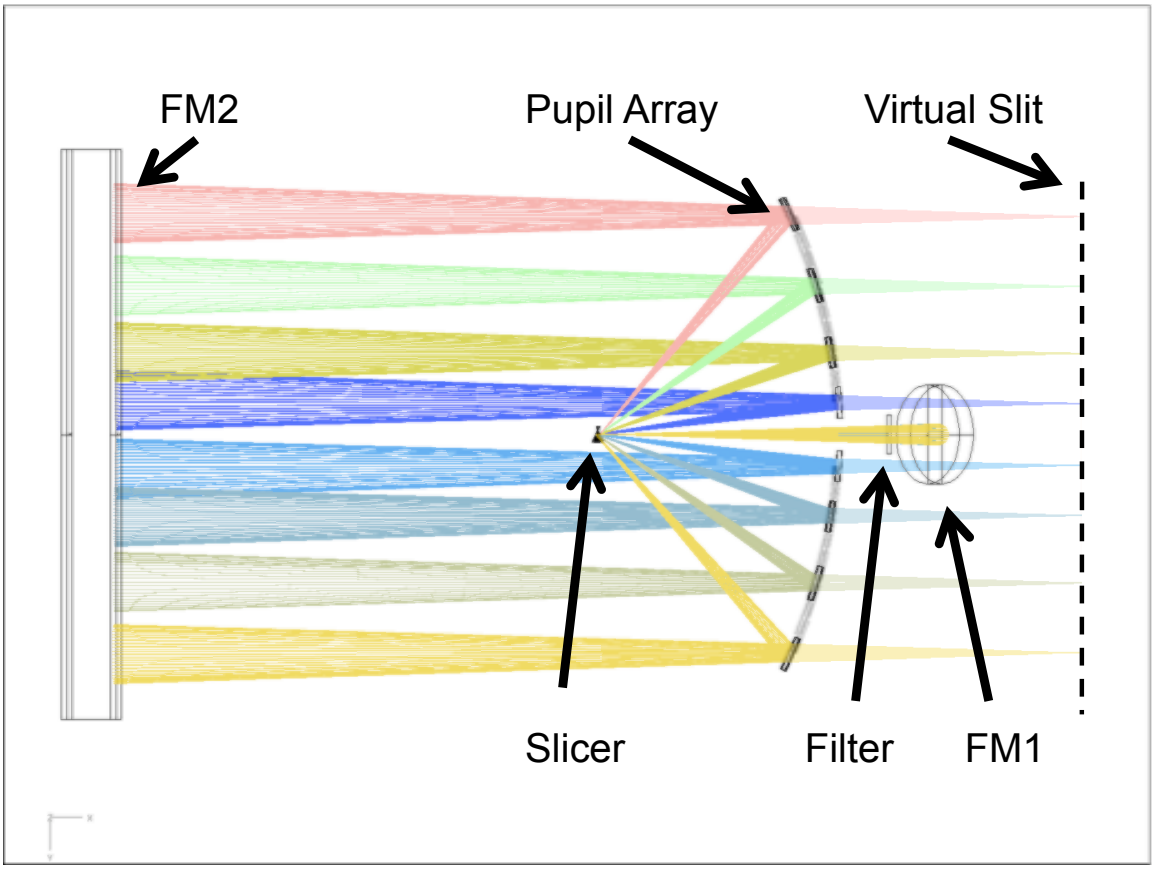

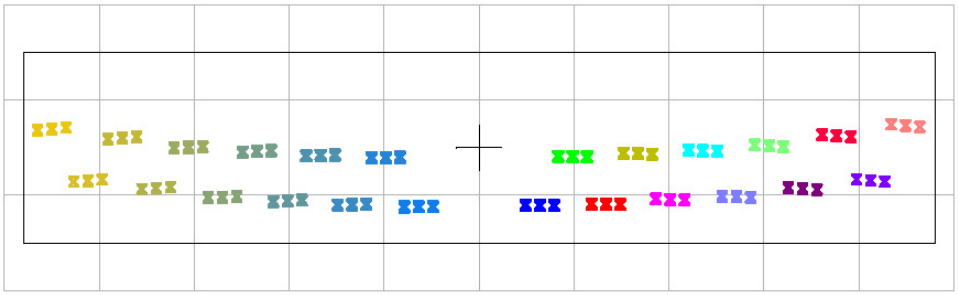

Figure 2.8. A ray trace of the integral field unit showing the beam path in this part of the instrument. The telescope beam is coming into the page from the reader's perspective; it is reflected by FM1, through an astronomical filter, and the focal plane field of view is fragmented by the slicer mirror stack. Pupil mirrors then send the twenty-four beams toward the remainder of the spectrograph. The slicer and pupil mirrors generate a virtual slit. The layout of this virtual slit is shown in the bottom panel; the background grid squares are 50 mm on a side, and each of the twenty-four slitlets is represented by three fields. The slitlets are staggered. This was necessary to allow the spectra to be closely spaced on the detector. The upward curvature across the slit was added to negate the effect of conical diffraction at the grating.

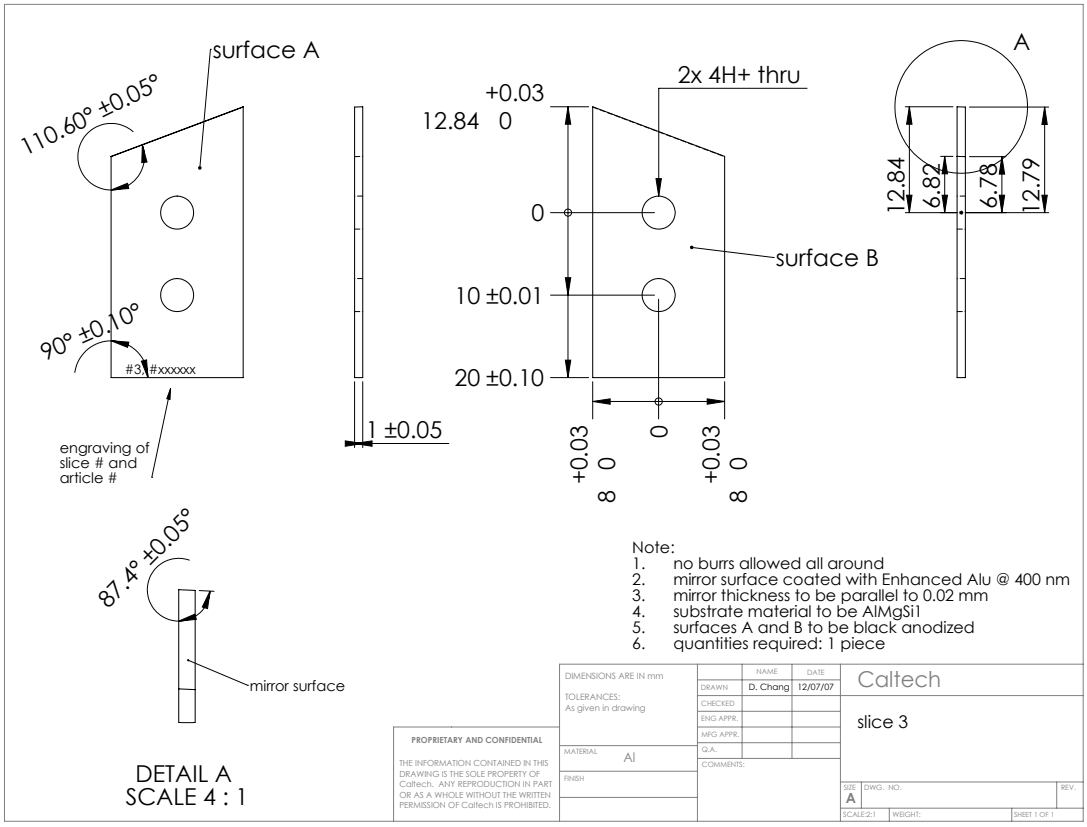

Figure 2.9. One of the twenty-four slicer mirror construction drawings, as prepared by Daphne Chang. The thin (1 mm) aluminum prism has one compound angle surface. The two central circular apertures are used for mounting the assembly together on a pair of dowel pins.

manufacturer's data (see appendix C). The mirror surface was given a protected aluminum coating optimized for the 370-470 nm wavelength range. The mirrors were then stacked on a specially made mount, and attached to the IFU base plate. None of the slicer parts were black anodized, although the pedestal, base and top clamp should have been. This choice was made as the delivery of the slicer was delayed and the part was necessary for scheduled telescope time. These parts were covered with a matte black aluminum foil prior to installation on the optical bench. Despite this, the pedestal is a strong scattering surface that is evident when observing near a strong point source that falls on that part of the hardware. It would be beneficial to consider a mount that incorporates light-trapping elements for future designs, such as those being developed for KCWI. A technical drawing of one of the slicer mirrors, as prepared by Daphne Chang, is shown in figure 2.9. The completed stack is pictured in figure 2.10, and the mirror reflectivity curve is shown in figure 2.11.

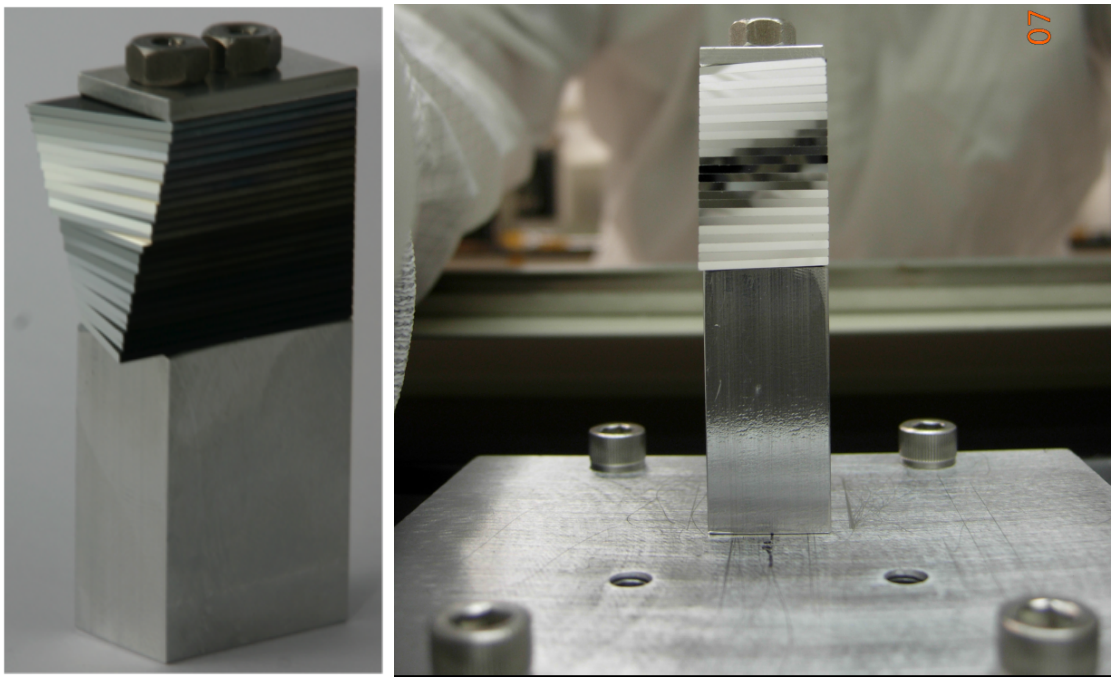

Figure 2.10. The slicer stack as seen from the side and the front. The twenty-four slicer mirrors are stacked on top of a pedestal and aligned using a pair of dowel pins (see Fig. 2.9). The assembly is clamped from above, and attached to a mounting plate, which is then bolted onto the IFU base plate.

2.2.2.3 Pupil Mirror Array

The pupil mirror array consists of two large backing plates and twenty-four mirror mounts with rectangular mirrors. The mirror mounts are aluminum rectangular prisms with a pair of built-in flexures that can be adjusted using fine threaded screws, changing the compound angle between the front face and mounting face of the block. This adjustment can be performed after the assembly is installed on the backing plates. A sketch of a mounting block is shown in figure 2.12. The front face of the mounting cube has shallow channels machined into it where Scotch-weld 2216 two part epoxy is injected, to bond a pupil mirror to the mount. A small weight is placed atop the mount during the epoxy curing process to prevent the elements from moving and to provide pressure for the bond to take effect. Details of the flexure mount design and bonding process can be found in Rahman (2010).

2.2.2.4 IFU Alignment

The first steps in IFU alignment are the attachment of the pupil mirror backing plates with installed pupil mirrors, and the slicer stack onto the IFU base plate. These are installed to machine tolerances ($\pm 100\,\mu$m). The IFU base plate is attached to the bench using three standoff blocks. These set the

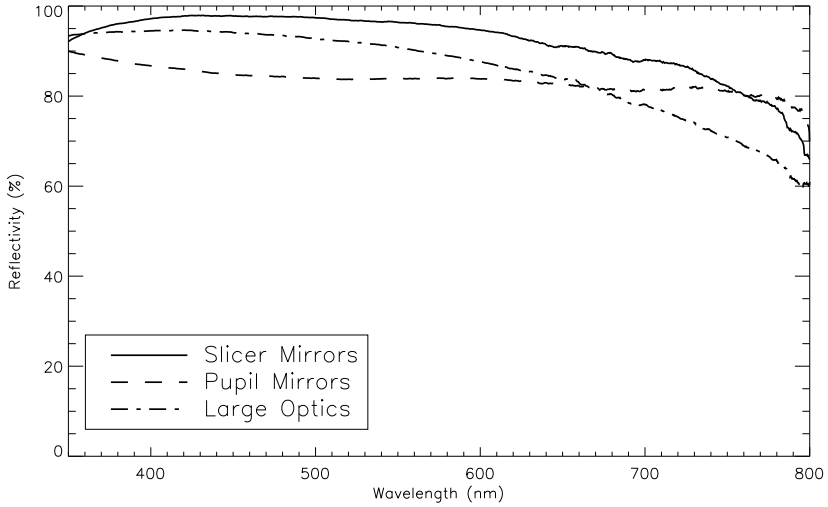

Figure 2.11. Reflectivity of CWI mirrors. The data are as measured in lab for the actual optics or witness samples provided by the manufacturers. The slicer mirrors were made by the Kugler Corporation, pupil mirrors by Custom Scientific, and the large optics by Optical Mechanics. The coatings were all simple aluminum coatings with a protective dielectric overcoat, maximizing reflection efficiency at the blue end of the spectrum. The decline in reflectivity toward the red necessitates that the mirrors be recoated with a broadband reflectivity layer to maximize CWI efficiency and scientific return. New protected silver coatings are being considered for the Keck version of the CWI instrument, KCWI.

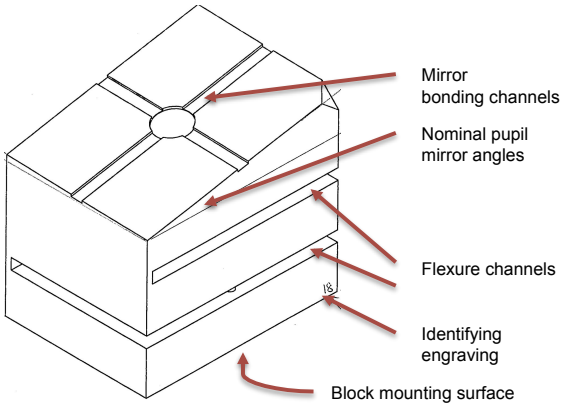

Figure 2.12. Schematic drawing of a pupil mirror flexure mount. The mount has two flexures, one along each of the two principal directions, which allow for small ($\pm 1°$) adjustments in angle of the mounted mirror with respect to its nominal orientation. These adjustments are controlled by a pair of 0-80 screws. The mount has built into it the (slightly undersized) compound angle for a specific pupil mirror. The surface channels at the top of the block are used for bonding the mirror substrate to the mount.

relative angle of 10° between the two surfaces. They allow for a 5 mm position adjustment of the mounting plate along the optical axis of the instrument. This distance is set by placing the slicer at the prescribed distance from FM1. At this stage, the calibration unit periscope mirrors are adjusted to project calibration objects onto the slicer (section 2.2.6) making sure that the reflected beams fall onto the pupil mirrors. The pupil mirrors are adjusted using the flexures, their footprints are examined on a screen placed behind the slicer stack. These are compared and matched to to a ZEMAX ray-trace footprint diagram. Once the remainder of the CWI system is configured, the pupil mirror angles are revisited. The pupil angles are adjusted, if necessary, to ensure that the beams are not being vignetted anywhere along the path, and that they are evenly spaced on the detector.

2.2.3 Gratings

2.2.3.1 Introduction

The diffraction elements are the key optics in any spectrograph. The principles of operation of diffraction gratings are described in any good optics text (e.g., Schroeder 1987; Palmer & Loewen 2005). The key characteristics of a grating for CWI (and most astronomical applications) are diffraction efficiency, dispersion, scattering characteristics, and physical size. Reflective and transmissive gratings were considered for CWI, including mechanically and holographically ruled versions of each. The main advantages of mechanically ruled gratings are that the technology is mature and well understood, the shapes of the grooves can be controlled to alter the diffraction efficiency of various diffraction orders. It is, however, difficult to make these optics large, and surface defects and irregularities are not uncommon, leading to less than ideal scattering characteristics. Holographically recorded gratings offer better scattering performance, as the features are typically uniform and smooth, they can be made large, and there is greater flexibility in setting the groove spacing. In particular, Volume Phase Holographic (VPH) gratings offer higher peak grating efficiencies than surface relief gratings, and, by adjusting angles of incident and diffracted light, a tunable bandpass (Arns et al. 1999; Barden et al. 2002). These gratings operate near the Bragg condition where the angle of incidence is approximately the same as the angle of diffraction. Varying the pair changes the wavelength at which peak efficiency occurs. A schematic illustrating the grating geometry is pictured in figure 2.13, theoretically computed grating tuning curves are shown in figure 2.14, and the model used to generate them is discussed in the following sections. The choice was made to use Volume Phase Holographic (VPH) gratings, mainly due to the high diffraction efficiencies and low scattering. This was a risk, and proved so, as one of the vendors contracted was not capable of delivering the grating ordered.

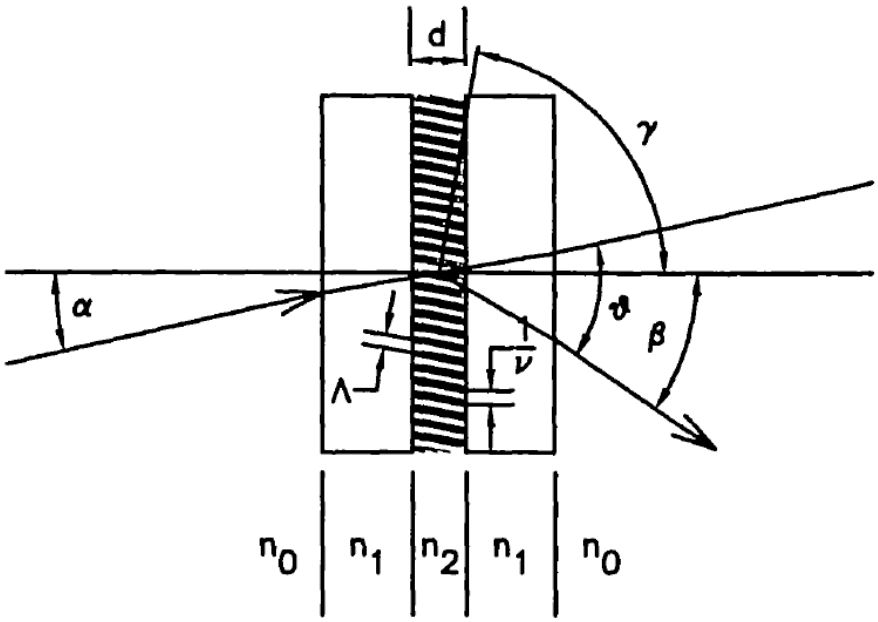

Figure 2.13. A schematic illustrating the geometry of a VPH grating. A layer of dichromated gelatin is sandwiched between two glass substrates. Figure adapted with permission from Barden et al. (2000)

2.2.3.2 VPH Grating Prescription

Kogelnik Approximation

Kogelnik (1969) derived the diffraction efficiency of a transmissive grating with sinusoidal index of refraction modulation of the diffracting layer. This analysis is applicable to VPH gratings, and the expressions derived are summarized in this section. The parameters involved in the calculation are listed in table 2.3. Another approach to modeling VPH gratings exists, recursive coupled-wave analysis (RCWA) (Moharam & Gaylord 1983). This numerical method reproduces the finer features of the grating efficiency curves, but is in good agreement with the Kogelnik formalism for the gratings considered here. The expressions below assume lossless gratings, with $\Delta n \ll n$.

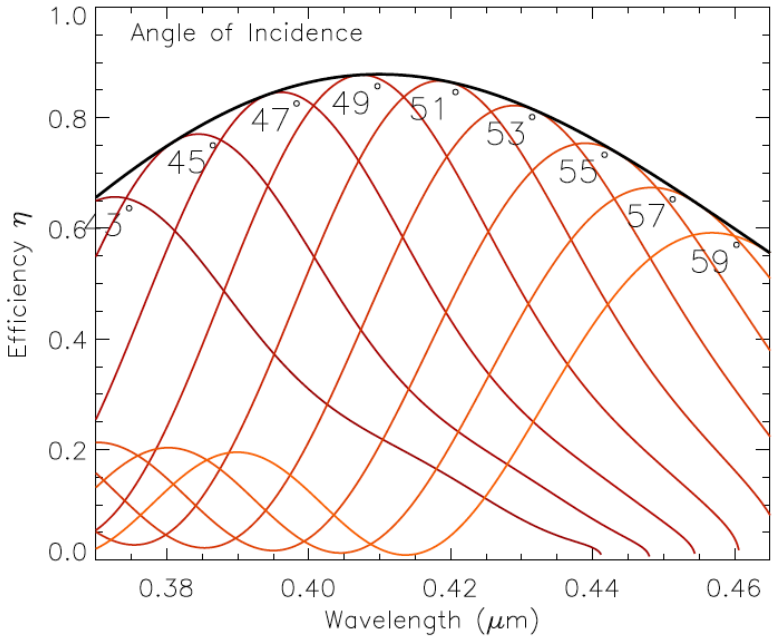

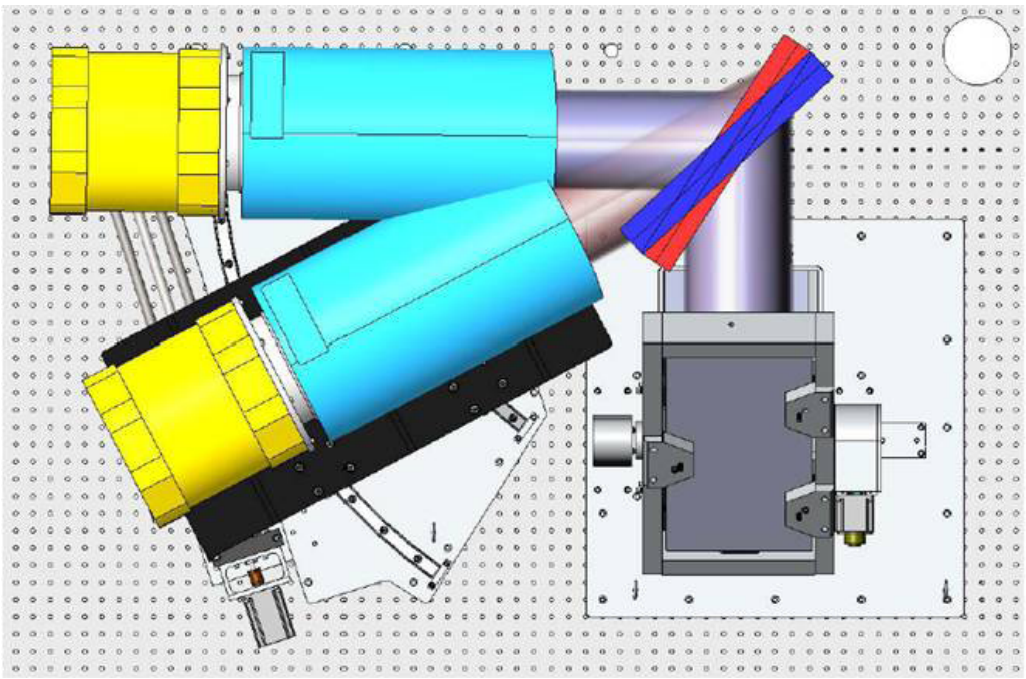

Figure 2.14. Grating peak efficiency as a function of angle of incidence (and diffraction) is shown in the plot to the left. The thick curve shows the superblaze, or the highest possible efficiency attainable by this particular grating at a given wavelength. The lighter curves indicate the grating bandpass for individual orientation settings. The right panel shows a cad rendering of the CWI camera and grating assembly in two such possible configurations. Notice that the grating and the camera need to be rotated about a common pivot point, with the camera rotation being approximately twice that of the grating.

Table 2.3. Parameters used in the Kogelnik coupled wave grating diffraction efficiency. Other variables are introduced, but they are intended to simplify the forms of the expressions.

Symbol	Quantity	Units	Value	Discussion
n	Mean gelatin index of refraction	—	∼1.3	Depends on the manufacturing process. Exposure of the DCG to light only lowers the material index of refraction, so the mean gelatin index is reduced from the starting value of ∼1.3
Δn	Amplitude of gelatin n variation	—	∼0.1	Depends on the manufacturing process. Longer exposure times, and light intensities lead to higher Δn; lower values are preferable and more easily achieved.
θ	Angle of incidence of light within the gelatin layer	—	*Var.*	Related to the angle of incidence of light onto the grating by Snell's law
ψ	Angle the index of refraction fringes make with the front surface of the diffractive layer.	—	$\frac{\pi}{2}$	A small change in this angle is used to reduce the impact of ghosting, and can be used to increase the spectral power of the system.
d	Thickness of the active gelatin layer.	μm	10	Thicknesses less than $\sim 4\,\mu$m are difficult to achieve.
ρ	Fringe frequency	lines/μm	*Var.*	The inverse of the fringe period (denoted Λ).
λ	Light wavelength	μm	*Var.*	
η	Diffraction efficiency	—	—	The calculated diffraction efficiency. Subscripts S and P designate the in-plane and out-of-plane polarizations of light.

$$\eta = \frac{\sin^2\left(\nu^2 + \xi^2\right)^{\frac{1}{2}}}{1 + \frac{\xi^2}{\nu^2}},$$
$$\nu = \frac{\kappa d}{\sqrt{c_R c_S}},$$
$$\xi = d\frac{K\cos(\theta - \psi) - \frac{\lambda K^2}{4\pi n}}{2c_S},$$
$$c_S = \cos\theta - \frac{\lambda K}{2\pi n}\cos\psi,$$
$$c_R = \cos\theta,$$
$$K = 2\pi\rho.$$

κ, for the two polarizations is given by

$$\kappa_S = \frac{\pi\Delta n}{\lambda},$$
$$\kappa_P = -\kappa_S \cos 2(\theta - \psi).$$

Maximum diffraction is achieved when the Bragg condition is satisfied, namely

$$\cos(\theta - \psi) = \frac{\rho\lambda}{2n}. \tag{2.1}$$

Defining ϕ as the angle the fringes make with the normal to the diffracting surface, $\phi = \psi - \frac{\pi}{2}$, Eq. (2.1) becomes:

$$2\sin(\theta - \phi) = \frac{\lambda}{\rho n}.$$

When this condition is satisfied, and for normal fringes, $\xi = 0$ and so

$$\eta_S = \sin^2\left(\frac{\pi d\Delta n}{\lambda\cos\theta}\right), \tag{2.2}$$

$$\eta_P = \sin^2\left(\frac{\pi d\Delta n}{\lambda\cos\theta}\cos 2\theta\right). \tag{2.3}$$

For unpolarized light:

$$\eta = \frac{1}{2}(\eta_S + \eta_P). \tag{2.4}$$

Grating Dispersion and Spectral Resolution

We find the dispersion and spectral resolution starting with the grating equation:

$$\sin\alpha + \sin\beta = m\lambda\rho. \tag{2.5}$$

Here α is the angle of incidence, β is the angle of diffraction, m is the diffraction order, and ρ is the fringe frequency, as before. Taking the derivative, holding α fixed:

$$\cos\beta\, d\beta = m\rho\, d\lambda,$$

$$\frac{d\lambda}{d\beta} = m\frac{\cos\beta}{\rho}, \tag{2.6}$$

$$\frac{d\lambda}{dx} = m\frac{d\lambda}{d\beta}\frac{d\beta}{dx}.$$

The last derivative is simply the inverse of the camera focal length: $d\beta/dx = f_{cam}^{-1}$. The spectral resolution element is:

$$\Delta\lambda = \frac{d\lambda}{dx}\Delta x,$$

Δx is the length on the detector corresponding to the smallest observable element. For a compact object this is either the size of the PSF or the seeing disc. For diffuse sources, it is the width of the image of the slit, $s' = \frac{F_{cam}}{F_{coll}} s$. As CWI is built to observe diffuse sources (and is seeing limited for point sources, so the resolution there is not much different):

$$\begin{aligned}\Delta\lambda &= \left(\frac{m\cos\beta}{\rho}\right)\left(\frac{1}{f_{cam}}\right)\left(s\frac{F_{cam}}{F_{coll}}\right) = \\ &= \left(\frac{m\cos\beta}{\rho}\right)\left(\frac{\cos\alpha}{BF_{cam}\cos\beta}\right)\left(s\frac{F_{cam}}{F_{coll}}\right) = \\ &= \frac{sm\cos\alpha}{BF_{coll}\rho}.\end{aligned}$$

In the above, B is the diameter of the beam in the spectrograph, and the definitions of the focal ratio, and the anamorphic magnification introduced by the grating are used. This gives the grating resolving power, assuming first order $m = 1$:

$$R \equiv \frac{\lambda}{\Delta\lambda} = \frac{B\lambda\rho F_{coll}}{s\cos\alpha} = \frac{D\lambda\rho F_{coll}}{s} \tag{2.7}$$

$$= \frac{BF_{coll}}{s}\frac{\sin\alpha + \sin\beta}{\cos\alpha}, \tag{2.8}$$

$$R_{\mathrm{CWI}} \equiv 2400\,\frac{\sin\alpha + \sin\beta}{\cos\alpha}; \tag{2.9}$$

the second to last line follows from the grating equation, the last expression includes the CWI parameters, and D is the length of the grating illuminated by the incident beam. When the Bragg condition is satisfied, $\alpha = \beta$, the grating equation can be used to rewrite Equation (2.9) as:

$$R \equiv \frac{\lambda}{\Delta\lambda} = \frac{2BF_{coll}}{s}\tan\alpha.$$

The grating dispersion is given by Eq. (2.6).

High Resolution Gratings

CWI has a requirement of spectral resolution $R \geq 5000$ across the full wavelength range. The beam size is fixed at 150 mm, and the collimator focal ratio is matched to the telescope F/16 beam, implying $\tan\alpha \gtrsim 1$, i.e., $\alpha \gtrapprox 45°$. This in turn places a constraint on the $\lambda\rho$ product from the grating equation, such that for R to satisfy the instrument requirement at Bragg, $\lambda\rho \gtrsim \sqrt{2}$. For a fixed ρ this relation defines the smallest wavelength for which the condition on R is satisfied.

For incidence angles $\alpha \geq 45^\circ$ the $\cos 2\theta$ term that distinguishes the two parts of Eq. (2.4) is significant, though both terms in the sum can be maximized simultaneously:

$$\eta_S \Rightarrow \frac{d\Delta n\pi}{\lambda \cos\theta} = (2l-1)\frac{\pi}{2},$$
$$\eta_P \Rightarrow \frac{d\Delta n\pi}{\lambda \cos\theta}\cos 2\theta = (2k-1)\frac{\pi}{2},$$

where l and k are positive integers. This gives us a condition for θ:

$$\cos 2\theta = \frac{2k-1}{2l-1}.$$

The simplest nontrivial case is for $k = 1$ and $l = 2$. This configuration is known as a Dickson grating (Dickson et al. 1994), and θ is constrained to

$$\theta \approx 35.26^\circ.$$

Other solutions are possible, and lead to gratings that operate at higher angles, but as they correspond to higher frequency efficiency sinusoids, their peaks are narrower, and much less desirable. This specific condition on the angle of incidence restricts the choice of the grating line density for a given wavelength:

$$2n\sin\theta = \lambda\rho,$$
$$\rho \approx 1.155\,\frac{n}{\lambda},$$

and gives an explicit constraint on the $\Delta n\, d$ product:

$$\frac{d\Delta n\pi}{\lambda\cos\theta} = \frac{3\pi}{2},$$
$$\Delta n\, d = 1.225\lambda.$$

Thinner gratings with higher Δn lead to broader efficiency curves.

The initial CWI high resolution blue grating was designed to be centered at 410 nm and with an index of refraction modulation of $\Delta n = 0.14$. This choice was made to strike a balance between the angle of incidence of the light onto the glass substrates (consequently the spectral resolution, and grating size) and the widths of the peaks. These values immediately constrain $\rho \approx 3.83\,\text{lines}/\mu\text{m}$ and $d = 3.58\,\mu\text{m}$. Figure 2.15 shows the theoretical efficiency for these parameters. The actual design values for the CWI grating differ slightly from these as we introduced an 0.5 degree fringe tilt to reduce the effect of ghosting (see section 2.2.3.2).

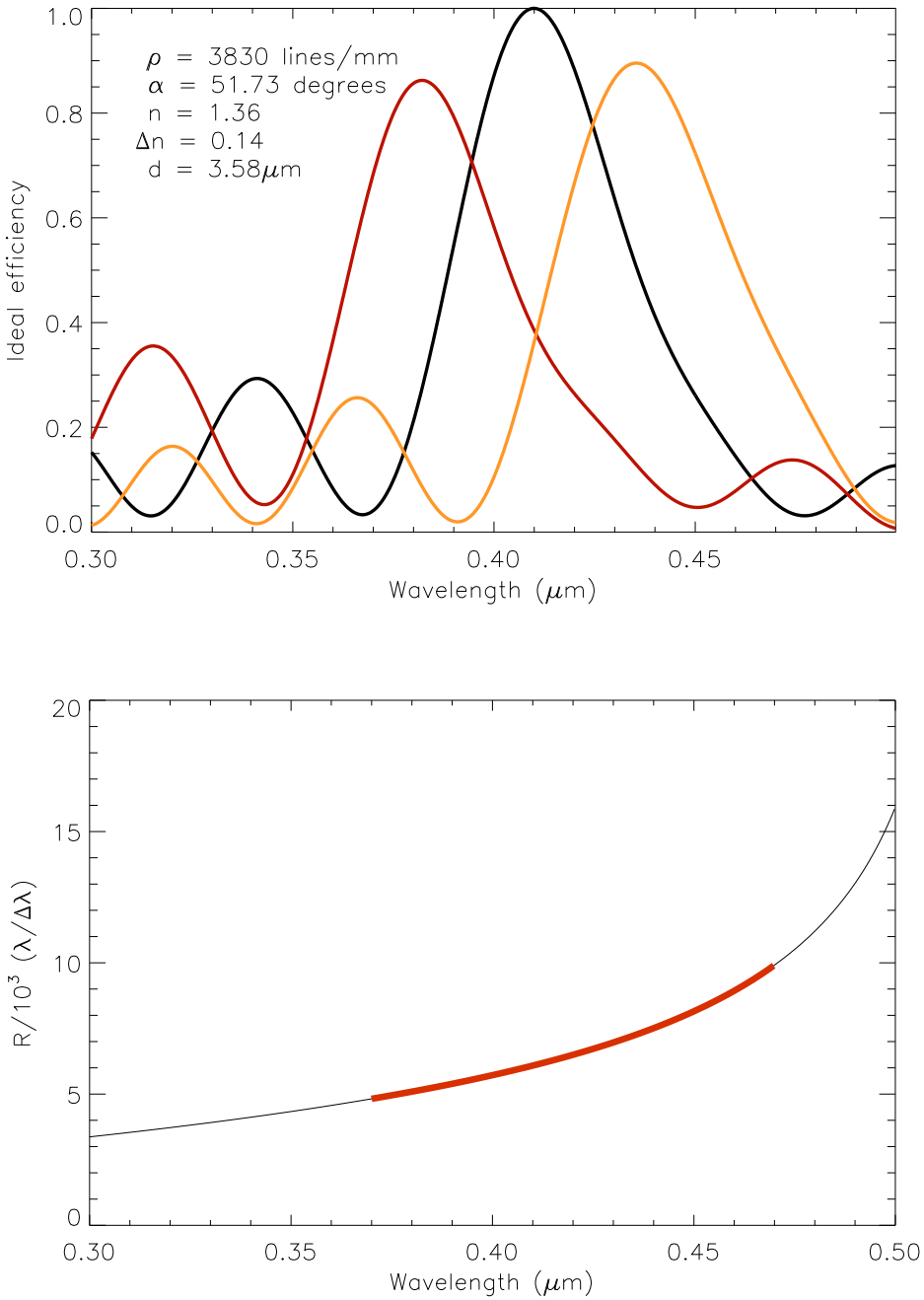

Figure 2.15. The top panel shows the theoretical diffraction efficiency as a function of wavelength for the example from section 2.2.3.2; it does not include any Fresnel reflection or absorption losses. The two curves on either side of the main peak correspond to a 5° tilt in the grating away from the central wavelength, showing the tunability of the configuration. The bottom panel shows the grating resolving power, the thicker part of the curve corresponds to the wavelength range at which the grating would be operated.

Low Resolution Gratings

The initial CWI application and design does not call for low resolution gratings, however future expansion is anticipated and such gratings may be added to broaden the science that CWI addresses.

For low resolution VPH gratings, the $\cos 2\theta$ term in Eq. (2.4) is not a substantial design driver, unlike for the high resolution gratings. The angles of incidence are small. Simply setting $\eta_S = 1$ ensures that the overall grating efficiency is nearly maximized (neglecting reflective and transmissive losses). As an example, let us consider a grating with peak diffraction efficiency at $\lambda = 500\,\mathrm{nm}$ and groove density $\rho = 800\,\mathrm{lines/\mu m}$. Let us also assume an index of refraction variation of $\Delta n = 0.07$ and $n = 1.43$. The Bragg condition for this grating corresponds to $\theta = 8.04°$.

Given all of these parameters, we can determine the needed thickness of the gelatin layer from

$$\eta_S = \sin^2\left(\frac{d\pi\Delta n}{\lambda\cos\theta}\right) = 1$$
$$\Rightarrow \frac{d\pi\Delta n}{\lambda\cos\theta} = (2l-1)\frac{\pi}{2}.$$

For $l = 1$:

$$d = \frac{\lambda\cos\theta}{2\Delta n} \approx 3.54\,\mu\mathrm{m}.$$

See figure 2.16 for the plot of the theoretically predicted performance for these parameters. Note that the peak is shifted a little blueward of 500 nm. This is due to the two polarizations peaking at slightly different wavelengths. The modification needed to allow for low resolution transmissive gratings is simple. The proposed modified layout is shown and described in figure 2.17. A more classical low resolution surface relief grating may also be an option, and will be considered when the changes are being further researched.

Grating Ghosts

A transmission grating can introduce ghosts into the system as a result of a fraction of the science signal being reflected off the detector. This light then traverses the instrument in reverse, a fraction of it is reflected and recombined by the transmissive grating, returning to the detector. A study of these effects has been performed by Burgh et al. (2007). The two cases relevant to CWI are: the reflective recombination off the gelatin layer (i.e., the grating acts as a reflective grating) and a transmissive recombination reflected back into the camera by the surface of the grating substrate closest to the IFU. An estimate of the magnitude of the ghosting effects follows.

Let q be the detector quantum efficiency and assume that in-band photons that do not generate photoelectrons are reflected, t the transmission of the camera, r the reflection at the glass-air interface of the grating, p the Fresnel reflection at the glass-gelatin interface, η the diffraction efficiency into the first grating order. If the number of photons incident onto the active area of the CCD during

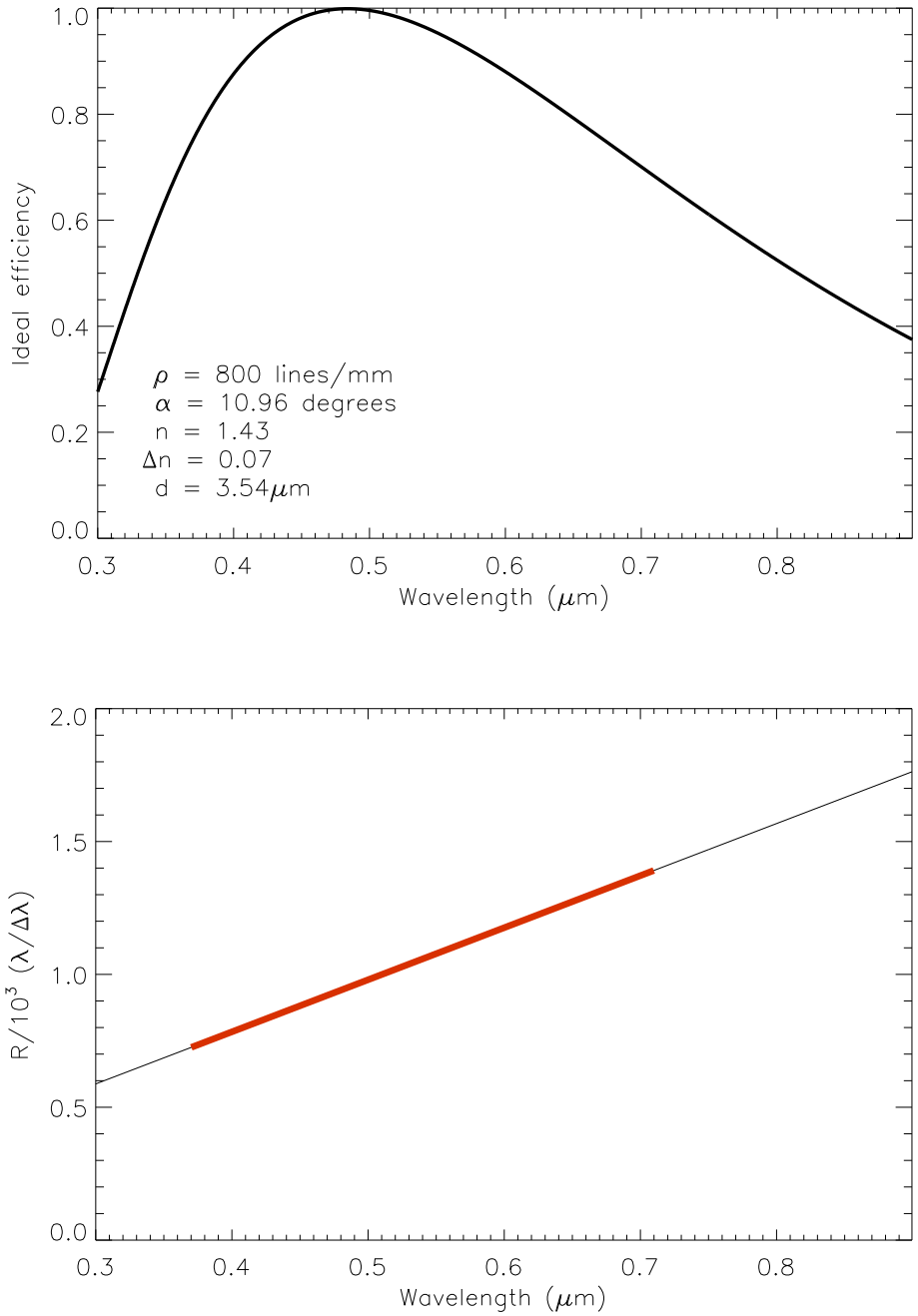

Figure 2.16. The top panel shows the theoretical diffraction efficiency as a function of wavelength for the example from section 2.2.3.2. This grating would not be tuned as its high resolution counterparts would; a single grating-camera configuration would cover the wavelength range from 370 to 700 nm. The bottom panel shows the corresponding grating resolution, with the operating range of the grating highlighted.

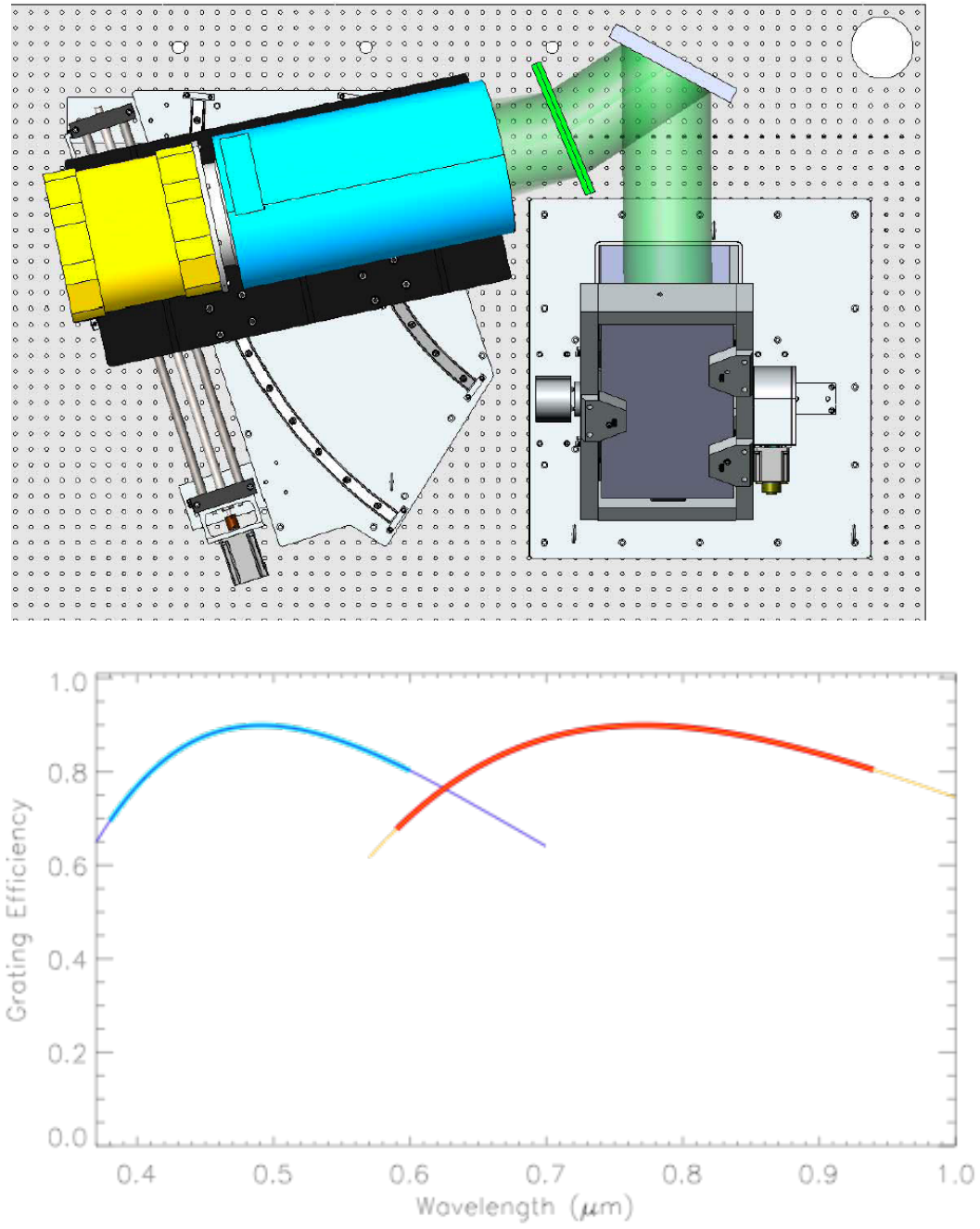

Figure 2.17. The top panel shows the CWI low resolution configuration. The spectrograph beam is reflected off FM4 onto a fifth folding flat, which directs the light at the grating. The 24 beams are diffracted into the Norris lens and focused onto the CWI detector. A single low resolution grating covers half of the full CWI bandpass, thus two are needed for the full wavelength range, as shown in the bottom panel. A slight, $\sim 0.5^{\circ}$, tilt would have to be added to the CWI detector.

an exposure is N, then upper bound on the the flux in the two types of ghosts can be estimated as

$$\begin{aligned} G_{Gel} &= N(1-q)t(1-r)p(1-r)tq \\ &= N\,q(1-q)\,t^2\,p(1-r)^2, \\ G_{Glass} &= N(1-q)t(1-r)\eta r(1-\eta)(1-r)tq \\ &= N\,q(1-q)\,t^2\,r(1-r)^2\,\eta(1-\eta). \end{aligned}$$

Approximate values for these quantities are: $q = 0.8$, $t = 0.8$, $p = r = 0.02$, $\eta = 0.8$. These quantities yield the following estimates for G_{Gel} and G_{Glass}:

$$G_{Gel} = 2.1 \times 10^{-3}\,N, \tag{2.10}$$

$$G_{Glass} = 3.1 \times 10^{-4}\,N. \tag{2.11}$$

Ray-traces show that these recombined ghosts focus to spots that are about 1 mm in diameter. Ignoring G_{Glass} which is an order of magnitude smaller than G_{Gel}, the ghost/signal ratio in the region affected by the ghost image is

$$\frac{G}{S} = \frac{G_{Gel}}{qN\frac{l}{L}} \approx 0.03, \tag{2.12}$$

where $l \sim 1$ mm is the size of the ghost image and $L \sim 20$ mm is the active size of the CCD. Thus the ghost for a uniform illumination of the CCD should not exceed a level of 5% of the signal in the affected pixels. When the full CCD is used for observation, the amount of light in the ghost triples, reaching a level of 15% of the signal. Any point sources in the field of view of the instrument will contribute more strongly to the ghost image. Images taken with CWI show these ghosts due to uniform illumination to be at ∼5% level for the full CCD.

The ghosts return to the detector due to the angles of incidence and diffraction satisfying the Bragg condition. In this configuration the initial diffraction of the science beam is mimicked by a diffraction and reflection of the ghost beam. Introducing asymmetry into the system by adding a small tilt to the diffraction grating fringes alters the light path of the ghost beams and moves the image of the recombinant ghost. The shift of the ghost image on the CCD away from the center is determined by the difference between the grating angle of incidence (α) and diffraction (β): $\Delta x \approx f_{cam}|\alpha - \beta|$. For the existing CWI grating, this tilt is 0.5°. This value is a touch too small to move the return images to the edge of the central 20 mm of the CCD (see figure 2.18). Future designs will include a much larger fringe tilt to remove the ghosts from the CCD entirely.

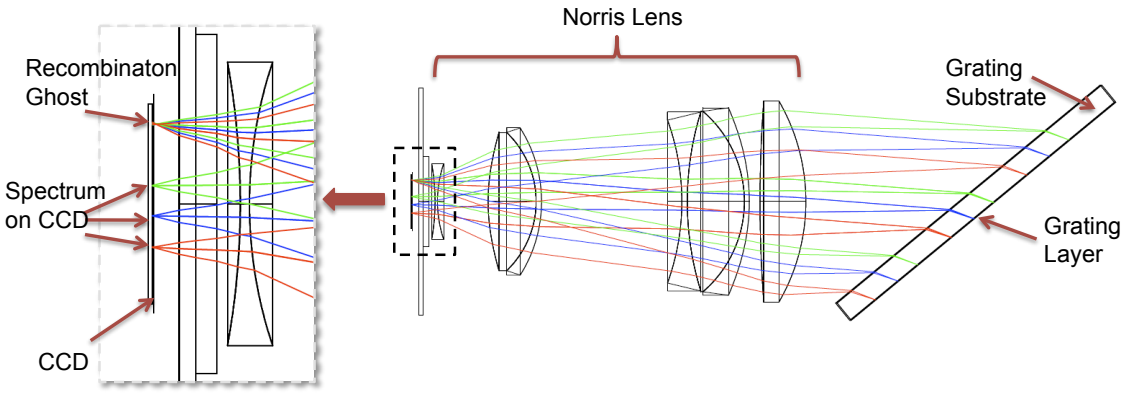

Figure 2.18. Ray trace showing the mechanism of one of the two recombination ghosts. Light initially incident on the detector from the telescope beam is not shown; this dispersed light partially reflects off the CCD, returns to the grating diffractive layer through the Norris lens, where it is recombined by the grating acting as a reflective grating, coming back to the detector. A tilt in the fringe layer allows the grating to be operated away from the Bragg condition making the returning light offset slightly from the center of the CCD, as shown in the figure. The location of the ghost is determined by the difference between the grating angle of incidence and diffraction,

2.2.3.3 Grating Suite Design

The spectrograph optics direct the twenty-four 150 mm diameter beams from the slicer mirrors forming a pupil near the grating. The high resolution dispersive element needs to be large enough to capture the beams in the most acute angle configuration at which it will be operated, near 60° incidence; therefore it must be at least 300 mm long in the direction perpendicular to the fringes, and wide enough to accommodate the beams. Adding some margin, and accounting for the limited size of clear aperture on the substrate, the grating sizes were specified to be at least $350 \times 220\,\mathrm{mm}^2$. The material chosen for gratings that were to be used around 4000 Å was fused silica. BK7 glass was deemed acceptable for redder gratings, though analysis of the CWI data using the existing grating centered at 4850 Å shows that the glass may be a source of radiation that introduces a low-level background into the system. Future gratings will all be made on SiO_2 glass.

Five gratings are required for CWI to cover the 380 to 950 nm wavelength range with resolving power $R \geq 5000$. The parameters for the initial design, based on the Kogelnik approximation, are shown in table 2.4, and the expected performance is displayed in figure 2.19. The parameters were chosen to maximize the instantaneous bandpass of the gratings while maintaining grating efficiency at or above 70% over the full wavelength range of the instrument.

Several vendors responded to preliminary grating suite designs, including Wasatch Photonics, ATHOL Corporation, Keiser Optical Systems, and, later, Chris Clemens of University of North Carolina at Chapel Hill. The vendors adjusted the grating designs to fit their processes and to maximize performance. CWI initially ordered the shortest wavelength grating, centered at 4150 Å,

Table 2.4. A listing of the design parameters for the CWI grating suite. The expected performance of the high resolution gratings is shown in figure 2.19. The parameters are intended as guidelines for the grating manufacturers to match the bandpass and resolution requirements.

	Wavelength			**Bandpass**			**Gelatin**		
Name	**Min.**	**Cent.**	**Max.**	**70%**	**50%**	**Fringe frequency**	**Index of refraction**	**Index modulation**	**Effective thickness**
	λ_{min} Å	λ_{ctr} Å	λ_{max} Å	$\Delta\lambda_{0.7}$ Å	$\Delta\lambda_{0.5}$ Å	ρ lines/µm	n	Δn	d µm
H4150	3600	4150	4700	125	210	3.896	1.4	0.07	7.26
H5000	4350	5000	5700	151	254	3.234	1.4	0.07	8.75
H6000	5400	6000	6650	181	305	2.695	1.4	0.07	10.50
H7200	6400	7200	8050	217	366	2.246	1.4	0.07	12.6
H8700	7800	8700	9700	263	442	1.859	1.4	0.07	15.23
L4800	3600	4700	6500	2300	2900	0.850	1.4	0.05	5.0
L7700	6000	7700	10000	4000	4000	0.490	1.4	0.05	7.8

from ATHOL. The company could not produce a grating by the designated deadline. A grating centered at 4900 Å, was then ordered from Wasatch Photonics. The projected performance for this grating, generated by Gerald Heidt at Wasatch Photonics, is shown in figure 2.20. The author has been working closely with Wasatch and Chris Clemens to develop a set of diffraction gratings for the Keck CWI instrument.

2.2.3.4 Grating Mount

The gratings are attached to the optical bench via an aluminum base plate that holds a Newmark RM5 rotary stage. Bolted onto the stage is an interface plate. This part is designed to facilitate grating exchange; figure 2.21 shows this plate and discusses its operation.

The grating cell is a simple clamshell design. It consists of a rectangular metal frame, two faceplates, and a base. The rectangular frame is 3/16" larger in both long dimensions than the grating substrate. 1/8" thick delrin inserts line two interior faces of this frame, and the grating is pushed up against these by nylon tipped setscrews. The two faceplates attach to the frame and have machined O-ring channels around the perimeter of the glass location. The faceplates overlap about 1/4" around the edges of the optic, keeping the clear aperture of the grating unvignetted. The thickness of the frame and the depth of the O-ring channel is such that the soft (50 on the shore A hardness scale) 3/16" O-rings are compressed a total of ∼1 mm. This amount of compression (5%) generates a stress of about 30 lb/in^2 on the grating, which is more than an order of magnitude smaller than the stresses necessary to fracture glass. This force is localized around the perimeter of the optic, where the two pieces of grating glass are glued. The total amount of force exerted on the glass is ∼400 N, an order of magnitude larger than the weight of the grating. This preloading ensures that the optic does not move appreciably when its location changes with respect to the gravity vector. In the worst-case, most unlikely scenario, where the change is differential, it will not

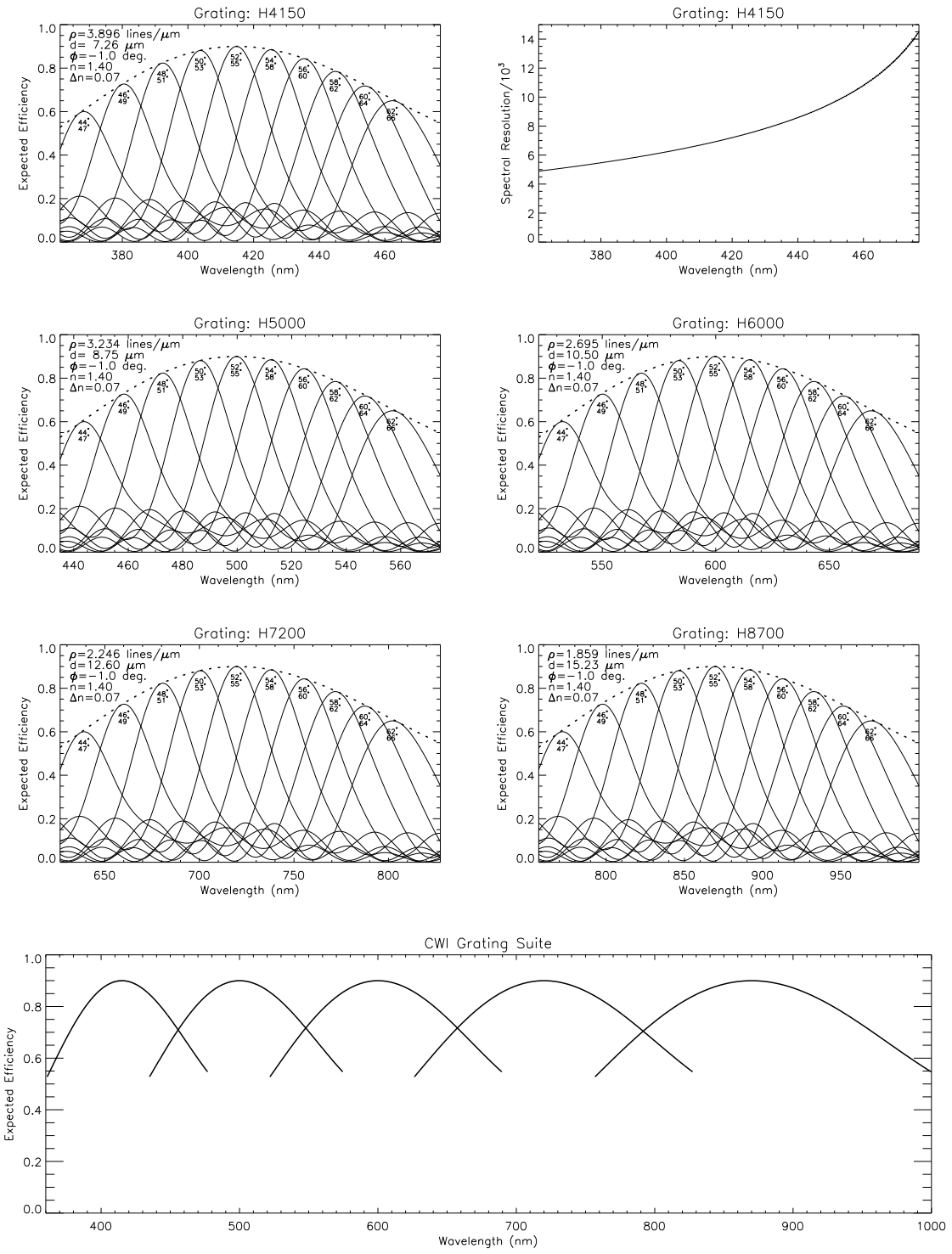

Figure 2.19. Plots showing the anticipated performance of the CWI grating suite. Five of the six smaller plots show the diffraction efficiencies for different grating orientations with a superimposed superblaze curve showing the maximum efficiency available for when the grating is tuned to maximize throughput at a specific wavelength. The top right plot shows the expected spectral resolution for the bluest grating, the plots for the other gratings are very similar. The wide, bottom panel displays the CWI coverage of the visible spectrum.

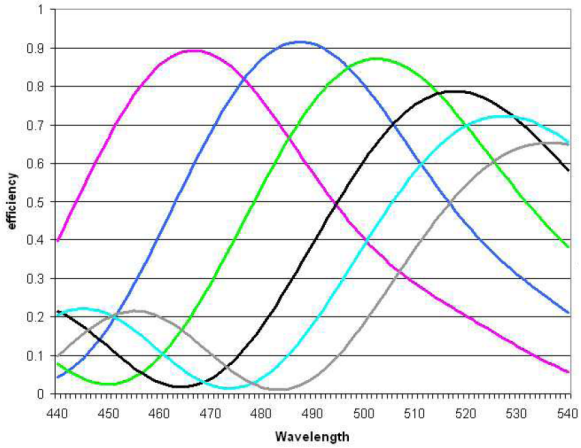

Figure 2.20. Predicted efficiency curves for various configurations of the the CWI green grating made by Wasatch Photonics centered at 485 nm. The grating has 3.050 lines/mm and an effective gelatin thickness of 4.5 µm. The wavelngths in the plot are given in nm, the efficiency includes reflective and absorptive losses. Figure courtesy of Wasatch Photonics.

exceed 50 µm over the long edge of the grating, causing a spectral shift of under 1Å. This is roughly the amount of change with flexure that has been seen in CWI during the first few observations. It could be beneficial to replace one of the O-ring seals with a hard stop. That would mitigate flexure, though care would need to be taken to ensure safety of the glass.

2.2.3.5 Grating Wavelength Calibration

In additional to the mechanical mounting of the camera and grating, the optics configurations have to be optimized to maximize the system efficiency. In particular, the grating angle must be adjusted to maximize efficiency near the center of the band. This is done empirically. This procedure begins with setting the camera angle. A series of arc-lamp exposures is taken for grating equal angle intervals around what is believed to be the optimum orientation based on the grating design (i.e., near the Bragg condition). The result of such a procedure is presented in figure 2.22. For the instrument configuration in existence at the time of writing, the camera-grating combination was optimized for four wavelengths. A polynomial fit is used to select the grating and camera positions to set the bandpass and the central wavelength of the instrument. Figure 2.22 shows this fit and the four measured locations, the curves are given by the equations that follow, though it must be understood that this calibration and the expressions will change when changes are made to the instrument. The camera encoder reading, ζ_C, grating encoder reading, ζ_G, low and high wavelength

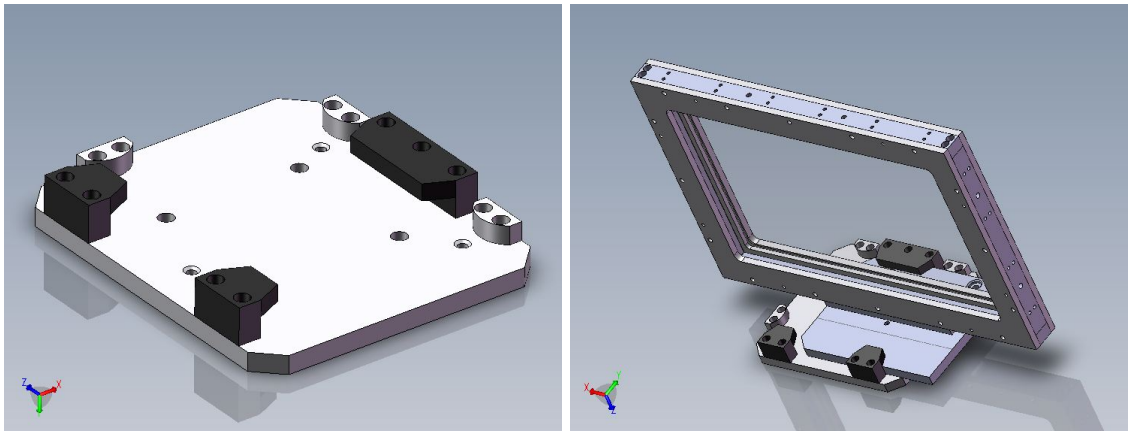

Figure 2.21. The left panel shows the grating interface plate which bolts onto a rotating stage that is attached to the optical bench. The grating is installed by sliding its base plate into the interface plate; this is typically done with the optical bench in its nominal orientation, with the grating and camera on the underside. Three black delrin hooks ensure that the grating is held in place safely when it is not bolted in. Three semicircular metal stops repeatably locate the base plate within the interface plate. The grating mount is pushed against these stops and three 1/4-20 thumbscrews fix the grating. The right panel shows the grating assembly sliding into the interface plate. The grating cell consists of a rectangular frame, two faceplates, and a base. The frame has mounting locations for handles that ease installation, threaded through-holes for setscrews to locate the glass, and attachment points for the faceplates. The faceplates have O-ring channels that contain 3/16" BUNA rubber cord stock that secures and protects the glass.

ranges, λ_L, λ_H are given, as a function of central wavelength, λ:

$$\zeta_C = 8483833 - 1767.516\,\lambda(\text{Å}), \tag{2.13}$$

$$\zeta_G = 139609 - 27.9087\,\lambda(\text{Å}), \tag{2.14}$$

$$\lambda_L(\text{Å}) = -494.088 + 1.05784\,\lambda(\text{Å}), \tag{2.15}$$

$$\lambda_H(\text{Å}) = 486.412 + 0.94375\,\lambda(\text{Å}). \tag{2.16}$$

2.2.3.6 Measured Grating Efficiency

The Space Astrophysics Lab is not equipped with hardware capable of directly assessing the efficiency of the grating. Such measurement requires a large beam that fills the grating, and a reference optic to compare the grating with. Possible usage of CWI as such a test apparatus is discussed at the end of this section. Attempts have been made to measure the throughput of the gratings that have been purchased for CWI. Three techniques have been used, and they show that the grating currently in use is suitable for scientific application.

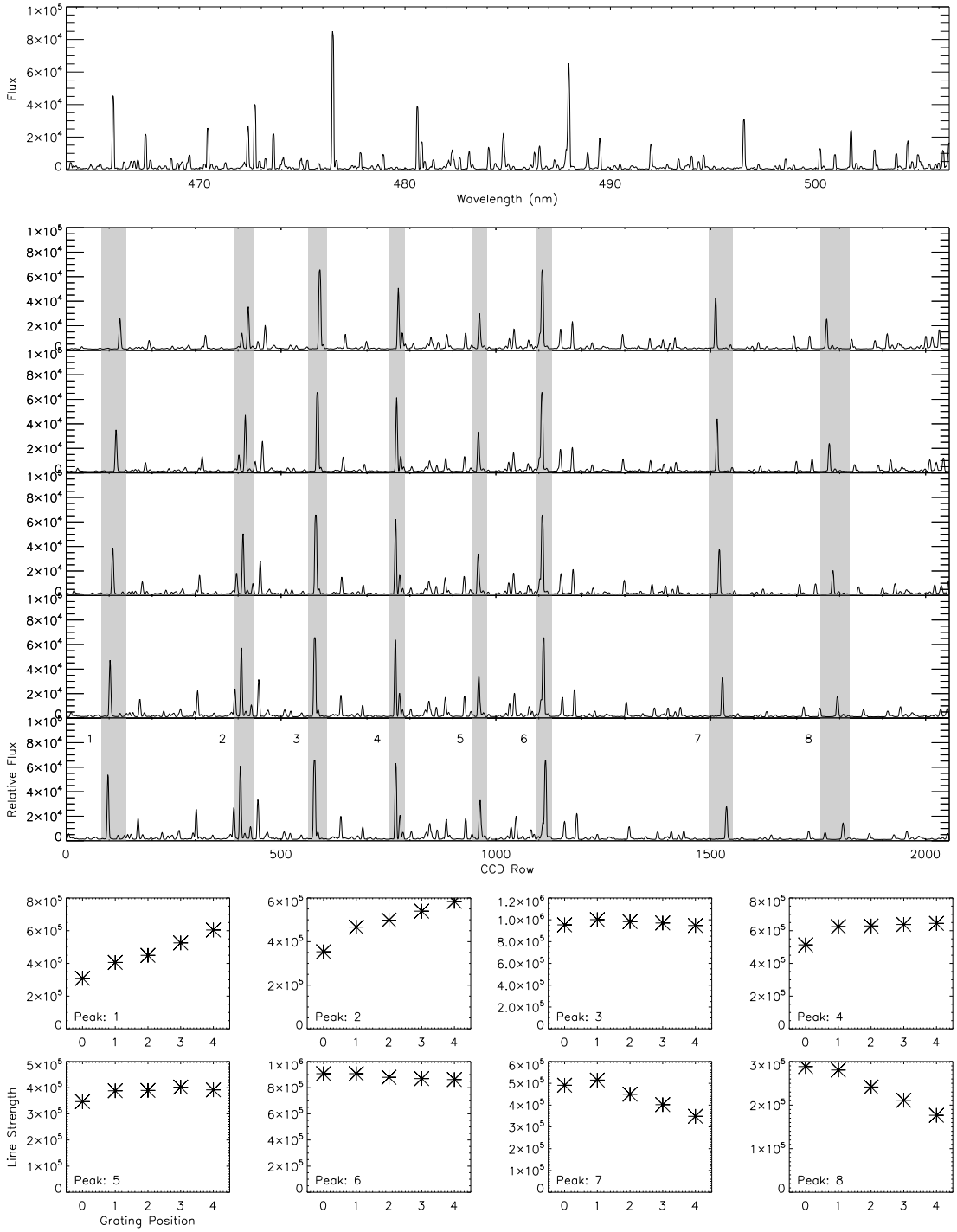

Figure 2.22. The CWI gratings must be "peaked" to maximize the central wavelength efficiency for a given camera angle. Caption continued on page 82

Figure 2.22 continued. The top plot, for reference, shows a resolution-degraded (to $R \sim 5000$) spectrum of the calibration lamp taken from Willmarth et al. (2006). The wavelength range corresponds roughly to that in the five plots at the center of the figure. These show the spectrum of the CWI arc lamp for five sequential images taken a short time apart, but with grating angles changed in 0.2° steps. There is very little change in the spectral coverage between the images, though there is a noticeable transition in diffraction efficiency, with the grating peak efficiency moving toward the blue as the sequence progresses. Eight peaks in the plots were compared; they are marked by the gray bars in the plots. Each peak was fit with a Gaussian profile and its total flux computed. The bottom eight plots show these fluxes as a function of exposure number, thus angle. The bluest peaks increase in intensity, the reddest peaks decrease with angle, the change slows toward the center of the wavelength range. In this sequence the grating configuration corresponding to grating position #2 was deemed optimal, as that is where the central lines appear to peak.

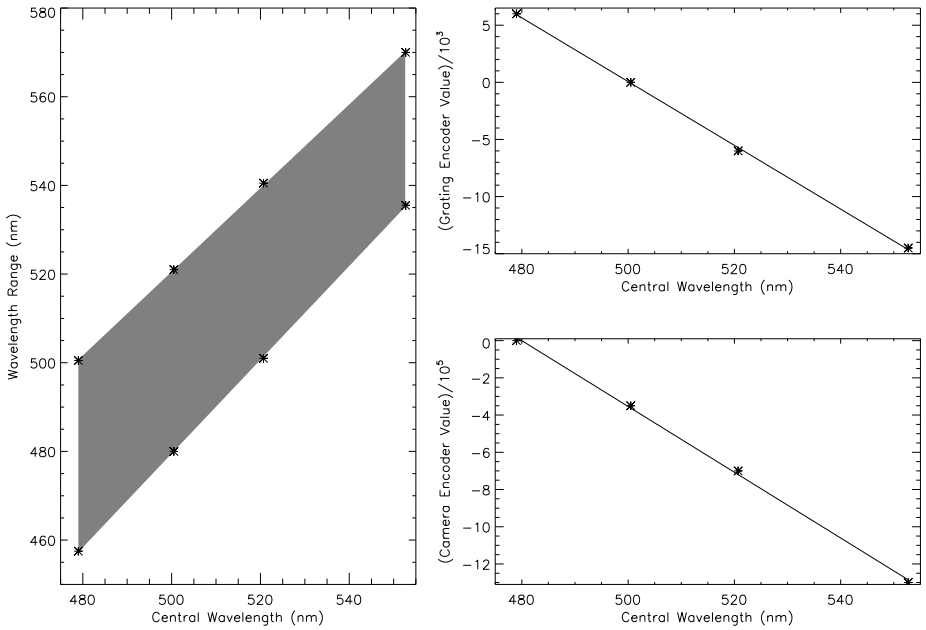

Figure 2.22. The left panel shows the approximate wavelength range that fits onto the CWI detector for the H4900 grating, when utilizing the full CCD. The two plots on the right show the camera and grating stage settings necessary to select a particular central wavelength. The values and fits shown here are for for demonstration purposes only. The calibration will need to be repeated if the camera mounting scheme changes, and for any new gratings.

Table 2.5. A tabulation of the component throughput relevant to estimating grating efficiency given the two methods discussed in the text that rely on the CWI instrument. The reflectivity of the slicer mirrors is likely an overestimate, as is that of the large mirrors. The pupil mirror reflectivity may be an underestimate. The computations ignore any scattering or vignetting losses.

Parameter	Stand. Star **500 nm**	Cal. Laser **532 nm**	**Notes**
Atmosphere	0.8	N/A	Extinction $A_V \sim 0.2$ mag.
Telescope	0.88[2]	N/A	
Filter	0.72	0.78	
Slicer Mirrors	0.96	0.95	Prob. overestimate.
Pupil Mirrors	0.85	0.85	
Large Mirrors	0.93[5]	0.90[4]	Prob. overestimate
Norris Lens	0.86	0.83	
CCD	0.9	0.87	
Total	0.20	0.30	
System	0.15	0.18	Measured values, see text
Grating	0.75	0.60	Estimated grating efficiency.

The first, and most direct, of these was a simple test with a green (532 nm) laser. The laser was placed behind a stack of neutral density filters to reduce the flux to fall within the linear regime of a silicon photodiode, which was used as a detector for this measurement. The laser was sent through the grating at various locations, and the first order diffraction beam was collected at the photodiode, rotating the grating to maximize the current reading. This was compared with the value observed when the detector was directly illuminated by the beam. The peak diffraction efficiency observed in this way was $\sim 65\%$; the modeled efficiency of the delivered grating at that wavelength is 70%.

The second method also involved the green laser. This time the laser was injected into the calibration unit integrating sphere and a small 5 mm aperture was projected onto the slicer. A photodiode was used to intercept the beam before the slicer to measure the level of the input signal. The CWI detector CCD served to measure the throughput of the instrument. This was found to peak $\sim$18%. Factoring out the measured mirror reflectivities, Norris lens throughput, and detector QE, the grating throughput is estimated to be $\sim$60%. Uncertainties in the mirror reflection measurements, diode calibration, and an underestimating the vignetting losses could explain the slight discrepancy. Table 2.5 lists some of the assumed values.

The third method is also an estimate that relies on removing the contributions of the other system components and measuring the collected charge on the detector from a standard star, BD+28 4811. The total throughput was found to peak at $\sim$10%. Removing contributions form the sky (assuming $A_V \sim 0.2$), telescope mirrors and other optics in the instrument (see Table 2.5, yields a grating efficiency of $\sim$75% at 500 nm.

The last two measurements are in the right ratio for the grating throughput at the wavelengths being observed, but are about a factor of 1.2 below the expected efficiencies from VPH grating models. A little under 10% of the difference can be explained by a lack of an antireflection coating on the current grating. Any vignetting losses within the system are not factored in, additionally, an overestimate in the reflectivity of any of the components, especially the large mirrors, and the slicer (which are quite likely) cause an underestimate in the estimated grating efficiency. The first measurement suffers from not testing the full aperture of the grating, so any thickness or fringe irregularities would not have been easily noticed.

The above observations highlight the need for a reliable way of measuring the grating efficiency while illuminating the full grating aperture. CWI, with a few simple additions, can be used as an experimental configuration for collecting such data. These augmentations include a large mirror with a well-known reflectivity that can be inserted at the grating location and a monochromatic light source injected into the instrument calibration unit. A comparison of the CCD image of the reflected light with that of the diffracted light would yield the grating diffraction efficiency. Ideally, the camera would see a direct beam from the instrument, instead of a reflection, but given the geometry of CWI this is not possible. KCWI, currently in development, will have that capability Martin et al. (2010).

2.2.4 CWI Mirrors

2.2.4.1 Mirror Overview

CWI has a total of nine reflective surfaces, including the two telescope optics, the slicer stack and pupil mirror array discussed in section 2.2.2. The remaining five mirrors were mentioned in section 2.2 and are discussed in more detail here.

The four large mirrors (FM2, FM3, FM4, and the collimator) are made from 2" thick borosilicate (Pyrex) glass. The choice was made to use a thin substrate to minimize the weight of the mirrors reducing the effect of flexure when the Cassegrain mounted instrument moves with the telescope. The design specifications of these mirrors are listed in table 2.6. The mirrors met the optical specifications, though the diamond saw used to shape the rectangular mirrors from circular blanks left the mirror edges outside of the specified tolerance. The mirror mounts described in the following section compensate for this. The as-built collimator radius of curvature is 4760 mm, and the CWI optical design was adjusted to match this value before any of the mounting elements were manufactured. The mirrors were given a protected aluminum coating optimized to the blue side of the CWI waveband; their reflectivity, as measured at Caltech, is shown in figure 2.11.

FM1 is a simple 4" diameter blank made to the same surface quality specifications, and given the same coating, as the large mirrors. The front surface of the mirror is masked with a specially prepared aluminum mask that baffles light significantly outside of the instrument field of view.

2.2.4.2 Mirror Mounts

The mirror cells for FM2, FM3, FM4 and the collimator were designed by Patrick Morrissey at Caltech in conjunction with engineers at Newmark Systems. The company manufactured these cells as well as the supporting mounts and actuating elements.

The mirror mounts consist of a heavy base plate, sturdy support pillars, and, in the case of FM3 and FM4, motorized bearings that rotate the mirror $\pm 1^\circ$ around their nominal positions. FM2 is attached to a linear stage that moves it along the direction of the beam.

The mirror cells are metal frames that are slightly oversized and are designed to hold the glass semikinematically. A frame has six nitrile pads, each opposed by a hard stop. Three such pairs squeeze the mirror from the front reflective surface and the rear (the hard stops on the reflective surface); each of these has an area of 1 square inch. Two pairs lie along the longer of the two mirror edges, each with a surface area of 1.5 square inches. One pair is at the center of the shortest side, these pads have a 3 square inch area. The nitrile pads are mounted on setscrews with swiveling ends. These allow the elements to be compressed against the glass, and to conform to the substrate surface. The hard stops are attached to stationary ball bearings, except for the collimator cell, where they are on setscrews like the nitrile pads. All pads were made flat, with the exception of the hard pads for the front surface of the collimator, which were molded to the mirror radius of curvature using glass offcuts from the manufacturing process. The setscrews are adjusted until the nitrile pads are compressed such that they exert a force equal to 2.5 times the weight of the optic. A force equal to, or slightly exceeding, the weight of a mirror would have been sufficient to hold the optic in place, even as the instrument moves around during observations, but the larger compression was chosen to ensure that the glass was protected during transport to and from the observatory, when it experiences larger accelerations. The mirror cell and sample mount are shown in figure 2.23.

The mounting procedure for all four large mirrors was similar. The cell was placed oriented so that the mirror reflective surface would be pointing down. The glass was lowered onto the front hard pads, and pressed up against the hard pads along the sides of the frame. The rubber pads were then adjusted until they came in contact with the glass. The 1/4-20 setscrews were then turned the the number of revolutions necessary to compress each pad the appropriate amount; this was done in small steps, to ensure that any initial gaps were removed and that the mirrors did not experience abrupt stress changes. Despite these efforts two of the four large mirrors were damaged by the mounts. The cause of this is not clear, but likely to do with the roughly cut, rather than fine-ground, mirror sides. Such a finish leads to nonuniform stress on the glass. The fractures are

Table 2.6. A summary of the CWI mirror specifications as given in the vendor quote request prepared by Anna Moore with input from the CWI team members. The mirrors were made to specifications by Optical Mechanics of Iowa, The collimator has a radius of curvature of 4760 mm, just within the listed range.

	FM1	**FM2**	**FM3**	**Collimator**
General description	Flat rectangular mirror	Flat rectangular mirror	Flat rectangular mirror	Spherical rectangular mirror
Full aperture dimensions	160×566 mm^2	291×435 mm^2	211×407 mm^2	245×651 mm^2
Full aperture tolerance	+0 mm, -1.0 mm	+0 mm, -1.0 mm	+0 mm, -1.0 mm	+0 mm, -1.0 mm
Clear aperture dimensions	114×515 mm^2	240×384 mm^2	160×356 mm^2	194×600 mm^2
Clear aperture tolerance	Not less than stated.			
Thickness	50.8 mm (D/11)	50.8 mm (D/9)	50.8 mm (D/8)	50.8 mm (D/13)
Thickness tolerance	±1 mm	±1 mm	±1 mm	±1 mm
Radius of curvature	Infinity	Infinity	Infinity	4800 mm
RoC tolerance	More than 10 km			±40 mm
Rear surface (S2)	Fine ground with 400 grit or better			
Front surface (S1) cosmetic quality	60/40	60/40	60/40	60/40
S1 wavefront error P-V λ=633 nm	$< \lambda/4$ (160 nm P-V)	$< \lambda/4$ (160 nm P-V)	$< \lambda/4$ (160 nm P-V)	$< \lambda/4$ (160 nm P-V)
S1 surface finish	≤2.5 nm rms	≤2.5 nm rms	≤2.5 nm rms	≤2.5 nm rms
S1-S2 parallelism	<3 arcmin	<3 arcmin	<3 arcmin	<3 arcmin
Material	Zero expansion materials are not required. Precision annealed Pyrex or equivalent material that does not require a custom cast is optimal, and preferable.			
Coating	Broadband coating with excellent performance at 370-445 nm			
Angle of incidence	5.5°	46°	45°	5°
Mass (=2.23×10^3 kg/m^3 V)	10.6 kg	14.3 kg	9.7 kg	18.1 kg

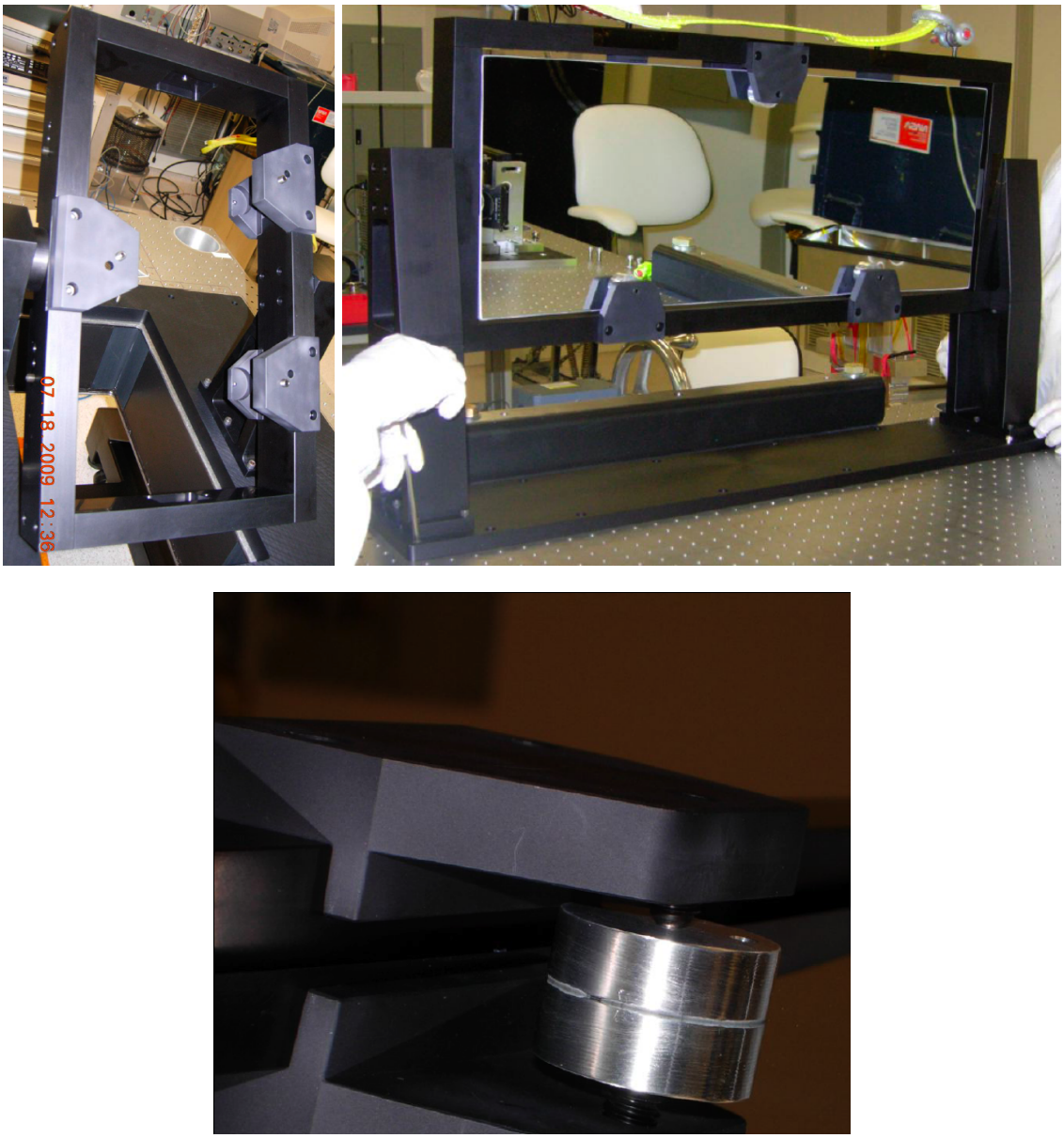

Figure 2.23. The top left panel shows the mounting cell for FM4. The three triangular protrusions on top of the cell hold rubber pads that will be pressing against the rear surface of the mirror. The corresponding protrusions on the underside have ball bearings on which hard pads sit. Two more such pairs lie along the longer mirror axis (vertical), and one along the shorter. A pocket intended to hold a hard pad is seen on the inside upper strut of the frame. The top right panel shows the installed collimator mirror, including the two sturdy pedestal legs, and the mounting plate. The bottom images shows one of the hard pads on the collimator surface. The ball bearing that allows the pad to swivel can be seen between the pad and the supporting structure.

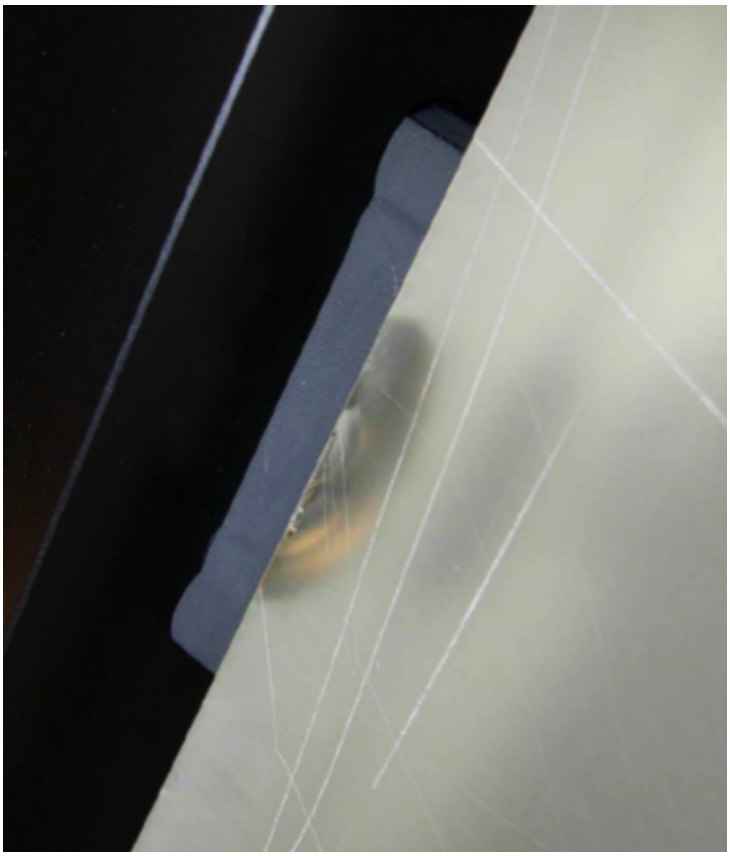

Figure 2.24. Damage to one of the large CWI mirrors. The exact cause is unknown, but the extent of the scallop-shaped cracks has not spread during multiple trips to and from the observatory.

scalloplike in nature. As the mirrors are still firmly set in the mounts, they were not removed and continue to work well. Figure 2.24 shows a photograph of the damage.

2.2.5 Camera

2.2.5.1 Norris Lens

CWI uses the legacy Norris lens to focus the spectrograph beams onto the detector CCD. This lens was designed for the Norris Spectrograph (Cohen et al. 1988; Hamilton et al. 1993) and is identical in design to the LRIS lens (Epps 1990). The camera was designed to operate at 12" from the beam pupil, has a large acceptance angle $\pm 4.5°$, and large aperture (10"). To ensure that the camera is suitable for the bluest wavelengths CWI is designed for, its throughput was measured in lab by Daphne Chang and the author.

The throughput measurements were performed on an optical bench at the Space Astrophysics Lab in Synchrotron Annex. The setup was as shown in figure 2.25. The detector was a UDT UV 100 uncalibrated silicon diode connected to a high-sensitivity electrometer. The light source was an

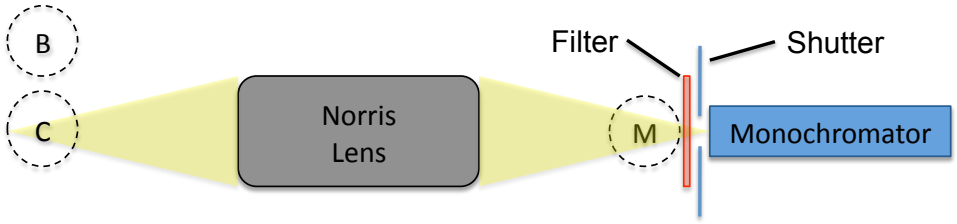

Figure 2.25. Schematic layout of the Norris lens throughput measurement. The monochromator is equipped with a shutter and its output can be filtered. There are three measurement positions. The first measures the output of the light source (site M), the second the light transmitted and refocused by the Norris lens (site C), the third is slightly offset from the second, measuring ambient and scattered light (site B).

Acton VM502 monochromator with both the entrance and exit slits opened to 1.5 mm, corresponding to about 6 nm bandpass. The monochromator output is approximately on the optical axis. The beam was measured in two configurations. In one, the emergent beam was collected onto the diode at the exit of the monochromator (site M). In the other configuration, the light illuminated about a 20 mm × 5 mm patch of the lens rear window of the camera (the side with the field flattener exit window of the camera that is usually the closest optic to the detector) and was refocused onto the detector diode about a meter away from the exit aperture of the camera (site C). A reading of the ambient background light near the focal plane of the Norris lens was also taken (site B).

In one set of measurements halogen-quartz lamp was used that is bright in the visible, but dims substantially toward the blue; in another a deuterium lamp was utilized. This source is dimmer than the halogen-quartz lamp in the visible band, but brighter in the UV. The halogen-quartz lamp was also used in conjunction with a set of narrowband filters to cut down on background light, with the monochromator set to 0th order. The deuterium lamp measurements were taken with the set of narrowband filters as well as a broadband filter (Melles Griot 03-FCG-167) with a transmission cutoff at 330 nm. This was done to eliminate any possible higher-order light getting through to our detector, as well as to reduce noise. The narrowband filters that were available were Andover Corporation filters at 382.91 nm (11 nm bandpass), 400.51 nm (3 nm bandpass), 434.22 nm (3 nm bandpass) and 453.76 nm (3 nm bandpass). Initial measurements done without the filters yield curves that gave much lower throughput values, and did not allow for accurate background subtraction at short wavelengths.

For each data point in figure 2.26, five measurements were taken:

MSO: Light intensity at the exit of the monochromator with the shutter open.

MSC: Light intensity at the exit of the monochromator with the shutter closed.

CSO: Light intensity at the camera focus with the monochromator shutter open.

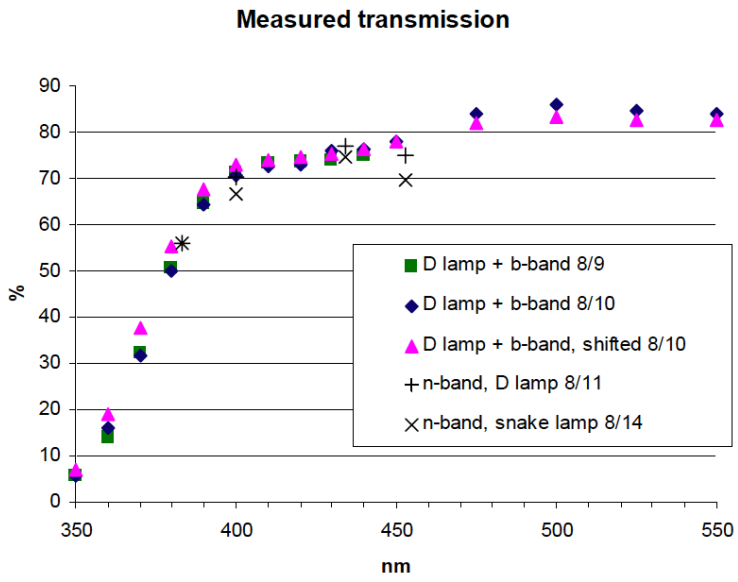

Figure 2.26. Measured transmission of the Norris lens in the 350-550 nm wavelength range. The optic has acceptable (50%) throughput at the blue edge (380 nm) of the CWI bandpass, and is excellent toward the red.

CSC: Light intensity at the camera focus with the monochromator shutter closed.

CSB: Light intensity near the camera focus with the monochromator shutter open, but with the detector out of the beam.

The last measurement was a check to verify that CSC gave a reasonable background value. The throughput was then calculated as

$$\text{Throughput} = \frac{\text{CSO} - \text{CSC}}{\text{MSO} - \text{MSC}}.$$

The data set labeled "shifted" contains data that was taken when the light source was shifted a centimeter away from the optical axis of the camera. The same five measurements were taken to determine the transmission of an off-axis beam.

2.2.5.2 Detector

CWI uses an *e2v* CCD 231-84. This is a 4112×4096 array with square 15 µm pixels. The manufacturer-measured dark current is 4.54 e^- at -100°C. The detector is read out by four amplifiers. Manufacturer measured read noise with a 50 kHz readout is ∼1.8 rms e^-. Measurements performed in the operational configuration of the instrument, at 150 kHz, yield, as shown in figure 2.28, read noise of just over 2.5 rms e in all four channels, and gain of ∼0.145 e/DN. The charge transfer efficiency (CTE)

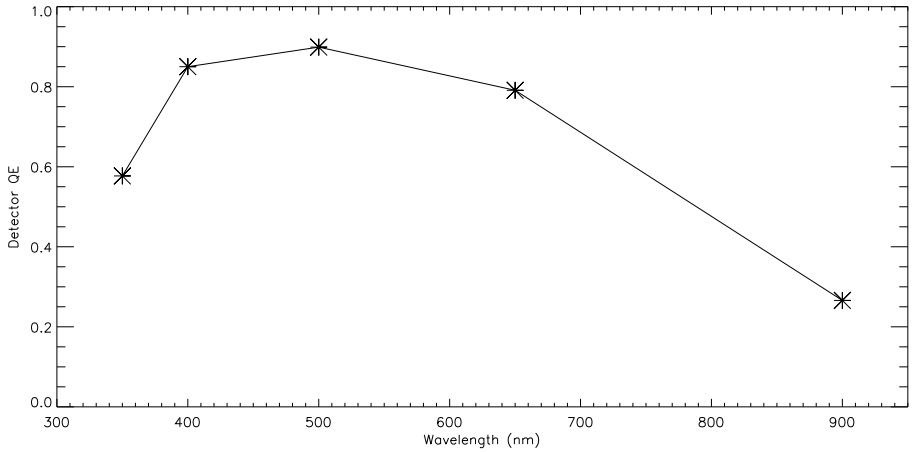

Figure 2.27. The quantum efficiency of the *e2v* CCD 231-84 used in CWI. Data provided by the manufacturer.

was found by *e2v* to be CTE>0.999997 in all quadrants and the parallel register. For scientific operations the CCD was binned 2×2 to reduce the impact of read noise (see appendix A).

A pair of knife-edge shutters can be installed to cover the outer two-thirds of the device for the nod-and-shuffle configuration these can be seen in figure 2.29 (see section 2.3.10 for their function). These shutters are 2 mm removed from the CCD front surface and have not yet been blackened. There is a, roughly, 1 mm vignetting zone under each shutter edge, consistent with the CCD-shutter spacing and F/2 beam speed inside the camera. The fairly large offset combined with the metallic surface leads to light leaking into the masked-off covered areas. Figure 2.30 shows the magnitude and extent of this leak. The effect can be mitigated by blackening the masks, moving them slightly closer to the CCD silicon surface, and reversing the orientation of the knife-edge masks.

The detector is installed in an IR Labs ND-8 dewar with a clear sapphire window. A Lakeshore thermal controller regulates heaters inside the dewar maintaining the CCD temperature near -104°C, though initial operation was at only -99°C.

2.2.6 Calibration Unit

2.2.6.1 Requirements

The calibration unit is needed to characterize the instrument and provide reference spectra for data reduction. It is built to simulate the telescope beam and inject it into the optical path of the spectrograph. It is located on the IFU side of the optical bench. The specific calibration functions the calibration system must fulfill are listed in table 2.7.

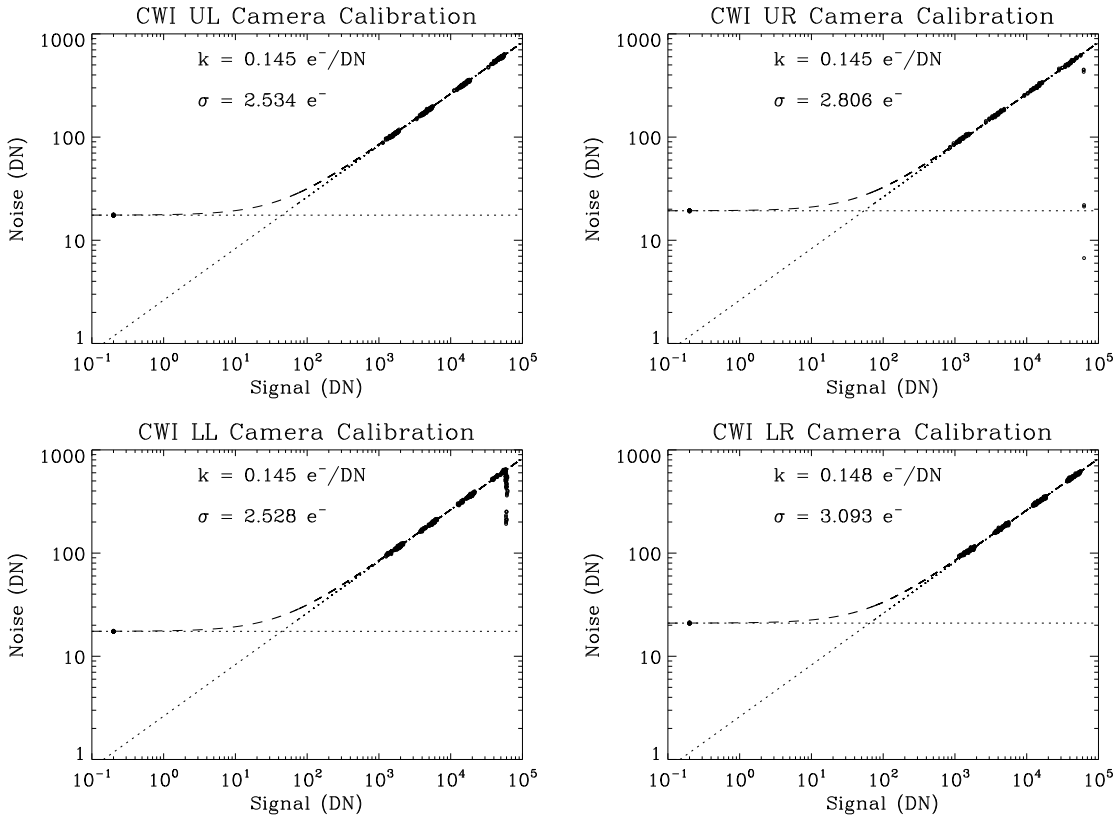

Figure 2.28. Photon transfer curves for the four amplifier channels of the CWI detector. The gain is ∼0.145 e/DN for each, with the read noise slightly between 2.5 and 3 electrons rms.

Table 2.7. A summary of the functions that the calibration unit is designed to perform, including the type of illumination, current status, and usage.

Task	**Comments**
Spectral Calibration	Flat-field illumination of the slicer with a thorium-argon arc lamp spectrum. Used extensively for instrument characterization and data reduction.
Instrument Flat-Fielding	Flat-field illumination with LED continuum lamp, dome flats, and twilight flats. Used for instrument characterization and data reduction.
Distortion Mapping	Regular pinhole grid illumination with either the arc or continuum lamp. Used for instrument characterization and data reduction.
Scatter Analysis	Single pinhole illumination with the LED continuum lamp. Not fully implemented as of this writing, but will be used for instrument characterization.
Grating Efficiency Measurement	Monochromatic flat-field illumination. Though this has not been implemented, the required changes and additions to the system are modest.

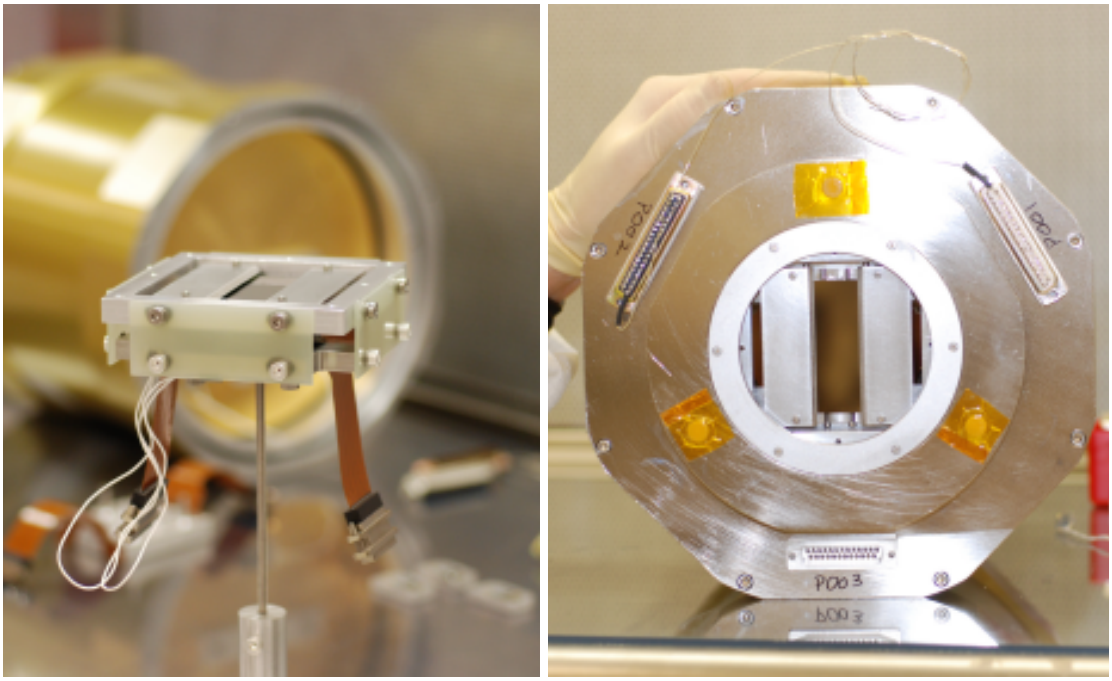

Figure 2.29. Photographs of the CWI detector and dewar. The left panel shows the detector with two Invar steel masks installed. The right panel shows the completed package through the Sapphire window. Visible under Kapton tape capturing them are the three standoff pads used for adjusting the detector position with respect to the Norris lens. Photographs courtesy Patrick Morrissey.

2.2.6.2 Optical Layout and Alignment

The calibration unit optical layout is a straightforward refractive optical relay, which includes an aperture stop. A reflective Offner relay was considered, which would have had superior chromatic performance, but did not fit within the small footprint available to the calibration system on the CWI optical bench. The schematic layout of the full system is shown in figure 2.31, a ray trace in figure 2.32, and image of the completed optics assembly is shown in figure 2.33. The optical layout includes a custom made doublet lens, though due to delivery delays the current instrument is fitted with an off-the-shelf optic. The custom lens is made of glass with high transmission in the 3500 Å-4500 Å, the blue edge of the CWI bandpass. The commercial lens is adequate for the current applications, but will need to be replaced before the instrument is used for the bluest part of the spectrum. Figure 2.34 shows the design drawing of this lens and the expected performance. The calibration unit will need to be refocused between the red and blue ends of the spectrum. This will be achieved by moving the calibration objects along the calibration optical axis to focus them on the slicer.

The calibration unit alignment procedure consists of five parts:

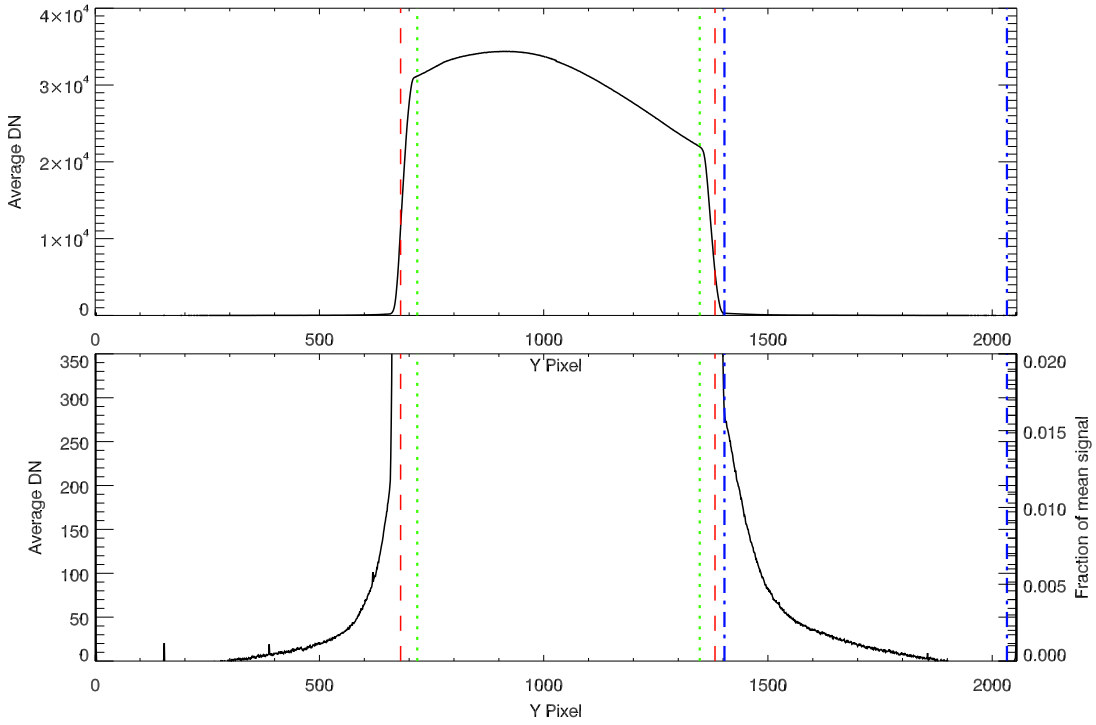

Figure 2.30. Performance of the nod-and-shuffle mask. A continuum lamp image was collapsed along the spatial direction, leaving a composite spectrum for the full CCD (binned 2 × 2). The top and bottom panels show the same curve, but on different scales. The abscissa is the detector pixel along the spectral direction, the ordinate the number of counts above the bias level registered. The approximate locations of the mask edges are marked by red dashed lines, the green dotted and blue dot-dashed lines show the regions of the detector identified as the target and sky spectra. The transition from the bright uncovered region of the detector to the dark masked one is approximately 35 pixels (or 1 mm), which is what is expected for a mask 2 mm away from a detector in an F/2 beam. The bottom panel, is a zoomed view at the lowest signal levels. It indicates that there is leakage of signal at the level of about 0.3% of the continuum approximately 100 pixels into the background storage region.

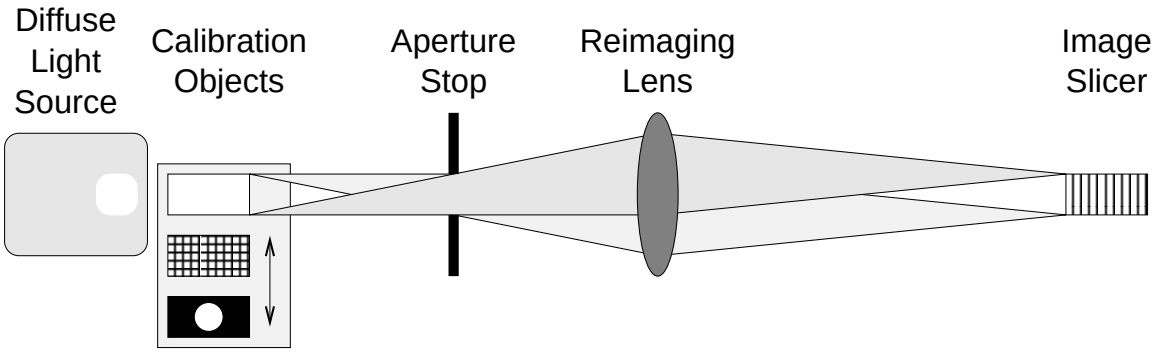

Figure 2.31. A schematic view of the CWI calibration unit. A diffuse light source illuminates one of several possible calibration targets which are then reimaged by a doublet lens onto the slicer. The aperture stop controls the exit pupil of the system.

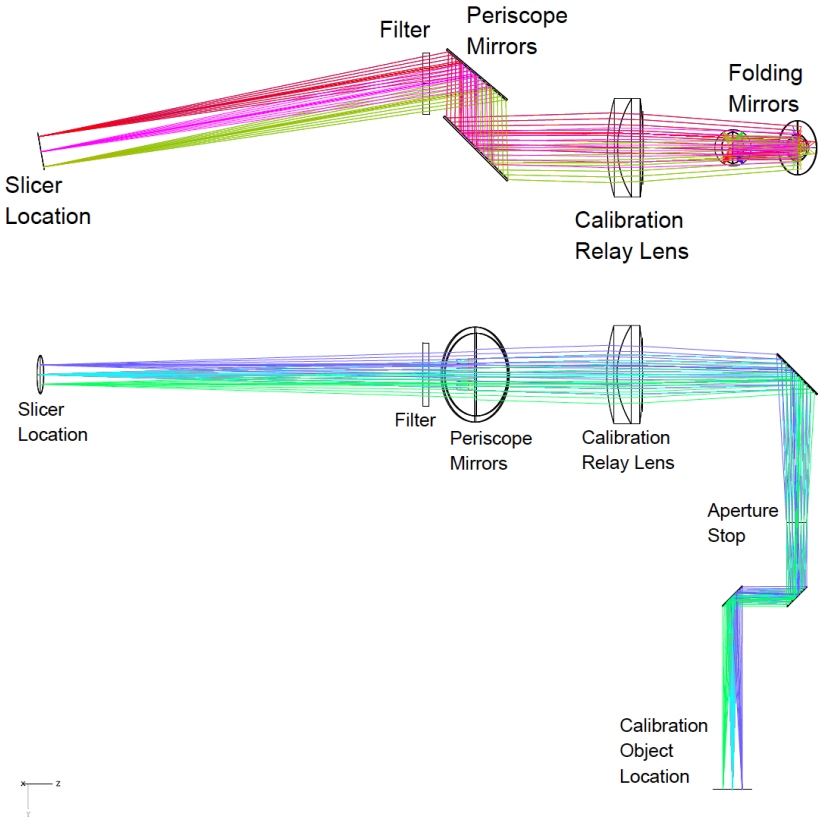

Figure 2.32. ZEMAX ray traces of the CWI calibration optics. The top two panel shows a side view while the bottom panel shows a top view of the optical layout. Calibration objects are reimaged by the relay lens onto the slicer; the position of the aperture stop determines the location of the exit pupil of the system, and matches the location of the exit pupil of the telescope. The periscope mirror configuration slides in place of the CWI FM1 mirror, injecting the calibration light into the system.

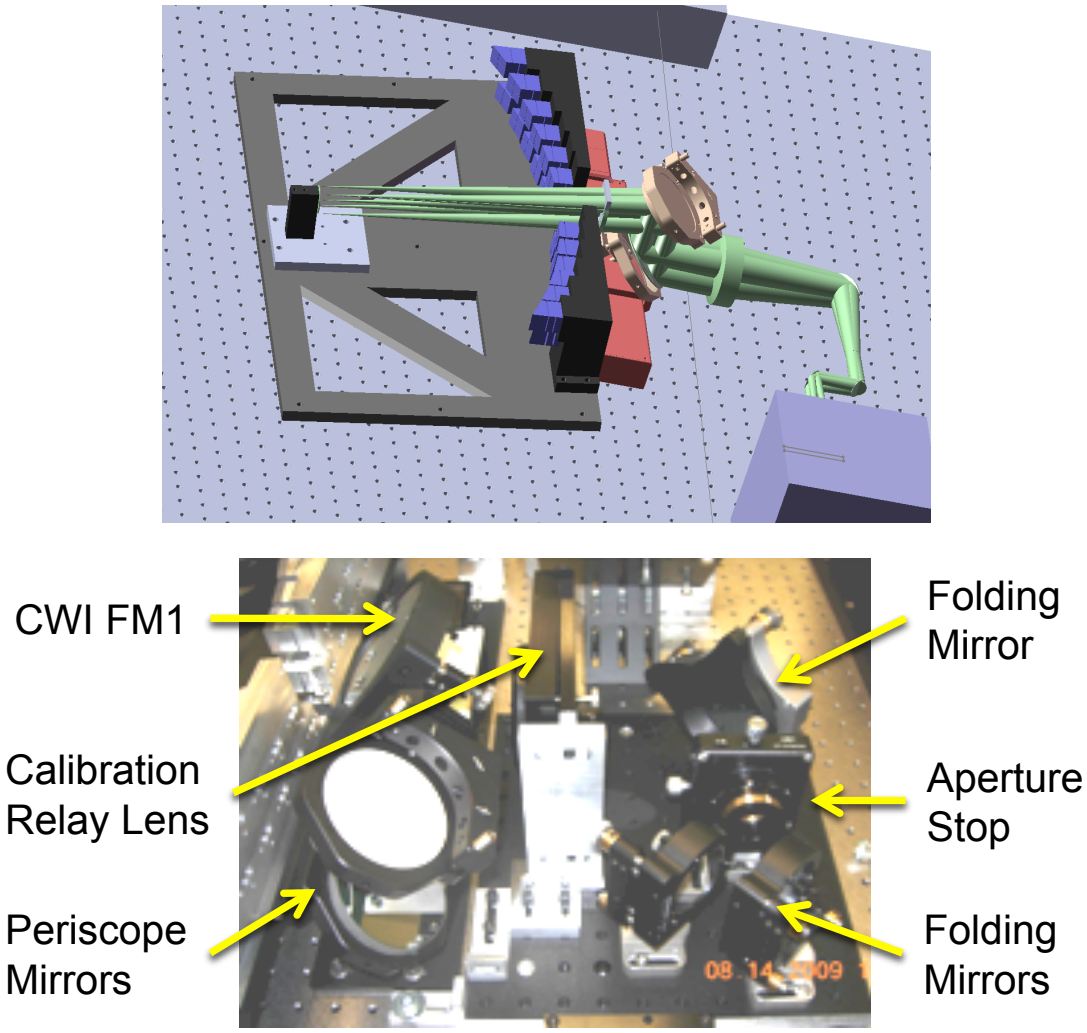

Figure 2.33. The top panel shows a CAD layout of the calibration unit in relation to the integral field unit and the remainder of the CWI system. The bottom panel displays the completed assembly.

Alignment of the calibration breadboard optics. A helium-neon lab laser is set up on an optical bench with the beam parallel to the surface. The calibration unit base plate is secured to the bench, and the three folding mirrors are attached to mechanical tolerances. The laser enters the area over the base plate from the direction where the slicer would be. The mirrors are then adjusted in position and angle, until the beam is centered on each and exits the base plate where the calibration light source will be. Finally, the calibration lens is inserted onto the breadboard, and its position is adjusted until the laser beam is not deflected. The lens cell is then removed from the mount.

Pupil location. An illuminated "F" shaped target is set up 18.9 m away from where the slicer stack location would be, which is the distance of the telescope exit pupil from the slicer. The laser is

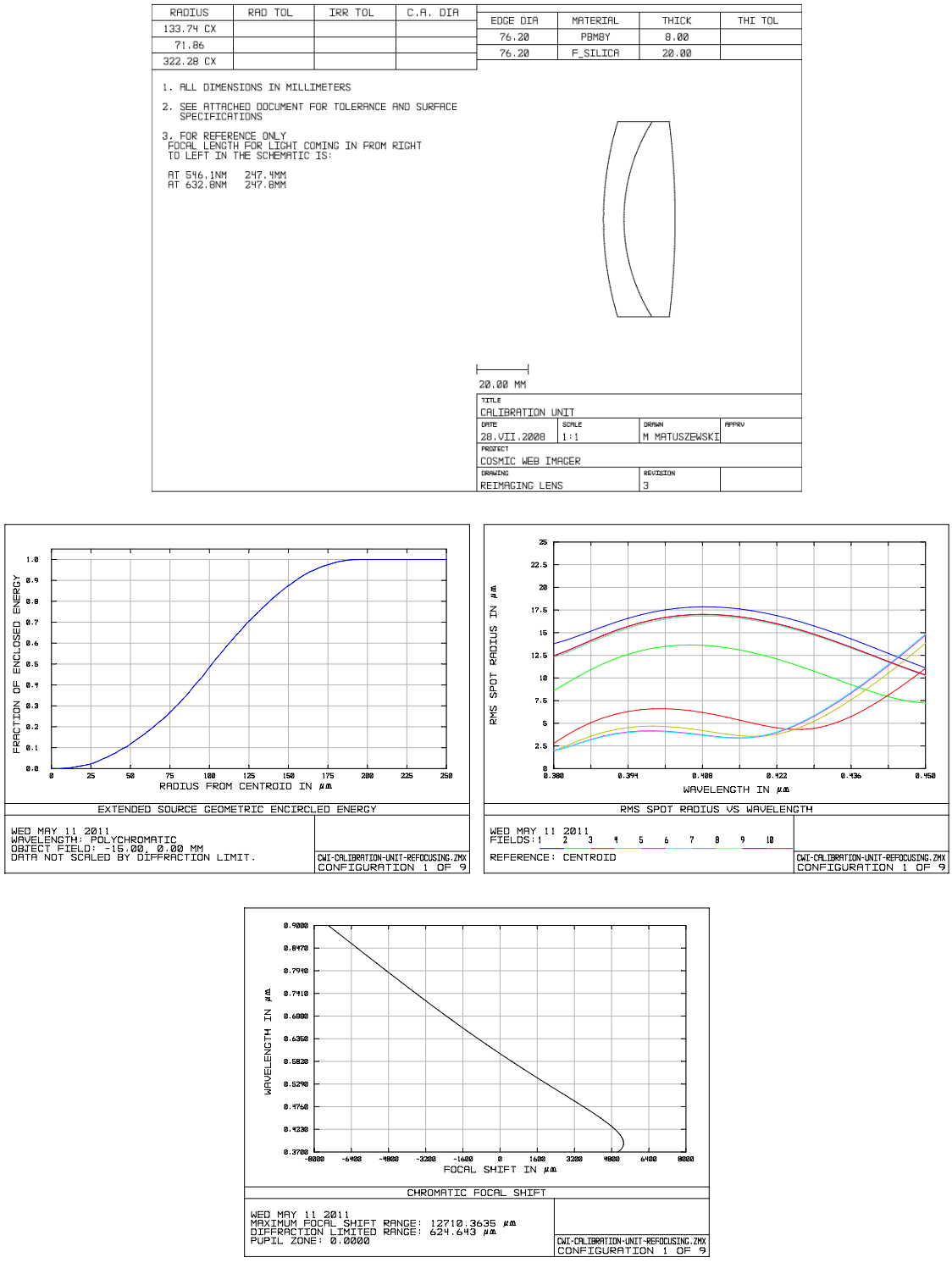

Figure 2.34. The design drawing for the calibration system reimaging lens. The lens is made of two types of glass that have high transmission in the UV. The encircled energy from a 120 µm pinhole is shown in the left panel in the middle row. The right-middle panel shows the RMS spot size as a function of wavelength for several field positions, out to 15 mm from field center. The bottom panel quantifies the chromatic focal shift; equivalently, the distance that the calibration targets will need to be moved to maintain best focus at the slicer.

used as a guide to ensure that the target is on the optical axis of the system, the laser is then removed. A commercial camera is placed at the slicer location, adjusted laterally to sit on axis, and focused. The image of the target is centered on the camera detector. An adjustable three-axis optical mount holding the aperture stop is mounted onto the breadboard, and the relay lens is reinstalled. The position of the aperture stop is adjusted along the three axes to center it on the camera CCD and to bring it to focus. This places the virtual pupil at the same distance and location as the virtual pupil of the telescope.

Calibration object location. An illuminated object is now placed at the nominal location of the slicer. Its focused image as reimaged through the calibration system optics is located. The fold mirror farthest from the slicer position is moved along the beam parallel to the edge of the breadboard until the image is at the prescribed distance from the mirror in the direction perpendicular to the edge of the breadbord.

Periscope mirror alignment. The breadboard is installed in its designated space on the CWI optical bench, and the laser is once again set up, this time illuminating the calibration system from where the calibration light source is to be located. The periscope mirrors are installed to mechanical tolerances, and their angles are adjusted until the laser beam is centered on their faces and arrives at the middle of the slicer stack.

Integrating sphere and calibration objects. The integrating sphere is attached to a mounting plate. Its exit port is aligned with the first fold mirror on the calibration breadboard. The calibration targets are installed on a linear stage across the face of the integrating sphere, in front of its exit port. An index card is used as a screen and placed next to the slicer stack mirrors, in the nominal slicer focal plane of the telescope. Light is injected into the sphere, and the sphere-calibration object assembly is moved along the beam direction until the calibration object image is focused on the screen.

2.2.6.3 Calibration Objects

There are five available calibration objects. They are installed in a special fixture attached to an 8" linear selector stage, which allows any of them to be placed in the calibration system beam at the exit port of the integrating sphere. The calibration objects are a rectangular flat-field, a uniform 24 $\times$ 15 grid of 120 µm pinholes on 1 mm centers, a uniform grid of 30 µm pinholes, a vertical array of 50 µm thick horizontal lines, and a single pinhole mounted on a vertical stage, allowing for placing its image anywhere on the IFU slicer. Any standard pinhole on a 9.5 mm diameter substrate can be installed. A 150 µm aperture was chosen to closely match the expected focused spotsize of the Hale telescope. The pinhole and slit arrays were manufactured as optically thick chromated masks on a 2.4 mm thick fused silica substrate by HTA Photomask. The design drawings for two of these

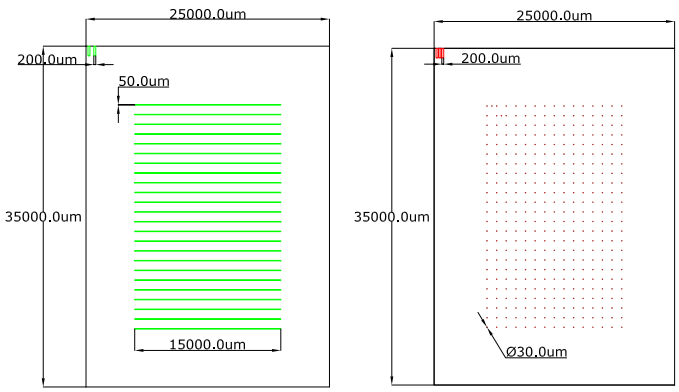

Figure 2.35. Drawings of two of the three specially manufactured calibration objects. The 35×25×2.4 mm fused silica glass is coated with an optically thick later of chrome (OD=5). The features are laser etched in a photoresist material, and portions of the chrome overcoat are removed chemically.

objects are shown in figure 2.35. The 35 mm×25 mm objects are inserted into milled-out pockets in the aluminum mounting plate, pressed by a pair of leaf springs against a layer of Kapton tape. This mounting plate is shown in figure 2.36.

The 120 µm pinhole sizes for one of the grids match the optical performance of the telescope, which has commensurate spot size at the CWI focus. The 30 µm pinholes were selected to test the optical performance of the CWI instrument independently of the telescope. The pinholes were spaced regularly on a 1 mm grid, 15 for each of the twenty-four 16 mm wide slices. This arrangement is not ideal when the instrument is slightly out of focus, as the spot images overlap on a slice, and mix between slices. A pattern on 3 mm centers, with 1.5 mm offset between neighboring slices, would be better for understanding the imaging performance of the spectrograph. The calibration optics are not an ideal 1:1 relay, and the magnification varies somewhat with wavelength. Consequently, the pinholes are not centered on the exterior slices.

In addition to the five targets outlined above, there is a dark setting where the light source is blocked by a portion of the calibration object mounting plate. A calibrated photodiode will be added to this setting to monitor the output of the calibration light sources.

2.2.6.4 Light Sources

The calibration system light source is an assembly that consists of a 6” integrating sphere with two 1.5” entrance ports, and one 1.5” exit port. The sphere is made of PTFE, which has good scattering properties into the ultraviolet. Attached to the two entrance ports are lamps. At the exit port is the 8” selector stage with an array of calibration objects. The integrating sphere exit port is a spatial flat-field light source.

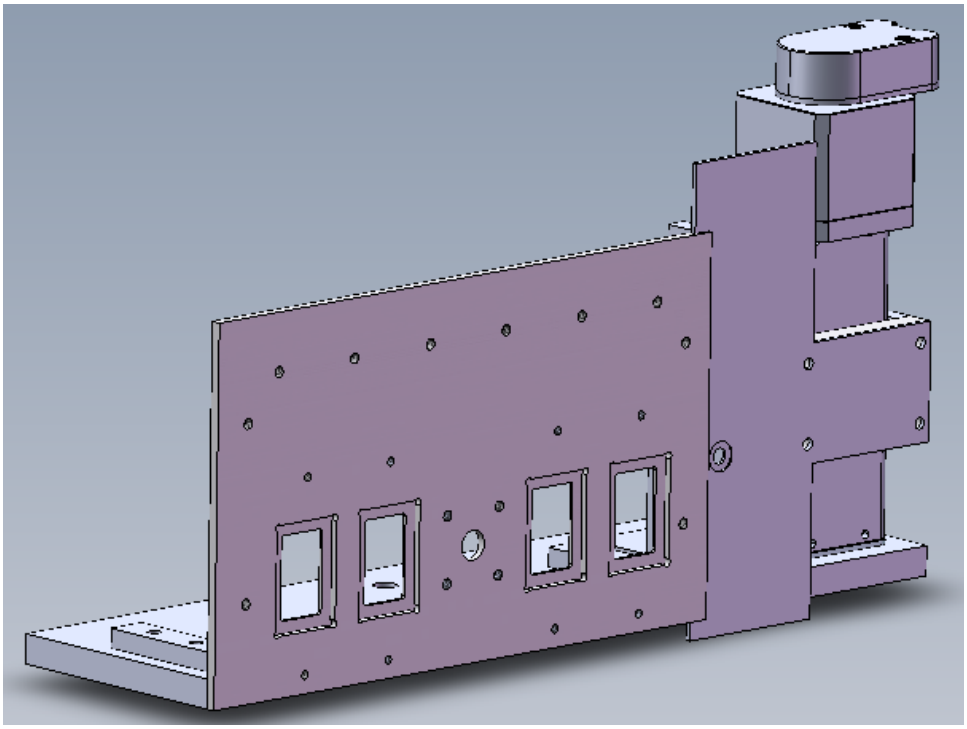

Figure 2.36. CAD rendering of the CWI calibration target mount. This assembly rests on a Newmark Systems NLS8 linear actuator. There are six calibration positions within the assembly, one of which is located in front of the calibration integrating sphere exit port at any given time. There are four windows intended for full-field patterns (flat-field, pinhole arrays, lines), a space for mounting a photodiode that monitors the calibration unit output (between the two pairs of windows), and a vertical Newmark Systems MS-2-24-E linear actuator that has attached to it a mounting plate for a pinhole, allowing this image of this aperture to be positioned anywhere on the CWI slicer. The photodiode was descoped in the interest of time. Multiple threaded holes have been added to the design to facilitate the mounting of cables and baffles.

The first lamp is a thorium-argon line emission arc lamp. The emission spectrum of this gas mixture has many strong lines in the 3500 Å to 7000 Å range. The bulb is encased in a simple enclosure with a borosilicate window. It shines into one of the entrance ports of the calibration integrating sphere. It is powered with an EMCO HC2012 12V hollow cathode lamp power supply, and cooled using a 3" fan. The lamp is controlled using a discrete TTL connection to the system computer in the Cassegrain cage. The lamp was manufactured by Delta Scientific of Mississauga, Ontario; its spectrum has been measured (Palmer & Engleman 1983), and is available in electronic form from NOAO `http://www.noao.edu/kpno/specatlas/`.

The second source is a continuum lamp that is composed of an array of light emitting diodes (LEDs). This choice was made as LEDs consume much less power, and generate less heat, than the usual choices for continuum light: halogen, tungsten, or deuterium bulbs. The spectral profile of a typical LED is Gaussian-like, with a FWHM ∼15 nm. There exist LEDs with peak wavelengths

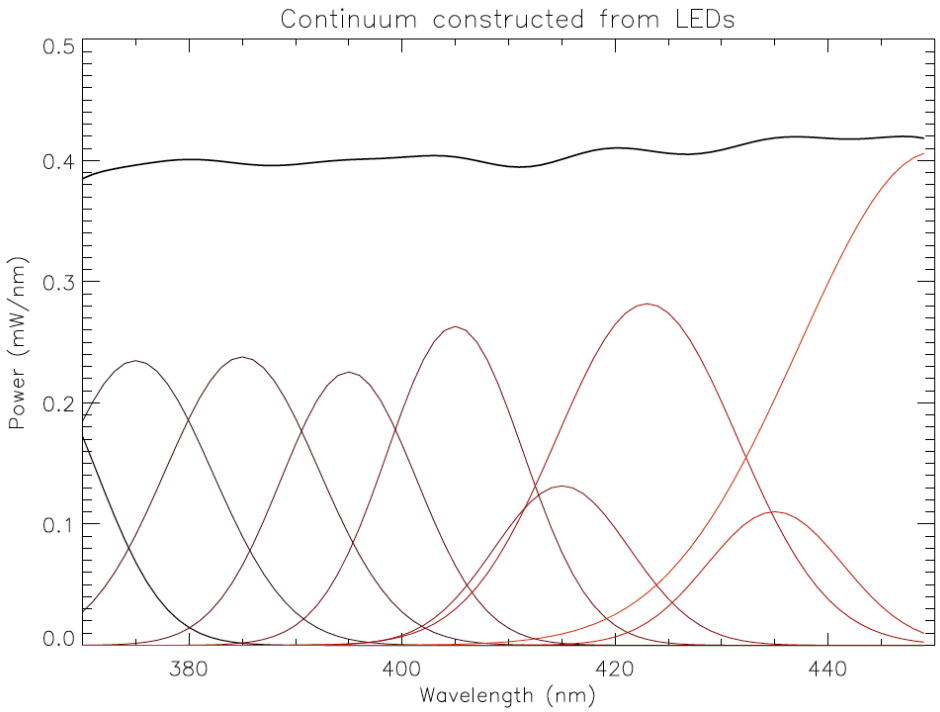

Figure 2.37. A composite spectrum generated by a series of LEDs. The individual LED spectra are shown as Gaussian-like curves. The LEDs will be controlled using high-frequency pulse-width-modulation (PWM) of the supplied current yielding duty cycles from 0 to 1 in steps of 1/256 or 1/65535, depending on the hardware chosen.

sparsely populating the UV-Vis-IR spectrum. As such, the LED spectral curves nearly form a basis for the full spectrum, and by varying the intensities and numbers of the diodes, arbitrary spectral distributions can be approximated. Figure 2.37 shows a sample continuum spectrum composed of nine individual LED spectra. The LED intensities can be varied either by adjusting the currents delivered to the devices, or by varying their duty cycles using high-frequency pulsations. The latter method is preferable, as it is simpler to implement using existing integrated circuits. This will be the method used in CWI. The existing design calls for the LEDs to be driven via an array of MAXIM MAX6966AEE+ integrated circuits. Each IC can source up to ten 20 mA channels, and control the duty cycle of each via 8-bit pulse-width modulation. The ICs will programmed through an SPI bus using a computer controlled USB to SPI converter. As of this writing, there is no intensity control for the LEDs, as there were more critical aspects of the project that required attention prior to the observing runs.

2.2.7 Guider

2.2.7.1 Guider Overview

The CWI instrument requires a guider to control instrument pointing during an observation. Although the telescope stability is very good, there is flexure that moves the CWI bench with respect to the Cassegrain mount as the instrument swings. The optical layout of the guider subsystem is described in section 2.2.7.2. The initial guider subsystem design called for a FLI Microline 8300 camera with an 18 ×13 mm progressive scan CCD with a 60 mm FL Nikkor Micro lens. The camera would take 5 s exposures, provide tracking, and aspect solution over a 4×3 square arcminute field of view. As there was insufficient time to develop the software necessary for this part of the subsystem prior to the initial run, the camera was replaced with the already existing Palomar auto-guider (Shepherd ????). The smaller light-intensified detector ($8\times9\,\mathrm{mm}^2$) is fitted with a Fujinon 2/3" 35 mm FL F1.6 Lens.

2.2.7.2 Guider Optical Layout

To obtain a large field of $4 \times 4\,\mathrm{arcmin}^2$ a $100 \times 100\,\mathrm{mm}^2$ portion of the telescope field of view needs to be used. The guider pre-optics include two rectangular fold mirrors that redirect the telescope beam toward a 150 mm diameter, 300 mm focal length, plano-convex field lens. This lens is located at the focal plane of the telescope, offset by close to 13 arcminutes from the center of the IFU field of view. The lens reimages the telescope pupil at its back-focal distance, and a commercial lens is placed there focusing the F/16 telescope beams onto the guider camera detector. The lens currently used for the instrument has a 35 mm focal length and, in conjunction with the Xybion camera, yields an approximately 2.9×2.2 square arcminute field of view. The FLI guider design was intended for use with a 60 mm focal length macro lens and would yield a slightly larger field of view. Changing the lens to a 35 mm focal length model would further increase the field of view to, approximately, a 6 arcminute diameter disk. The current configuration that uses the observatory furnished Xybion camera is functional, but CWI would benefit from having a dedicated guidance system that would not need to be reinstalled, aligned, and calibrated for every observing run.

2.2.7.3 Guider Sensitivity Estimate

The following computations make use of the following variables: telescope area A, telescope diameter D_T, system efficiency (including the atmosphere) η, guider integration time t, guider lens focal ratio f, detector read noise N_r, sky background flux F_b, star flux F_s, detector plate scale p, detector pixel size s, the detector physical dimensions x, y, and the focused spot point-spread function (PSF), including seeing d.

The guider field of view is computed from the characteristics of the guider detector and optics:

$$l_x = x\frac{\Theta}{D_t f},$$
$$l_y = y\frac{\Theta}{D_t f},$$

where $\Theta = \text{arcsec in 1 radian} = 206265\,\text{arcsec/rad}$. The Xybion camera CCD is $8.8{\times}6.6\,\text{mm}^2$ and an F/1.8 setting is used on the lens, leading to $(l_x, l_y) = (3.3, 2.5)$, in arcminutes. The FLI camera has a $18{\times}13.5\,\text{mm}^2$ CCD with a F/3.5 macro lens attached, and would give a $(l_x, l_y) = (3.5, 2.6)$.

Sky background at Palomar varies from about 19^{th} mag/arcsec^2 to 22^{nd} mag/arcsec^2 on dark nights. Using the value from Allen's Astronomical Quantities (Cox 2000),

$$B = 22\,\text{mag} \simeq 1.1 \times 10^{-17}\text{erg/s/cm}^2\text{/arcsec}^2\text{/Å}.$$

For sky of magnitude m the flux, assuming a bandpass of 2000Å:

$$\begin{aligned} F_b &= \frac{B}{E_\gamma}\,\Delta\lambda\,A\,\eta \\ &= 2.2 \times 10^2 \times 10^{-0.4(m-22.0)}\left(\frac{\eta}{0.1}\right)\frac{\text{electrons}}{\text{s arcseec}^2}, \end{aligned}$$

where the total guider system throughput efficiency, including the atmosphere, telescope, and instrument optics was assumed to be $\eta \sim 10\%$.

A star of apparent magnitude $m_V = 0$ corresponds to a flux $f = 3.4 \times 10^7\text{photons/s/cm}^2$. Taking into account the instrument and its efficiency:

$$\begin{aligned} F_s &= 10^{-0.4m} f t A \eta / d^2 \\ &= 2.6 \times 10^5 \times 10^{-0.4(m-16)}\left(\frac{\eta}{0.1}\right)\left(\frac{1"}{d}\right)\frac{\text{electrons}}{\text{s arcsec}^2}. \end{aligned}$$

The detector noise consists of two main components: read noise (N_R, e/pix), and the dark current (N_D, e/pix/s). The fluxes corresponding to these two quantities can be expressed as

$$\begin{aligned} F_R &= \frac{N_R}{s_x s_y p^2 t} \\ &= 120 \times \left(\frac{N_R}{10\,\text{e/pix}}\right)\left(\frac{11\,\mu\text{m}}{s_x}\right)\left(\frac{13\,\mu\text{m}}{s_y}\right)\left(\frac{22.5\,\text{arcsec/mm}}{p}\right)^2\left(\frac{1\,\text{s}}{t}\right)\frac{\text{electrons}}{\text{s arcsec}^2} \\ &= 20 \times \left(\frac{N_R}{5\,\text{e/pix}}\right)\left(\frac{40\,\mu\text{m}}{s}\right)^2\left(\frac{11.6\,\text{arcsec/mm}}{p}\right)^2\left(\frac{1\,\text{s}}{t}\right)\frac{\text{electrons}}{\text{s arcsec}^2}, \end{aligned}$$

Table 2.8. The signal to noise ratio for a bright, moderate, and dim sky for stars with $15 \leq m_V \leq 21$ with a 5 s exposure with the FLI guider. The third column from the right uses star counts from Table 19.12 in Cox (2000) to estimate the number of stars brighter than the given magnitude that are expected in the field of view of the guider. The second to last column gives the approximate probability of not finding a star brighter than a given magnitude within the guider field of view, assuming Poisson statistics with the mean given in the previous column. The last column gives the approximate number of stars expected in an annular region around the CWI IFU at the offset of the guider. This takes into account that the instrument can be rotated to adjust the orientation of the IFU. The probability of there not being a bright enough star available to guide at a specific target is effectively nil.

m	**Bright Sky V=18.5**	**Moderate Sky V=19.9**	**Dim Sky V=21.3**	**Stars (FOV) (≤m)**	**No star Prob.**	**Accessible Stars (≤m)**
15	204	220	226	0.3	0.74	8
16	111	130	137	0.6	0.55	16
17	55	72	80	1.0	0.36	27
18	24	36	43	1.4	0.25	38
19	10	16	21	2.1	0.12	57
20	4	7	9	3.1	0.05	84
21	2	3	4	4.4	0.01	112

where the middle expression corresponds to the Xybion camera, and the bottom is scaled for the FLI design, which includes 8×8 binning of 5 µm pixels. The above also assumes that the noise performance of the newer FLI camera is better. The values are expressed in electrons/s/arcsec^2.

The flux equivalent to the dark curent is given by

$$\begin{aligned} F_D &= \frac{N_D}{s_x s_y p^2} \\ &= 300 \times \left(\frac{N_D}{1\,\mathrm{e/s/pix}}\right)\left(\frac{11\,\mu\mathrm{m}}{s_x}\right)\left(\frac{13\,\mu\mathrm{m}}{s_y}\right)\left(\frac{22.5\,\mathrm{arcsec/mm}}{p}\right)^2 \frac{\mathrm{electrons}}{\mathrm{s\,arcsec^2}} \\ &= 300 \times \left(\frac{N_D}{10\,\mathrm{e/s/pix}}\right)\left(\frac{40\,\mu\mathrm{m}}{s}\right)^2\left(\frac{11.6\,\mathrm{arcsec/mm}}{p}\right)^2 \frac{\mathrm{electrons}}{\mathrm{s\,arcsec^2}}, \end{aligned}$$

Where the dark current values are scaled to account for pixel size difference.

Guider signal-to-noise ratio is computed using

$$\sigma \equiv S/N = \frac{F_S t}{\sqrt{F_S t + F_B t + (F_R t)^2 + (F_D t)}}.$$

The signal-to-noise ratio contour plot for a 5 s is shown in figure 2.38. Either guider can achieve a SNR∼10 for a 19$^{\mathrm{th}}$ magnitude star.

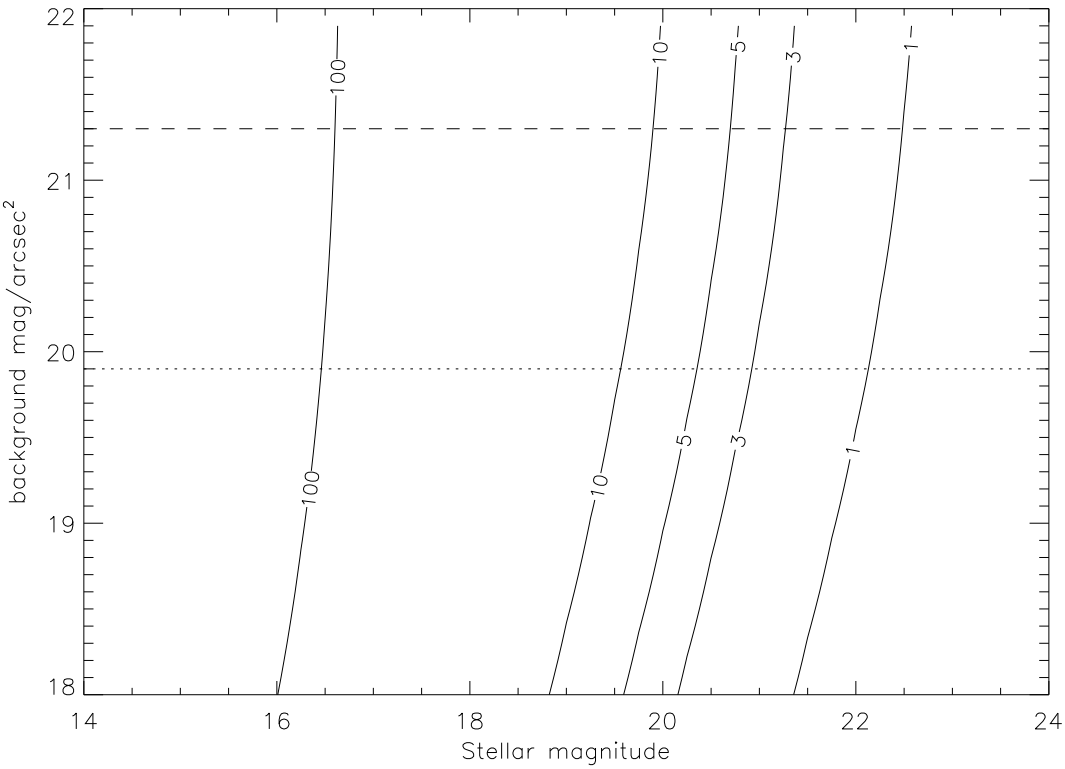

Figure 2.38. Signal-to-noise ratio contours shown for the FLI guider in the stellar magnitude vs. sky background plane for a 5 s exposure (though the curves are very similar for the Xybion camera). The dashed horizontal line indicates the expected sky brightness at Palomar on dark nights, the dot-dashed line the same for half-moon.

2.2.7.4 Guider Filter

Currently there are no filters installed on the guider. The index of refraction of the atmosphere varies by $\Delta n \sim 1 \times 10^{-5}$ from 400 to 700 nm. As a consequence polychromatic light incident on our atmosphere is dispersed. The apparent angle of incidence between the red and blue edges of the object can be as large as 1.3" at 45° elevation, rising to 2.2" at 30°. These are nonnegligible quantities. One solution is to install a chromatic filter. As the calculations above were performed assuming star counts in the V band, this should not change the performance significantly. It would be advantageous to install a removable a neutral density filter to allow for system alignment and pointing adjustments earlier in the evening, prior to astronomical twilight without saturating the guider detector.

2.2.7.5 Guider Mount and Adjustment

The guider mount for the Xybion camera was adapted from the existing mount for the same camera used by the Pulsar Camera (Kern 2002). Standoffs were added to adjust the camera height above the bench to match the field lens and folding flat mirror positions. The location of the field lens was set during engineering time to be near the focal plane of the telescope. The guider camera was installed to mechanical tolerances and brought to focus at the field lens. The mount for the FLI camera is a simple L-bracket design that allows in place adjustment of the camera along the bench, with the height and tip angles controlled by shimming.

2.2.8 Optical Bench, Mounting Structure, and Enclosure

The CWI layout requires that optics be installed on two sides of a breadboard. This mounting bench is a $6\times4\,\mathrm{ft}^2$, 6-inch-thick structure. It has a regular 1/4-20 threaded hole pattern on a 1-inch-square grid on both surfaces. The bench has a rigid, but lightweight, hexagonal steel cell core, four 4-inch round utility cutouts for cables in the corners, a large rectangular opening for the beam from fold mirror 3 to fold mirror 4, and three sets of three mounting locations for the structure that interfaces the instrument to the telescope. These locations are stainless steel through-hole inserts that are welded into the breadboard; they allow for the mounting structure to be attached using shoulder bolts. A design drawing of the bench is shown in figure 2.39. The bench, mounting structure, and rotating support are pictured in figure 2.40. The rotating mount allows access to both bench surfaces during the integration phase. The breadboard and rotating stand were designed by the author in conjunction with engineers at Newport. The mounting structure is the interface of the instrument to the telescope, mating with the Cassegrain ring via four mounting pins. The mounting structure and a handling cart for the observatory were designed by Daphne Chang.

2.3 Data Reduction

2.3.1 Overview

The end product of the CWI data reduction pipeline is a sky-background- subtracted data cube. It takes a series of steps and calibration products to arrive at that data format. As CWI is a new instrument, the data reduction process is not mature and likely to change with increased understanding of system and the scientific return. Figure 2.41 shows the key steps of data reduction, and the following sections discuss the individual stages.

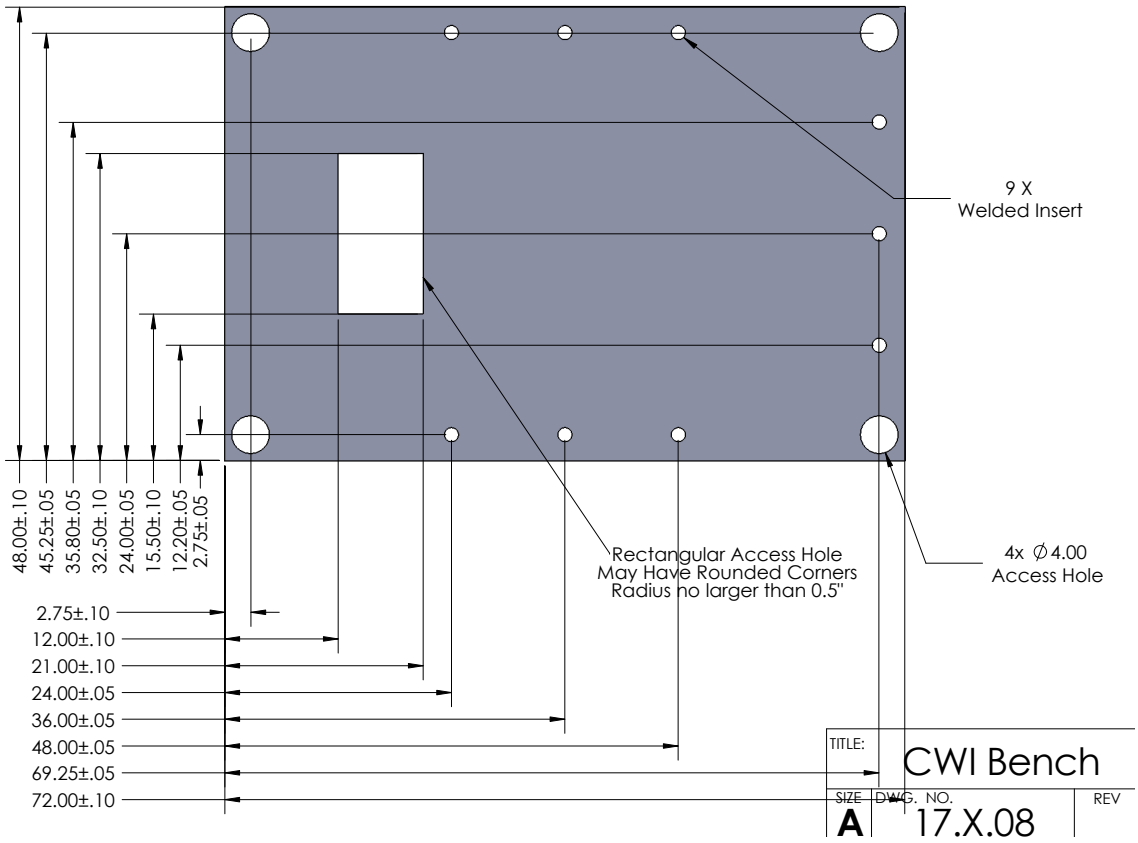

Figure 2.39. Construction drawing for the CWI bench. The bench is constructed of 6" thick lightweight hexacore material. Visible are the cable access holes, the opening for the science beam to cross to the other side of the bench, and the attachment locations of the mounting structure.

2.3.2 Image Preparation

The raw FITS format (Wells et al. 1981) image, as read out by the CCD at the time of this writing, needs to have several corrections applied to it. The first row read out by each of the four amplifiers onboard the detector is saturated and is discarded. The top half of the image (corresponding to two of the amplifiers) is shifted by a single pixel to the right. This is corrected for. Several extensions are added to the file, including a flag array, and two arrays to accommodate error values. All of these arrays are the same size as the original images.

2.3.3 Cosmic Ray Removal

The CWI detector, as do all CCDs, collects charge from cosmic rays colliding with the detector substrate. The accumulation of this signal is the primary reason for keeping individual exposures shorter than the total desired integration time. Cosmic rays are rejected and masked using Laplacian edge detection via the `LA_COSMIC` package (van Dokkum 2001), as translated into IDL by Joshua Bloom.

Figure 2.40. The CWI optical bench installed on the rotating structure. Attached to the breadboard is the mounting structure that connects the instrument to the telescope. This consists of three square 3" tubes bolted to the bench, serving as reinforcement and a mounting point for the welded structure above it. A 1" thick steel top plate is a rigid platform for four specially notched interface pins that insert into the telescope Cassegrain ring. Welded to this plate are three triangular legs that are rested on the aforementioned bars. A FARO arm that was used for positioning some of the elements is seen mounted to the bench.

2.3.4 Gain and Bias Correction

Prior to and after observation a series (usually 10) of bias exposures is taken. A median image is constructed from these, and this resultant median-bias is subtracted from all other data taken that night. The amplifier gain (e^-/DN), as calculated from the photon transfer curve procedure performed each night, is applied to each image.

2.3.5 Slice Image Straightening and Realignment

The powered (collimator, Norris lens) and diffractive (grating) elements of CWI introduce a curvature into the spectra.

This procedure to correct for this starts by finding slice image edges in a flat-field image for a particular camera-grating configuration. This can be done with either a calibration or a twilight

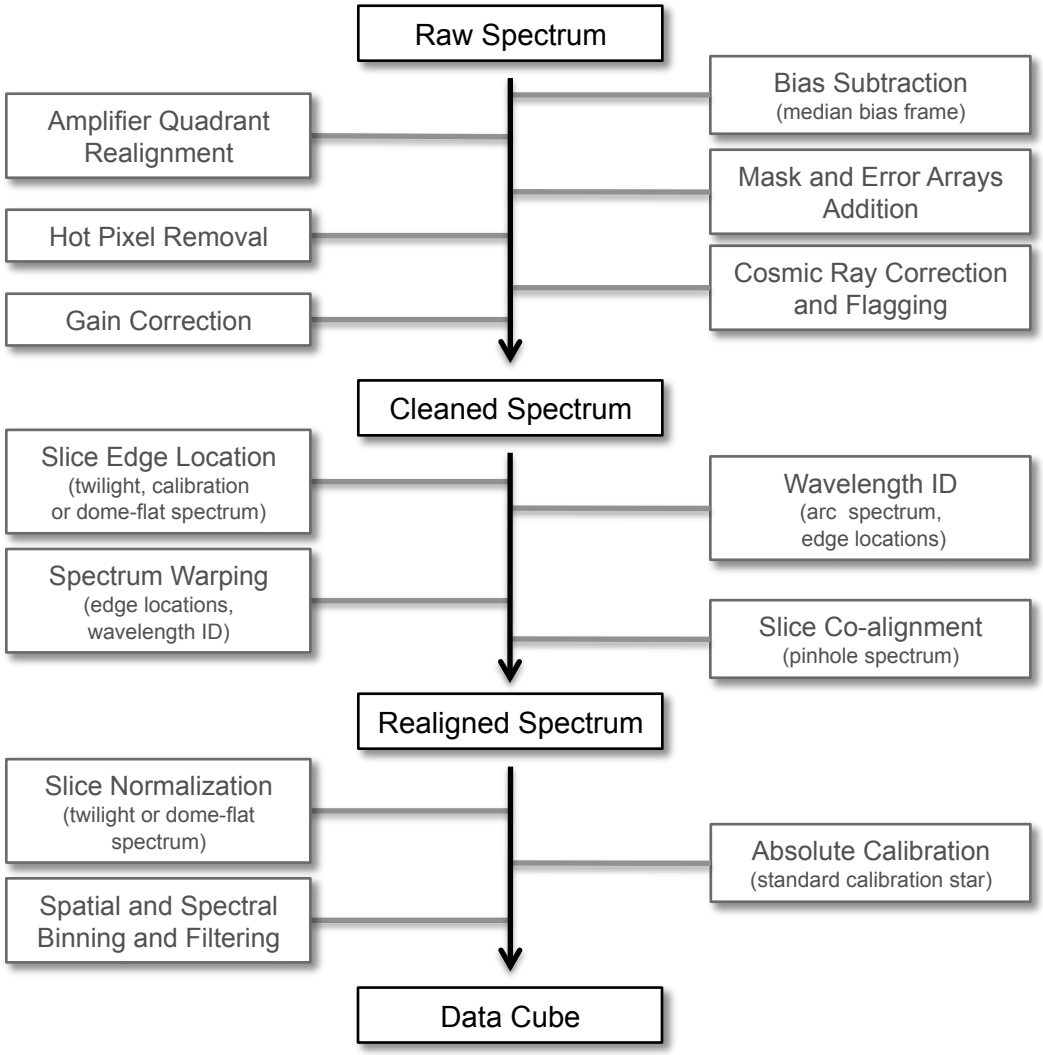

Figure 2.41. A flow diagram of the CWI data reduction pipeline. Initial processing sanitizes the raw image, corrects for readout misalignment, hot pixels, removes cosmic rays, and converts the DN image into photoelectrons. The next stage warps the curved slitlet spectra on the detector into spatially and spectrally aligned rectangular spectra. The last step of the data pipeline corrects for instrument and atmospheric response, ending in binning the data to generate a cube. Calibration products necessary for particular actions are listed in parentheses for relevant steps. The pipeline is discussed in more detail in section 2.3.

flat. The process is explained further in figure 2.42. In some early CWI data the first and last slice images fell outside the detector active area. In these cases the software extrapolates the location of those edges from the remaining 23 values. The slice widths are configured such that the reformatted pixel corresponds to 0.67 arcseconds for the CCD binned into 2×2 blocks and 0.33 arcseconds for the unbinned 4 k×4 k array.

The second step combines the edge locations with a thorium-argon spectrum from the calibration system. Several (n = 3 to 6) peaks from the spectrum are matched with spectra extracted from the left, center, and right parts of each slice yielding up to 3n points with (x_d, y_d) image coordinates. These are then associated with destination points in a straightened spectrum (x_s, λ) , corresponding to the left edge, center, and right edge of a corrected slice, with wavelength being the second dimension. A custom IDL routine, `MOD_POLYWARP` is used to generate a polynomial coordinate transformation kernel between the two sets of points, fitting a third-degree polynomial in wavelength, second degree along the spatial dimension. An existing IDL routine `POLYWARP` can create a similar polynomial transformation matrix, though it requires that the transformation degrees be the same for the two dimensions. An associated routine `POLY_2D` can perform the warping transformation on an image array, however, it interpolates data, thereby not preserving the photon counts. A custom procedure, `RECTIFY`, that utilizes the transformation kernels was written to correct the spectra, this procedure also propagates mask values and errors to the new coordinate system. Figure 2.43 shows the before and after format of a single slice. The wavelength direction is sampled in 0.125 Å intervals for an unbinned device and 0.25 Å when the CCD is binned 2×2. The wavelength scale is encoded in the FITS header of the image as an air wavelength, according to the prescription given in Greisen et al. (2006).

2.3.6 Flat Fielding

The CWI data flat-fielding consists of two separate processes. The first uses a wavelength-realigned and curvature-corrected twilight or dome-flat spectrum to normalize the instrument efficiency as a function of wavelength and position on the IFU. A central slice is chosen as a reference, typically one for which a standard calibration star spectrum was registered during the night. The ratio of the intensity of the median-filtered continuum spectrum of that slice to all other slices is calculated for wavelengths at which these spectra overlap. As the spectral response is expected to be smooth, third degree polynomials are fit to the resulting slice ratios along the spectral dimension for each spatial pixel. This step yields a a transformation mask that when applied to a geometrically corrected spectrum normalizes the recorded flux to that of the reference spectrum.

The second step uses the spectrum of a standard spectral calibration star to obtain the absolute response of the instrument and atmosphere. The spectrum of this star can be splashed over several slice images. The fraction of the flux contained in each slice image is evaluated, and the CWI

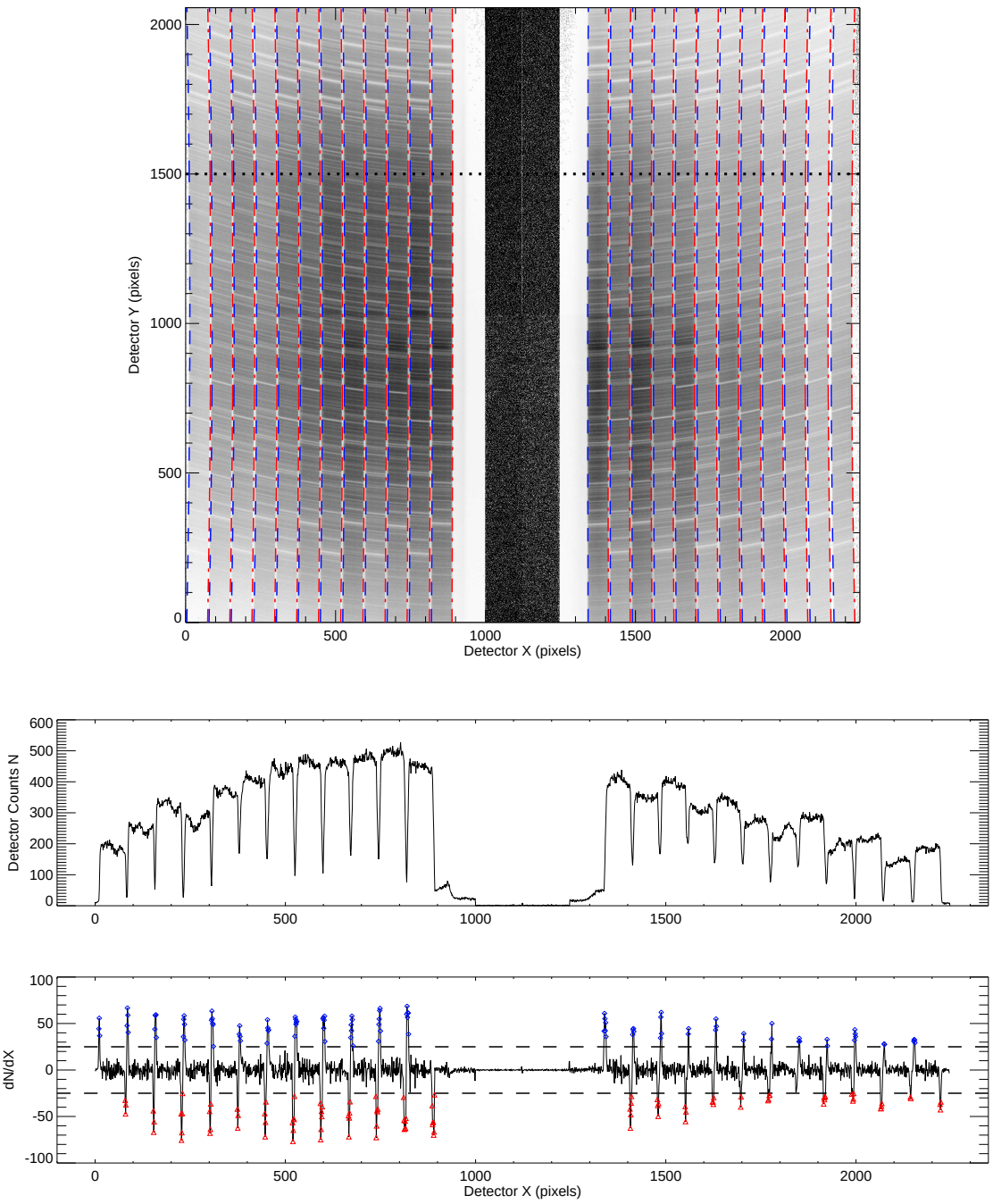

Figure 2.42. Edges of the individual slices are found by taking multiple cross sections through a CWI flat-field image, such as the twilight flat shown in the top panel. An example cross section is shown in the bottom panel. The top plot is the flux detected across the detector, the bottom plot shows its derivative. The locations of the edges are marked by the peaks in the derivative, the red triangles mark the peaks corresponding to right edges of the slices, the blue diamonds mark the left edges. This process is repeated for every 100th row in the flat-field image. The points are then fitted with second- or fourth-degree polynomials to generate a functional form for the edges. The results are shown as the blue dashed (left edges) and red dot-dashed (right edges) lines on the top panel.

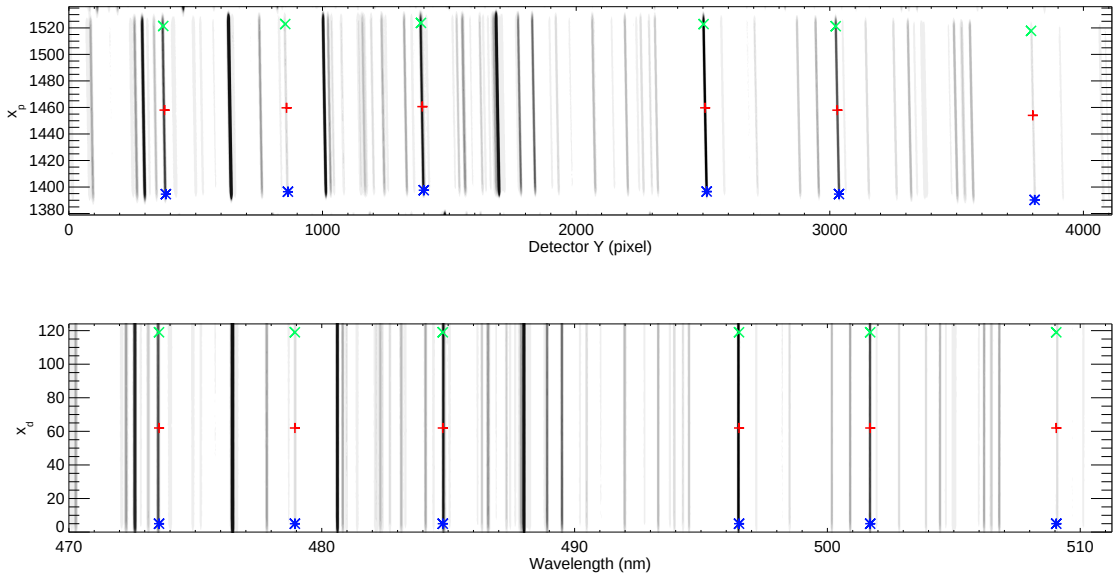

Figure 2.43. Part of the CWI spectrum straightening procedure. The top panel shows a curved spectrum of a single slice as imaged by the detector. The locations of the points used to calculate the transformation are indicated with green $\times$, red $+$, and blue $*$. The spectrum recovered using the warping function is shown in the bottom panel, with the anchoring points marked as in the top panel.

observed flux is compared with calibrated spectra of the star to obtain absolute response. This absolute response combined with the normalization obtained in the first step are used to generate an instrument response map for CWI, which is applied to the collecteddata. Figure 2.45 shows the spectrum of the reference star, and figure 2.44 shows the CWI instrument response map.

This process of flat-fielding factors out the full instrument response with the exception of pixel-to-pixel variation within the detector. This variation would best be removed using uniform illumination of the detector that is not segmented by the IFU or dispersed by the grating. At the time of writing such data is unavailable, thus the effect of pixel-to-pixel variation is taken into account as systematic error.

2.3.7 Spectral Resolution

The instrument spectral resolution has been constrained using the calibration system arc lamp in a flat-field configuration. The peaks in the ThAr spectra were identified and fitted with Gaussians. This yielded the values of their full width at half maximum (FWHM). These widths are a convolution of the natural peak widths, CWI optical performance, and the demagnified to 125 µm spectrograph slit. The measured values are clustered near 125 µm, indicating that CWI resolution is slit limited and that the instrument achieves its required spectral resolution. This measurement was conducted

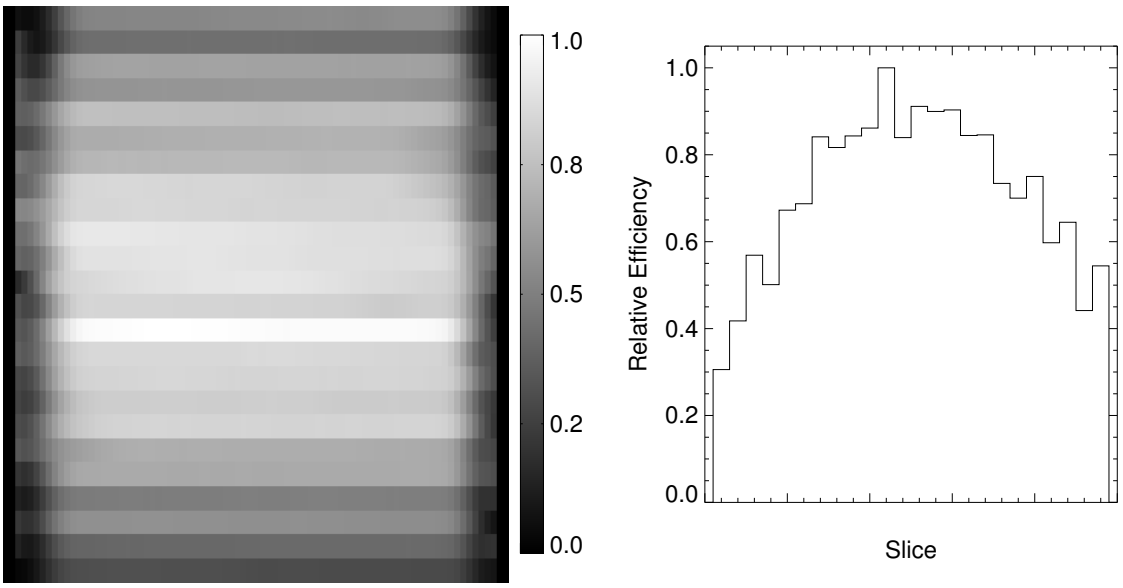

Figure 2.44. Demonstration of a relative flat-field image generated from a twilight flat recorded during the May 2011 observing run. The left image shows the relative intensity for a single wavelength bin (0.25 Å) scaled to the largest value. The right panel shows a cross section of the flat-field for the individual slices.

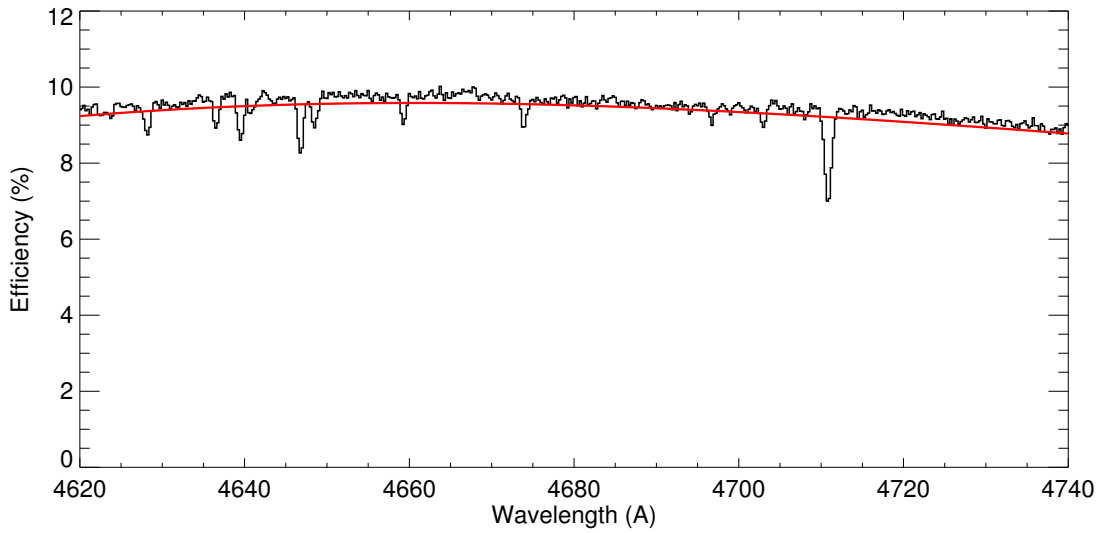

Figure 2.45. A measurement of the CWI efficiency using observation of an HST spectrophotometric standard, BD+33d2632 (Turnshek et al. 1990). The spectrum shows absorption lines characteristic of a B2IV star, including HeII 4713Å. The spectrum is blueshifted by ~ 100 km/s, which is consistent with observations (Greenstein & Sargent 1974). A third degree polynomial, shown by the solid red line, was fitted to the continuum.

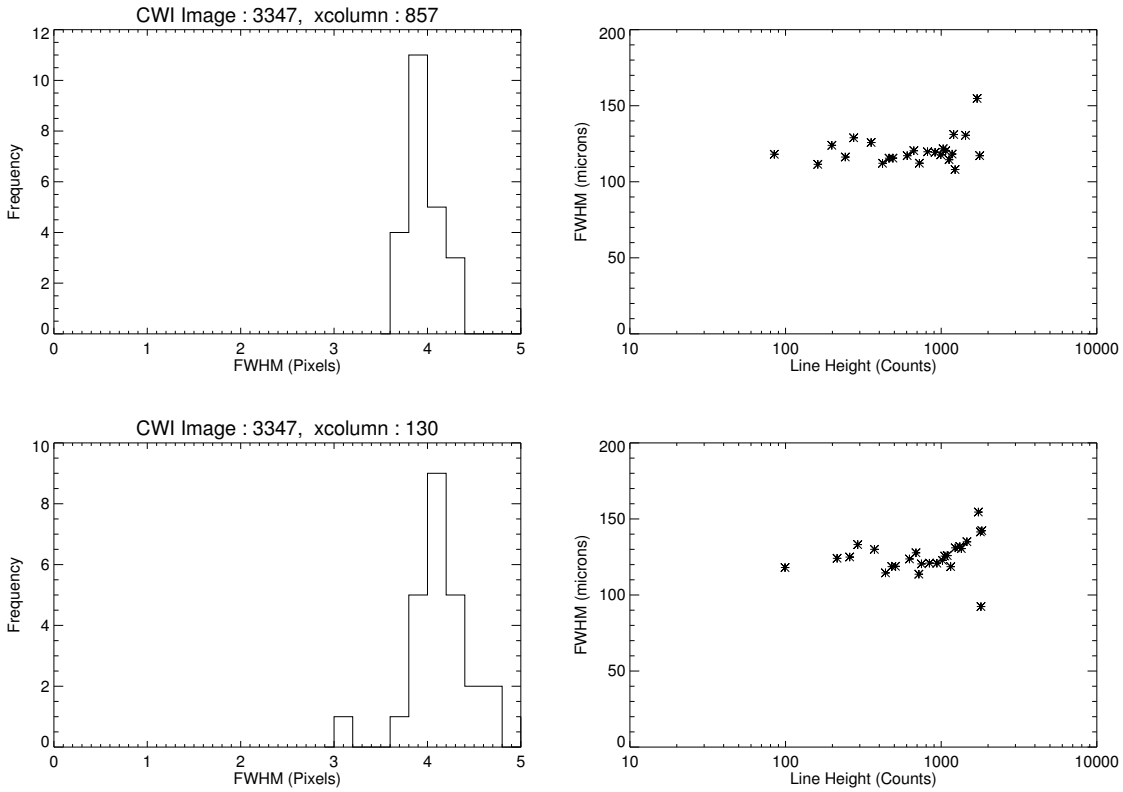

Figure 2.46. Measured FWHM of peaks present in the ThAr calibration spectra. The top two plots are for the spectrum taken from one of central IFU slices, the bottom two plots are for a slice lying closer to the edge of the IFU. The left panels give the distribution of the measured FWHM in pixels, while the right panels plot the FHWM vs. the height (in detector count DN) of the corresponding peaks. The data is taken from CWI image #3347, which was obtained during the October 2010 observing run. The CCD was binned 2×2, each resultant pixel being a 30 µm square. The spectral widths appear to be nearly equal for both slices.

near 4700 Å, where the linear dispersion is 8 Å/mm, implying $R \sim 4700$. Figure 2.46 shows the measured FHWM values.

2.3.8 Spatial Resolution

CWI spatial resolution is limited by the slit width in the direction parallel to the dispersion direction: it is set by the slice width (1 mm) and telescope plate scale (2.5 arcsec/mm). Spectral resolution along the slices is limited by atmospheric seeing and optical properties of the instrument, including the camera. Figure 2.47 shows the cross section through a spectrum of an observed calibration star. Its FWHM is ∼2 arcsec ≈ 6 pixels. This is consistent with the ray-trace modeled spot sizes with RMS radii ∼25 µm. The spectral direction is sampled by binned detector pixels, oversampling the PSF.

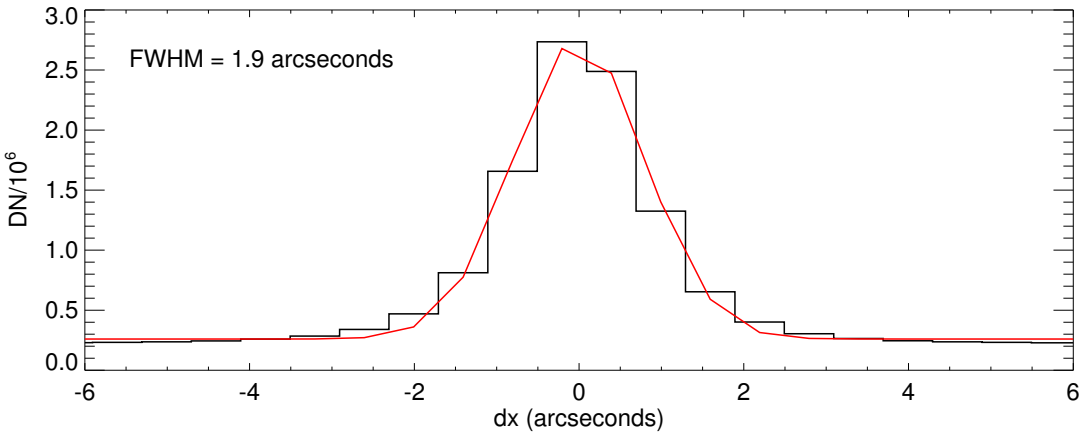

Figure 2.47. Observed PSF of a calibration star obtained in June 2011 (black histogram) and a Gaussian fit to the distribution (red line). The telescope seeing was approximately 1 arcsecond. The FWHM is 1.9 arcseconds. The broadened PSF is due to the convolution of the seeing disk with the instrument spot size. The latter is somewhat degraded due to the astigmatic nature of the CWI focus and the instrument having been focused to optimize the focus in the spectral direction, maximizing spectral resolution.

2.3.9 Data Cube Construction

Sky coordinate data is entered into the three-dimensional array generated using the procedures outline above. Telescope pointing information is inserted into image headers by the data reduction pipeline, in accordance with the world coordinate system standard for celestial coordinates (Calabretta & Greisen 2002). The data-cube pixels are $0.6\,\mathrm{arcsec} \times 2.5\,\mathrm{arcsec} \times 0.25\,\text{Å}$ when the detector is binned 2×2 and $0.3\,\mathrm{arcsec} \times 2.5\,\mathrm{arcsec} \times 0.125\,\text{Å}$ for an unbinned device. As of May 2011, the instrument has not used its field of view rotation capability; consequently, the coarser spatial sampling is in the declination direction, with finer sampling along the right ascension axis. Data from separate exposures is coadded. There is a slight amount of flexure that alters the wavelength solution, this is corrected for by using locations of airglow lines within the targeted fields. The corresponding variance arrays are added, while mask arrays are `OR`ed.

2.3.10 Observing Modes

CWI can operate in two principal detector configurations: full-chip and nod-and-shuffle. For observations aimed at faint and diffuse emission that extends at least the size of the IFU, both configurations require that a background field be selected in addition to the target field. The background needs to be near the target field, to curtail the impact of spatial sky-background variation and minimize telescope motion.

The full-chip configuration is a standard setup, where the entire surface of the CCD is exposed to light and is read out after a simple integration that is sufficiently long for the sky background residuals to become the dominant contributor to the noise. This constrains the frequency with which background sky spectra can be obtained, undersampling typical timescales on which the sky spectrum varies.

Nod-and-shuffle requires that two thirds of the detector be masked off, with only the central third uncovered, restricting the spectral bandpass to 1/3 of that available in full-chip observations. The three regions are parallel to the serial register of the CCD. Figure 2.48 outlines how this method operate, while Cuillandre et al. (1994) and Sembach & Tonry (1996) describe it in mode detail. Nod-and-shuffle observations allow for frequent switching between target and background fields, ensuring that any variation in sky-brightness level is well sampled. The penalty is a slight loss of observing time while the telescope pointing is changed and guide-stars reacquired. This process takes approximately 20 s, therefore, depending on the switching frequency, nod-and-shuffle can add as much as 15% overhead to the exposure time (i.e., a 20 min exposure on target interleaved with a 20 min exposure on sky, sampled in 2 min intervals will take approximately 48 min, including CCD readout).

2.4 Observing Cadence and Target Selection

2.4.1 Observing Procedure

CWI instrument documentation is in development by Patrick Morrissey, Shahinur Rahman, Chris Martin, Anna Moore, and the author. This section summarizes the some of the key activities and steps needed to allow for good quality data acquisition and accurate data reduction.

The majority of the following steps should be performed once the detector has been cooled to the nominal temperature. They are important ingredients in the data reduction pipeline, the observational strategies for scientific targets are discussed in the next section rather than here:

Obtain a median bias. It is crucial to have a high quality bias frame to subtract from the data. This requires a stack of (typically 10) zero exposure-time images. Inspection of the quality of the individual bias frames allows for the diagnosis of any additional undesirable detector noise in the system. This data also yields a measurement of the read noise of the detector. As taking a bias frame does not take long, it would be best to obtain this data before each night of observing.

Generate a photon transfer curve. Knowing the gain and read noise for each of the CCD read-out amplifiers is necessary to accurately convert the DN to photoelectron counts. Depending on the details of the images required for the computations involved, this step could take 30 to

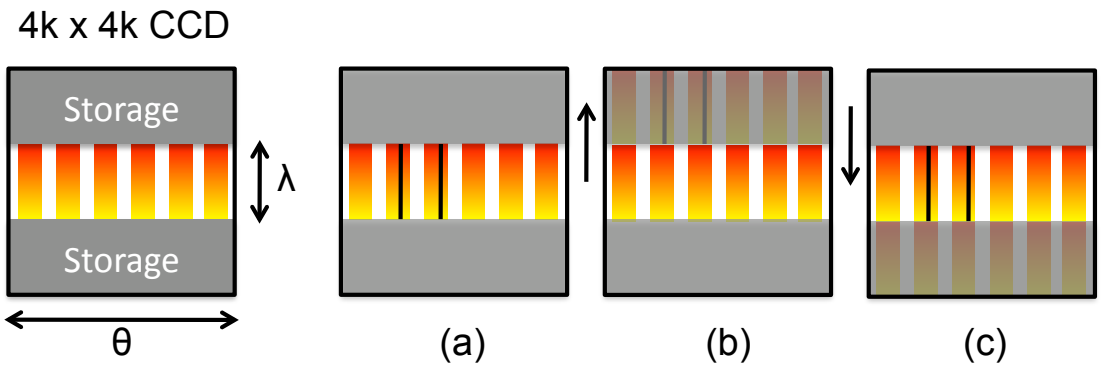

Figure 2.48. A schematic showing the nod-and-shuffle operational principle. The top and bottom thirds of the CCD are masked off. Observation start with pointing the telescope at the science target and recording a spectrum for a time t_{NS} (typically 2 to 4 minutes) (panel a). The camera shutter is then closed, and the CCD is then driven to shift the charge from the uncovered region of the device to the upper storage area. At the same time the telescope is pointed at a sky-background field. The shutter is reopened and an the central area of the CCD is exposed to a sky-spectrum for time t_{NS} (panel b). The shutter is once again closed, the charge on the CCD is shuffled hiding the sky spectrum in the lower part of the device, bringing the target spectrum back to the middle third. The telescope is returned to the original position and on-target integration resumes (panel c). After time t_{NS} this shutter is once again closed and the detector and telescope are reconfigured to the state in panel (b). Steps (b) and (c) are then cycled through until the total integration time on both target and sky are the required length for the observation to be sky-background limited (20 to 30 minutes for CWI). Different nod-and-shuffle cadences are possible, and CWI will explore these during future observing runs. One example that will be explored is a more symmetrical cadence that begins with a $t_{NS}/2$ background exposure, continues with an interleaving of n target and $n-1$ background, each length t_{NS}, ending with another $t_{NS}/2$ background pointing.

60 minutes. Collecting this data before each observing night would be best, but as the gains are unlikely to change very much from one night to the next, that frequency is not necessary.

Obtain calibration images and verify focus. Before the dome is opened for the night set of calibration images should be collected for each camera-grating orientation that will be used during the night. These include arc-lamp and continuum lamp flat-field exposures, and 100 μm pinhole image for both sources. The arc spectra should be inspected to make sure the spectrograph is focused on the slicer.

Collect dome flats. Dome flats should be taken before the dome opens for all camera-grating orientations that will be used during the night,

Take twilight flats. Twilight flats should be taken for all instrument configurations that will be used during the night.

Focus the guider. Near the end of twilight the position of the telescope secondary must be adjusted to focus the star images on the CWI guider camera.

Align and focus the instrument. The focus of the instrument is offset form the best guider focus. At the time of writing this offset in the location of the secondary is approximately 0.2 mm. A star (typically 5th to 9th magnitude) is then brought onto the slicer to verify pointing. If necessary, the pointing is adjusted to center the star on the IFU slicer.

Take data. Collect desired data, following the cadence appropriate to the signal level and observing mode being used (see section 2.3.10).

Periodically obtain calibration spectra throughout the night. To ensure proper flux calibration, spectral standard stars should be observed periodically throughout the night, at least once for each instrument setting. Ideally the spectra would be recorded in several images on a number of slices, but in the interest of maximizing time allotted to science observations a pair of images should suffice.

2.4.2 CWI Observing Runs

CWI has had a total of six observing runs which are listed below. The targets and volume of data collected are summarized in table 2.9, the details of the targets are discussed in further in the following sections.

July 2009. This was a 4 night commissioning engineering run. At that time CWI had not yet gotten the delivery of a science grade diffraction grating. A low efficiency optic was used instead. The FLI guider camera was also tested; although the hardware functionality was deemed acceptable, the amount of work needed to develop it as a permanent guider for the instrument was deemed unfeasible at that time. The time was used to align the instrument to the telescope, understand instrument focusing, identify locations that need to be baffled, and identify necessary changes and improvements.

November 2009. A 4 night observing run that was lost to particulate pollution in the air: ash following the 2009 Station fire. The dome opened for approximately four hours during which CWI observed LB QSO 301-0035.

March 2010. Of the three allotted nights the dome was opened for parts of two nights, for a total of 8 hours. The closures were due to humidity and clouds. The sky background appeared brighter during these observations. Objects targeted were QSO HS 1549+19, and parts of M82.

May 2010. Three nights of observation. The shutter on the Norris lens broke at the start of the first night and half of the dark time was lost to repairs. The dome was open for the rest of that and the following night; clouds forced it to close midway through the third night. QSO HS1549+19, M82, M11, and the Ring nebula were observed.

September 2010. CWI was on the telescope for two nights. Fog cut observations short on the first night, but the dome was open the full second night. $L\alpha$ Blob 2 from the SA22 field and NGC891 were targeted

October 2010. The instrument was installed for six nights, the first three of which were clear, the last three were lost to inclement weather. LB QSO 301-0035, Lα Blob 2, NGC1098, GAS3504, GAS4329, Stephan's Quintet were observed.

April 2011. CWI observed for three nights, the first third of the second night was lost to humidity and clouds. The nod-and-shuffle observing mode was utilized for the first time; some observing time was lost to debugging and refining the instrument, telescope, and guider control software involved. QSO HS 1549+19 was the primary target.

June 2011. CWI was alotted three nights. The first night was clear and spectrophotometric, while the second and third were marred by scattered clouds and overhead cirrus. The spectrograph targeted QSO HS 1549+19 on the first night and produced a tiling of M51 for the remaining two.

2.4.3 Observations of Lyman α Blob 2

Lyman α blob 2 (LAB2) is one of a pair of diffuse Lyα emitting clouds identified by Steidel et al. (2000) in an overdense field at $z \approx 3.09$, known as SSA22. Subsequent follow-up narrowband observations have led to the detection of close to 300 Lyα emitters down to the survey limiting sensitivities of 10^{-18} erg/s/cm^2/arcsec^2 (Hayashino et al. 2004; Matsuda et al. 2004, 2011). Subsequent observation have revealed an obscured AGN within LAB2 (Basu-Zych & Scharf 2004). CWI observed LAB2 in October 2010. The data set consists of ten 20 minute exposures on the LAB2 source at $\alpha_{2000} = 22^{\rm h}17^{\rm m}39^{\rm s}$, $\delta_{2000} = +00°13'27''$. interleaved with eleven 20 minute exposures on a nearby sky position with no known structures near at the redshift of interest $\alpha_{2000} = 22^{\rm h}17^{\rm m}32^{\rm s}$, $\delta_{2000} = +00°14'30''$. The data reveals that LAB2 likely lies at the intersection filamentary structures (see figure 2.49). The spectra of regions identified as the filaments show a bimodal distribution of emission with components shifted to the blue and red of the nominal location of the LAB2 peak. The blue and, to a smaller extent the red, components of the emission exhibit double peaked features characteristic of Lyα fluorescence observed in both components (although the structure may also be explained as radiation from nearby QSO SDSS J221736.54+001622.6 being reflected by the

Table 2.9. Listing of CWI targets observed during the first several observing runs, including target coordinates (J2000), total integration time on the target, and a note about additional data available. A discussion of the motivation behind observations of several of the targets and some preliminary results are discussed in the text.

Object Name	**RA J2000**	**Dec J2000**	**Exposure time (s)**	**Observation date(s)**	**Notes**
QSO LB 301-0035	03 03 41.08	-00 23 21.7	3600	Nov. 9, 2009, Oct. 3, 2010	There is matching 3600 s of background spectra from the same date. An additional 6000 s of lower quality data from the Nov. 2009 nights is also available. This has much higher background and higher detector read-noise contribution as the CCD was not binned at that time.
QSO HS 1549+10	15 51 52.4	19 11 04	14400	Mar. 9–10, 2010, May 14–16, 2010, Apr. 28–30, 2011	There is a matching 14400 s of background data and an additional 2400 s of target time from the March 2010 observing run that lacks background data.
Lyman α Blob 2	22 17 39	+00 13 30.1	16800	Sep. 8–9, 2010, Oct. 1–2, 2010	Matching background observations exist. The on target time obtained was 2400 s with clouds possibly afecting the observations, another 3600 s saw slighly elevated detector noise.
M82	9 55 **	69 ** **	7200	Mar. 10, 2010, May 15–16, 2010	There are 1800 s of sky background observatons. CWI targetted several regions of the galaxy, including the mid-north cone, the center, and the bridge.
M11	18 51 00	-6 16 00	300	May 14, 2010	Single exposure.
Ring Nebula	18 53 35.1	+33 01 45.03	660	May 14, 2010	Two exposures.
NGC 891	+2 22 **	+42 ** **	4200	Sep. 9, 2010	Several pointings within the galaxiy were obtained. Additionally, 1200 s of sky background were collected.
NGC 1098 (M77)	2 42 40.77	-0 0 47.8	2880	Oct. 1–2, 2010	Twenty-four 120s exposures.
GAS 3504	01 18 23.44	+13 37 28.4	1800	Oct. 2, 2010	Two exposures.
GAS 4329	01 58 16.23	14 17 47.9	1920	Oct. 2, 2010	Two exposures.
Stephan's Quintet	22 3* **	33 5* **	15300	Oct. 2, 2010	Seventeen pointings of 900 s each at various locations tiling the group.

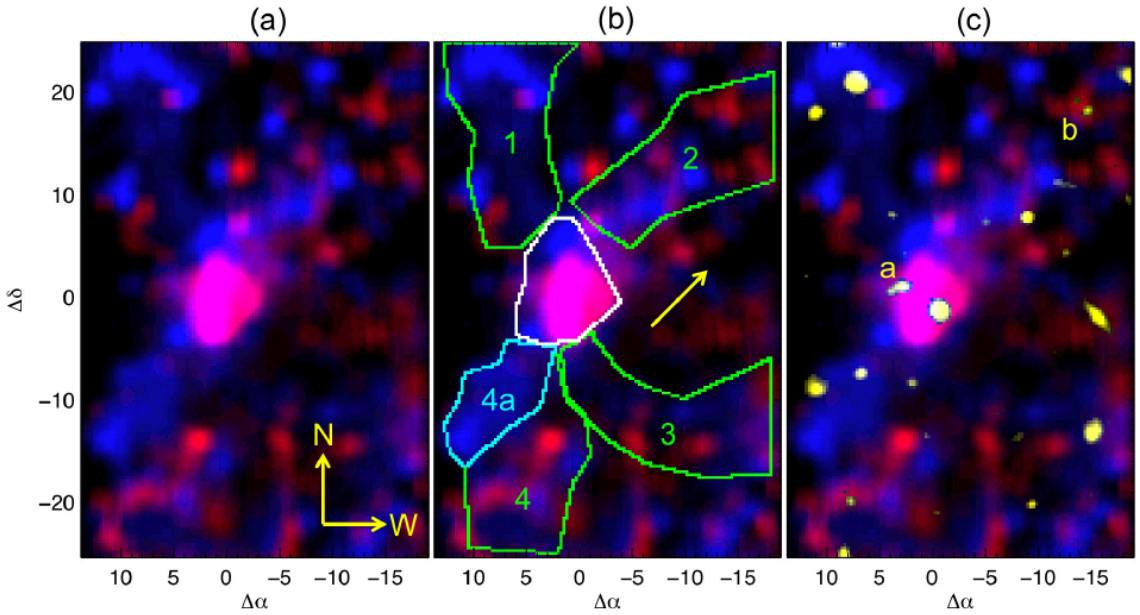

Figure 2.49. An overlay of two adaptively smoothed 8 Å slices through the LAB2 data cube. The color coding corresponds to the observed spectral shift with respect to LAB2. All three panels show the same image. Panel (a) serves as the reference, indicating the cardinal directions. Panel (b) identifies the filamentary regions that cross at LAB2, the yellow arrow identifying the direction of the angular momentum vector. The third panel overlays emission sources identified in the narrowband image collected by Steidel et al. (2000). Sources labeled with *a* and *b* are galaxies with spectroscopically confirmed redshifts that fall within the large scale structure surrounding LAB2.

illuminated gas). The gas is likely infalling along the filaments onto LAB2, and we may be witnessing an early stage of galaxy formation. The energy source of the emission is not certain; the glow may be due to the release of gravitational potential energy, or radiation from the enshrouded QSO that is being reprocessed b the gas. Both scenarios lead to an estimate of the total baryonic mass of few $\times\, 10^{11}\,\mathrm{M}_{\odot}$. The kinematics of the gas imply that if we are observing gas infalling onto LAB2, the deduced angular momentum approximately that of a $\sim 10^{12}\,\mathrm{M}_{\odot}$ halo, consistent with the baryonic mass estimate. The spectra of the filament regions identified in figure 2.49 are discussed in figure 2.50. The bimodality of the emission structure appears to also be observed in the bimodal galaxy redshift distribution of the sources near the LAB target region within SSA22. Details of the data reduction for this source, its analysis, and more detailed discussion of the results can be found in Martin et al. (2011).

2.4.4 Observations of QSO HS1549+1919

QSO HS1549+1919 is a $G_{\mathrm{AB}} = 17$, $z \approx 2.83$ quasar located at $\alpha_{2000} = 15^{\mathrm{h}}51^{\mathrm{m}}52^{\mathrm{s}}.4$, $\delta_{2000} = 19°11'04''$. This quasar has been used to investigate IGM metallicity (Simcoe et al. 2006), and

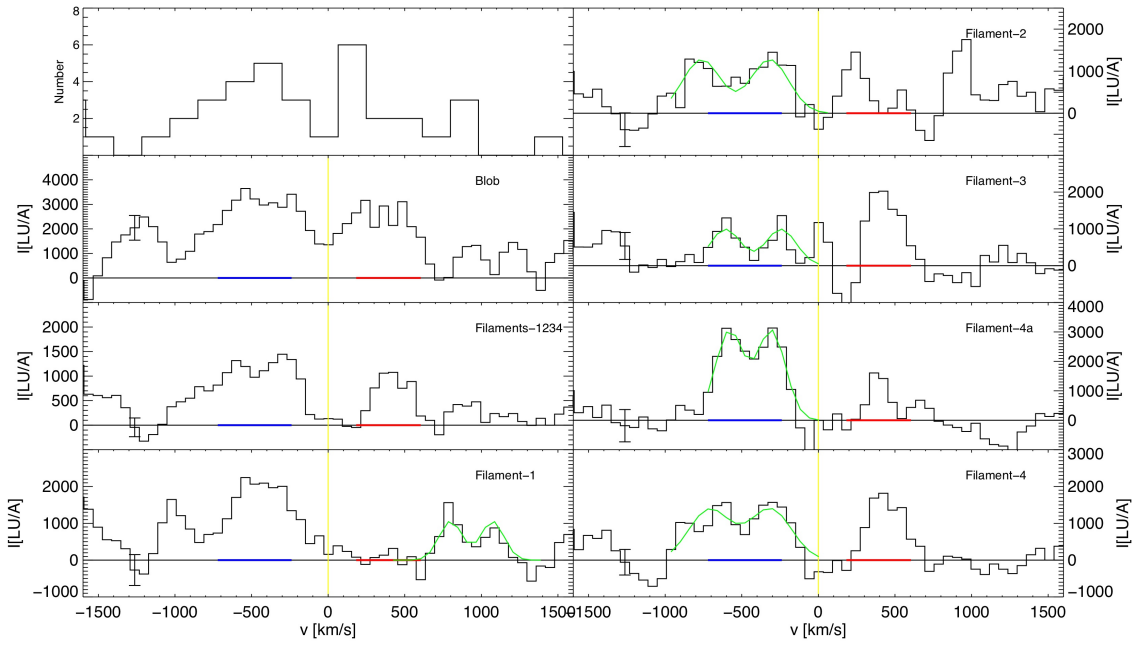

Figure 2.50. Spectra of the regions outined in figure 2.49. The top left panel shows the redshift distribution of galaxies in the SSA2 around LAB2; note the apparent bimodality in the distribution. The second panel on the left is the spectrum of LAB2, while the third is the sum of spectra of the four identified filaments. The remainder of plots are spectra of the individual filaments. The red and blue segments on the abscissa correspond to the parts of the spectra that were identified as the blue and red regions in figure 2.49. Light green curves show fits to the assumed double-peaked Lyα emission convolved with broadening due to gas dispersion (Gould & Weinberg 1996; Neufeld 1990)

has been interpreted as the illuminating source associated with Lyα fluorescence coincident with a DLA absorption feature in the spectrum of Q1549-D10, a $G_{\rm AB} \approx 23.7$, $z \approx 2.92$ QSO that lies 49 arcseconds from QSO HS1549+1919 (Adelberger et al. 2006). Narrowband imaging of this field shows an abundance of Lyα emitters near the redshift of QSO HS 1549+1919 (Steidel 2011). CWI observed this target and region around it in the spring 2010 and spring 2011 for a total of 9 hours, with a matching total for sky background fields. The observations tiled the CWI field of view around the quasar, including slight sub-slice-width dithering to sample the spatial distribution better than the 2.5" slit-width. A summary of pointings and targets is shown in table 2.10. Most of the data has been reduced and is being analyzed, preliminary maps exhibit filamentary-like structures linking more patch features observed in narrowband images. Figure 2.51 shows a comparison of a slice through a CWI data cube with narrowband and broadband images of the same area, including the likely filamentary region. CWI observations of this field are continuing; data obtained in 2011 has been taken in the newly implemented nod-and-shuffle configuration, and also benefited from a blocking filter upgrade and improved baffling as compared with the 2010 spectra.

Table 2.10. A summary of CWI observations of QSO HS 1549+1919. The pointing strategy during the 2011 campaign has been to tile an approximately 100" x 60" region with three CWI IFU configurations shifted in right ascension with respect to one another, while dithering in declination between exposures by a quarter of a slit. 2010 observations were mostly aimed at the central source quasar and performed in a full-chip configurations. 2011 data was taken utilizing the nod-and-shuffle technique.

Target	RA (J2000)	Dec (J2000)	Exposure Time	Notes
QSO A	15:51:52.4	19:11:04	23 ks	6 ks of this was taken in the N+S configuration in 2011; the rest in full-chip mode in 2010. The 2010 data has an elevated background level due to a source of scattered light that was eliminated for the 2011 campaign.
QSO E	15:51:54.3	19:11:03	9.6 ks	N+S configuration, 2011.
QSO W	15:51:50.8	19:11:03	6.6 ks	N+S configuration, 2011.
Sky A	15:51:49.6	19:10:49	3.6 ks	full-chip, possibly closer to the quasar than optimal, 2010.
Sky B	15:51:47.7	19:10;33	9.6 ks	full-chip configuration, also closer to the QSO than optimal, 2010.
Sky D	15:51:40.7	19:12:36.5	6.6 ks	4.6 ks in N+S. Used mostly with QSO W.
Sky E	15:52:6.3	19:12:35.2	11.8 ks	11.6 ks. Used in both modes, interleaved observations with QSO A and QSO E.

2.4.5 Non-IGM Observations

Although the primary goal of CWI is to observe the dim and diffuse intergalactic medium, and the environments that galaxies form and evolve in, the format and sensitivity of the instrument permit the study of other objects and phenomena.

2.4.5.1 The Ring Nebula

CWI observed the Ring Nebula (M57) for 10 minutes in May 2010. The resultant spectrum is shown in figure 2.52. The spectrum is generated by treating the entire integral field unit as a single spectrograph pixel. This approach allows for a much deeper, yet still moderately high resolution at $R \sim 5000$, spectrum to be obtained from a low aspect ratio object than what a typical long-slit spectrograph approach permits.

2.4.5.2 Cigar Galaxy

CWI observed the Cigar Galaxy (M82) on two separate occasions: once in March 2010 and once in May of the same year. The first pointing served to verify CWI performance, while the second

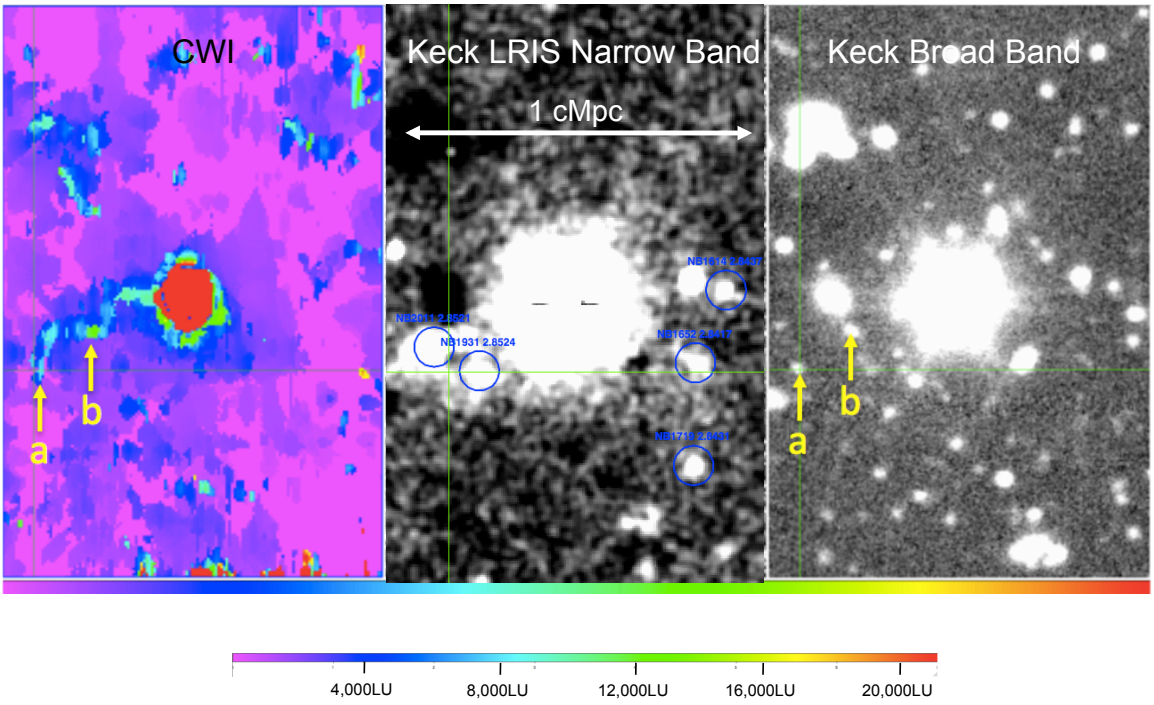

Figure 2.51. Comparison of the 1 Å wide $40 \times 60\,\mathrm{arcsec}^2$ CWI field of view centered on QSO HS 1549+1919 shows an apparent filamentary structure emanating toward the east, which seems consistent with Lyα emitting diffuse features observed in the narrowband and broadband images shown in the two panels to the right.

investigated the nature of the apparent superwind bubble observed with GALEX (Martin 2010). Figures 2.53 and 2.54 summarize the CWI observations.

2.5 Summary and Future Work

We have successfully designed, built, tested, commissioned, and now used the Cosmic Web Imager built for 200" Hale telescope at Mt. Palomar. The instrument is returning quality data and has been used to study galactic structure formation, quasar environments, galactic feedback effects.

Work on CWI needs to continue on two fronts: data reduction and analysis, and instrument upgrades and improvement. We have collected a substantial volume of scientific spectra and instrument calibration and characterization data. Methods building on existing algorithms from other branches of spectroscopy (classical, echelle, fiber-based IFU) are being adapted and new ones developed for use with CWI. Initial data analysis is encouraging, with several publications based on to-date observations expected within the next several months. The data serves as feedback to ongoing efforts to improve observing and targeting procedures and the instrument. Understanding of

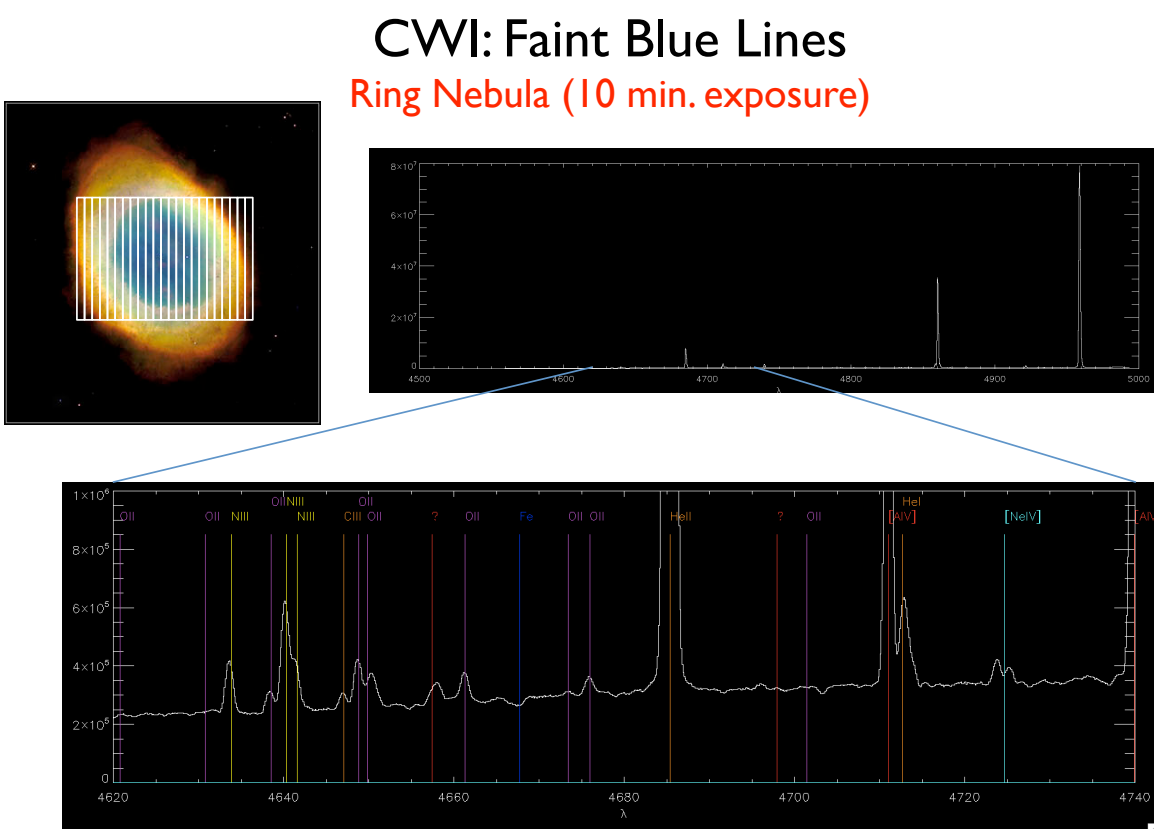

Figure 2.52. CWI The top left panel of the figure shows the IFU pointing superimposed on a Hubble postage stamp of the Ring Nebula, the top right plot shows the combined spectrum recorded within the entire field of view, the bottom plot a zoomed in version of the indicated wavelength range. The close spacing of the faint blue lines verifies the instrument spectral resolution, while the high signal-to-noise accentuates the instrument sensitivity. Image of the Ring Nebula courtesy of NASA, STSci, and AURA.

the characteristics of the Cosmic Web Imager are proving key in the design of the Keck telescope version of the instrument.

Augmentations to the instrument can, and should, be made. These changes fall in two categories. The first category improves the performance and facilitates the use of the existing instrument, this includes implementing flexure compensation using existing actuated mechanisms on folding mirrors; recoating optical elements to increase overall instrument efficiency; adding baffling to further reduce stray and scattered light; blackening and slightly altering the design of the nod-and-shuffle mask to reduce scatter at the CCD; adding a mechanism to insert and retract the nod-and-shuffle mask without the need for opening the detector dewar; building a dedicated guidance system; developing an instrument manual and set of observer tools (CWI is currently considered an expert instrument that requires users to be familiar with its details). The second category of changes adapts the instrument to expand its applications. These changes are: obtaining high resolution diffraction

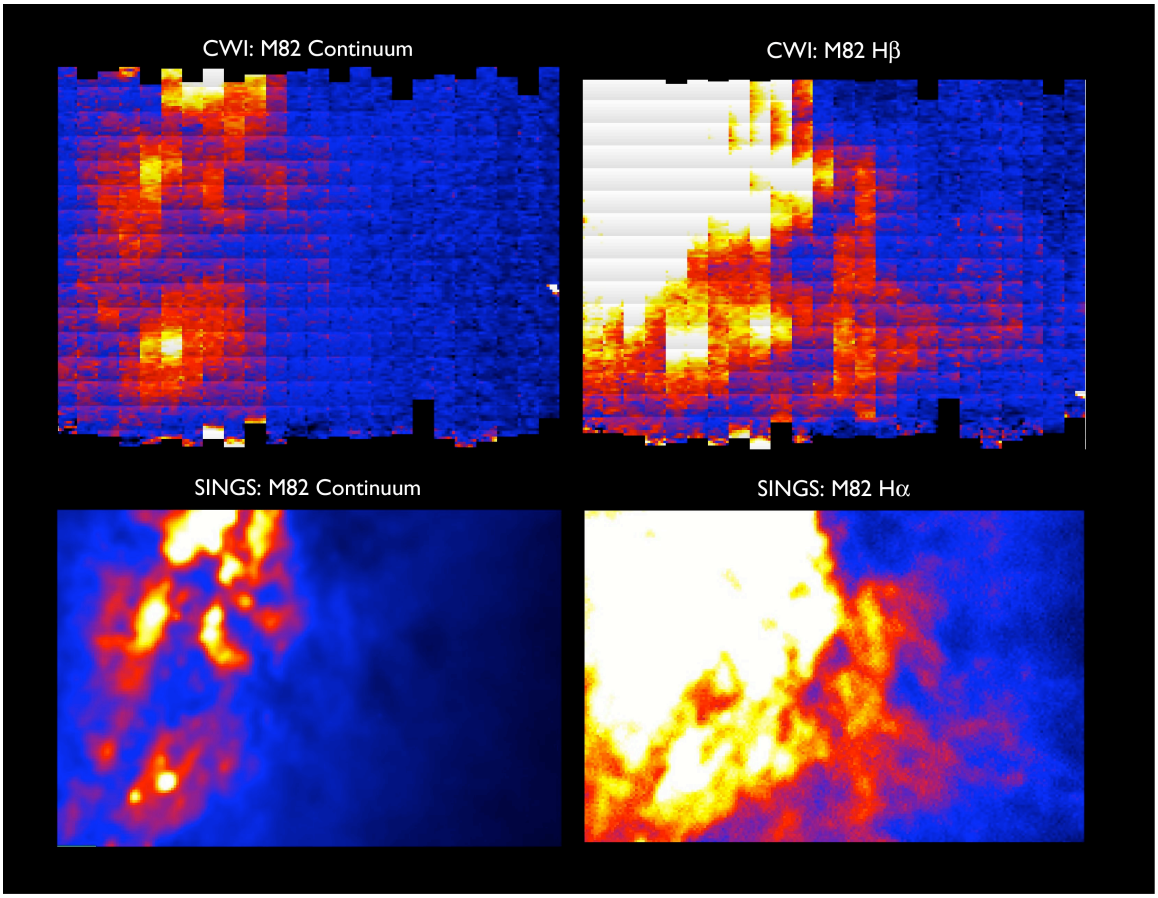

Figure 2.53. A comparison of the CWI observed M82 central region reconstructed with an early version of the CWI pipeline with the same area observed by the SINGS survey (Kennicutt et al. 2003). The morphological similarities are evident, demonstrating the integral field capability of CWI and reasonable spatial resolution.

gratings to cover the 380 to 900 nm wavelength range; adding a low resolution option; developing hardware to measure the diffraction efficiency of large VPH gratings.

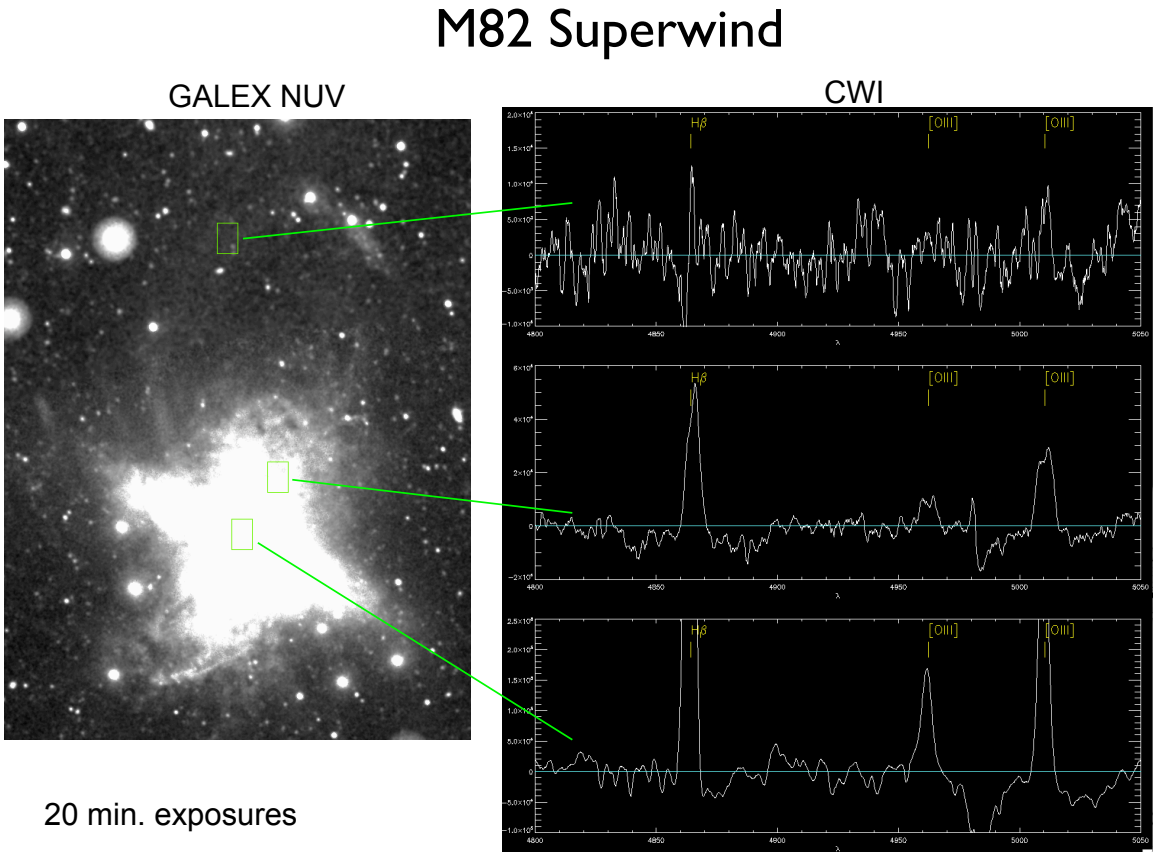

Figure 2.54. CWI was pointed at three regions within M82, one near the center, one near the middle of the North cone, and one within the discovered by GALEX superwind bubble. The locations of the pointings with respect to the galaxy are shown in the top left panel on a GALEX NUV image. A spectrum for each of the three locations is shown in the plots. The more central regions show prominent nebular line emission, while the pointing probing the edge of the bubble appears to show a P-cygni profile in the Hβ line; more observations are needed to confirm this spectral shape and to ascertain the morphology and kinematics of this source.

Chapter 3

FIREBall: The Faint Intergalactic Redshifted Emission Balloon

3.1 Introduction

The Faint Intergalactic Redshifted Emission Balloon (FIREBall) is a 1 m class balloon-borne ultraviolet telescope coupled to an integral field spectrograph (IFS). The instrument is the result of an international effort, bringing together scientists and engineers from Centre National d'Études Spatiales (CNES) and Laboratoire Astrophysique d'Marseille (LAM) in France, and Columbia University, California Institute of Technology, and the Columbia Scientific Balloon Facility (CSBF–NASA) in the United States. The scientific motivation for FIREBall is detailed in Chapter 1. Figure 3.1 captures some of the dependencies and thought processes behind the choices made during the design and construction of the instrument. The details of this schematic are discussed in this section.

The balloon platform is an excellent testbed of new astronomical technology, especially that intended for the far ultraviolet, as those wavelengths are not accessible from the ground. It is relatively low cost, offers reasonable turnaround times between flights, and gives unrestricted access to the instrument hardware until just prior to flight. This allows improvements and repairs to be made quickly and efficiently.

Scientific ballooning does have several drawbacks. Firstly, launches, especially for heavier payloads, are dependent on capricious weather. Secondly, flight times are short, though with the advent of long duration (LDB) and overpressure balloons, this is becoming less of a concern. Lastly, there is nonnegligible risk of significant damage to, or loss of, the instrument at launch or landing, as well as a chance of atmospheric winds pushing the balloon outside of the flight boundaries, forcing a premature termination and loss of scientific observations.

FIREBall has flown twice. The first launch was in July 2007 from Palestine, Texas. Although a key component of the telescope pointing system was irrecoverably damaged during take-off, the remainder of the subsystems performed nominally and allowed us to characterize the instrument,

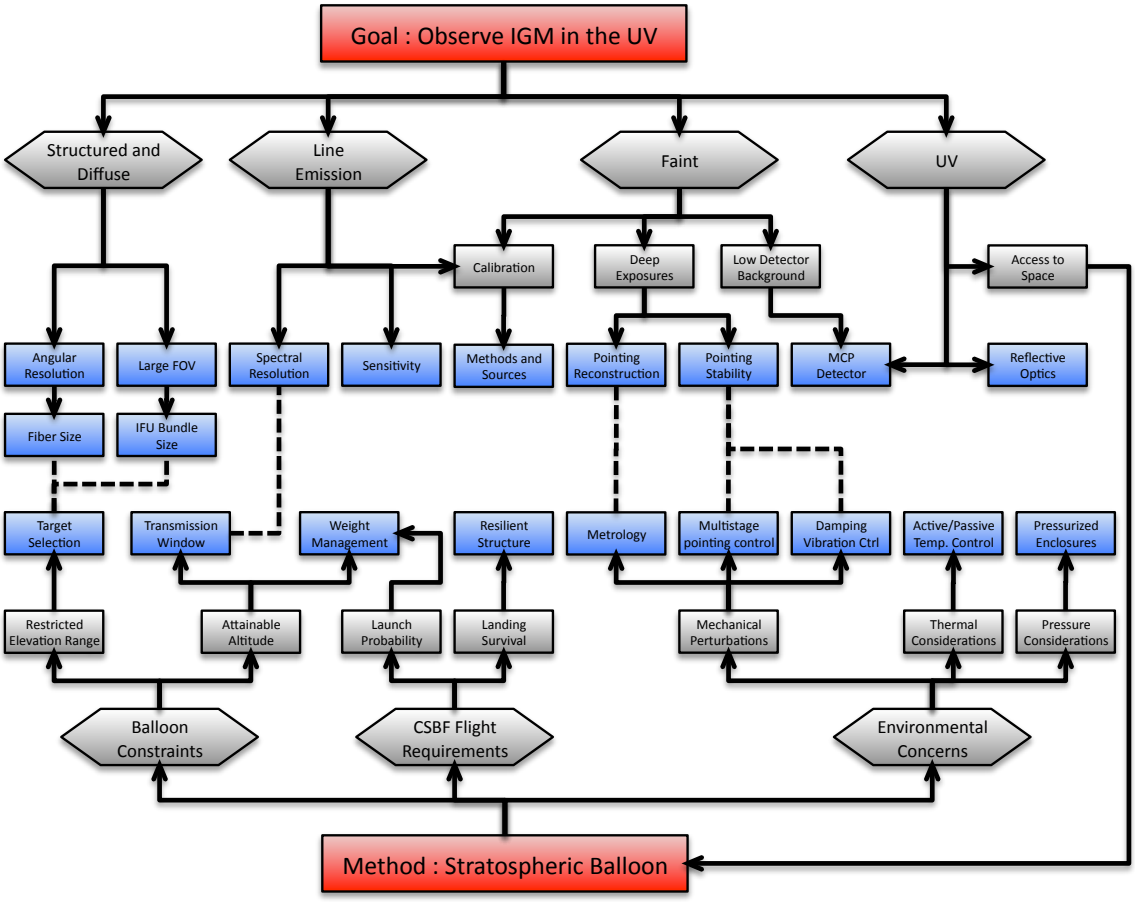

Figure 3.1. Some of the design drivers and considerations behind specific technology and functionality choices. Solid arrows indicate direct dependencies; dashed lines connect items that are corelated.

identifying necessary and desired improvements. The gondola was recovered, having suffered damage at landing to the structure frame and one of the large telescope mirrors. The equipment was refurbished for a second flight, and most of the modifications suggested by the first campaign were implemented. The first successful science observations took place in early June 2009 after a launch from Fort Sumner, New Mexico. The telescope observed three science and two calibration targets over six hours.

The project builds on a rich heritage of UV experiments, which is highlighted in the next section. The ideas, accomplishments, and results presented in this chapter are the fruits of the large, diverse collaboration. It is difficult to credit specific contributions to individual members, as many people were key to making the instrument work. With that in mind, the sections that follow detail the experiment design, requirements and choices made; discuss system integration, testing, and calibration; describe the second FIREBall flight, highlighting changes from the first campaign; and, finally, focus on the data reduction, analysis and results. Emphasis is placed on the areas where the author

Table 3.1. The key FIREBall design parameters, their values and the drivers responsible for them

Parameter	**Value**	**Rationale**
Telescope diameter	1.0 m (collecting area)	Required for faint emission regions
Telescope design	Actuated 1.2 m siderostat, Fixed 1 m f/2.5 parabola	Reducing aberrations using an on-axis parabolic design, pointing accomplished by actuated flat
Wavelength range	1985Å-2300Å	Accessible balloon window
Spectral resolution	$R \sim 5000$, 0.4Å	Maximize emission-line contrast over background, resolve kinematics, and resolve doublet lines
Field of view	3' diameter	Maximize cosmic volume viewed
Spatial resolution	10"	Separate emission from galaxies, other foreground objects
Sensitivity	30000 LU (direct), 3000 LU (statistical) in 6h observation	Sufficient to detect bright regions and constrain IGM emission
Pointing/Tracking	Control : 5" Knowledge: 3"	Efficient observation. Derived from spatial resolution requirement.
Altitude	$>$ 120 kft	Atmospheric throughput considerations
Flight time	$>$ 6 h dark time	Maximize exposure time

made significant contributions. The text outlines some of the changes that the author thinks should be implemented to improve the instrument performance, ease of use, and scientific return in future flights.

3.2 Instrument Design and Requirements

The FIREBall key instrument design features and flight requirements are summarized in table 3.1 and are further discussed in the sections below.

3.2.1 Atmospheric and Flight Constraints

The principal species responsible for the attenuation of ultraviolet wavelengths in the atmosphere are oxygen gas and ozone, with small contributions from nitrous dioxide, and additional loss due to Rayleigh scattering. FIREBall makes use of a narrow stratospheric far ultraviolet transmission window that coincides with a dip in the ozone absorption cross section and a falloff in the oxygen cross section; these features are shown in figure 3.4. The nature of this transmission window can be studied computationally. The 1976 US standard midlatitude summer atmosphere (Minzner et al. 1976) gives pressure and temperature as functions of altitude, as well as number density profiles of the relevant

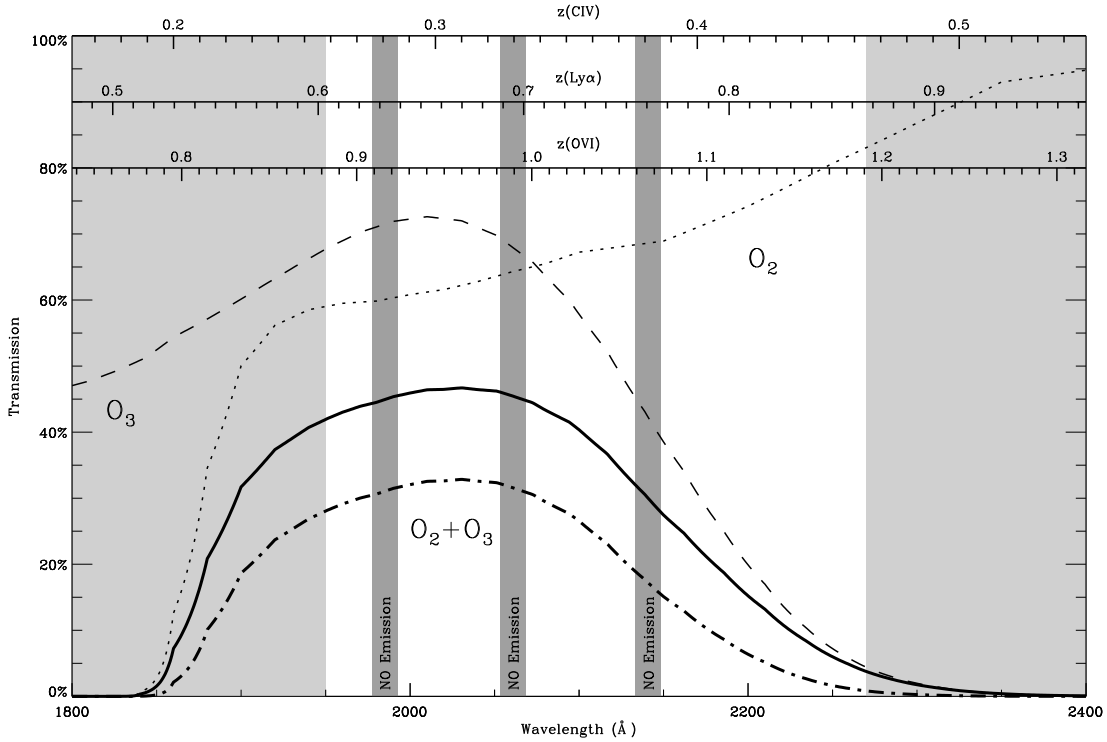

Figure 3.2. A computed atmospheric transmission curve for observations from an altitude of 34 km (112 kft, 7 mbar), roughly that for the second FIREBall flight. The calculation included absorption by O_2, N_2 and N_2O, and Rayleigh scattering effects. The solid curve shows the transmission for a target at the maximal elevation of the FIREBall telescope, 70°, the dot-dashed curve for the minimum, 40°. The dashed and dotted curves show the oxygen (O_2) and ozone contributions to the transmission losses. The light gray areas lie outside of the FIREBall bandpass; the narrow bands near the center correspond to three nitric oxide airglow bands. The accessible redshift ranges for the three principal FIREBall emission lines are overplotted on the axes near the top of the image. The accuracy of the curve and the assumptions made in generating it are discussed in Section 3.2.1.

species. The absorption cross sections were taken from literature: oxygen (Frederick & Mentall 1982), ozone (Molina & Molina 1986) and nitrous oxide (Hubrich & Stuhl 1980; Selwyn et al. 1977). The effect of Rayleigh scattering was approximated using expressions from Allen's Astrophysical Quantities (Cox 2000). The oxygen cross section used in the calculation is fairly featureless, though higher resolution measurements show multiple Schumann-Runge absorption bands at wavelengths shorter than 2050 Å. This choice was made to improve the clarity of the plots. Figures 3.2 and 3.3 present some of the results. It is worth noting the strong dependence of the transmission on both the altitude and telescope elevation. This is caused by the balloon being near the top of the atmospheric ozone layer, not quite fully above it. Relatively small changes in altitude have a large effect on the ozone column density being observed through. Consequently, the altitude achievable by the balloon is of key importance to the FIREBall science mission. Figure 3.5 shows four available

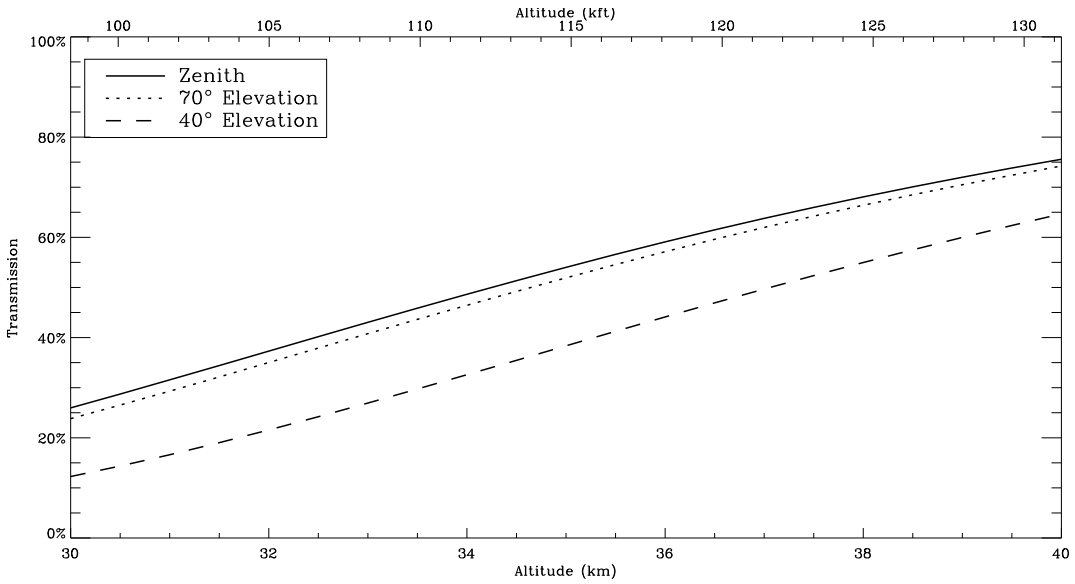

Figure 3.3. Change in atmospheric transmission as a function of observing altitude for three different astronomical target elevation angles: zenith (solid line), 70° (dotted line), and 40° (dashed line). FIREBall can only access regions of sky between the latter two angles. Note that a change in balloon altitude of 1000 m (3000 ft) changes the total transmission for a fixed target elevation by about 5%. This fairly steep dependence is due to the balloon float altitude being near the top edge of the ozone layer, where the O_3 density decreases quickly with increasing altitude.

CSBF balloon sizes that are capable of lifting a 6000 lb gondola (gross weight, including CSBF hardware and ballast). The maximum altitude shown in the graph is usually reached on initial ascent, and is maintained during daytime hours. The higher temperature forces some of the helium out of the zero-pressure balloon, making it droop at sunset. Most of the ballast must be used to keep the payload at a desirable altitude. In the case of the second FIREBall flight, the nighttime altitude was around 113 kft, which was several thousand feet lower than the scientifically desirable altitude.

3.2.2 The Gondola

A schematic of the gondola layout is shown in figure 3.6. The vessel was built by our collaborators at CNES. The structure stands at 5 m tall and 2 m on a side at the base. The space frame is made mostly of carbon fiber and epoxy tubes terminating at aluminum nodes. Some of the tubes have aluminum inserts to prevent length changes with temperature (as carbon fiber has a negative CTE and aluminum positive). The gondola floor is also made of carbon fiber. The frame is the support structure for all the subsystems and the optical bench for the instrument. It is built to protect the scientific hardware from mechanical shocks at launch and landing. The gondola is covered with an insulating thermal blanket —black on the inside, white on the outside—with the exception of one of

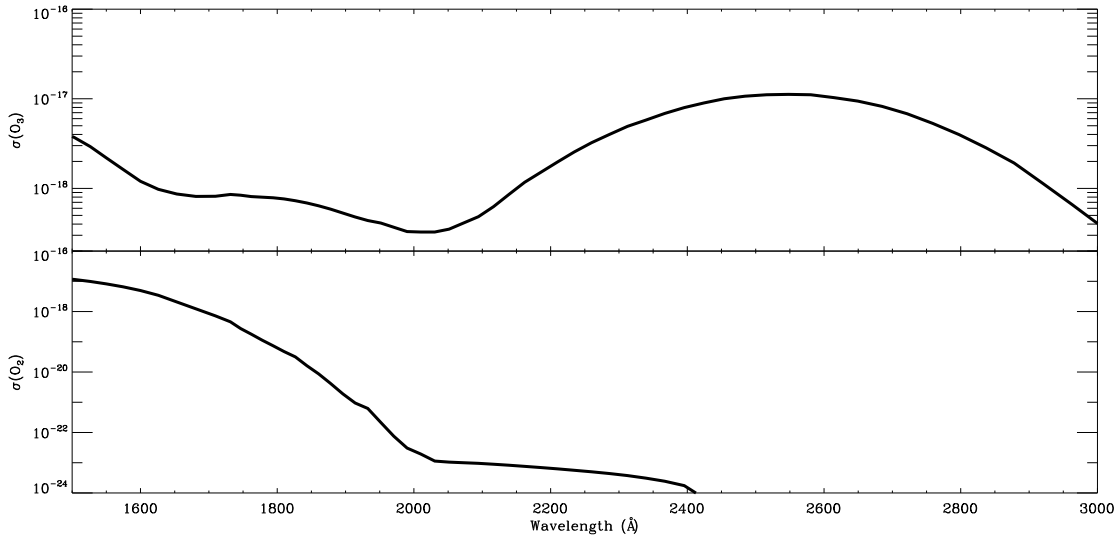

Figure 3.4. Oxygen (O_2) and ozone absorption cross sections. Data from Ackerman (1971). The far UV balloon window around 2000 Å is predominantly due to the slight ozone absorption cross section trough near that wavelength and the falloff in the oxygen cross section with increasing wavelength.

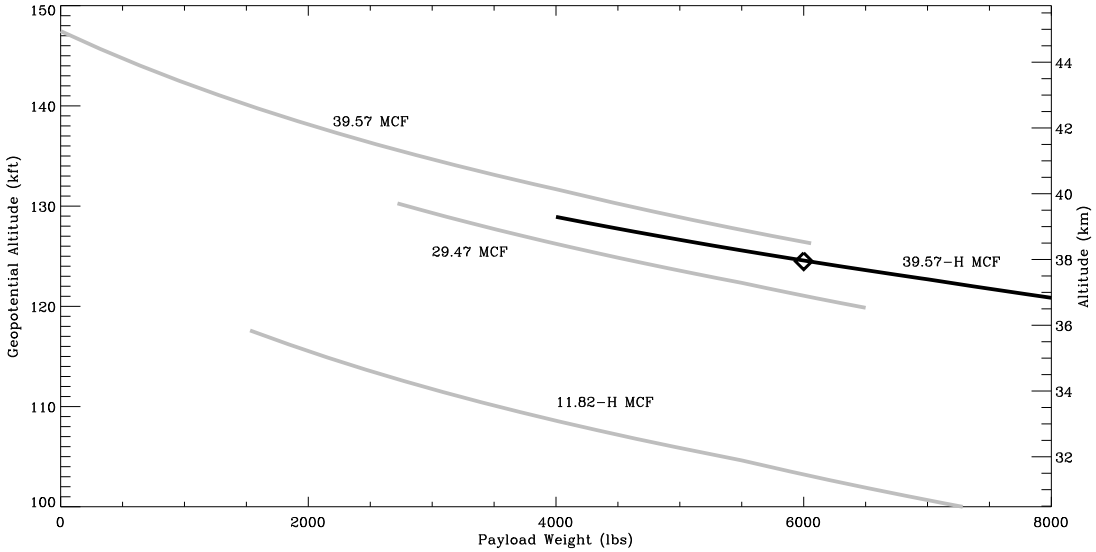

Figure 3.5. Calculated maximum balloon altitudes for four CSBF balloons capable of lifting the 6000 lb FIREBall gondola. The balloon markings represent their volume in millions of cubic feet. The values are based on the 1962 US standard atmosphere. Data courtesy of the CSBF.

the four sides, which was given a reflective Mylar cover. As FIREBall is launched in the morning, this feature was added to reflect solar radiation from the instrument, preventing significant undesirable daytime heating.

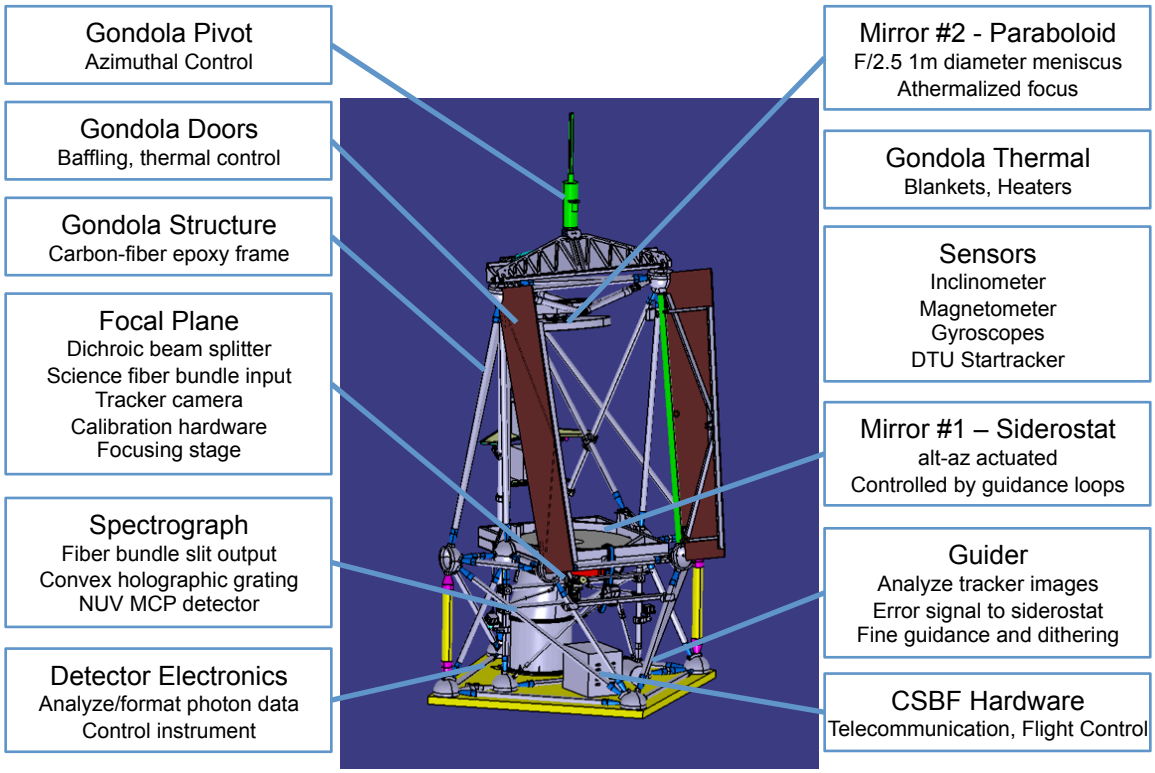

Figure 3.6. The layout of the FIREBall gondola with the instrument subsystems indicated. A few of their features are also highlighted. See further discussion in section 3.2.2.

3.2.3 The Telescope

3.2.3.1 Telescope Optical Design

The FIREBall telescope is an alt-azimuth mount modified prime focus instrument. It consists of a 1.2 m diameter flat mirror mounted on a gimballed frame and a fixed 1 m diameter 2.5 m focal length paraboloid, which serves as the aperture stop for the system. A ZEMAX ray trace of the telescope is shown in figure 3.7. The flat mirror functions as a siderostat: its tip-tilt stage and the gondola pivot orient the mirror to deflect the beam from the target region of the sky onto the paraboloid mirror. The entire visible sky is not accessible to the FIREBall telescope, however. There is a mechanical limit constraining the instrument to observing above 40° elevation; although unfortunate, this is not a large concern for FIREBall, as the UV throughput of the atmosphere decreases quickly at gondola altitudes with decreasing elevation (see figure 3.3). The view is also restricted by the balloon, which expands to close to 130 m in diameter at float altitudes. Given the length of the balloon train (90 m) the maximum available elevation is about 70°. The siderostat mirror is slightly larger than the paraboloid to ensure that the latter is filled regardless of the elevation being observed. The field of view of the telescope is limited by comatic aberrations associated with the paraboloid mirror. In the case of FIREBall, the image of a point source needs to be smaller than the size of an individual fiber

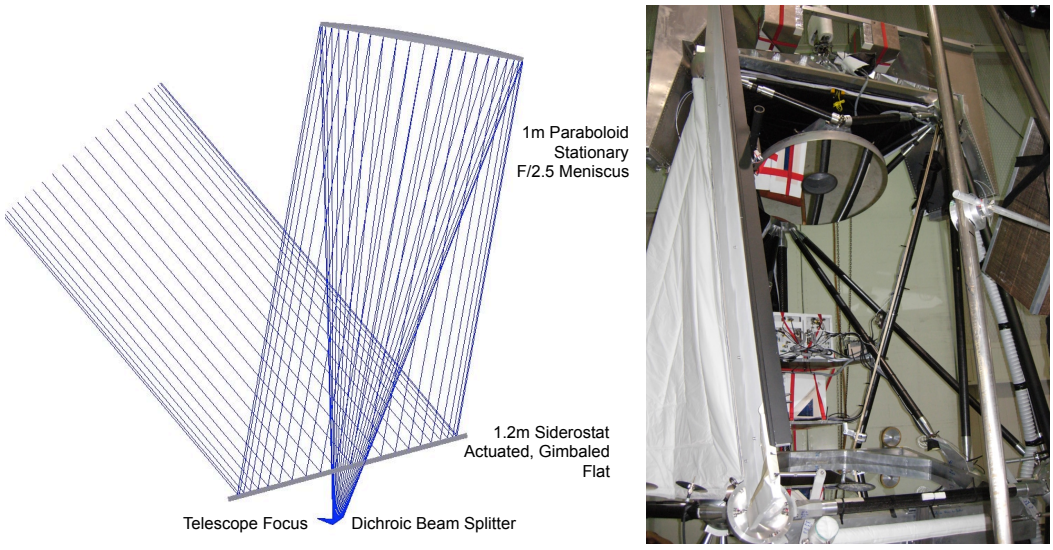

Figure 3.7. A ZEMAX ray trace of the FIREBall telescope (left panel). Light enters from the top left, reflects off the flat siderostat mirror and is then focused by the paraboloid. The right panel shows a photograph of the assembled hardware.

in the integral field unit (IFU) bundle (100 μm; see section 3.2.6 for the details of the spectrograph and IFU design). Following the discussion in Schroeder (1987), this implies that the usable fraction of the telescope focal plane is a 20 mm diameter disk (27 arcmin). Unless the imaging requirements are relaxed, any future mission that will need to make use of a larger field of view, or require finer spatial resolution, will need a field corrector. The siderostat's actuated gimballed mount also serves as the mechanism that stabilizes the telescope pointing in the rough stratospheric balloon environment (FIREBall pointing is discussed in more detail in section 3.4).

In addition to the standard astronomical observing configuration, the telescope can be commanded to an autocollimation arrangement. In this mode, the siderostat is tilted so that the axes of both large mirrors nearly coincide. Light sources from the focal plane of the telescope are projected off the paraboloid, reflected off the siderostat back onto the paraboloid, and refocused back onto the focal plane. This configuration is used for optical alignment and spectrograph calibration.

The FIREBall telescope mirrors are made of Corning ultralow expansion (ULE 7972) glass. The material was chosen for its thermal characteristics to reduce the chance of the mirrors' fracturing due to temperature changes affecting the gondola during a flight. The mirrors are unusually thin for their size, at 3", yielding a diameter to thickness ratio of ∼16. This was necessary to keep the weight of the gondola low. Heavier mirrors would require heavier mounts, increasing the overall mass of the balloon payload, resulting in a negative impact on the maximum attainable altitude (see section 3.2.1). Additionally, decreasing the weight of the glass reduces the risk of damage to the optics at landing. The blanks were figured by Optical Mechanics of Iowa, and given an Al coating

with a MgF_2 overcoat at Goddard Space Flight Center. The coating layer thicknesses were optimized for the balloon window bandpass around 2005 Å. Measurements indicated reflectance ∼90% for the large optics prior to both FIREBall flights.

3.2.3.2 Telescope Optics Mount

The mounts for the primary and siderostat mirrors were designed at LAM. The details of this design can be found in Rossin et al. (2008). Figure 3.9 shows a cross section through the mount of the paraboloid. The mount has been built to hold the optic firmly in place, unlike ground-based telescopes where the mirrors are held gently, as they do not have to withstand substantial motion and shocks during operation. A modified whiffletree design supports the optic at 18 points on the rear surface of the mirror. The mounting loci are Invar pads that are bonded to the glass with a 100 µm layer of 3M 2216 epoxy. Each pad has connected to it a titanium flexure monopod. These are grouped in nine pairs, three pairs supporting an intermediate mounting box. The axes of every pair of monopods intersect at the center of mass plane of the mirror; this arrangement imitates holding the glass at 9 points in that plane. Handling the glass by a structure attached in this way generates no additional torques on the mirror. Each box has attached to it a pair of larger monopods that connect it to an aluminum backing frame. The extensions of these monopods would intersect at the center of mass plane of the glass, smaller monopods and three boxes. The mounting frame is attached to the gondola structure. For the siderostat mirror, this frame is part of the gimballed table. The siderostat is installed to mechanical tolerances, and the tip-tilt mechanism is used to fine tune the mirror orientation. The paraboloid backing frame attaches to the gondola structure via six carbon fiber tubes with a differential screw at the end of each. The location and angle of the paraboloid mirror can be adjusted slightly from the nominal position by changing the lengths of these six struts. Initially the mirror is installed to within mechanical tolerance for precalculated strut lengths. It is then adjusted as needed to align the telescope. A CAD model of the paraboloid mount is shown in figure 3.8. Modal analysis of the mirror mounts shows that all normal modes of the structure have frequencies higher than 17 Hz and lie outside the bandpass of the gondola pointing loop (see section 3.4). The mounts performed to specifications during both flights. There was a noticeable disshape of the gondola and change in location of the paraboloid axis between the gondola resting on the ground and being suspended by the pivot. The mounting of the paraboloid mirror failed at the end of the first flight. The glass broke loose from its supports, but was restrained by a set of Kevlar safety ropes. There was damage to the rear surface of the optic. The mirror was repaired and recoated for the second flight. There was no damage to the telescope optics after the second flight, likely due to the introduction of a rip-cord parachute by CSBF, and to what appears to have been a softer landing than after the first flight.

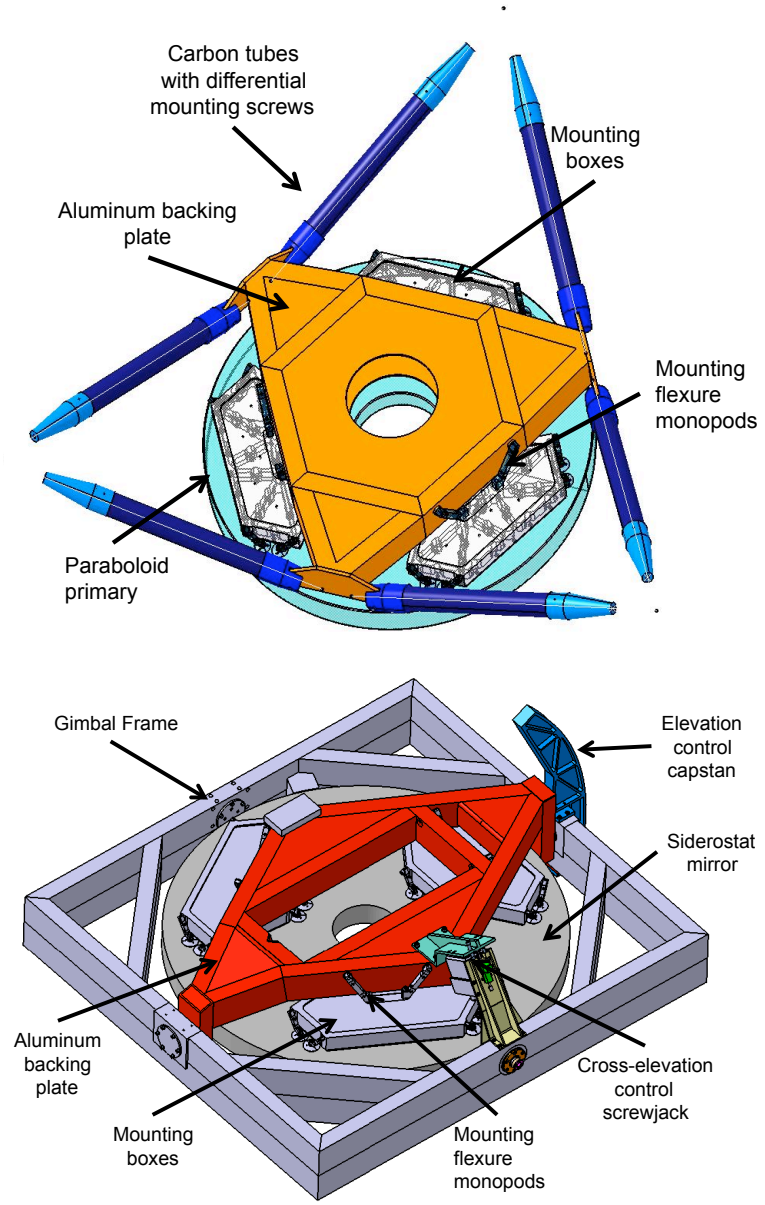

Figure 3.8. CAD renditions of the mounted paraboloid (top) and siderostat (bottom). The paraboloid is attached to the gondola by six differential screws that allow for the adjustment of the optic with respect to the gondola frame; these are at the end of each of the six protruding struts. The bars of the gondola that connect the focal plane to the primary have been specially designed with metal inserts to athermalize the distance between the two. The bottom panel shows the siderostat mirror in the gimballed frame. The capstan that guides the motion in the elevation direction is seen in the top right part of the image; the cross-elevation motor is shown near the center. Mirror surfaces are pointing down in both drawings. Figures courtesy of C. Rossin.

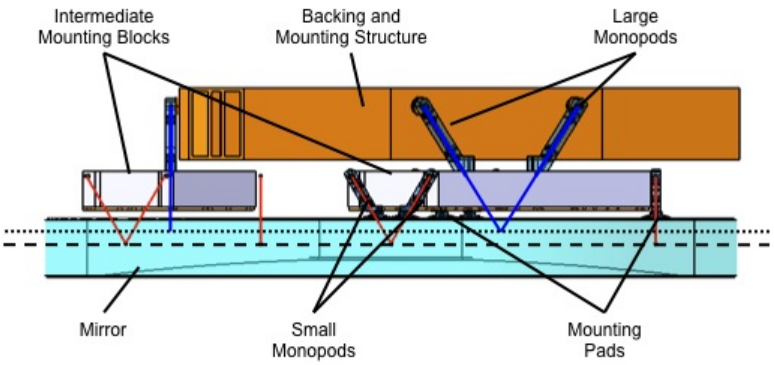

Figure 3.9. A cross section through the paraboloid mirror mount. The small monopods are installed so that their extensions intersect at the center of gravity of the paraboloid (dashed plane); the larger monopods would intersect at the combined center of gravity of the paraboloid, the boxes and the small monopods (dotted plane). Figure courtesy of C. Rossin.

3.2.3.3 Telescope Optical Alignment

The focal plane and paraboloid alignment procedure was designed and performed by Robert Grange, Bruno Milliard, and Marina Ellouzi from LAM, with Ryan McLean and the author from Caltech. The optical alignment is executed with the telescope in the autocollimation position (see section 3.2.3). The paraboloid is installed with mechanical tolerances bringing its axis close to the designated focal plane location. The gondola is suspended for this procedure, as the shape of the structure deforms when it is lifted, which is the flight configuration.

The first step is to focus the instrument. This is done by inserting a 35 micron pinhole in the IFU bundle location and doing a standard through focus analysis, as described in section 3.2.3.4.

The second step uses optical aberrations native to the telescope to locate the intersection of the optical axis of the paraboloid with the instrument focal plane, and to adjust the focal plane hardware to move that axis onto the IFU bundle. In the autocollimation configuration, light emanating from an object in the focal plane bounces off the paraboloid twice and is then reimaged at the focal plane. The focal plane is viewed by the focal plane camera (see 3.2.4.5). The compound angle of the siderostat mirror can be adjusted to move the return image of any of the focal plane sources anywhere within the focal plane. When this image is placed at the location diametrically opposite to the object with respect to the intersection of the focal plane with the paraboloid axis, all aberrations, up to and including third order, vanish. The resultant image appears perfect. Furthermore, any shift in the location of the image results in the appearance of comatic aberration, with the characteristic coma arrow pointing toward the location of the perfect image. The size of the aberration grows with the distance from the ideal spot location. ZEMAX ray trace modelling for the procedure arrangement is shown in figure 3.11. For this alignment, the flight dichroic beam splitter was replaced with a half-silvered mirror. This change improves the level of the signal in the return image that is detectable by

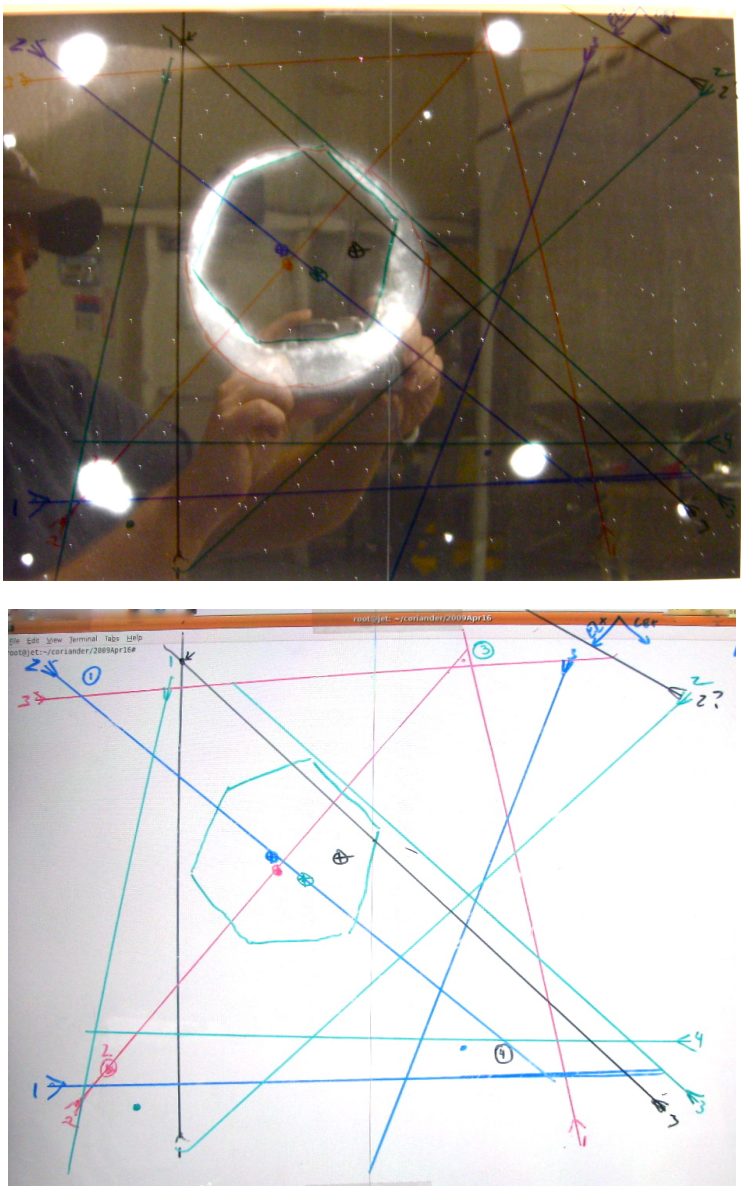

Figure 3.10. Two images of the last in a series of alignment steps used to place the IFU at the paraboloid axis. The markings for the four pinholes have been color coded. The locations of the pinholes are marked with encircled numbers (except the one at the bottom left where the number is next to the circle). The image locations, and coma arrow directions at those locations, are indicated with chevrons which are then extended as lines. The expected locations for the unaberrated images have been marked with dots, and the corresponding axes locations with crossed circles. Notice that they all fall within the IFU fiber bundle. As the diameter of the bundle is under 3 mm, this amount of accuracy is sufficient to have adequate image quality across the full spectrograph field of view.

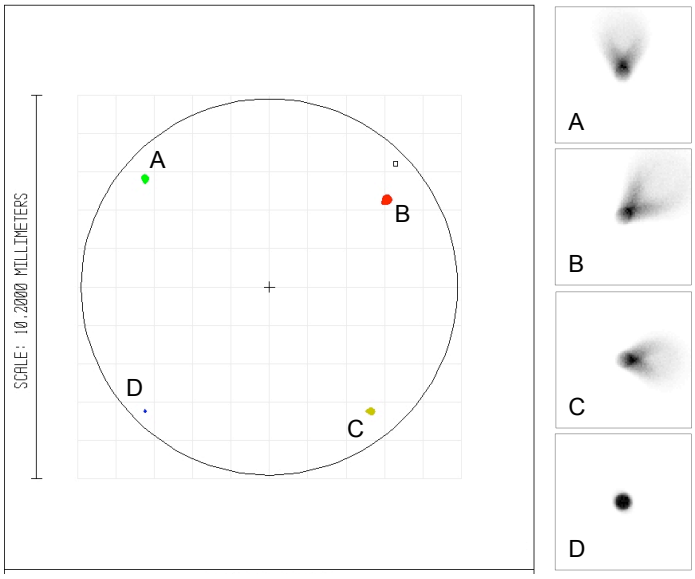

Figure 3.11. A ZEMAX ray trace modelling how aberrations are used to locate the paraboloid axis on the focal plane. The location of the paraboloid axis is marked with crosshairs near the center of the left panel. The position of the illuminating 50 µm pinhole is shown with a box near the top right of that panel. The large circle is approximately the size of the field of view of the focal plane imaging camera. Return images of the pinhole are shown at four locations, labeled A-D. The four panels on the right show zoomed views of the four images. The boxes are 400 microns on a side, and the pixel size corresponds to that of the focal plane imaging camera. Note that the perfect pinhole image is diametrically opposed to the pinhole location with respect to the paraboloid axis, and the characteristic coma arrows point at the location of the perfect return image.

the focal plane imaging camera by roughly a factor of 100, as the focal plane light sources undergo only reflections off that optic. The images of the five focal plane pinholes surrounding the IFU bundle are moved around within the field of view of the focal plane camera. They are scrutinized, and the coma directions are noted on a transparency overlaid on a monitor. Once several — typically three — remote image locations have been studied for a given pinhole, the point where the perfect image is expected is marked. It is taken to be the center of the region where the coma delineating lines intersect. The midpoint between the location of this perfect image and the pinhole is marked as a data point in locating the paraboloid axis. Once this procedure has been completed for at least three of the pinholes, the corresponding axis positions are evaluated. They were typically closely spaced. The focal plane is then shifted so that the fiber IFU bundle is moved onto the measured paraboloid axis position. Figure 3.10 shows the last overlay created before the 2009 FIREBall flight. The paraboloid axis lies on the IFU fiber bundle, and the dominant comatic aberrations are under 20 microns, much smaller than the size of a fiber over the full science bundle.

3.2.3.4 Telescope Focusing

Telescope focusing is performed preflight and in-flight. The basic focusing procedure relies on the confocality of the guider camera and the UV focal plane (section 3.2.4.6). The gondola is in-flight or suspended above ground in the hangar. The light source is a natural star or an artificial one (section 3.3.2.1). The focusing stage (section 3.2.4.3) is lowered until the spot visible on the guider is clearly out of focus. A series of images is taken as the stage is moved up in steps. The size of the image of the star is measured by the guider computer, and the spot size, as a function of focus stage position, is plotted. The data is fitted with a quadratic, the minimum of which determines the location of best focus. The stage is then brought down below this point and shifted upward to remove any mechanical backlash. Preflight focusing can also be performed using the focal plane imaging camera (section 3.2.4.5) with the telescope in the autocollimation configuration. A suitable return spot from a pinhole on the focal plane pinhole mask is chosen, and the focusing stage is moved as in the other method. The camera images are then studied to minimize the return spot size.

3.2.4 The Focal Plane

3.2.4.1 The Focal Plane Overview

For FIREBall the term "Focal Plane" refers to the subsystem that includes the actual focal plane of the telescope, IFU fiber bundle mounting hardware, the guider camera, several illumination sources, the dichroic beam splitter, and the focusing stage. A labeled schematic of the focal plane is shown in figure 3.12.

3.2.4.2 Dichroic Beam-Splitter

The science beam is separated from the remainder of the light by the dichroic beam splitter. This rectangular ($110 \times 80\,\mathrm{mm}^2$, 5 mm thick) optic is made of BK7 optical glass. The normal to the front surface of the dichroic is designed to be at a 35° angle to the axis of the paraboloid. The UV reflective coating was deposited at Cascade Optical by Muamer Zukic, and its characteristics are shown in figure 3.13. The dichroic substrate has an 0.2° wedge to eliminate coma in the beam transmitted toward the guider camera, which is the consequence of a tilted optic in a quickly converging beam. Four leaf springs press the glass against a milled-out aluminum pocket that is lined with a single layer of Kapton tape to isolate and cushion the optic from the metal.

3.2.4.3 Focusing Stage

The IFU fiber bundle attachment block, dichroic, and guider camera are mounted on a linear actuator that moves them along the paraboloid axis. The stage is a Danaher Motion DS4 linear actuator, fitted with a NEMA 17 stepper motor, limit and home switches, and a power-off break. The

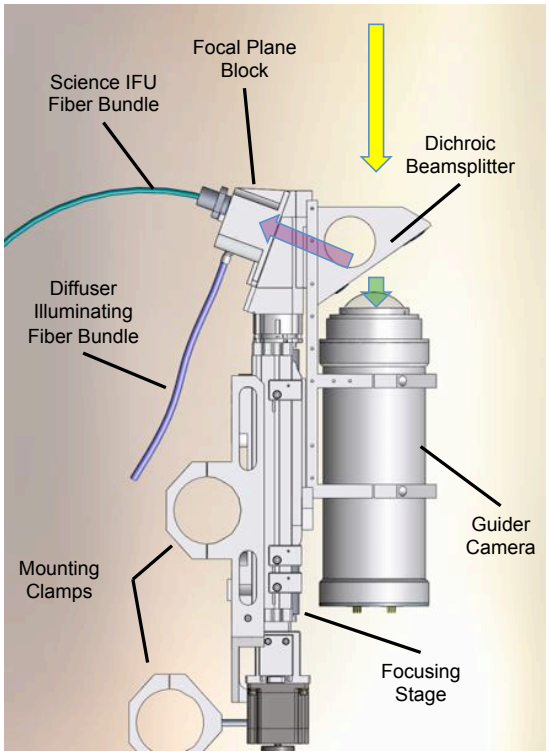

Figure 3.12. A CAD rendering of the FIREBall focal plane. The actual subsystem mounts at a 10° angle with respect to the vertical, to match the paraboloid axis tilt. The incident telescope beam is shown entering from above (depicted with an arrow), split into the UV science beam reflected into the IFU fiber bundle, and the transmitted light entering the guider camera. The full assembly attaches to the gondola via three mounting clamps (only two visible in this perspective). There are a number of position adjustments that can be made. The length of the strut connecting the lower mounting clamp to the bulk of the focal plane can be changed, tilting the focal plane. The focusing stage and everything mounted on it (guider camera, dichroic, focal plane block) can be rotated on the underlying structure, in and out of the page. The same objects can be shifted to the right by inserting shims onto the focusing stage. The full assembly can be shifted along the gondola bars perpendicular to the image. Finally, the focal plane block can be slightly adjusted in two axes perpendicular to the incoming light. CAD rendering courtesy of R. Chave.

components were assembled using grease with good vacuum characteristics. The stage has 2 inches of linear travel with 8 micron resolution. The motor, break and limit switches are controlled by an IMS MicroLynx controller that is housed in the guider electronics pressure vessel. A Honeywell JEC-C Linear Variable Differential Transformer (LVDT) was added for the second flight to have an absolute measurement of the focal plane stage position. Although the motor controller keeps track of the motor steps commanded, it does lose location when power is cycled, and does not notice skipped steps within the motor. The LVDT produces a voltage proportional to the displacement of the stage from a reference position. This is read out by an output stage that conditions the voltage,

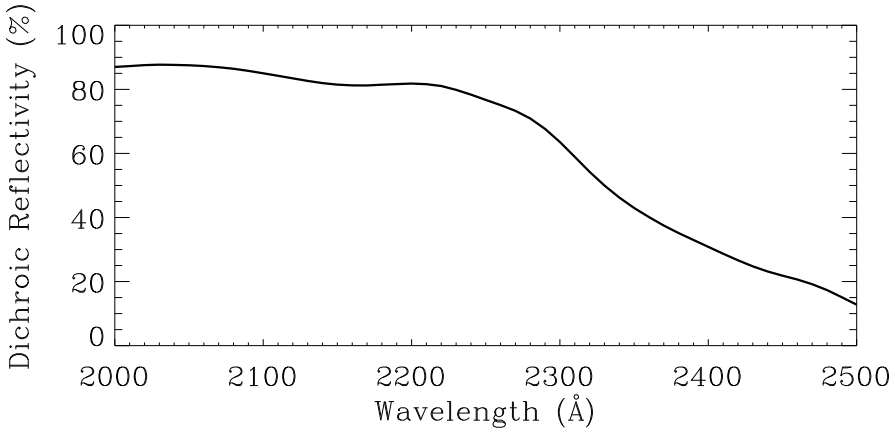

Figure 3.13. The reflectivity of the FIREBall dichroic as a function of wavelength. The curve is based on manufacturer's measured data and takes into account the strongly conical nature of the FIREBall light beam.

allowing it to be digitized by an ADC onboard the guider control computer (see section 3.4.3.2). This voltage is used as a proxy for position when focusing the telescope. The stage was first installed without the power-off break, but was found to slip, so that element has been added. The two limit switches are positioned once the focal plane has been mounted on the gondola. The upper switch is set to avoid collision between the focal plane and the siderostat mirror; the lower switch is set to protect the IFU fiber bundle from excessive bending. Once the ground focusing procedure has been performed, the home switch is positioned so as to correspond to the best focus location.

The focal plane assembly is equipped with a Minco heater, attached to the underside of the focal plane stage, set to 19°C. The assembly is loosely wrapped in a thermal blanket for flight. This does not interfere with any focusing motions. The guider camera enclosed in a pressure vessel is an additional heat source in the area. This configuration maintains a steady temperature at the focal plane, reducing thermal changes in focus.

3.2.4.4 The UV Focal Plane Block

The UV focal block is the mounting area for the IFU fiber bundle, and contains several calibration illumination sources. The location and geometry around the UV focal block is shown in figures 3.12 and 3.14. The UV focal plane consists of a stainless steel flat pinhole mask that has a central aperture for the insertion of the IFU fiber bundle. It has an opening for a diffuser and several pinholes. The pinhole mask construction drawing and a CAD rendering of the associated UV focal plane illumination hardware are shown in figure 3.15. Due to some corrections the mask underwent before the first flight, the surface of the part is abraded and the material has insufficiently fine granularity or uniformity. Though some surface roughness is needed to cause the mask to act

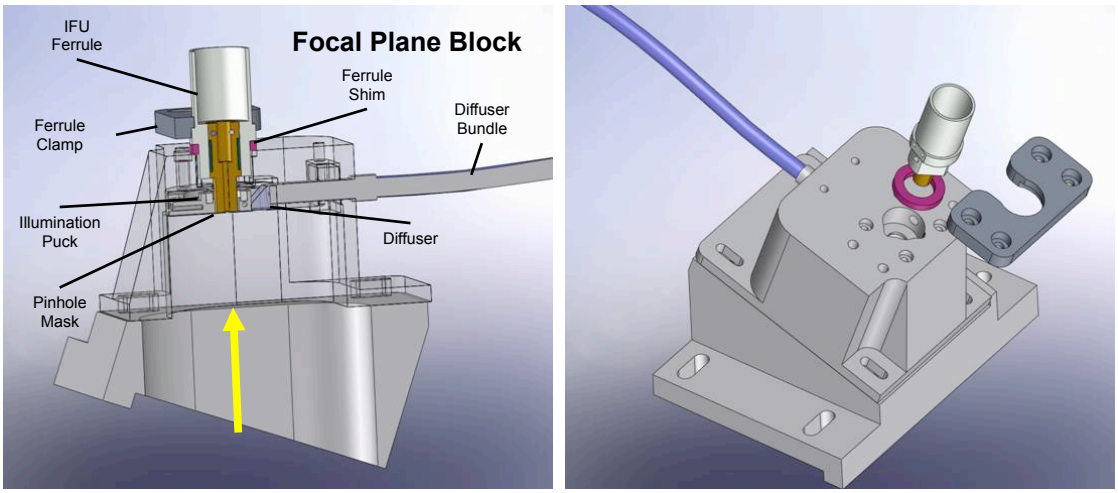

Figure 3.14. A cross section through the FIREBall focal plane block. The direction that light enters the IFU fiber bundle is indicated with an arrow. The first thing the beam encounters is the pinhole mask with an aperture for the IFU bundle (see figure 3.15). Behind the pinhole mask is an illumination puck, which holds the light sources for the pinholes (four Maglite light bulbs). Attached to the pinhole mask is a diffuser prism. The fiber bundle is shimmed and clamped into the focal plane block so that the front of the IFU is coplanar with the pinhole mask. CAD renderings courtesy of R. Chave.

as a diffusing screen, the irregularities must be much smaller in size than the features of the return images of the pinholes. It was often difficult to discern the direction of the comatic aberration arrows due to nonuniform scattering from the mask.

The IFU fiber bundle plugs into the focal plane block from behind, and it is clamped in against an annular shim which determines the relative location of the front face of the bundle and the pinhole mask. The pinhole mask is used during instrument alignment as a projection screen for sources within the fiber bundle, and as such must be coplanar with the fiber bundle. A depth gauge was used to measure the offset between the pinhole mask and the fiber bundle, and the shim was adjusted to reduce this offset to under 25 microns. A mechanical measurement of the bundle face location is dangerous to the optic. Any future IFU bundle design should be implemented so that the location of the front face of the bundle is known and mechanical tolerances are relied upon, or safer measurement techniques can be used. The pinholes are illuminated by four MagLite Krypton light bulbs. These are nestled in a circular puck that attaches to the focal plane block behind the pinhole mask. The illumination is not direct, as there is a thin ring of Speculon material directly under the pinholes that was to act as a diffusing light guide.

It became evident during the paraboloid alignment procedure (see section 3.2.3.3) that the pinholes should not be located diametrically opposed to one another with respect to the center of the IFU fiber bundle. The current arrangement causes the images of the pinholes to appear near other

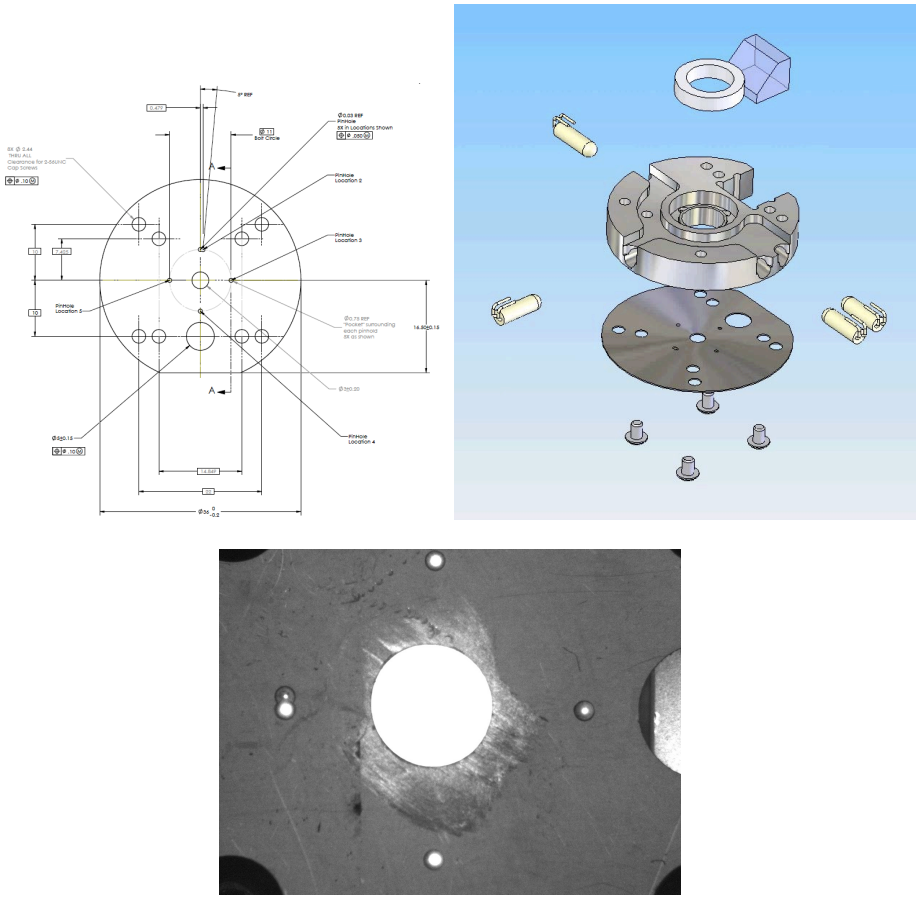

Figure 3.15. The UV focal plane pinhole mask. The central opening is for the science fiber bundle; surrounding it are five 35 micron pinholes in a cross pattern on an 11 mm circle. Below the IFU opening is a 5 mm diameter cutout for the focal plane diffuser. The remaining apertures are used for mounting. The last panel is a zoomed photo of the pinhole mask showing the central IFU bundle opening, the five surrounding pinholes and part of the diffuser prism opening to the right. Note the damage to the pinhole mask surface due to deburring of some of the manufacturing defects prior to the first flight. The top right panel shows an exploded view of the hardware behind the pinhole mask, including the illumination puck, light bulbs, light-integrating ring, and diffuser prism.

illuminated pinholes, making the characterization of their optical aberrations difficult. Three pinholes, spaced by 120°, should be sufficient. The light bulbs that illuminate the pinholes tend to run hot and have burned out several times. Their irradiation pattern does not match well with the way that they are installed with respect to the pinholes. They should be replaced with surface mount LEDs, which have long lifetimes and dissipate less heat. The LEDs should be mounted under the pinholes with a layer of diffusing material underneath.

The diffusing prism is made of fused silica. It relies on total internal reflection to relay light from an illuminating fiber to the opening in the pinhole mask. It is attached to the mask using

a cyanoacrylate adhesive. The surface of the prism facing the focal plane has been sandblasted to make it an optical diffuser. This element did not perform to specifications. The flat-field that it was supposed to generate was not uniform, showing a strong gradient. It is not clear whether this was caused by nonuniformity in the illuminating fiber, or a prism geometry-fiber numerical aperture mismatch. The diffuser design should be revisited for the next FIREBall campaign.

3.2.4.5 Focal Plane Imaging Camera

A modification that was suggested for the second FIREBall campaign by Bruno Milliard (LAM) was the inclusion of a focal plane imaging camera. The intended use of this device is to help with alignment of the focal plane and telescope optics. The author was responsible for the bulk of the optical layout and subsystem design; the mechanical drawings and fabrication were attended to by Robert Chave.

The camera and associated optics mount to the side of the crowded focal plane region of the telescope. A pair of 1" reflective prisms in a periscope configuration, an M7528-MP Computar lens and an EX2C Computar focal length doubler image the focal plane pinhole mask and IFU fiber bundle onto a monochrome AVT F-146 (Guppy) camera. The light path from the focal plane of the telescope to the center of the lens is 350 mm. The camera has been designed to have 10 micron spatial resolution, which is sufficient to resolve the pinholes and the aberrations in their images. The tip and tilt of the prisms can be adjusted to center the IFU fiber bundle on the camera screen; this adjustment needs to be repeated when the focal plane block is moved to align the IFU with the telescope paraboloid axis. The focal plane imaging optics do not vignette the light within the telescope, and the mechanical package was designed to avoid interference with the actuated siderostat mirror above. The layout and a photo of the completed alignment tool are shown in figure 3.16. The camera is powered and read out through a FireWire connection attached to a Linux PC. Provisions were not made for this system to be operational in flight, as the addition of another computer and either an extra telemetry channel or video multiplexing were deemed not feasible within the available time and budget. The camera and optics were removed from the system prior to flight, once they had served their purpose. A sample image taken by the camera is shown in figure 3.16, and the camera's function is discussed in section 3.2.3.3.

3.2.4.6 Guider Camera

The guider camera is located behind the dichroic beam splitter. It is a QImaging Retiga EXi FireWire camera with a $8.7\times6.6\,\mathrm{mm}^2$ frame-transfer monochrome CCD. The camera is equipped with a custom three element focal ratio reducing lens that transforms the F/2.5 telescope beam to an F/1.1. The lens was designed by Shahinur Rahman; figure 3.17 shows the details which can be found in his dissertation (Rahman 2010). The field of view of the guider is $\sim28\times24$ arcmin^2. The

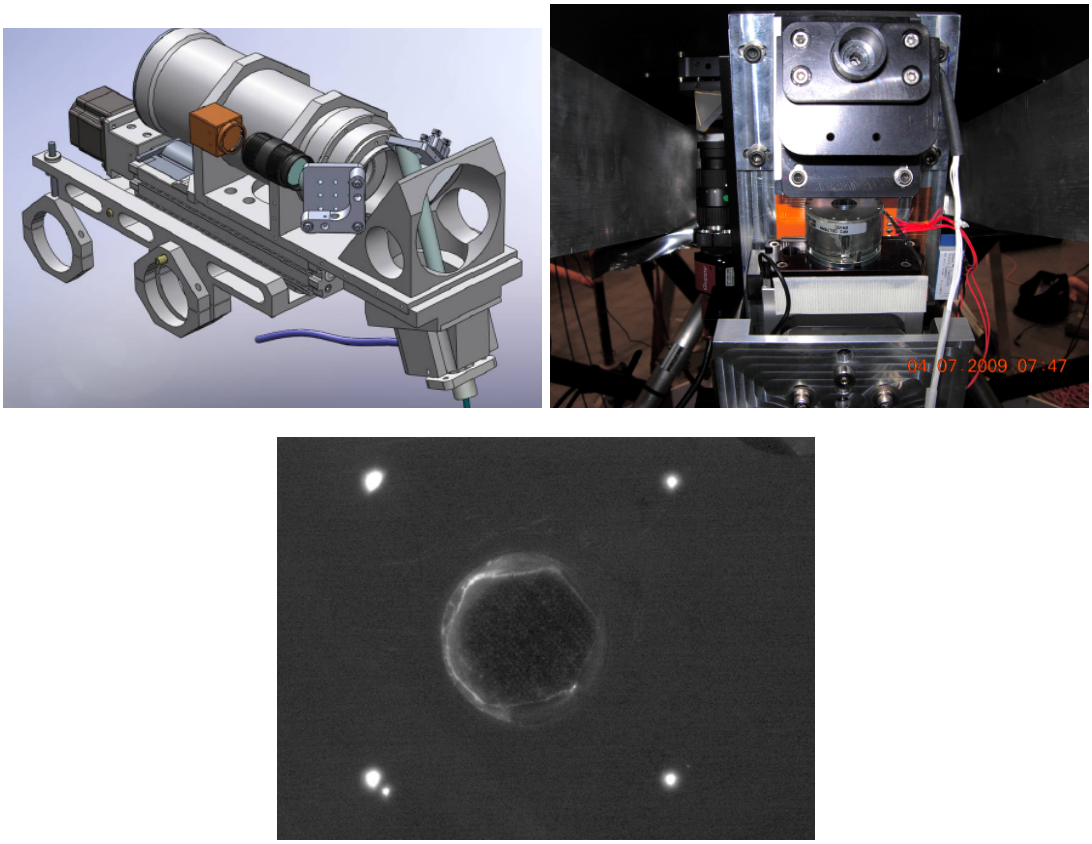

Figure 3.16. A CAD rendering of the focal plane imaging camera (left) and a photograph showing it mounted on the FIREBall focal plane (right). The perspective of the photograph is from the direction the IFU fiber enters the assembly (bottom right side of the CAD drawing). The bottom panel shows an image taken by the camera. All four pinhole areas are illuminated, and the central IFU fiber bundle is visible. There is a faint return image of the top left pinhole visible just right of the bottom right pinhole. The exposure time for this image was fairly long, so the pinholes appear saturated.

camera is encased in a cylindrical pressure vessel, as it was not designed to operate near vacuum. The cylinder is mounted in a cradle, and its location within the focal plane can be adjusted along its axis of symmetry. It can also be rotated around that axis to align the CCD with the natural axes of the telescope.

The guider is aligned to the focal plane on a laboratory optical bench. A specially mounted stand, mimicking the gondola bars that the focal plane attaches to, allows for orienting the focal plane on its side. A large (1 mm) pinhole light source is inserted into the focal plane where the IFU fiber bundle would be, making sure it is coplanar with the pinhole mask. A 12" focal length spherical mirror is placed to return the beam from the pinhole reflected off the dichroic, reimaging it on the focal plane mask. A schematic of the arrangement is shown in figure 3.18. The alignment

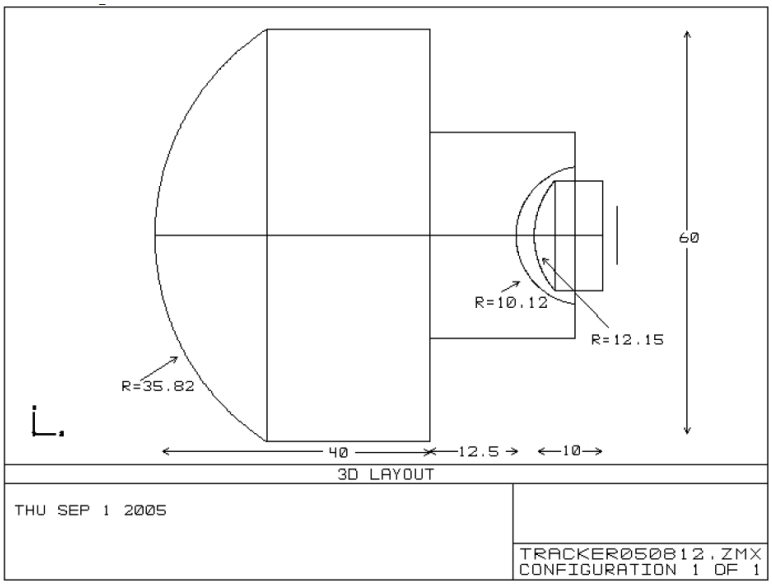

Figure 3.17. FIREBall guider focal-ratio-reducing lens construction drawing courtesy S. Rahman.

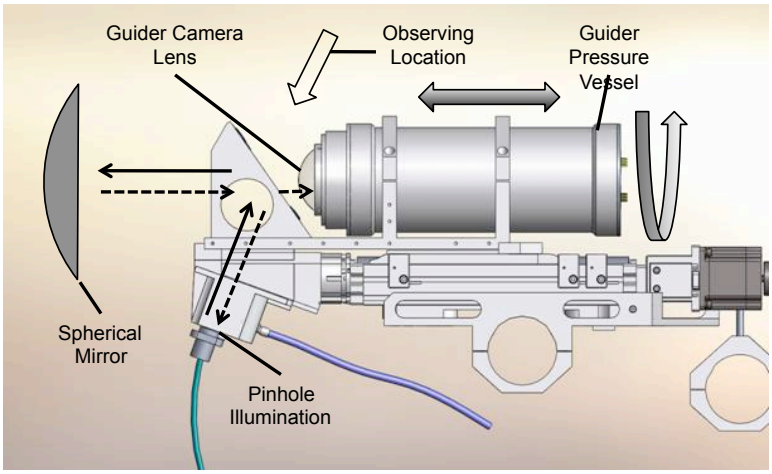

Figure 3.18. The arrangement used for making the guider camera confocal and concentric with the UV focal plane, as viewed on the bench from above. Light from the focal plane is partially reflected off the dichroic. It is then refocused back by a a spherical mirror onto the focal plane mask. The focal plane is observed from the direction of the white arrow. There are images of the pinhole returned to the focal plane and images observed by the guider camera. The camera can be moved in piston motion within the supporting cradle to adjust focus.

starts with placing the spherical mirror such that the return image is nearly focused and nearly centered on the pinhole mask, and the center of the mirror is intersecting the axis of the guider lens. As the dichroic has a slight wedge to it and is effectively transparent glass at visible wavelengths, this procedure relies on Fresnel reflections off of its two surfaces. The consequence is that there are three return images at the focal plane separated horizontally by a short distance. The central image

is the true image, as that is reflected by the front of the dichroic twice. At the guider camera, there are two images. The image that comes to focus further from the spherical mirror is the one that was reflected off the front face of the dichroic; this is the one that is used. Ideally this procedure would be performed using the focal plane imaging camera, but that hardware was not yet available during this part of the instrument integration process. The spherical mirror is moved along the beam until the return image is focused on the focal plane. The mirror is then adjusted in the plane perpendicular to the beam and in tip-tilt to overlap the image of the pinhole with the pinhole, and to move the image on the CCD to the chip center. The guider camera is then moved along the beam to verify that it is coaxial with the spherical mirror by looking for lateral motions of the pinhole image. The location of the guider at which the pinhole image comes to best focus is measured, and the guider camera is clamped there. A retaining ring is added onto the camera canister to provide a hard stop marking the location, so it can be easily recovered when the camera is adjusted for other purposes.

Aligning the guider CCD axes with the telescopes axes is done with the gondola resting firmly on the ground. One of the elevation or cross-elevation motors is turned off; the other is commanded via a computer. A point source is projected onto the telescope using the ETR (see 3.3.2.1) and placed at the center of the guider field of view. The siderostat mirror is then moved along one axis, and the coordinates of the spot image on the guider CCD are noted. The guider canister is loosened in the cradle and is rotated until the difference in the relevant coordinate from one end of the chip to the other is under three pixels. A relative rotation of this magnitude (2.3×10^{-3} rad) is of no consequence to pointing reconstruction or the stabilization and guidance loops, as it introduces sub-arcsecond errors for the typical tracking offsets observed (∼hundred pixels). The current design does not include a locating pin that would mark the axial position of the canister within the focal plane. This should be added in the future to streamline instrument integration.

3.2.5 The FIREBall Detector

FIREBall uses the nonflight GALEX NUV03 microchannel plate detector. The device was built at UC Berkeley and Caltech. Its design, assembly, calibration, and operation are described in (Siegmund et al. 2004). The detector is a 65 mm diameter active area, microchannel plate intensified, cross-delay line readout sealed tube with associated electronics. A schematic of the detector is shown in figure 3.19. The tube window is made of fused silica and has deposited on it a Cs_2Te cathode. The detector is operated between -5200 and -900 V rails. Each interacting photon produces a photoelectron in the cathode. This charge is accelerated in the detector electric field and induces an electron shower through silicon microchannel plates. The cascade generates an avalanche of $\sim10^7$ electrons. The charge cloud is deposited onto an anode cross-grid and disperses to readout circuitry at both ends of the anode for each axis. The timing difference in the arrival of the pulses is used

Table 3.2. A listing of the data collected by the detector. The position along each detector axis is encoded in 15 bits, with 10 more bits containing information about the TAC and gain nonlinearities. The GALEX RAW 6 data format, which this is based on, is described in Morrissey et al. (2007).

ID	Bits	Description
X_{AmC}	12	X-axis fine position
Y_{AmC}	12	Y-axis fine position
X_B	3	X-axis coarse position
Y_B	3	X-axis coarse position
X_A	5	Wiggle
Q	5	Pulse height

to determine the location of the signal on the detector. This time difference is measured using a dual coarse-fine mechanism. The three most significant bits of the pulse location are determined by a coarse counter; this is interpolated with a time-to-amplitude converter (TAC), which provides a 12 bit fine correction. There is an additional corrective term that accounts for nonlinearities in the TAC (the so-called Wiggle), and for position measurement errors due to varying gain on the detector (Q). The above data is converted to position via

$$X = X_{AmC} + \alpha_X X_B, \tag{3.1}$$

$$Y = Y_{AmC} + \alpha_Y Y_B. \tag{3.2}$$

Here $\alpha_{X,Y}$ are integer constants around 2000. They are determined empirically by minimizing the spot-sizes on the detector. For FIREBall these values were found to be $\alpha_X = 2005$, $\alpha_Y = 1991$.

The detector head is sealed under high vacuum (10^{-9} torr) and is equipped with a passive getter pump. It can operate at ambient room conditions (1 atm, $\sim$20°C). As it was built for spaceflight, the detector is light and has a small footprint. The microchannel plate detector has a peak efficiency of 5%; its response as a function of wavelength, as measured during the GALEX design and integration phase, is plotted in figure 3.21. Associated with the detector are electronic components that convert the analog signal to digital, the so-called front-end electronics (FEE). These are external to the detector, residing in a separate hermetic enclosure. These electronic components are also legacy GALEX hardware. The FEE contains a digitizer, digitizer controller, data interface box (DIB) and a low voltage power supply. This hardware interfaces with the FIREBall instrument through a custom-configured PC-104 Linux computer fitted with an Xylinx FPGA board. The high-performance board allows for the system to register high photon-rate events. Figure 3.22 shows the mounted FEE electronics and FIREBall detector computer. A more detailed description of the FIREBall detector interface, associated electronics, and protocols can be found in Rahman (2010).

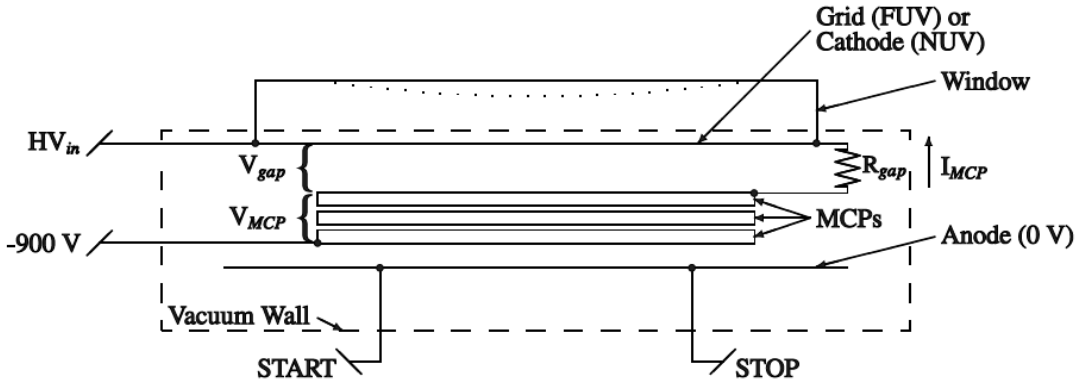

Figure 3.19. A cross sectional schematic of the GALEX/FIREBall MCP detector. Photons are incident on the detector from above, first encountering a SiO_2 window with a Cs_2Te cathode. The photoelectron generated by such a photon is then accelerated through a stack of three microchannel plates, where it is converted into a shower of $\sim 10^7$ particles. This cloud is then collected on the anode and disperses toward its two ends. The difference in arrival time of these two pulses is converted into position information. Image taken from Morrissey (2004).

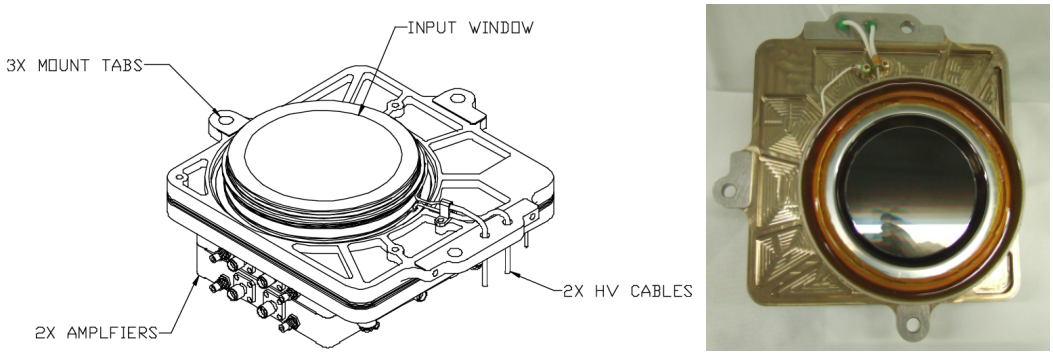

Figure 3.20. A mechanical drawing of the GALEX/FIREBall NUV detector, showing the location of mounting tabs, amplifiers, and high voltage wire connections. The right panel is a photograph of the detector. The mounting tabs were used to attach the detector to its mounting plate inside the FIREBall spectrograph. Construction drawing taken from Jelinsky (2001).

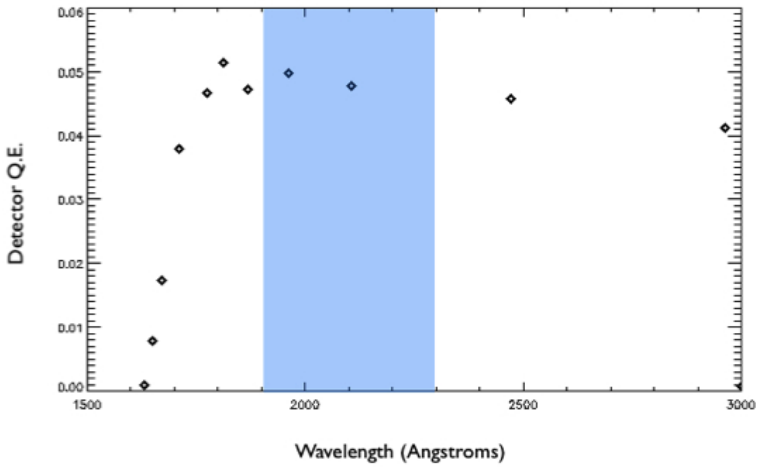

Figure 3.21. The detector quantum efficiency as a function of wavelength for the GALEX NUV03 detector (used for FIREBall) shortly after its manufacture at SSL (Berkeley). The highlighted region indicates the FIREBall wavelength range.

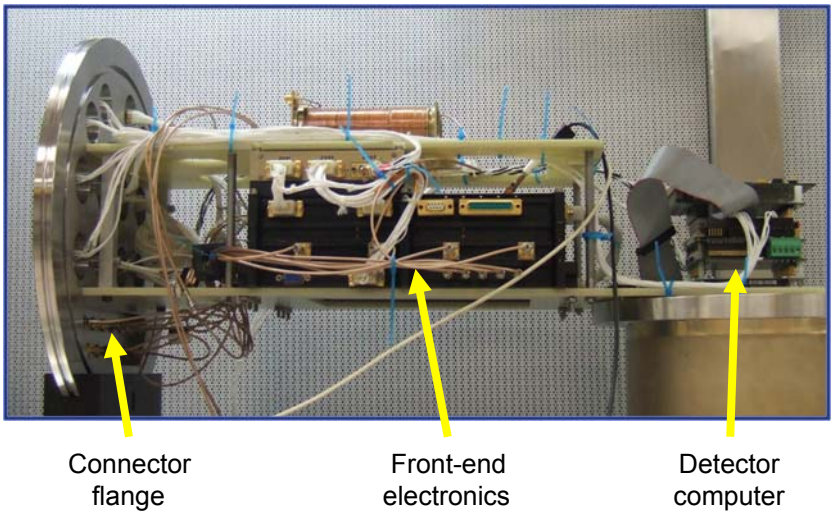

Figure 3.22. A photograph of the FIREBall front-end electronics and detector computer. The components are mounted on a pair of G10 fiberglass plates and electrically connected to other components through multiple vacuum feedthroughs welded into the front flange. The entire assembly slides into a cylindrical aluminum vacuum enclosure. The electronics generate substantial heat and came close to overheating during the first FIREBall campaign. The aluminum enclosure was black-anodized to improve radiative heating prior to the 2009 flight, and no thermal problems were experienced during the second campaign.

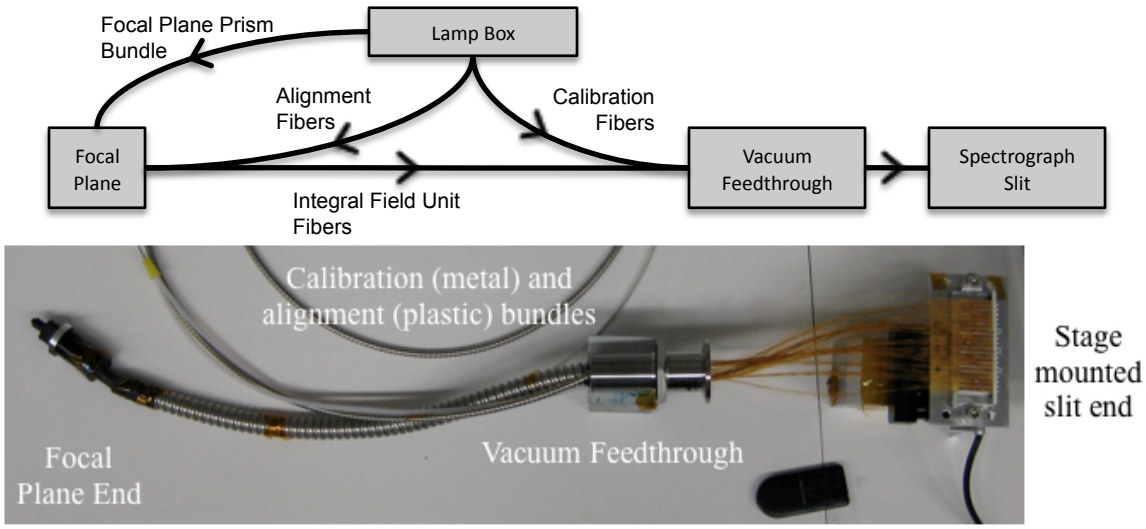

Figure 3.23. The configuration of FIREBall fiber bundles. The top panel shows the schematic layout, the bottom the photograph of the completed fiber bundle assembly for the second flight. The IFU bundle is encased in a flexible stainless steel sleeve, as is the calibration bundle. The alignment bundle is protected by Teflon tubing. The slit end of the fiber bundle is mounted on a short travel linear actuator used for focusing the spectrograph. Photograph courtesy S. Tuttle.

3.2.6 Integral Field Unit and Spectrograph

The integral field unit (IFU) and the spectrograph were designed and built by the Columbia University and LAM groups in our collaboration. Members from CNES and Caltech, including the author, were involved in the optical alignment of the spectrograph and IFU fiber bundle. The description of the initial design can be found in Grange et al. (2005); the design, implementation, and performance are detailed in Tuttle et al. (2008); Tuttle (2010); Tuttle et al. (2010). The discussion of the spectrograph and the integral field unit follows these sources closely.

3.2.6.1 Integral Field Unit Fiber Bundle

FIREBall makes use of four fiber bundles. Three are part of the integral field unit fiber assembly: the integral field unit bundle, the alignment bundle, and the calibration bundle. The fourth is a commercially acquired multimode fiber bundle used to illuminate the diffuser prism in the focal plane (see section 3.2.4).

The FIREBall IFU fiber bundle is built of of 325 fused silica, 100 μm core diameter fibers with Polymide cladding. It was made modularly in sets of up to 21 fibers. Fibers are cut to a slightly oversized length. One end is polished using a sequence of increasingly finer grit polishing paper. Up to 21 fibers are laid flat on an aluminum surface, and the polished surface is butted up against an aluminum block. The fiber alignment is inspected under a microscope, and Epo-tek 302-3M epoxy is applied 2-3 mm away from the optical surfaces of the fibers to prevent wicking onto them. Once

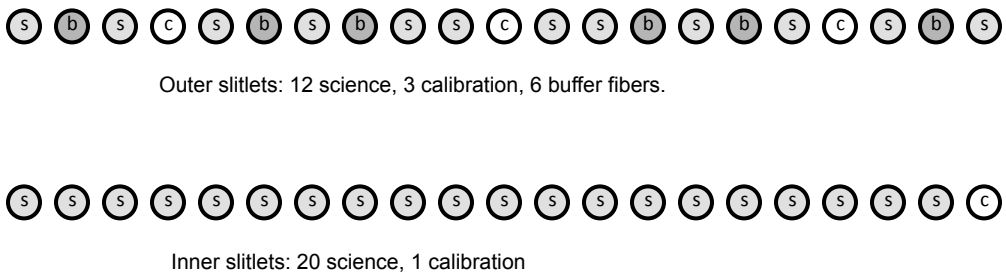

Figure 3.24. The two types of slitlets in the FIREBall spectrograph slit. The seven innermost slitlets have 20 science fibers and one calibration fiber. The outer 12 (six on each side of the slit) have 12 science fibers, and 3 calibration fibers each.

the binding agent is cured, the min-slitlet is epoxied to a 3 mm $\times$ 7 mm aluminum block. The fibers are allowed to overhang the block slightly to protect them from the epoxy wicking onto the surface. There were two types of slitlets made for the second FIREBall flight. They are shown in figure 3.24. The inner slitlets contain 20 science fibers and one calibration fiber. The outer ones include 12 science, 3 calibration, and 6 buffer fibers. The purpose of the buffer fibers is to space out the science fibers on the detector to prevent blending of spectra; however, they were not included in the central regions of the slit in order to maximize detector usage there. Of the original 284 science fibers, 280 remained intact for the flight, and of the 43 calibration fibers, 37 survived. The fibers are susceptible to static cling, so it is not a surprise that some were damaged during manufacture and handling. Figure 3.26 shows the distribution of calibration and science fibers on the detector. The 19 slitlets were screwed onto a fixture attached to a small actuator. They were shimmed to place the fiber fronts close to lying on a 1200 mm radius of curvature to improve the optical performance of the spectrograph. The spectrograph slit end of the bundle is mounted inside the spectrograph on a small linear actuator that is used for focusing the spectrograph during instrument integration. The stage is not configured to operate in flight.

The loose ends of the fibers are pulled through a custom vacuum feedthrough. They are arranged in a hexagonal pattern in a mold that is part of a ferrule that plugs into the focal plane block. The science fibers are surrounded by several layers of buffer fibers that serve to protect the bundle during polishing. They are placed so they extend about an inch past the end of the ferrule. Seven illumination fibers are inserted at the vertices of the hexagonal bundle. The mold is injected with epoxy fixing the fiber locations within the focal plane end of the bundle. The mold is then installed into the ferrule, and the majority of the excess fiber protruding from the front of the ferrule is trimmed, leaving under 20 mm. The bundle is polished with progressively finer grit paper, following the same procedure as the slit end. The assembly is shown in figure 3.25. The final length of the science fiber IFU bundle is approximately 50 cm, and the measured efficiency at 200 nm is 70%.

Figure 3.25. The FIREBall IFU ferrule. The top left panel shows a break-out of the ferrule assembly. The two-part mold that the fibers are epoxied into slides into the cylindrical opening in the ferrule shell, and is then pinned in place. A photograph of the assembly is shown in the top right panel. A close-up view of the hexagonal mold is in the bottom left panel. The bottom right image shows a face on-view of the fully assembled bundle. The active fibers appear illuminated, whereas the buffer fibers seem black.

3.2.6.2 Spectrograph Optical Design

The FIREBall spectrograph was designed to comply with the scientific requirements of high resolution ($\lambda/\Delta\lambda \sim 5000$) and large field of view (6 square arcminutes — leading to a 50 mm long input slit). It must conform to the mechanical constraints derived from the geometrical layout of the gondola (must fit in the space designated for it), and must be configured to allow a short light path from the location of the telescope focal plane. The spectrograph optics must match the output focal ratio of the output of the fiber slit (F/2.5). A folded Offner design was chosen, as it was found to be more compact than the standard Rowland circle or Wadsworth spectrographs. The optical

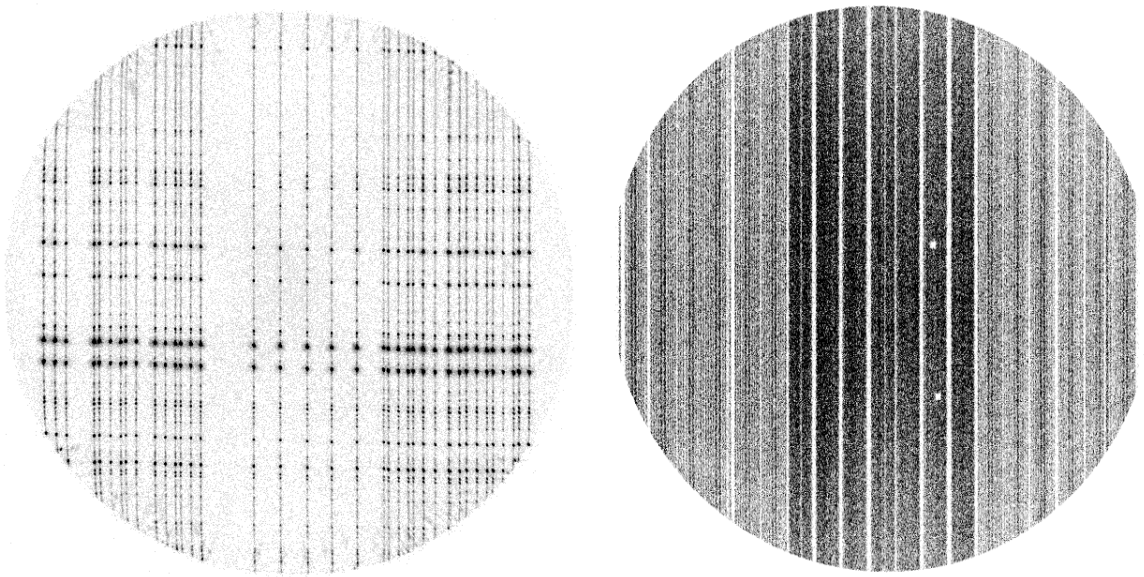

Figure 3.26. The left panel shows the layout of the 37 calibration fibers on the detector, illuminated by the PtNe lamp. The right panel shows the science fibers illuminated with a deuterium lamp. Note the closer spacing of spectra near the center of the detector. Detector hot spots have been masked out and appear as small white rectangular gaps in the image.

Table 3.3. Specifications for the FIREBall spectrograph optics. The two major changes to the grating from FIREBall flight 1 to flight 2 were reducing the groove density from 5000 to 4800 lines/mm, and adding a thicker MgF_2 overcoat to the aluminum coating.

	Offner sphere	**Grating (Flight 2)**
Diameter	480 mm	232 mm
Radius of Curvature	880 mm	470 mm
Coating	Al + MgF_2	Al + MgF_2
Coating Thickness	62 nm + 41 nm	Proprietary
Efficiency (at 200 nm)	91%	35%
Groove Density (lines/mm)	n/a	4800

path and schematic geometry are shown in figures 3.27 and 3.30, while figure 3.28 shows the two elements. The mirror reflectance is plotted in figure 3.29.

The diffraction grating operates in -1 order and forms a spectrum near the entrance slit of the spectrograph. The optical characteristics of the spectrograph components are given in table 3.3. The interior of the spectrograph housing has been painted black with Aeroglaze to minimize scattering and improve thermal coupling with the exterior environment.

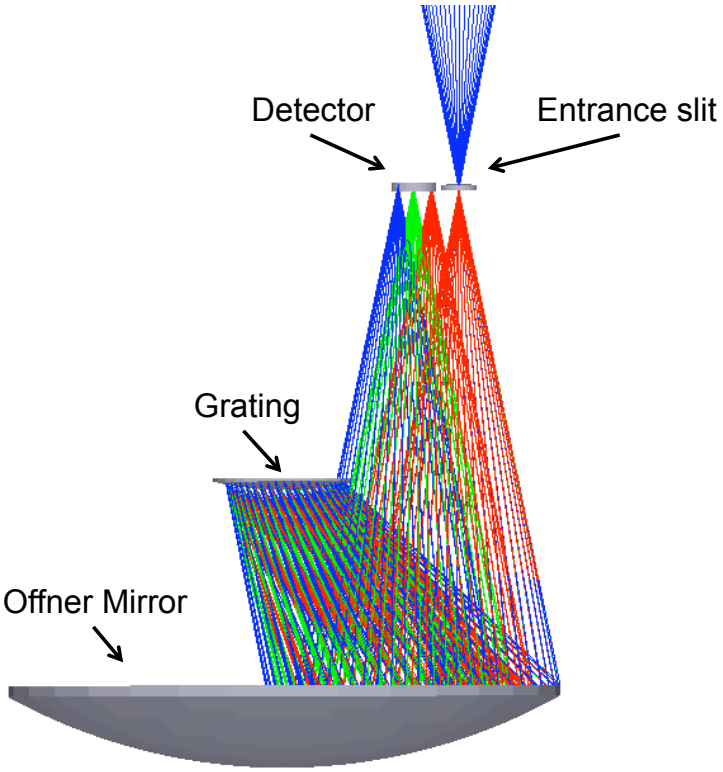

Figure 3.27. Light path inside the FIREBall folded Offner spectrograph design. A row of fibers forms the entrance slit to the instrument. The expanding F/2 beams reflect off a spherical Offner mirror onto a convex grating. The dispersed light is then refocused by the Offner mirror onto the detector.

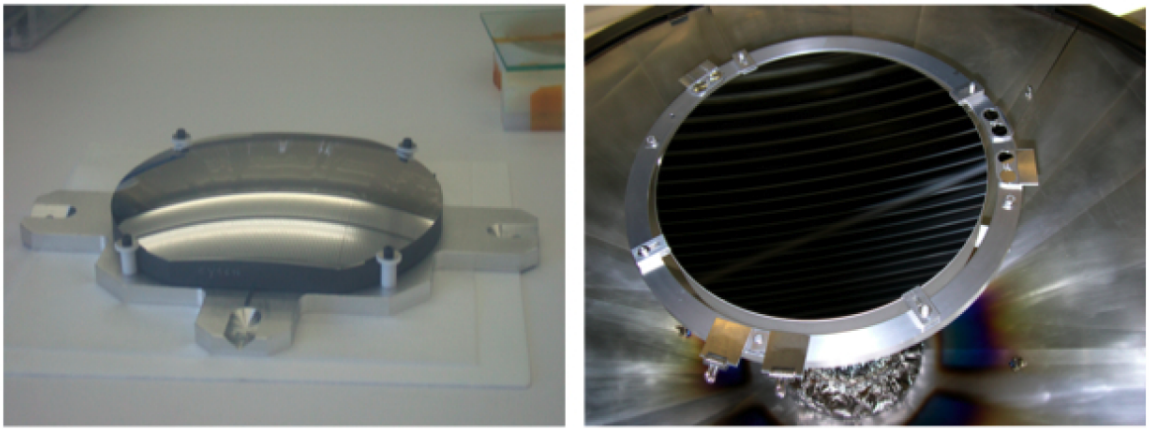

Figure 3.28. The left panel shows the Al and MgF_2 coated FIREBall grating, the right panel the freshly coated Offner sphere inside the GSFC coating chamber.

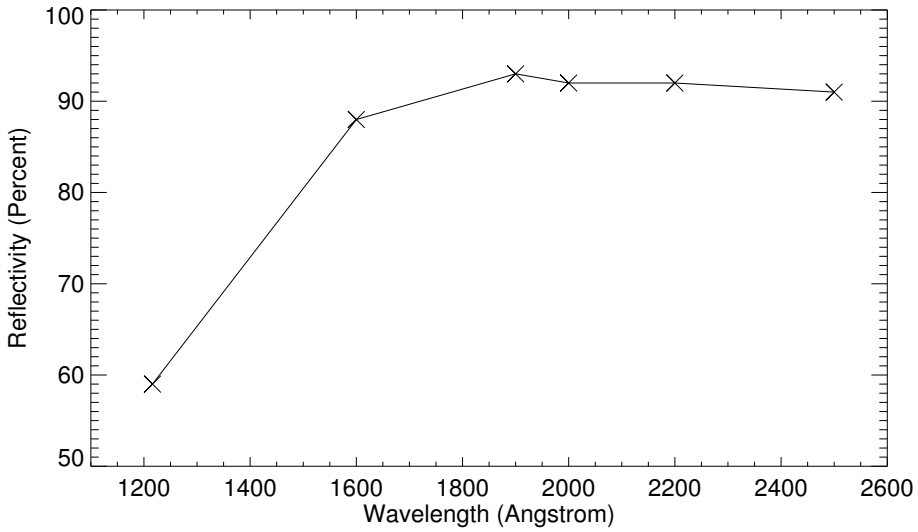

Figure 3.29. Reflectance of the FIREBall Offner sphere measured using witness samples that were placed around the edge of the optic as it was coated at GSFC.

3.2.6.3 Grating

The grating blanks were figured by Winglight Optics. They are spherical elements with 470 mm radius of curvature and 232 mm diameter. The gratings for both flights were ruled holographically by Horiba Jobin-Yvon. A laminar groove profile was chosen to enhance efficiency. The grating for the first flight had a groove density of 5000 lines/mm and a bare aluminum overcoat. The diffraction efficiency was measured by LAM to be 17%, which was about a factor of two lower than modeling suggested. A similar problem was seen in the manufacture of the near-UV diffractive elements of the Cosmic Origins Spectrograph for the Hubble Space Telescope. A combination of groove spacing and MgF_2 thickness appears to be causing a resonance responsible for decreasing the diffraction efficiency (Wilkinson et al. 2002; Kuznetsov et al. 2004). In light of this, the grating was changed for the second FIREBall flight. The groove spacing was reduced to 4800 lines/mm, and the aluminum coating was given a thick protective MgF_2 overcoat. This increased the grating efficiency to 35%, more in line with theoretical values.

3.2.6.4 Spectrograph Mechanical Design and Thermal Considerations

The spectrograph is constructed as a three-level structure. The bottom level is an Invar (steel-nickel alloy) plate with the Offner sphere bonded onto it. The middle level has mounted onto it a plate with the grating attached. The top plate holds the spectrograph slit and the detector head. The three levels are connected by two sets of hexapod mounts constructed of carbon fiber rods with aluminum ball ends. The aluminum ends are attached to the strut via a pair of differentially threaded screws,

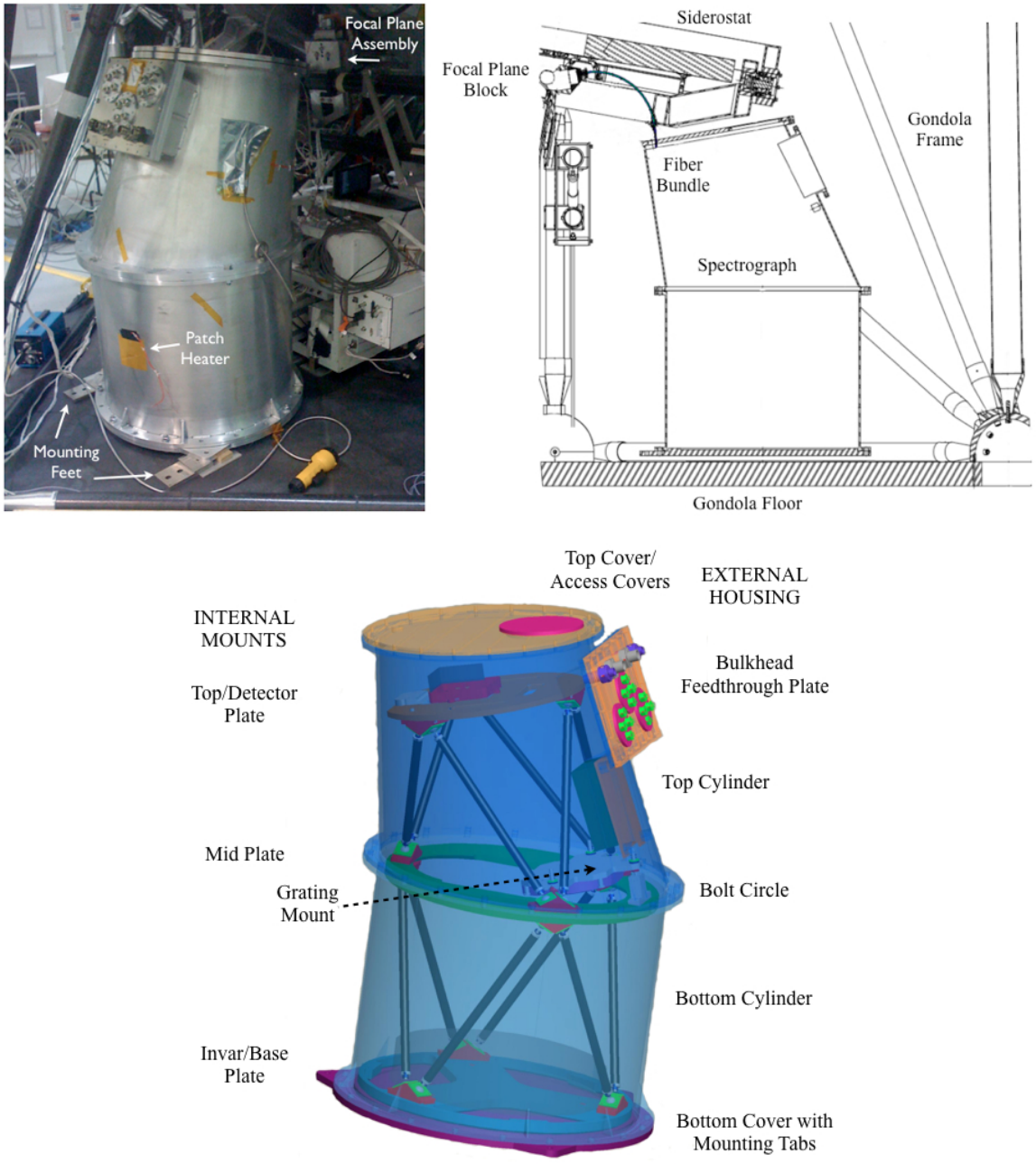

Figure 3.30. The mechanical layout of the FIREBall spectrograph. The top right panel shows the location of the spectrograph within the gondola. Note the proximity of the top of the spectrograph housing to the siderostat mirror frame. The top left is a photograph of the installed unit. The bottom panel shows the internal structure of the spectrograph. Visible, though not labeled, are hexapod struts that allow for small adjustments in the relative positions and orientations of the Offner mirror, grating, and detector/slit mounting plate. Figures courtesy S. Tuttle.

allowing for the length of each to be adjusted. These 12 struts are visible in the bottom panel of figure 3.30. The coordinated changes in the lengths of the struts allow the relative configuration of the Offner sphere, grating, and entrance and exit slits to be adjusted.

The spectrograph is encased in a hermetic aluminum enclosure with access panels in the top plate and a cable interface panel on one side near the top.

The spectrograph is wrapped for flight in MLI, and several heating elements are attached to the outside surface of the housing. These are configured to maintain a steady temperature of 20 to 25°C throughout the flight, which is the nominal operating temperature of the detector. Holding the temperature within a narrow range prevents large thermal changes to the optical path and detector response.

3.2.6.5 Spectrograph Alignment

Spectrograph alignment begins with mounting the Offner sphere, grating, and detector plates to within mechanical tolerances. They are then adjusted until the image spectrum falls onto the detector. The spectrograph entrance slit is moved along the optical axis using a linear actuator to focus the spectra. The aberrations observed in the image spectra are modeled using ZEMAX ray tracing software, and the nature of the misalignment is understood and corrected for by adjusting the hexapod strut lengths within the spectrograph. The process is repeated until the spectrum of a single fiber is $\sim$100 µm in FWHM. The details of this process are described in Tuttle (2010).

3.2.7 Telemetry

Communication between the gondola hardware and the ground is essential to the success of the mission. FIREBall has four computer subsystems, in addition to the CSBF hardware. These are the gondola master computer, the detector computer, the fine pointing module computer, and the guider computer. Each set of electronics is commanded from, and relays housekeeping information and data back to, the ground. There are two uplink and three downlink channels. All of these channels were provided and maintained by the CSBF. They are summarized in figure 3.31 and outlined below. The primary communication station was at the launch site for each flight; however, the second flight included a provision of routing data through a secondary ground station in Winslow, AZ. This was not needed, as the signals were strong enough for effective communication with the gondola electronics through the end of the mission near the Utah–California border.

3.2.7.1 Digital Command Uplink

The digital command uplink is a very low throughput serial connection (1200 baud) that uses a proprietary CSBF-NASA encoding algorithm to transmit and error check the data being sent to the gondola. FIREBall utilizes this link to command all four computer subsystems. The command

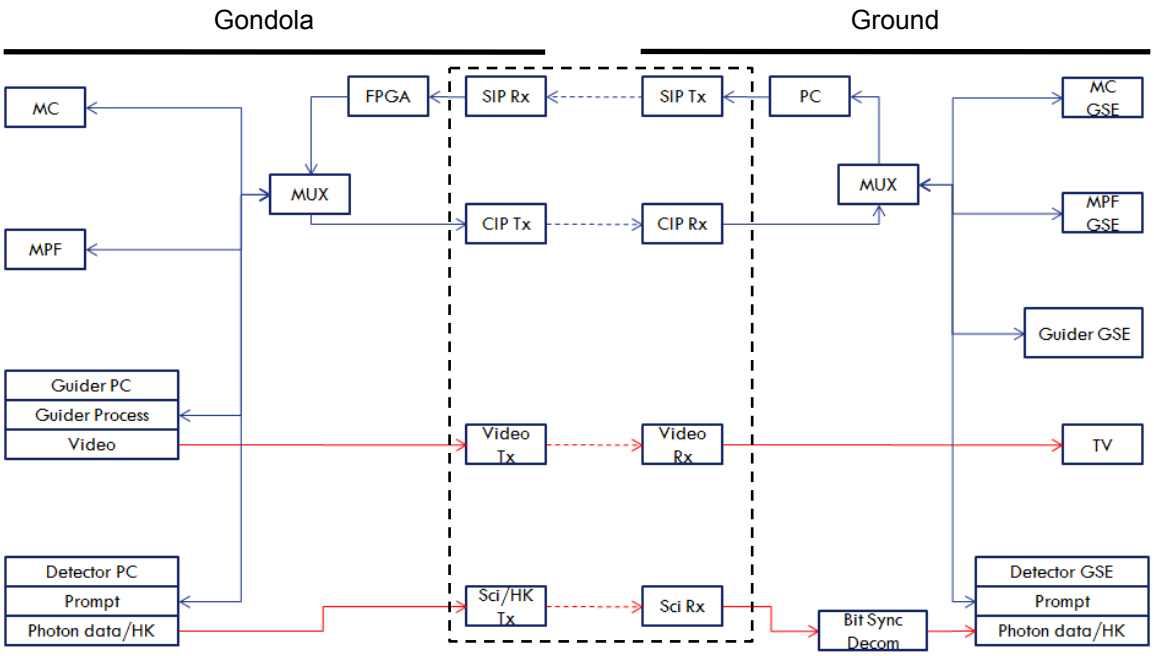

Figure 3.31. A summary of the FIREBall telemetry structure. The gondola-side electronics are on the left-hand side of the diagram. These include four computers: gondola master computer, fine pointing control computer, optical guider computer, and detector control computer. The gondola also houses a multiplexor (MUX) that processes two serial data streams, an FPGA board that decodes the command uplink, one receiver and three transmitters. The ground side consists of three matching receivers, one transmitter, a PC to encode commands going to the gondola, and a multiplexor allowing the use of one serial link for all four of the ground stations associated with the gondola-side computer systems. Hard links are indicated by solid lines, wireless connections by short-dashed lines. The transmitters and receivers were furnished by the CSBF and are bounded by a dashed box in the diagram; the remainder of the hardware was built and programmed by the FIREBall team.

streams are combined using a hardware multiplexor; its output is modified to conform to the encoding and passed onto the transmitter on the ground. The effective throughput rate for this channel was measured to be ∼150 baud.

3.2.7.2 Discrete Command Uplink

The digital command uplink consists of a series of short commands (up to 12) that toggle switches on the gondola. These commands were used for toggling power to the FIREBall subsystems, including the master computer, mirror heaters, video and data transmitters, CSBF ballast drops, and CSBF hardware.

3.2.7.3 Serial Downlink

The serial downlink is a standard 38.6 kbaud connection. It is shared among the four FIREBall computers using the same set of multiplexors as the digital command uplink. Each computer is allotted 9600 baud, with some, but insignificant, loss due to the multiplexor encoding.

3.2.7.4 Data and Video Downlinks

There are two gigabit transmitters operating at different frequencies aboard the gondola. One transmits the guider video as a standard NTSC signal. This is then viewed as a television signal. The other is used to download the detector data, as it is acquired, with detector housekeeping information folded in. The detector data stream requires bit- and frame-synchronizing hardware on the ground to decode the information, which is subsequently processed and displayed by the detector ground station.

3.3 Instrument Calibration and Data Reduction

3.3.1 Overview

The collected data are initially organized in a photon list, with information about each count collected by FIREBall kept in a FITS table. Later this is transformed into a three-dimensional histogram, a so-called data cube, which contains the photon flux as a function of sky coordinates and wavelength. Associated cubes that chart the detector response and relative exposure time are also created. This section discusses the steps taken to transform the raw data collected by the GALEX NUV detector (see section 3.2.5) into the data cube, detailing the calibration methods, tools and data products necessary to perform the task.

The path to process and convert the event stream coming from the detector is shown in figure 3.32. For all but the last step the data is kept in a photon-list format, where each detector event is listed and processed individually. The detector data and calibration is discussed separately in section 3.2.5, and the pointing reconstruction is dealt with in section 3.4. The remainder of the steps are outlined here.

3.3.2 Methods and Tools

3.3.2.1 Artificial Star (ETR)

The ETR, or artificial star, is a calibration tool developed by LAM that projects a point source onto the FIREBall telescope. The point source can be generated using a halogen (visible) or deuterium (UV) light source. It is used predominantly to calibrate the gondola pointing system (section 3.4), but also for IFU fiber bundle–guider mapping (section 3.3.2.5).

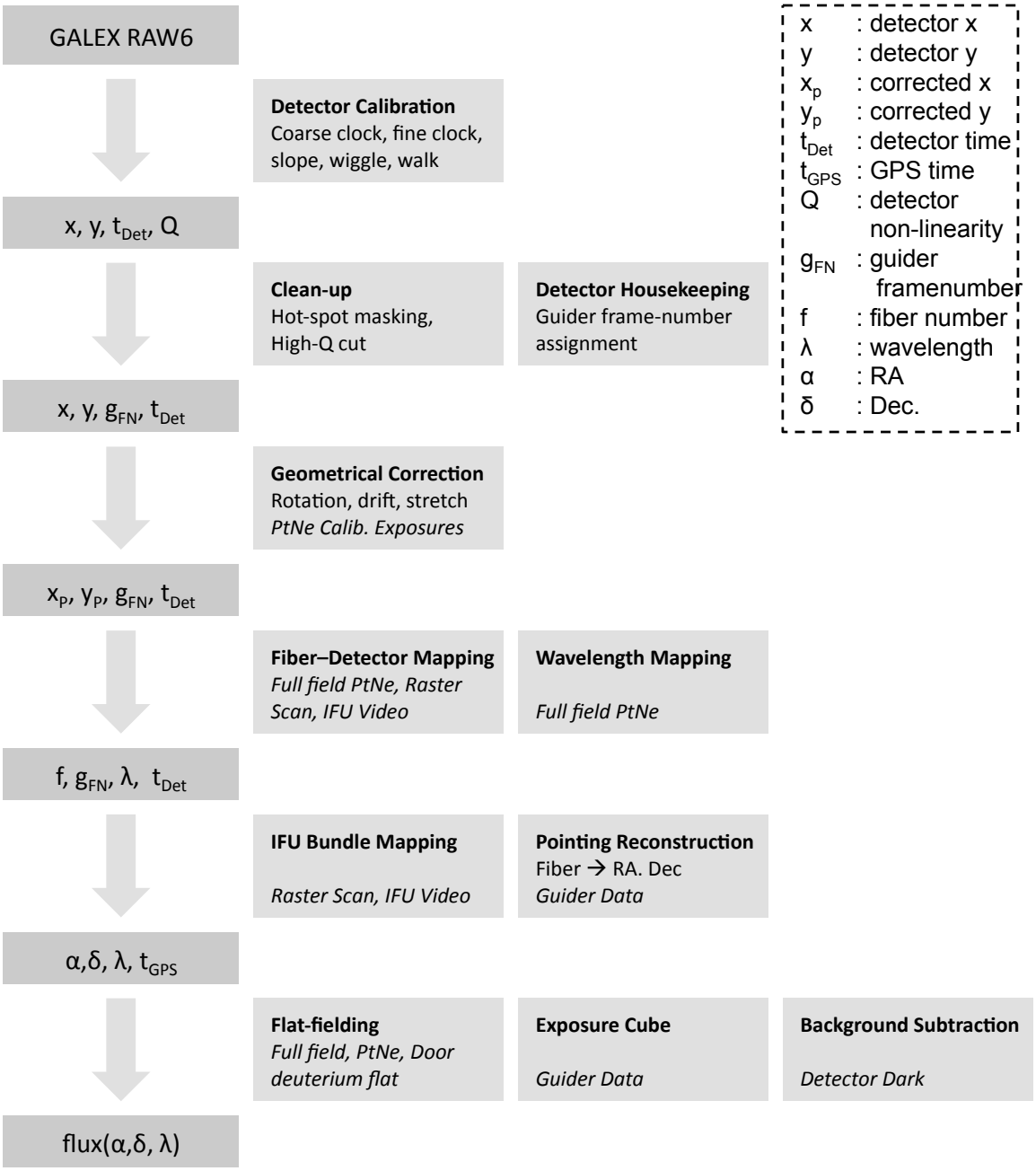

Figure 3.32. A schematic showing the data-reduction process for FIREBall. GALEX RAW 6 data (Morrissey et al. 2007) is translated into a FITS table photon list. It is then cleaned up by masking detector hot spots and removing spurious counts. Next the data is transformed to correct for geometrical changes. Each detector count is then assigned an IFU fiber that it is deemed to have originated from, and an associated wavelength. Pointing information is folded into the mix, yielding RA and Dec information for each count. Finally, the photon lists are histogrammed in three dimensions and corrected for instrument response and exposure time variations. The evolution of the variables associated with each count is shown in the left column, while the calibration methods and data products used at each step are indicated in boxes to the right. The legend identifies the relevant variables.

Table 3.4. A synopsis of the FIREBall photon list data structure.

ID	Type	Description
T	Double	Detector computer clock value
X_B	Int	x-axis coarse position
X_{AmC}	Int	x-axis fine position
Y_B	Int	y-axis coarse position
Y_{AmC}	Int	y-axis fine position
Q	Int	Gain nonlinearity
X_A	Int	x-axis wiggle
Y_A	Int	y-axis wiggle
X	Double	raw x position
Y	Double	raw y position
X_P	Double	transformed x position
Y_P	Double	transformed y position
F	Long	Assigned fiber number
W	Float	Wavelength
FN	Long	Guider computer frame-number
UTC	Double	UTC time
$FLAG$	Long	Status flag
RA	Double	Right Ascension
Dec	Double	Declination
$TargetID$	Int	Target field identifier
GPS	Double	Same as UTC
$Field\_RA$	Double	RA of the target field
$Field\_Dec$	Double	Dec. of the target field

The ETR is a modified gondola telescope very similar in design to that of FIREBall, but re-arranged upside down (Milliard et al. 1994). A fiber source, usually 100 microns in diameter, illuminates a 40 cm parabolic primary mirror axially from above. The concave mirror collimates the light toward an actuated siderostat flat that reflects the beam obliquely downward at the FIREBall siderostat mirror. The position of the ETR with respect to the gondola and the angle of the ETR flat can be adjusted to project the beam from different elevations, and onto different parts of the FIREBall siderostat. The ETR beam illuminates only a small fraction of the FIREBall pupil.

3.3.2.2 Calibration Light Sources

The Columbia members of our collaboration were responsible for the design and implementation of calibration light sources. Details of this design can be found in Sarah Tuttle's dissertation (Tuttle 2010). The FIREBall design calls for two light sources onboard the gondola: a continuum source, and a line source. A deuterium lamp was used as the former, a platinum-neon arc lamp as the latter. These are housed in a cylindrical pressure vessel to permit convective cooling of the bulbs. The light is redirected by a series of beam splitters and mirrors to a fused silica window, through which it is coupled to a pair of fiber bundles. One of the fiber bundles illuminates the diffusing prism in the focal plane; the other leads directly into the spectrograph, and its fibers interweave with the science

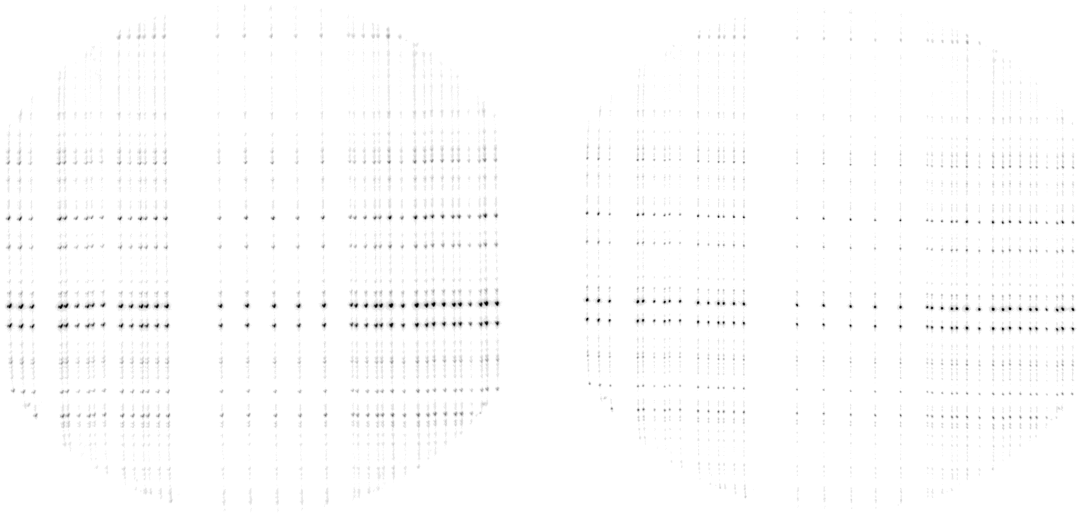

Figure 3.33. Detector image of PtNe spectra of the 37 calibration fibers in the spectrograph entrance slit. The left panel shows the coadd of all the calibration exposure prior to the application of any corrections; the right panel shows the same data after the corrections have been applied.

fibers from the IFU fiber bundle (see section 3.2.6). The deuterium lamp burned out after FIREBall was declared ready for the second flight. The decision was made not to replace it, as doing so would have jeopardized our flight opportunities. Consequently, only the PtNe arc-lamp was available in flight. An external deuterium lamp was available for ground calibration and testing throughout both campaigns.

3.3.2.3 Platinum-Neon Lamp Calibration

The PtNe spectral lines of the calibration fibers in the spectrograph slit form a grid on the detector. An example spectrum is shown in figure 3.33. This grid is an excellent tool for correcting for any geometrical distortions and transformations due to thermal effects on the optics and the detector readout electronics. There were a total of 8 calibration exposures taken during flight and at the hangar the night before the launch.

The PtNe lamp was also used to illuminate the full IFU fiber bundle through the focal plane diffuser with the telescope in autocollimation. Although the flat-field generated in this way is not uniform, it does fully illuminate the entrance to the IFU. This data is used for wavelength calibration of the individual IFU fibers and for determining the locations of the fiber spectra on the detector.

3.3.2.4 Deuterium Flat-Field

An external deuterium lamp was inserted into the gondola enclosure. It illuminated the inside surface of the closed gondola doors. These scattered the light into the telescope optical path, resulting in near flat-field illumination of the IFU fiber bundle. This data yields the relative response of the

individual IFU fibers. The approximately 1-hour-long image was collected once before the second FIREBall flight in Fort Sumner, NM.

3.3.2.5 Raster Scan

The raster scan calibration injects deuterium lamp light into the artificial star as the gondola is suspended above the ground (see section3.3.2.1). The point source image is moved in a snakelike pattern over the IFU fiber bundle by adjusting the orientation of the siderostat mirror. The location of the spot on the guider CCD as a function of time is stored by the guider camera, and its spectrum is recorded at the detector. The collected data has two applications: first, determining the location of individual IFU fibers within the guider CCD (section 3.3.3.6), and second, locating single fibers on the detector (section 3.3.3.3). This calibration was performed once before the second FIREBall flight, in Fort Sumner, NM.

3.3.2.6 IFU Bundle Movie

The Columbia members of our collaboration created a movie of the IFU bundle. A 100-micron pinhole visible light source was mounted on a linear actuator. It was then moved along the spectrograph slit end of the IFU bundle, illuminating individual fibers. The focal plane end of the fiber bundle was filmed using a CCD camera with a macro lens, very much like the focal plane imager. The result is a 1-to-1 mapping of the slit end of the bundle to the focal plane end, including the locations of the individual fibers in the fiducial CCD coordinate system.

In the future, the pinhole source should be replaced with a slit perpendicular to the fiber bundle slit. As the fibers on the spectrograph slit do not lie in a perfect line, the outliers are not illuminated by a pinhole. There was one fiber in the FIREBall flight bundle that was not recorded in this movie but did emerge in the spectra taken with the spectrograph. Figure 3.34 shows the movie collapsed along the time direction for the flight bundle and a single frame with one fiber strongly illuminated. The built-in shape-finding IDL procedure FIND was used to generate a list of locations of fibers in CCD coordinates.

3.3.3 Data Reduction and Instrument Characterization

3.3.3.1 Rotation Correction

The first correction derived using the calibration fibers illuminated with the PtNe lamp is the relative rotation of the detector axes with respect to the dispersion direction of the spectrograph. Nonlinear regions of the detector are masked, and the rotation angle is estimated by looking at the slant of the fibers. This angle is found to be around 1°. An IDL routine is then used to rotate the detector data through a series of angles around this value. For each rotated spectrum, the data is collapsed

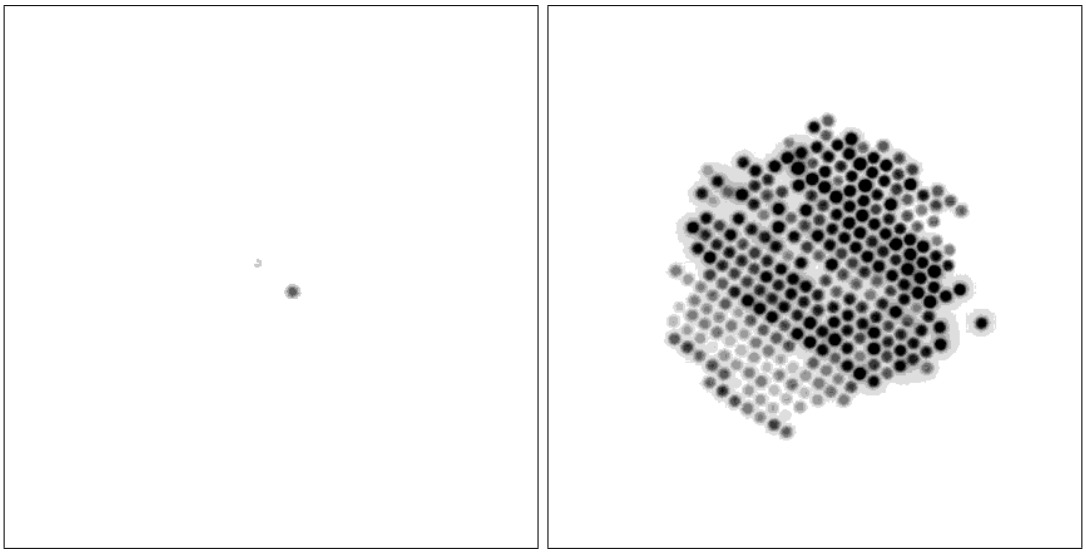

Figure 3.34. The left panel shows a single frame from the IFU bundle movie used for mapping. The right panel shows a sum of the nearly 10,000 exposures taken with all IFU fibers visible.

along the new y-axis and histogrammed along the new x-axis. The peaks corresponding to the 37 calibration fibers are found and fit with Gaussian curves using the `MPFITPEAK` package (Markwardt 2009; Moré 1978). This generates a series of widths for individual fiber spectra as a function of rotation angle. This data is fitted with a quadratic, and the minimum is noted. The abscissa of this point marks the rotation angle between the detector axes and the dispersion direction. This angle was found to vary between 0.993° and 1.013° for the 8 calibration files. The easy to remember 1° rotation value is used for the FIREBall data. An 0.015° deviation over the entire height of the detector image corresponds to a misalignment of the top and bottom of the spectrum by 1.3 pixels. This is less than 1/10th of the typical 15 pixel FWHM of a fiber.

The rotation correction is applied around the geometrical center of the four stim pulses generated by the detector electronics.

3.3.3.2 Distortion and Translation Correction

The first in-flight calibration exposure is used as a reference for the others, as it is one of the longest in-flight calibration images. The distortion mapping is broken down in two parts, one for each axis. For the detector x-axis correction, each exposure is collapsed along the wavelength direction, histogrammed, and the fiber peaks are fit with Gaussians, in the same way as is done for the rotation correction. The x coordinates of the fibers for a calibration exposure are fit with a linear form to the x_r reference exposure coordinates:

$$x = a(t)x_r + b(t), \tag{3.3}$$

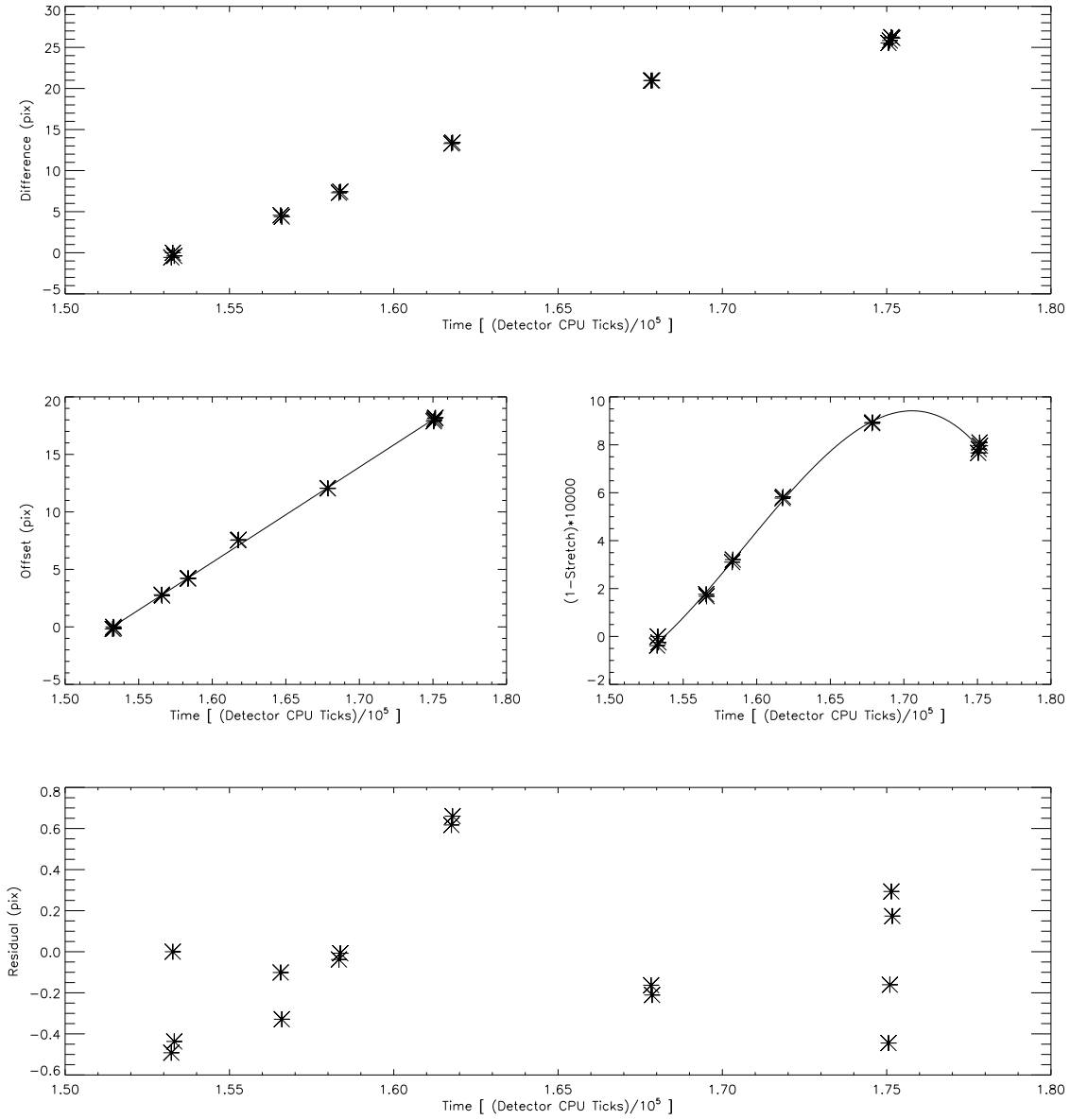

Figure 3.35. The x coordinates of the fiber spectra are fitted to construct a universal coordinate system for the FIREBall data set. The top panel shows the largest discrepancy in calibration fiber position for various calibration exposures as a function of time. The two middle panels are the fits to a and b as functions of time. The bottom panel is the same as the top, but after the corrections have been applied.

where $a(t)$ is a stretch, and $b(t)$ an offset, both changing during the flight. The slope term, $a(t)$, is fit with a first-degree polynomial as a function of time, $b(t)$ with a third-degree polynomial. The fits and the residuals are shown in figure 3.35. The residuals have been multiplied by 10^4 to show the maximum effect at the very extreme edge of the detector. As the thermal conditions were different

before flight, a separate fit is found for data taken then.

The new detector count coordinates are given by

$$x_p = (x - b(t))/a(t). \tag{3.4}$$

The values $a(t)$ and $b(t)$ for the period in the hangar prior to flight are given by

$$a_b = 1.0015, \tag{3.5}$$

$$b_b = -26.25. \tag{3.6}$$

The in-flight values are

$$a_f(t) = 0.143 + 1.623t - 1.020t^2 + 0.213t^3, \tag{3.7}$$

$$b_f(t) = -126.40 + 82.52t, \tag{3.8}$$

where t is in units of Detector CPU ticks divided by 10^5. Another collection of data that requires correction is a series of deuterium door flats. For completeness, the correction values for that set are

$$a_d = 1.002, \tag{3.9}$$

$$b_d = -34.637. \tag{3.10}$$

The y-axis correction is done in a similar way. All spectral peaks with a maximum height greater than 10 counts are marked, and their positions are measured using `MPFITPEAK`. The transformations necessary to move the peaks to their locations in the reference spectrum are computed. In flight, these are found to depend on time:

$$y_p = c_f(t)y + d_f(t), \tag{3.11}$$

$$c_f(t) = 0.237 + 1.329t - 0.768t^2 + 0.147t^3, \tag{3.12}$$

$$d_f(t) = 101.026 - 65.951t, \tag{3.13}$$

where t is in units of Detector CPU ticks divided by 10^5, as before; y is the old position and y_p is the new position after rotation and x corrections.

The transformation needed for the preflight data does not depend on time, but there is a significant slant (x-dependence) of the y coordinate.

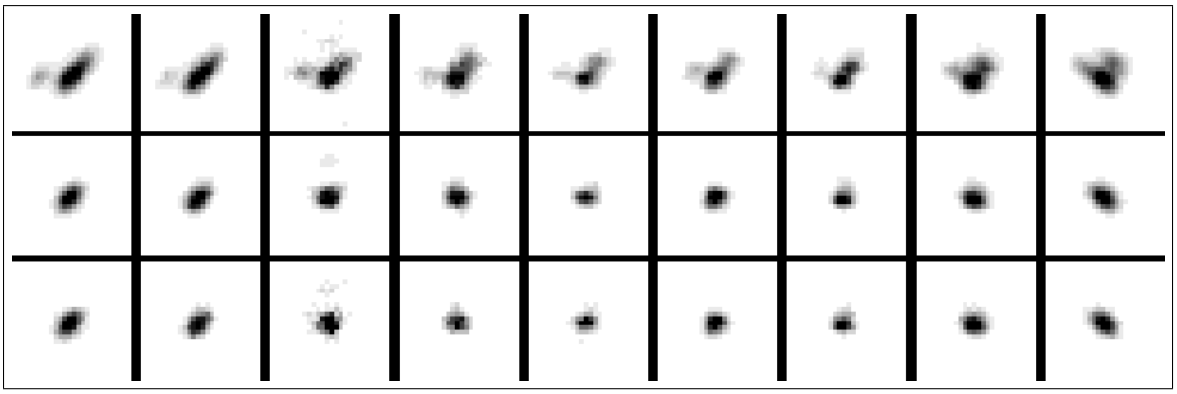

Figure 3.36. Zoomed views of nine PtNe calibration spots. The top row shows the combined image for all in-flight calibration exposures prior to any of the corrections described in text being applied. The middle row are the same spots after the corrections have been applied. The bottom row shows the spots from the single reference calibration exposure that were used as the reference for the mapping. Each thumbnail is 30 detector pixels, or 300 μm on a side.

$$y_p = g_b(x)y + h_b(x), \tag{3.14}$$

$$g_b(x) = 0.998 + 1.351 \times 10^{-7}x, \tag{3.15}$$

$$h_b(x) = 7.738 - 2.144 \times 10^{-3}x. \tag{3.16}$$

There is a similar slant in the door-flat data:

$$y_p = g_d(x)y + h_d(x), \tag{3.17}$$

$$g_d(x) = 0.999 - 4.569 \times 10^{-8}x, \tag{3.18}$$

$$h_d(x) = 8.905 - 1.495 \times 10^{-3}x. \tag{3.19}$$

The cause of the drifts and stretches has not been isolated, but most likely they are due to thermal effects on the electronics and mechanical structure of the IFU, detector mounting, and spectrograph.

The effect of the combined x- and y-axis corrections is shown in figures 3.33 and 3.36. When compared with the reference exposure, the full width at half maximum of the corrected coadded spots does not change in x, but increases by about half a pixel in y. As the RMS width of lines in y is 10 pixels; the imperfect y correction degrades the instrument spectral resolution by about 5%.

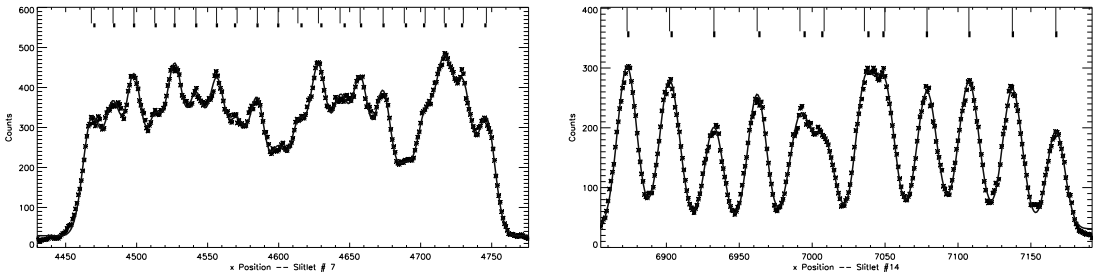

Figure 3.37. Sample fits to two slitlet histograms. Actual data is marked with asterisks; the calculated fit is shown with the thick solid line. The approximate initial peak locations are indicated with the thick short lines near the top of the charts, the final calculated positions with the thinner vertical lines. The x-axis is in detector pixels; the y-axis gives detector counts. The left panel shows one of the central slitlets that contain 20 closely spaced science fibers. The right panel depicts on of the slitlets away from the center of the full slit, containing fewer science fibers. These correspond to the two types of slitlets presented in figure 3.24.

3.3.3.3 Fiber Locations on the Detector

The calibration fibers illuminated with PtNe light allowed the conversion of the flight data and preflight data into the same coordinate system. The science fiber locations on the detector need to be located to allow for assignment of detected photon events to IFU location. These locations have been determined in two different ways:

The first makes use of the full field PtNe diffuser image. The detector counts are collapsed along the wavelength (y_P) direction. Each fiber creates a Gaussian profile; the resultant histogram is a superposition of such Gaussians. The graph is inspected, and approximate peak locations are marked. The image is then cut into individual slitlet histograms (see section 3.2.6). Each of these is then fitted, using the `MPFITFUN` routine, with a linear combination of Gaussians for which the height, position, and width are allowed to vary. The latter two are bounded to fit the physical values. The position is taken to be within 10 pixels of the initial approximate position, and the standard deviation of the Gaussian to lie between 5 and 12 pixels. Fits for a couple of the slitlets are shown in figure 3.37. The edge slitlets have more sparsely distributed fibers, with the exceptions of two pairs near the center of each, and are easier to fit. Central slitlets must have up to 20 fibers deblended.

The second method uses data from the raster scan (see section 3.3.2.5). In this data, individual fibers are illuminated for short periods of time, and so only regions of the detector corresponding to those fibers receive counts. These are collapsed along the detector y_P-axis as before. The resultant peaks are fit with Gaussians. A comparison of the locations of the 280 IFU fibers found using the two methods is shown in figure 3.38. A manual inspection of fiber spacings and locations, in comparison

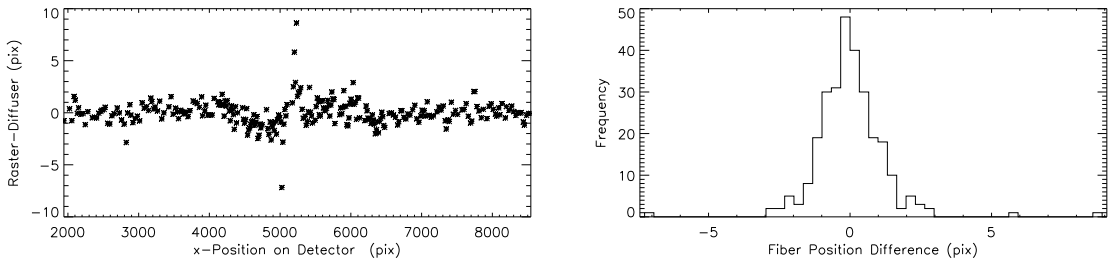

Figure 3.38. Difference in the x position of the 280 IFU fibers as measured by the raster scan data and the diffuser data. The two are in good agreement, with the vast majority of locations differing by no more than two pixels.

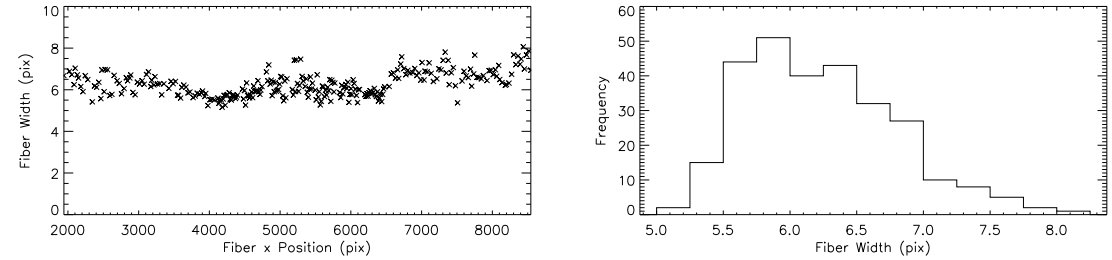

Figure 3.39. Fiber widths (Gaussian σ) on the detector as measured using the diffuser image. These correspond to FWHM $\lesssim 150\,\mu$m.

with camera images of the spectrograph slit, led us to use the positions derived using the raster scan. The peak widths (Gaussian σ) are shown in figure 3.39. They vary slowly across the slit.

3.3.3.4 Fiber Assignment

Every detector count has to be assigned to a fiber. As the fiber images overlap on the detector, a probabilistic method that deblends neighboring fibers must be used.

First, a probability distribution function that is consistent with a particular set of data is computed. Next, a cumulative distribution function is calculated from that PDF. Finally, detector counts are assigned to fibers using the CDF.

Obtaining the PDF starts with assuming that each fiber has a Gaussian profile

$$g_N(x) = \text{Gaussian}(x; x_N, \sigma_N), \tag{3.20}$$

where x_N is the location of the Nth fiber on the detector and σ_N is its width. To understand how much each fiber contributes to the PDF, a vector $\mathbf{c}$ is generated via

$$c_n = \sum_{\substack{|x_p - x_n| < \delta \\ y_{min} < y_p < y_{max}}} \gamma(x_P, y_P), \tag{3.21}$$

where the sum is over all counts $\gamma(x_P, y_P)$ that lie within a specified y_p range (y_{min} and y_{max} are chosen so that so that the full interval is filled for all fibers), and that are within a narrow range, $\delta \approx 2.5\,\mathrm{pix}$, of the location of the fiber. The narrow ranges around the fibers are used, instead of the full x range, as there is the least amount of overlap between fiber profiles at those locations. A "mixing" matrix $\mathbf{M}$ is constructed to characterize how much each fiber contributes to a particular 2δ wide bin around every fiber location, with

$$M_{ij} = \int_{x_j - \delta}^{x_j + \delta} g_i(x; x_i, \sigma_i)\, dx. \tag{3.22}$$

The linear combination $\mathbf{v}$ of Gaussians that is necessary to generate the c is given by

$$\mathbf{M}\mathbf{v} = \mathbf{c}, \tag{3.23}$$

$$\mathbf{v} = \mathbf{M^{-1}}\mathbf{c}. \tag{3.24}$$

The matrix $\mathbf{M}$ is nearly diagonal, as only the closest fibers contribute to a particular location on the detector; thus $\mathbf{M}$ can be inverted easily by Gaussian quadrature. This is done in IDL.

The probability that a particular detector count $\gamma(x_P)$ came from a particular fiber n is then given by

$$P_n(x_P) = \frac{v_n g_n(x_P)}{N(x_P)^{-1}}, \tag{3.25}$$

$$N(x_P) = \sum_i v_i g_i(x_P). \tag{3.26}$$

A cumulative distribution function (series) is constructed by

$$CDF_{\leq n}(x_P) = \sum_{i \leq n} P_i(x_P). \tag{3.27}$$

A uniformly distributed random r number is then drawn from the interval $[0, 1]$ and the detector count is assigned the fiber number f, such that:

$$CDF_{\leq f}(x_P) \leq r < CDF_{\leq (f+1)}(x_P). \tag{3.28}$$

The above assignment procedure works well when there are ample counts from the source to drown out the detector background. It is especially applicable to stellar sources. In their case, the distribution functions have to be recomputed for very short observation periods (0.5 s) to ensure that the fibers that receive many counts actually are assigned those counts. For dim sources where there are no discernible peaks in individual fiber counts over short periods of time and on-sky dithering washes out any long-term peaks, the computed PDF is replaced with one where all $c_n = 1$.

3.3.3.5 Wavelength Assignment

Wavelength calibration for the science fiber bundle is accomplished using the full-field diffuser PtNe exposure. A small interval around each fiber x_P location is isolated, and the y_P values of the counts are histogrammed. Up to seven peaks in the resultant spectrum are automatically marked and matched with a resolution degraded standard PtNe spectrum (Sansonetti et al. 1992). PtII lines are removed from the standard spectrum, as they do not appear in the emission of the FIREBall PtNe bulb. For each fiber, the wavelength is fitted with up to a third-degree polynomial as a function of y_P; the degree of the polynomial fit depends on the number of matched peaks. Figure 3.40 shows a sample wavelength fit for one of the 280 fibers. Once a detector count has been assigned a fiber number, its y_P coordinate is translated into a wavelength. This solution offers an opportunity to measure the spectral resolution of the instrument. Measuring the lower bound on the full width at half maximum (FWHM) of the arc-lamp peaks in the calibration spectra gives, under the assumption that at least some of the PtNe peaks do not have a significant intrinsic width, a lower bound on the spectrograph resolving power. A distribution of the FWHM values for peaks in the calibration fiber spectra is plotted in figure 3.41. This indicates that lines with FWHM of $\sim$0.6 Å should be resolvable, indicating a spectral resolving power of at least 4000, somewhat lower than the desired 5000.

3.3.3.6 IFU Bundle – Guider CCD mapping

The mapping between the front face of the IFU fiber bundle and the guider CCD pixels needs to be known to permit pointing reconstruction. The locations of the fibers in the IFU are known in the fiducial coordinate system of the camera used for the IFU bundle movie and are denoted by (f_X, f_Y) (section 3.3.2.6). The raster scan (3.3.2.5) yields the approximate guider CCD coordinates (c_X, c_Y), that maximize the throughput through specific fibers. There is no guarantee that these

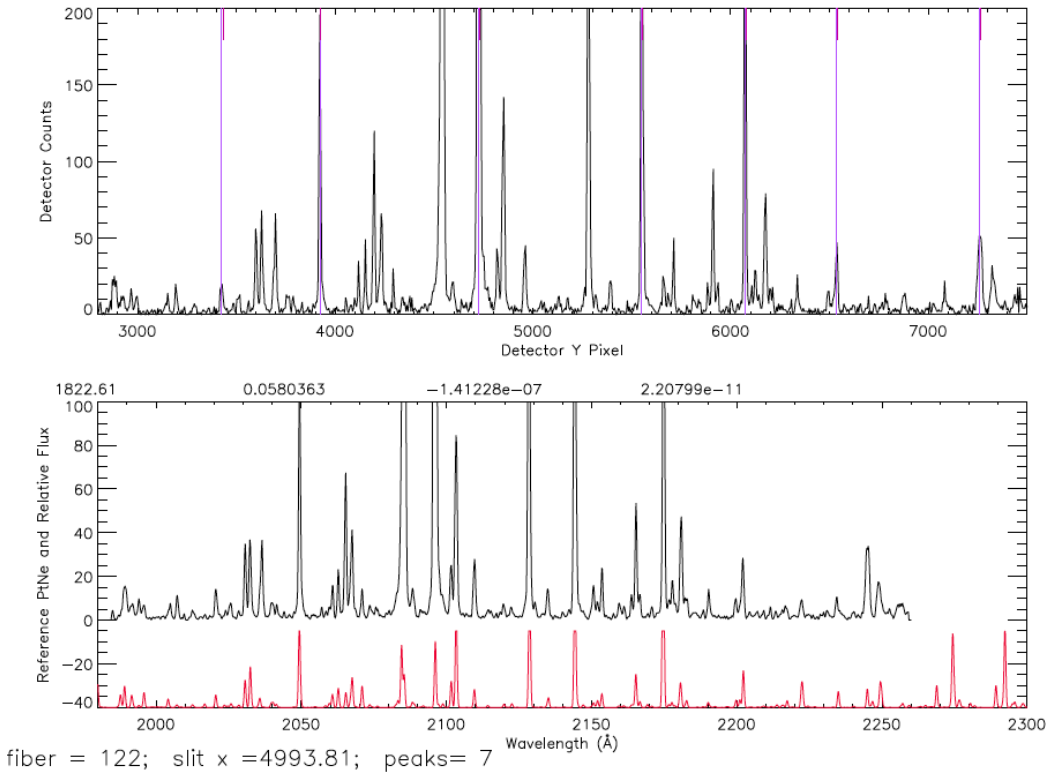

Figure 3.40. One of the 280 fiber assignment plots. The top panel shows the PtNe diffuser spectrum for this fiber, number of counts as a function of y_P. The identified peaks are marked with vertical lines. The bottom panel shows the same spectrum with y_P transformed into wavelength (top plot) and the reference NIST calibration spectrum (bottom plot). The numbers above the bottom panel are the 4 coefficients of the third degree polynomial fit converting y_P to λ.

coordinates coincide with the centers of the fibers, but the same fiber may receive light at different times during the raster procedure. Linear regression analysis combines the raster information to find the transformation $\mathbf{L}$ that generates a new set of coordinates, (g_X, g_Y), that approximate $\vec{c}$: $\vec{g} = \mathbf{L}\vec{f} \approx \vec{c}$. The coordinates are are taken to be the locations of the fibers on the guider CCD in the subsequent processing. Figure 3.42 shows the IFU fiber bundle in those coordinates and a photograph of the IFU end of the fiber bundle.

3.3.3.7 Detector Background

FIREBall observations are detector background limited, and it is crucial that the detector dark image be subtracted from the data. The in-flight detector background is on the order of 1 count/cm^{-2}/sec. As the data is in the form of a photon list rather than an image, a simple subtraction will not work. Rather, the data and dark photon lists must be processed in the same manner, generating a data cube. Subtraction is performed on these structures.

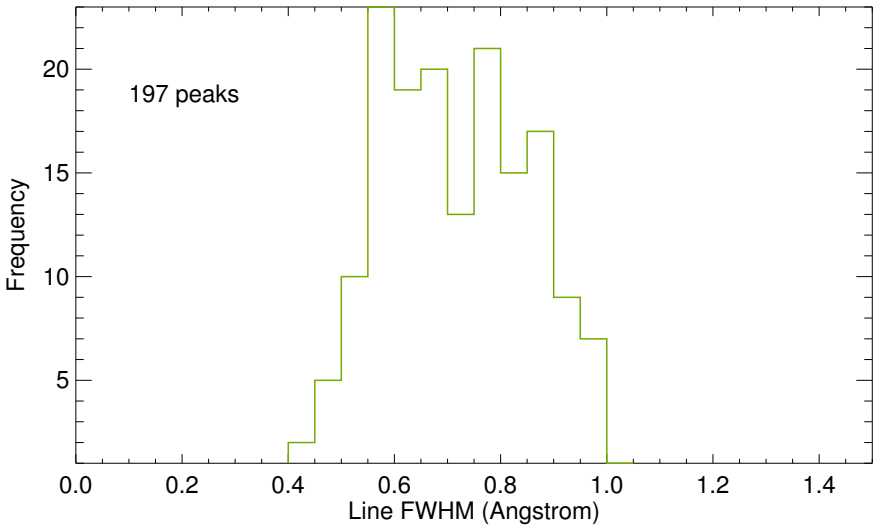

Figure 3.41. Distribution of FWHM of PtNe arc-lamp peaks in the spectra of the 37 FIREBall calibration fibers. The lower bound of the distribution is near 0.5 Å yielding a spectral resolving power $R \sim 2000/0.5 \sim 4000$. The detector spectrum was sampled in 0.1 Å bins and Individual peaks were fitted with a Gaussian. Some of the wider peaks are likely due to blending of multiple lines or intrinsic width.

The existing detector dark data was obtained at Caltech in 2005. The background count rate is approximately 1 count/cm^{-2}/s outside of six hot spot regions on the microchannel plate. Unfortunately, this data was collected at a temperature of 25°C, whereas the detector was at 15°C in flight. There is some concern that the detector response is significantly different between those temperatures. Furthermore, there is some uncertainty about the quality of the detector dark image, and plans have been made to collect a new image in the second half of 2011. Figure 3.43 highlights the concerns about the quality of the dark data, focusing on the intermittently changing event count rate, while figure 3.44 exhibits apparent irregular illumination of the detector.

Once an adequate dark exposure is available, it will be processed separately for each FIREBall target. The photon count time stamps for the dark will be altered to match the interval of target observation. This will then be divided into shorter subexposures that match the lengths of FIREBall observations, for which the stim pulse locations will be matched between the on-sky and dark data, superimposing the detector images. Fiber-free regions of the detector will be compared, and the dark scaled to match the background level of the science image. This dark data will be processed through the same pipeline as the science data, including wavelength and fiber assignment, culminating in a wavelength-sky-coordinate data cube.

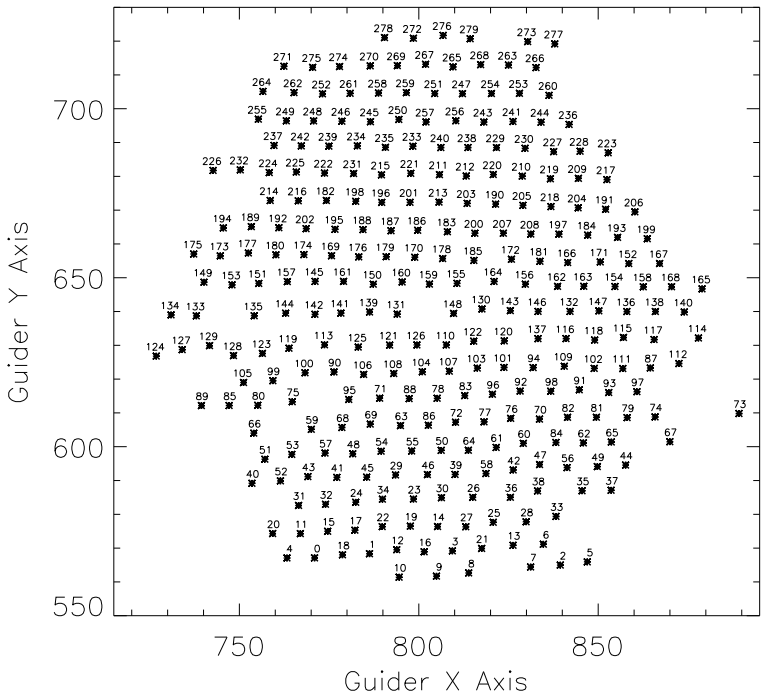

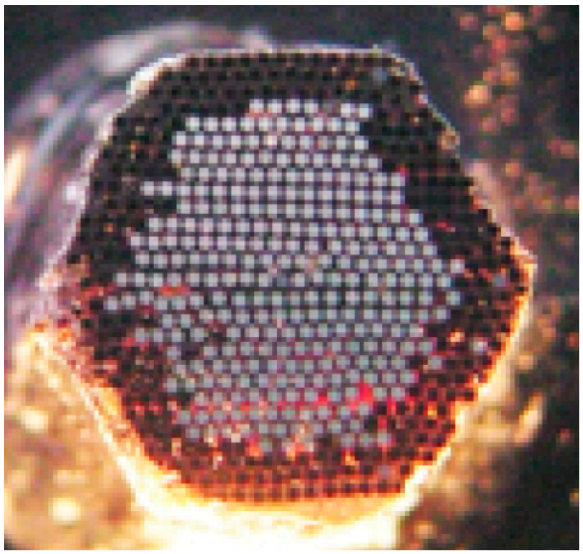

Figure 3.42. The top panel shows the locations of the IFU fibers on the guider CCD as obtained using the process outlined in section 3.3.3.6. The sequential number of the fiber along the spectrograph slit is printed next to each location. The bottom panel is a photograph of the IFU end of the fiber bundle illuminated through the slit end.

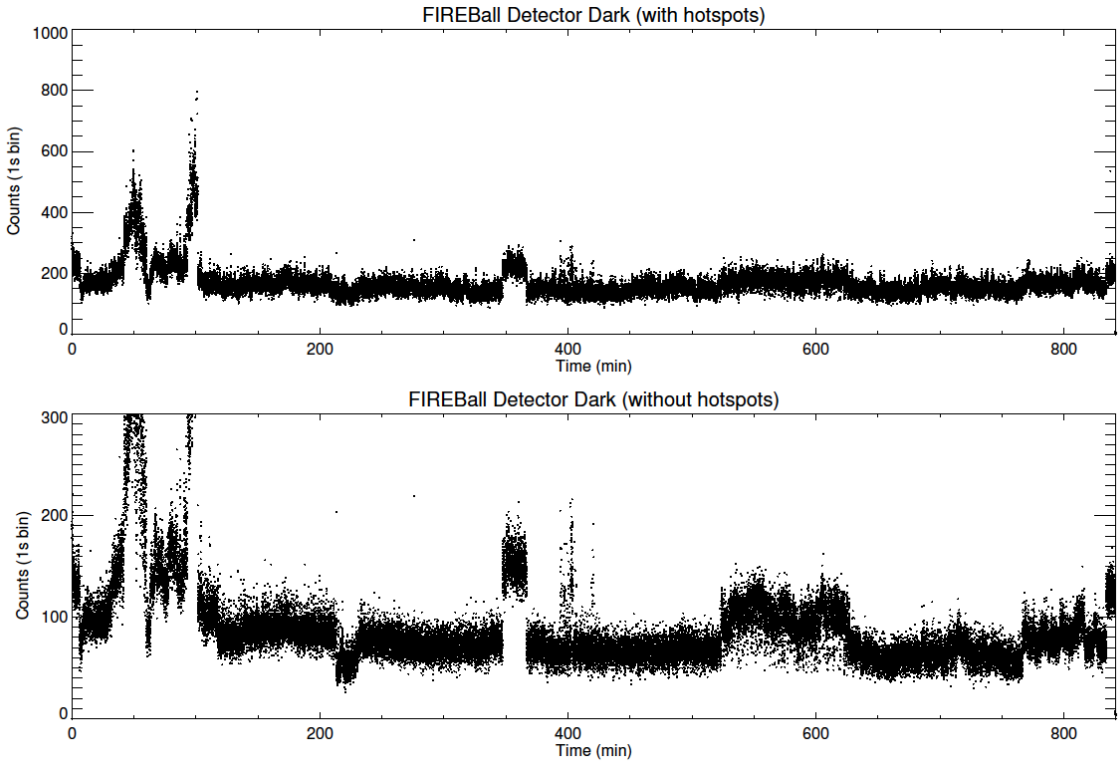

Figure 3.43. Detector count rate for the detector dark taken in 2005. The six hot spots contribute as much to the count rate as the remainder of the detector. The variability in the signal level is also evident, indicating nonuniform conditions and, possibly, inadequate baffling. Several fragments of the 14 hour exposure are usable, but they are insufficient to produce a high quality detector dark.

3.3.3.8 Celestial Coordinate Assignment

Pointing reconstruction is described in section 3.4.6. Its end product is a WCS coordinate solution for every guider frame during the observations (Calabretta & Greisen 2002). As each detector count is associated with a single guider exposure, the fiber that collected it is known, and the location of the fiber is known on the guider detector. Thus it can be tagged with RA and Dec information. At the end of this step, every detector count is associated with a triplet (α, δ, λ).

3.3.3.9 Data Cube Construction

The photon list for every target is binned into a three dimensional array. The voxels are 3" $\times$3" $\times$0.25 Å in size. This generates the basic data cube. To arrive at normalized flux in meaningful units, a second three-dimensional array needs to be constructed: an instrument response cube. This includes spectral response information, fiber-to-fiber efficiency differences, and the variation in exposure time as a function of on-sky position due to dithering. A sample exposure-time-only instrument response cube, collapsed along the wavelength direction, is shown in figure 3.45.

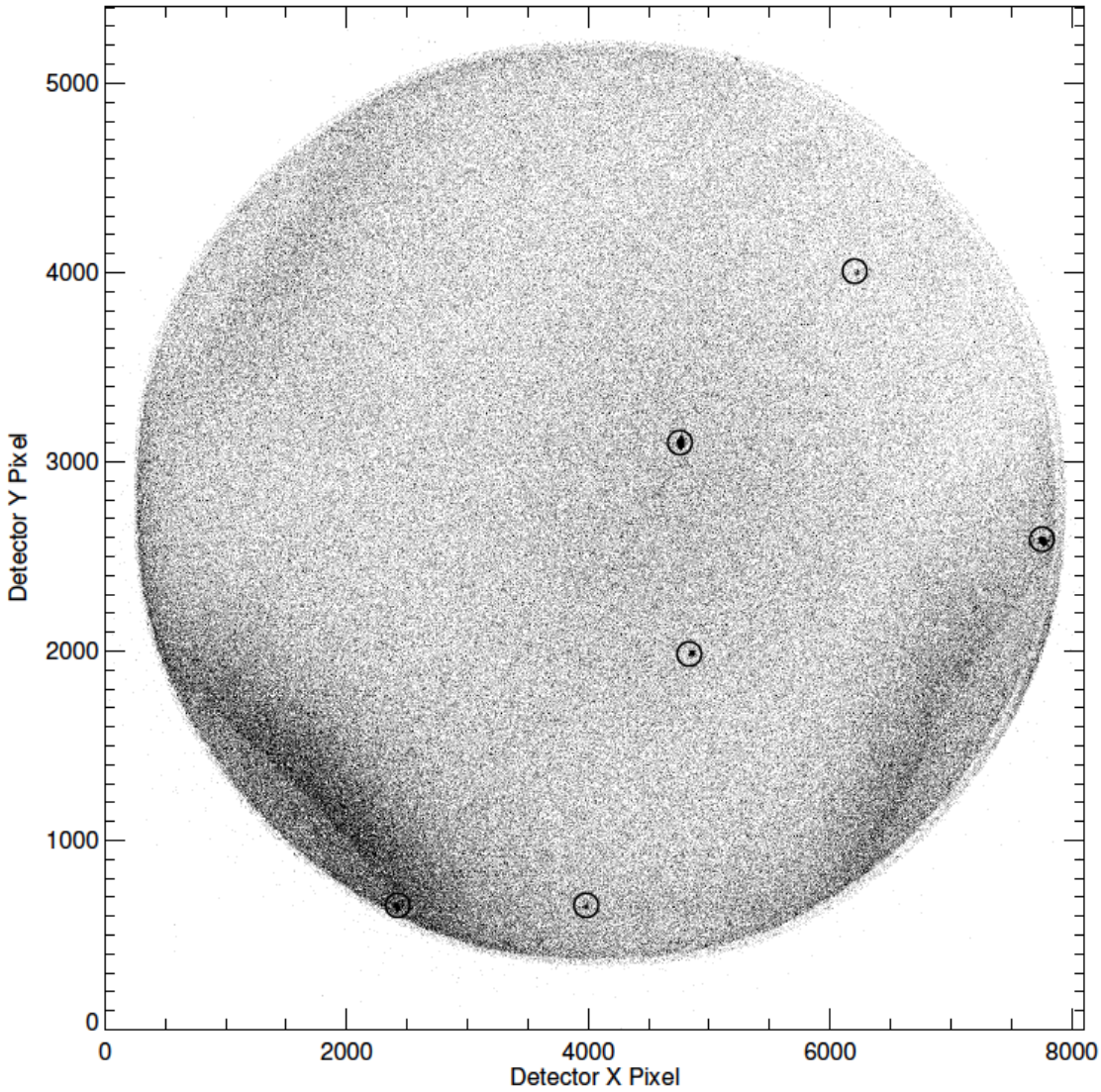

Figure 3.44. A two-dimensional histogram of the registered detector counts during the detector dark exposure described in section 3.3.3.7. The image color scale is inverted, darker regions having received more counts. The dark looks unlike the GALEX NUV detector dark (Morrissey et al. 2007); there appears to be nonuniform illumination with an excess of light incident from the bottom left and bottom right in the image. The six known hot spots have been circled.

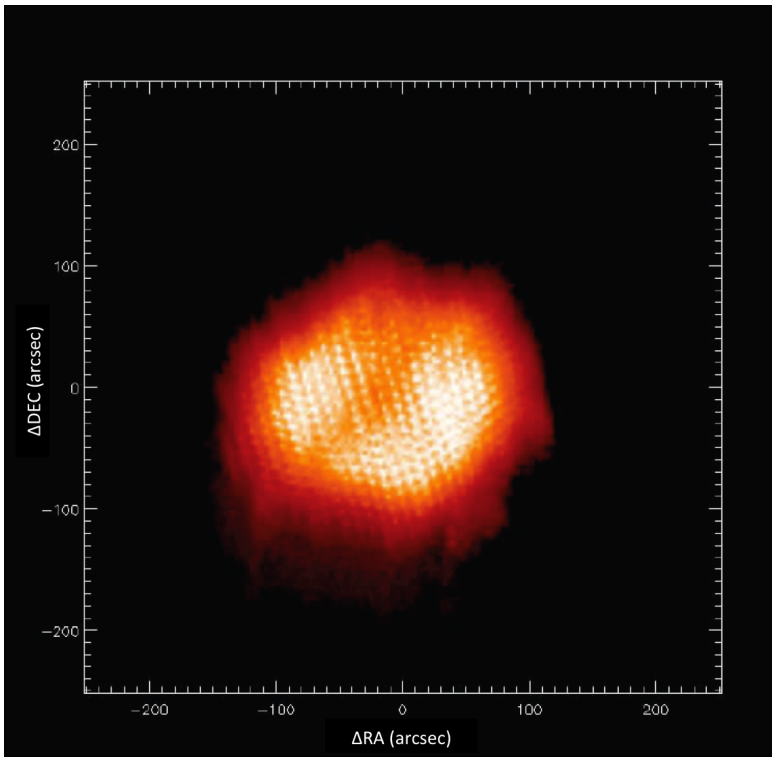

Figure 3.45. A slice through an example of an instrument response cube for a single target. This example only takes into account the effective exposure time as a function of position; all wavelength information has been collapsed. The values have been histogram equalized to emphasize the structure within the map.

3.3.3.10 Efficiency Estimate

FIREBall observed two calibration stars during the flight; their properties are summarized in table 3.5. Since FIREBall is intended to observe diffuse emission, its fiber size and spacing is not well matched to point sources. Extracting efficiency information from the point source data requires that the peak values detected be used for the estimate, as they correspond to the occasions when the image of the calibration stars fall directly onto individual fibers, and are thus representative of the efficiency when observing diffuse targets. The results of this analysis are shown in figure 3.46.

3.4 Telescope Pointing and Aspect Reconstruction

3.4.1 Pointing Requirements and Environmental Concerns

FIREBall was designed to detect diffuse emission around galaxies, along cosmic web sheets and filaments. To obtain deep observations with high signal-to-noise ratios, the instrument must be pointed at fixed targets for extended periods. The typical sizes of emission regions being observed are on the order of 30 to 100 arcseconds across. The FIREBall IFU offers a hexagonal field of view 140

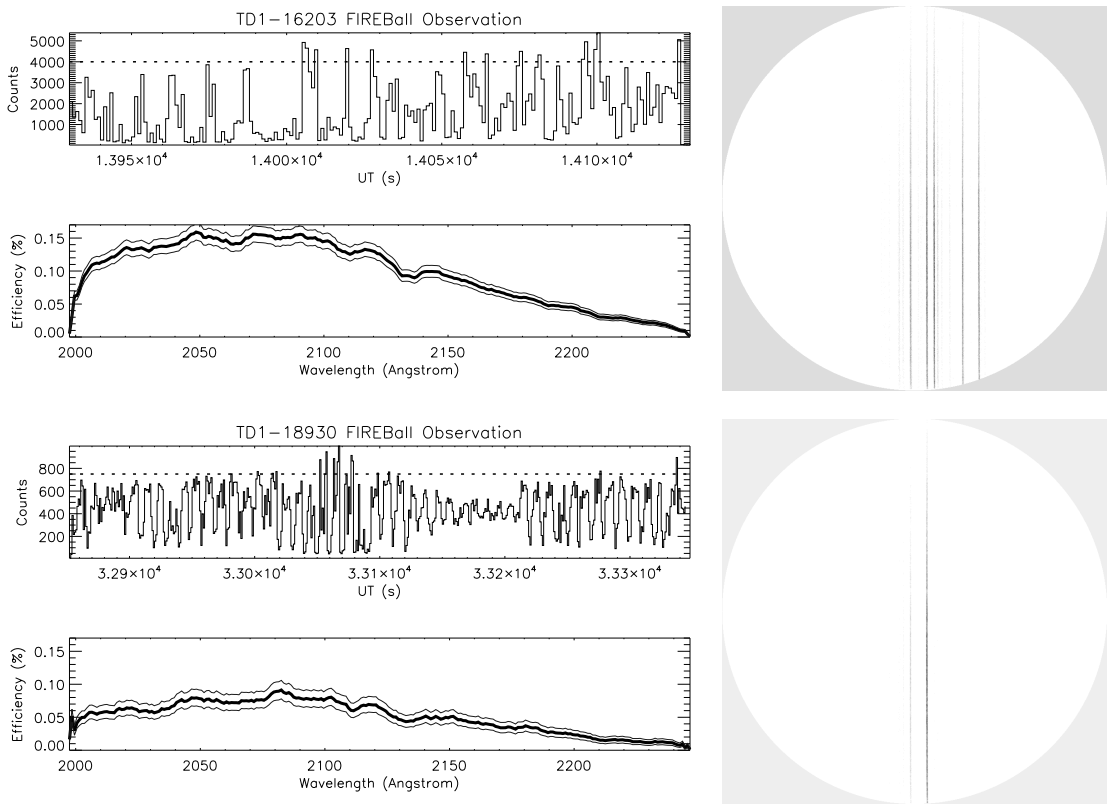

Figure 3.46. FIREBall instrument throughput, including the atmosphere, using two calibration stars observed in flight. The top plot in each case shows the number of counts arriving at the detector as a function of time, binned in 1s intervals. When the image of the star moves on the IFU fiber bundle, the amount of light falling on the detector varies, depending on whether the image is hitting a fiber or interfiber space. The tallest peaks in the histogram are representative of the total throughput. The spectra from the tallest peaks are then compared to UV photometric data from the TD1 satellite (Vreux & Swings 1977) to arrive at an approximate instrument efficiency. The lighter bounding curves show the 1σ errors on the estimate. The right panels are detector images of the two observations. As the vast majority of the light falls near the center of the detector, the efficiency curves are valid across the entire wavelength range; the changing bandpass with detector location does not play a role here.

Table 3.5. FIREBall calibration star information. Note that the two stars were observed at very similar altitudes and mean elevations. It is peculiar that the additional 700 m altitude droop and tiny change in observation elevation would cause a more than a factor of two decrease in the peak throughput. As of this writing, it is unclear what the cause of the difference in throughput is.

	TD1-16203	**TD1-18930**
RA (J2000)	$12^h18^m50.^s47$	$16^h04^m48.^s96$
Dec. (J2000)	$+75°09'37.''4$	$+70°15'42.18''$
Spectral Type	A1V	A0
B Magnitude	5.5	6.97
Observation Time	200 s	496 s
Observation Elevation	49.80°	49.67°
Observation Altitude	35.44 km	34.8 km
Peak. Trans.	0.15%	0.08%

Table 3.6. Estimate of the FIREBall instrument throughput within the balloon window wavelength band. The value might be an overestimate, as the Offner sphere and siderostat mirrors were not recoated prior to the second flight, and the reflectivity may have deteriorated in the two years since 2007. Combining this information with the observed throughput in flight suggests atmospheric transmission at the 15%-25% level.

Element	**Estimated Throughput**	**Comments**
Siderostat Mirror	85%	Measured at GSFC
Paraboloid Mirror	85%	Measured at GSFC
Dichroic Beam Splitter	80%	Measured by Manufacturer
Fiber Bundle	60%	Measured at Columbia University
Offner Sphere	85%	Measured at GSFC
Grating	35%	Measured at LAM
Detector	7%	Measured for GALEX
Total	0.6%	Not including the atmosphere.

arcseconds across, with each fiber covering an 8 arcsecond diameter circular region. The telescope must be held to better than 30 arcseconds to make sure that the target region is within the field of view. Accurate point source and background masking or subtraction requires that the location of these sources be well-known, at the subfiber level. This further restricts the pointing requirement to about 1/2 a fiber, or 4 arcseconds on the sky. FIREBall makes use of photon-counting microchannel plate (MCP) technology. This relaxes the pointing requirement somewhat, shifting the emphasis on postflight aspect solution reconstruction. However, as we anticipate using higher quantum efficiency (QE) CCD detectors for this project in the future, which will operate with longer integration times during which the telescope will have to be kept steady, we retain the 1/2 fiber pointing requirement.

The physical conditions affecting the giant balloon and heavy gondola at the float altitude of 115,000 ft make meeting this requirement difficult. The payload experiences temperature, pressure

and altitude changes, strong, often shearing, winds, and periodic ballast drops. These effects on the motion of the gondola have to be counteracted to allow for the telescope to meet the above-mentioned requirements.

3.4.2 Pointing Stabilization and Control

The pointing and stabilization of the FIREBall telescope are accomplished by way of two actuated elements. The first is the gondola pivot; it has an unlimited range of rotation, allowing for pointing at arbitrary azimuth. The second is the siderostat mirror, mounted on a gimballed frame. This allows the tilt angle of the optic to be set so as to observe at any elevation in the range of 40° to 70° — the lower cutoff due to instrument geometry and the poor atmospheric transmission at that elevation, the upper cutoff due to vignetting by the balloon. The mirror also has a cross-elevation tip mechanism that can rotate it in the range ±2° from the nominal orientation. The two motions of the siderostat are controlled by the fine stabilization control, which makes use of a precompensating open loop, and a compensating closed loop. This FIREBall pointing solution is based on those used by the CNES members of the collaboration on the FOCA (Milliard et al. 1994) and PRONAOS (Serra et al. 2002) experiments. The pivot and siderostat motors are heritage hardware from those projects. The control instrumentation and algorithms are described in more detail in Huguenin (1994).

Telescope pointing and stabilization is a multistep process. The initial pointing solution is arrived at by combining the gondola GPS location information with magnetometer orientation data and the desired observation target coordinates. The pivot and siderostat are adjusted to the appropriate azimuth and altitude settings. The boresight is thus kept pointed at the scientific target with an accuracy of a few dozen arcminutes, enough to hold the field within the field of view of an optical target recognition camera (Joergensen & Pickles 1998). Once the initial pointing solution is acquired, the pointing is refined via a two-stage process. The first stage, called precompensation, is an open loop control of the siderostat velocity, correcting the telescope boresight for 95% of the gondola's rotation velocity. The second stage is a closed loop control using error offset signals from an optical monitor. This corrects the residual errors from the precompensation, leaving a nominal RMS guidance error of 3 arcseconds on each axis. The computers responsible for these control loops collect and combine information from a battery of sensors. These devices are listed in table 3.7. A schematic of one of the three FIREBall control loops is shown in figure 3.47.

The gains, offsets, and phase shifts of the analog signals provided by the gyroscopes, and the gains and offsets of the optical guider signals, must be adjusted to optimize for best pointing performance. This procedure is performed during the instrument integration and calibration stage prior to flight. It starts by suspending the gondola above the ground, and illuminating the telescope with the artificial star source (section 3.3.2.1). Gondola motion is then excited in one of the several normal

Table 3.7. A list of gondola sensors involved in the telescope pointing and stabilization.

Sensor	**Function**
Gyroscopes	Three gyroscopes measure the gondola velocity around each of the three principal axes. Their output is coupled into the gondola precompensation loop.
GPS Sensors	Global positioning devices are used in targeting calculations, and for metrology.
Magnetometers	Two magnetometers measure the gondola orientation with respect to the ground.
Inclinometer + Potentiometer	Measure the location of the siderostat mirror with respect to the gondola. Used for configuring the telescope.
DTU Sensor (Joergensen & Pickles 1998)	The first of two optical sensors used in the fine pointing loop. It has a 13.4 × 18.4 square degree field of view, supplying a full astrometric solution to the gondola hardware at 2 Hz. Stabilizes pointing to ∼1 arcminute rms.
Optical Guider	The second of two optical sensors. Returns pointing offset errors at a maximum of 30 Hz. Reduces the rms pointing error to ∼ 3 arcseconds.

modes. The fine pointing system is turned on, and the gains, offsets, and phases of the gyroscope and optical sensors are adjusted to minimize the motion of the artificial star on the optical guider CCD. Several of the parameters can be adjusted digitally from the gondola master computer, while others require manual trimming of potentiometers on a proprietary signal-mixing tracker card.

3.4.3 Optical Guider

3.4.3.1 Guider Sensitivity Estimate

The optical guider serves as the fine sensor in the pointing control loop (see section 3.4.2). It must be able to analyze exposures and calculate pointing offsets at 30 Hz over a field of view large enough to allow for dithering excursions the size of the fiber bundle. The sensitivity and full field of view of the guider must be high enough to detect at least one star with a signal-to-noise ratio sufficiently high to obtain a centroid.

The field of view of the guider is limited to 28×22 arcminutes by the size of the detector and the focal ratio of the associated optics. The point-spread-function (PSF) of these optics has an rms radius of approximately 10 µm, meaning a point source is generally spread out over 9 pixels. As there is jitter in the pointing and the instrument, this PSF will be smeared out over several more pixels. Assuming the throughput to the guider is $\eta \sim 0.15$, following the discussion in appendix A, using the camera specifications, the guider will reach a signal-to-noise ratio of 10 at stellar magnitude

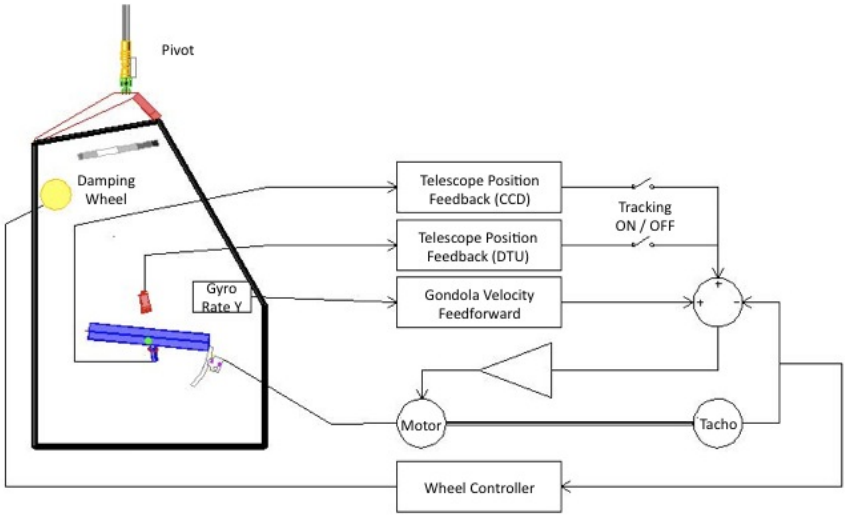

Figure 3.47. A schematic view of one of the two guidance control loops acting on the siderostat. The rotation of the gondola is measured by a gyroscope attached to the gondola structure. That velocity information is sent with a 50% angular gain as an open loop signal to the siderostat to precompensate for the line of sight changes due to gondola rotation. The information is then combined with the measured pointing angular errors from one of the guidance cameras, closing the error signal loop. The camera signal is injected with low gain, and trims the velocity of the siderostat mirror computed from the pre-compensation. Such a two-stage guidance solution is more stable than conventional guidance with no pre-compensation. A similar two-stage stabilization is used for the gondola pivot, which uses the gondola azimuth errors from the magnetometer as input for the closed loop stage, in place of an optical pointing error. Figure courtesy of J. Evrard (CNES).

13.5. This is consistent with the guider's in-flight ability to track on stars down to 12th magnitude. Following Table 19.5 of Cox (2000), there are ∼20 stars $B < 12.5$, leading to a mean expected number of tracking stars in the guider field of view of ∼3.4. Assuming Poisson statistics, at least one suitable tracking star should be available in roughly 97% of the fields. During extensive pointing system testing, and both FIREBall flights, only a single target field was encountered that lacked an adequate star for tracking.

3.4.3.2 Camera Hardware

The guider camera is a Retiga EXi frame-transfer CCD, and is capable of nearly simultaneous exposure and readout. The camera is being reused from the HEFT project (Harrison et al. 2000; Chonko 2006). It has 1360 × 1036 6.45 micron pixels and can be read out at 20 MHz. There is additional readout overhead; it takes about 80 ms to transfer data from the full chip to the control computer. The readout of a 200×200 pixel array takes approximately 25 ms. The detector has $8e^-$ read noise, and for the short exposures involved the dark current is negligible. The peak camera

efficiency is ∼60% at 550 nm. The camera bandpass is ∼200 nm. The exposures were triggered by a TTL signal generated by the guider computer. The data and command communication between the camera and computer is via a standard FireWire (IEEE 1394) interface.

3.4.3.3 Guider Control Electronics

The guider control electronics are built around a PC104 stack computer running Ubuntu Linux 6.86. The computer and associated electronics are housed in a stainless steel cylindrical pressure enclosure. The enclosure can be heated to assure that the electronics do not freeze out, though the computer does tend to run hot, and low temperatures were not a problem during either flight. There were a couple of instances during the first flight where the computer overheated and had to be shut down to cool. The enclosure was painted matte black to facilitate radiative heat loss, and overheating was not a problem at all during the second FIREBall campaign. A photograph of the simple mounting scheme of the electronics is shown in figure 3.48, and a list of the components is given in table 3.8, detailing their functions. The power and data are transmitted through vacuum feed-through connectors on the front face of the enclosure. Custom cables connect the guider electronics to other gondola subsystems.

3.4.3.4 Flight-Side Software

The flight computer runs Ubuntu Linux, and the guider control software is written in C and C++. The system has been configured to limit the number of resident applications running, and does not rely on using XFree86 window manager software. All of the graphics display is done via direct access to the video memory using low level routines through the SVGAlib library. The camera is controlled with a driver furnished by the camera vendor, QImaging, and the routines included in the company's Linux Software Development Kit. The GPS module was read out as a serial port, and its output parsed using routines modified from those provided by the manufacturer. Communication with other subsystems on the gondola is accomplished via serial connections and the standard serial protocol.

The guider control software consists of three main parts: data and hardware initialization, main control loop, and an image processing task. The functions of these parts are summarized in table 3.9. Initialization occurs once, when the program is started. The main loop runs continuously, listening for messages on several communication channels, and adjusting camera mode settings and parameters accordingly. The image loop process is spawned every time the camera finishes an exposure. This separate thread processes the image, extracting source location. The full CCD algorithm is based on a modification of the blob extraction code used for the HEFT mission written by Edward Chapin and James Chonko (Chonko 2006). A similar algorithm has been written to locate sources within smaller regions of the CCD. The software calculates pointing error offsets between a designated

Table 3.8. List of computer parts and stand-alone hardware housed in the guider electronics pressure enclosure

Component	**Part No.**	**Function and Comments**
Motherboard	ADL855PC-370C	General processing. Chosen for relatively low power consumption and processing power. Contains a Intel Celeron-M 1.5GHz processor with 1024K cache.
GPS Board	WinSys PCM-Gps	GPS receiver.
FireWire Board	MSMW104+	Control of, and communication with, the guider camera.
I/O Board	104-AIO-12-8	Used for generating the trigger signal for the guider camera, generating pointing offset voltages for telescope control loops, and reading out the LVDT (focus stage position information).
Comm. Board	104-COM-8	A serial communications board used to exchange information with the flight computers, detector computer, and ground control station.
Hard Disk		A standard 2.5" HDD. The flight unit was 80 Gb in capacity, which proved to be a little small for the amount of data that was being stored on a daily basis. Transfer of this data off the machine was also lengthy. It would be good to have a larger capacity hard drive for future flights. Replacing the platter disk with a solid state storage device might also allow us to move away from the bulky PC enclosures we used for the first two flights. The operating system is configured to make use of the DMA data transfer capabilities of the drive to allow for shorter read/write times.
Power Supply	HE104-HP-16	Accepts the gondola-provided DC voltage and regulates it to the voltages needed by the PC stack.
Video Converter	Grandtec UltiMate 2000EX	Not part of the computer stack, this device powers off the computer supply and converts the standard RGB monitor signal into an NTSC signal for the video downlink.
Motor Controller	IMS MicroLYNX	A stand-alone motor controller that takes serial communication input from the computer, outputting a 4-phase signal to drive the focal plane stage.
Environment Recorder	Omega	A small, battery powered device that records the temperature and pressure inside the enclosure.
Temperature controller	TC145	A temperature controller attached to a Minco heater to maintain the hardware at room temperature or above.

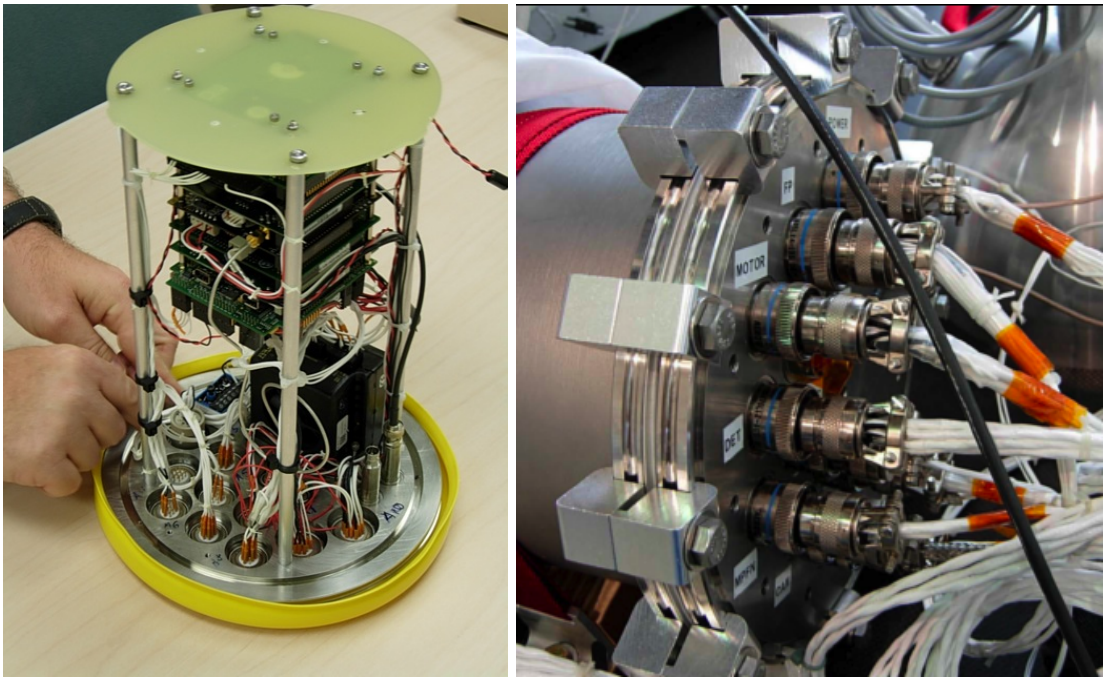

Figure 3.48. Photographs of the guider electronics. The left panel shows the PC104 computer stack attached to a G10 fiberglass plate (translucent yellowish-green surface at the top of the image). The components of this computer are listed in table 3.8. The MicroLYNX motor controller, temperature controller, and pressure-temperature recorder are attached to the flange, at the bottom of the image. All electrical connections are made through this enclosure bulkhead. The right panel shows the guider flange aboard the gondola with all the electrical connections completed.

Table 3.9. A summary of the tasks performed by the three principal parts of the guider software

Initialization Runs at the start of the program	**Main Loop** Always running	**Image Processing Task** Runs after each exposure
Start logs	Parse telemetry stream	Reject hot pixels
Configure ports	Update logs	Extract sources
Test communication	Reconfigure camera	Generate offset data
Start camera driver	Reconfigure guider mode	Update gondola pointing
Initialize camera trigger	Update GPS information	Update display
Exercise focus stage	Reconfigure display options	Send information to ground
Queue camera exposures		Send information to detector
Set guider mode parameters		Queue next camera exposure

tracking point and the centroid of a star, passing them to the gondola flight control hardware as an analog voltage, and to the detector computer as a serial message.

The program is configured to start automatically when the guider computer is turned on, and runs until a shutdown command is issued. It is in constant communication with the ground station,

Table 3.10. A summary of the FIREBall guider computer communication channels

Channel	**Purpose**	**Type**
Camera	Camera control and image download	FireWire
Ground station	Command interface and housekeeping data download	Serial (9600b)
Detector computer	Pointing updates, guider frame timing	Serial (112kb) & TTL
Gondola computer	Pointing commands, switching sensors, pointing information	Serial (112kb)
GPS	Time and position information	serial (9600b)

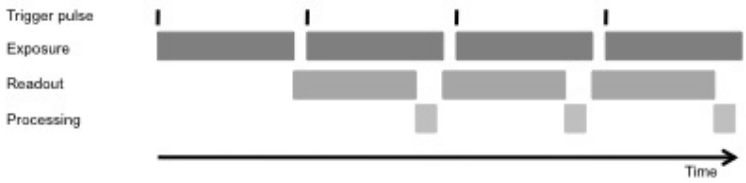

Figure 3.49. Schematic showing the guider timing. Exposure starts as soon as the camera receives a trigger pulse. Once the exposure is finished the readout starts. After that is done, the guider software processes the collected data. The delay from the middle of the exposure period to when error offsets are available is $\sim$ 160 ms for the large window and 40 ms for the region of interest readout. Note that the exposure and readout are simultaneous.

gondola flight hardware, and the detector computer. The communication channels are outlined in table 3.10.

The guider camera operates in free-run mode with simultaneous exposure and readout. When the full chip is utilized, exposures are triggered every 110 ms with an exposure time anywhere between 1 and 100 ms. In small-window mode, where only a subregion of the device is used, exposures are triggered every 33 ms. Image processing begins almost immediately after the readout is complete. A timing schematic is shown in figure 3.49.

The guidance utilizes one of two modes: a full CCD mode (roughly 28 $\times$ 22 square arcminutes), and a region-of-interest (ROI) mode (roughly 4 $\times$ 4 square arcminutes). The pointing error signals are generated in the same way for both. The operator designates a tracking pixel and selects a tracking star; the distance between the centroid of the source and the tracking point is converted into a pair of analog voltages, one for each CCD axis. These are fed to the main gondola tracking loop (see figure 3.47). In the full CCD mode, a bounding box around the star keeps track of which of the several sources in the field is the object of interest. This bounding box is typically the same size as the ROI mode window. In ROI mode, as there is usually only one bright source, the strongest star in the field is used for tracking. Dithering is accomplished by automatically adjusting the tracking

Table 3.11. The raster definition file is a simple text file. It contains 4 preamble lines that define the time step, number of steps, whether the raster is relative or absolute, and how many times to repeat the pattern. Coordinates of dither points follow.

Quantity	**Units**	**Notes**
TIMESTEP	Seconds	The length of time between consecutive raster steps are taken.
STEPS		The number of steps within the dither pattern.
RELATIVE	Yes/No	Whether the raster is to be performed as an offset from the current tracking point (Yes), or whether the provided points are absolute CCD coordinates (No).
REPEAT		Number of times to repeat the dither pattern.
X Y		Coordinates of raster offsets or locations. The number of entries of this kind is equal to the value of STEPS (above).

Table 3.12. An example dither file. The sequence would move the tracking point around a 1 pixel square, changing location every 0.5 seconds. The motion would be relative to the starting location and would not repeat.

```
TIMESTEP 0.5
 STEPS    4
 RELATIVE 1
 REPEAT   1
    0     0
    0     1
    1     1
    1     0
```

pixel. The software allows for arbitrary dithering offsets to be added to the tracking points specified via a loadable configuration file, whose format is given in tables 3.11 and 3.12. A snakelike pattern was the only one used in flight (see Fig. 3.50).

The guider display can be adjusted for contrast, brightness, and gamma corrected to emphasize the dimmest sources. In addition to the most recently obtained image, the guider display includes focus stage position information, GPS time and position data, guider frame number, track-star size, and a zoomed view of the object being tracked. Photographs of the guider displays are shown in figures 3.51 and 3.52.

The guider hardware and software communicates with the detector computer. It sends an analog pulse after each CCD readout, and a serial message after image analysis. These messages are folded

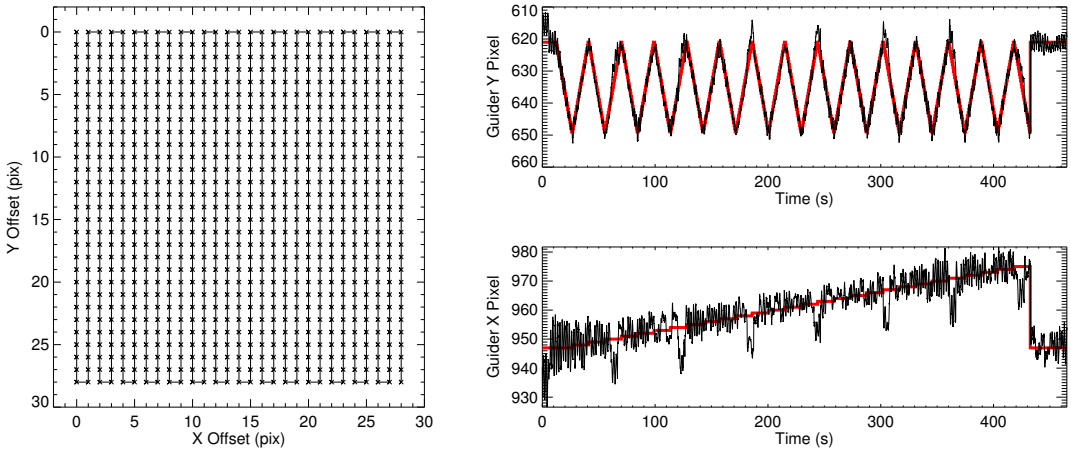

Figure 3.50. The left panel shows the dither pattern used during the FIREBall flight. The relative offset starts at (0, 0) moving the tracking point 28 pixels along the y-axis, then shifting one pixel in the x direction, backtracking in y. The time step between the discrete locations is half a second; the full dither takes seven minutes to execute. The dither covers a 35×35 square arcsecond area. The right panel shows the centroid location of a tracking star during a dither observation in the 2009 flight. The thick background line indicates the designated tracking pixel; the thinner foreground line shows the measured star centroid. There is substantial jitter around the designated location; this is discussed further in section 3.4.

into the photon-counting detector's data stream, and are used for postflight pointing reconstruction (see section 3.4.6). Additionally, the flight side software stores a variety of information to facilitate postflight data processing. This data is detailed in table 3.13.

3.4.3.5 Ground-Side Software, Telemetry and Command Interface

The ground side software is a graphical user interface (GUI) that facilitates communication with the guider computer. The software was written in Microsoft Visual C++ on a Windows computer for the first flight, and rewritten in Tcl/Tk on Linux hardware for the second. This change was implemented to allow the program to run on a variety of platforms without the need for proprietary libraries. The layout was similar for both GUIs. A screen capture of the layout from the first flight software is shown in figure 3.53. A short list of some of the telemetry commands and messages is given in table 3.14. The command format is based on that used by CNES for interinstrument serial communication. It contains start and stop bytes, message counter, message length, a cyclic redundancy check byte (CRC), and message information in hexadecimal format; it is detailed in table 3.15. The flight-side software returns a message echo confirming the receipt of a valid message. The ground software can generate an astrometric solution to the observed starfield by calling the Astrometry.net Lang et al. (2010) software suite. This information is then used, in conjunction with

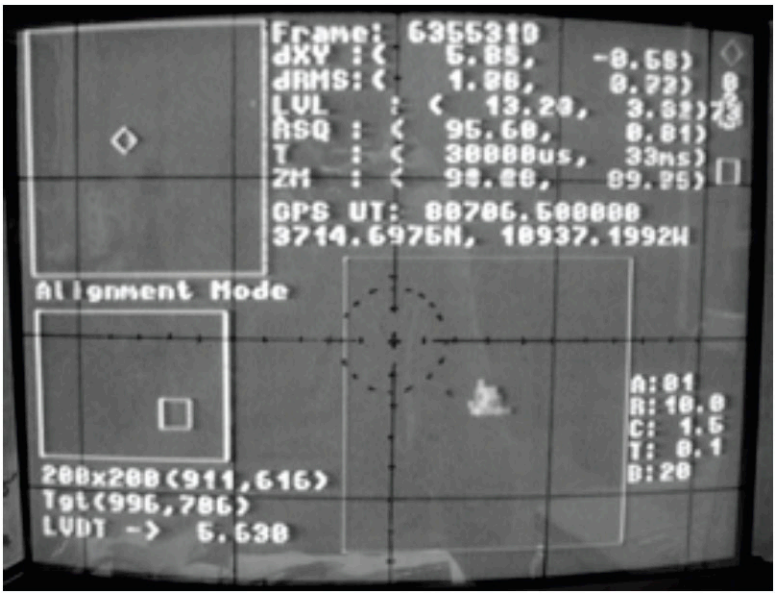

Figure 3.51. Display in the region-of-interest guider mode. The square at the top left shows the full ROI. The diamond is centered on the tracking point. There is a star on the right side of this diamond. The rectangle at the bottom left of the screen shows the location of the ROI on the full CCD. The square on the right shows a zoomed view of the image of the star; this is used for assessing the quality of telescope focus. The data at the top right includes the guider frame number, the current offsets of the star from the tracking point (in pixel units), a leaky average of the rms offset, data on the background level in the ROI, the location of the star within the ROI and its size. Also displayed are GPS information (UT, latitude and longitude) and the exposure and trigger times.

Table 3.13. A summary of the data stored on board the guider computer. The frequency with which it is saved and its intended purpose are indicated.

Type	**Timing**	**Comments**
Guider images	0.9 Hz or 5 Hz	Stored in both full chip and region of interest modes. As the image processing tasks make intensive use of the system, only every tenth full frame is saved (0.9 Hz), and every 6th frame in the ROI mode (5Hz). The images are used to reconstruct pointing.
GPS information	continuous	UTC time and balloon location and altitude. Combined with target coordinates to yield altitude-azimuth information.
LVDT reading	0.2 Hz	Location of the focal plane focusing stage
Pointing offset information	9Hz or 30Hz	The offset between the designated tracking point and the barycenter of the tracking star.
Multiple star locations	9Hz	The locations of up to 10 stars in the field of view of the guider are stored for each full frame.

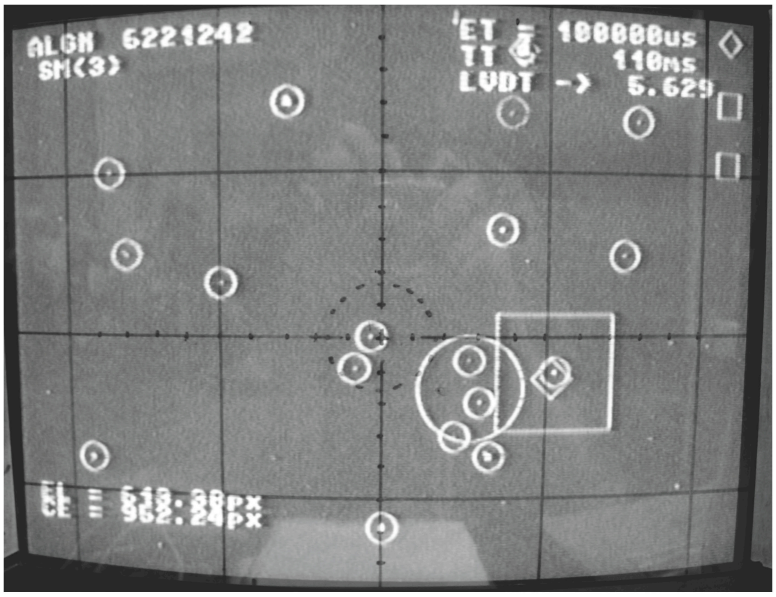

Figure 3.52. Display in the full CCD guider mode. The sources that have been found are encircled (18 in this image). The location of the IFU fiber bundle is marked with the larger white circle. The tracking point is marked with a diamond near the IFU bundle circle, and is surrounded by a bounding box. The star that is currently being tracked on is inside the diamond. The guider frame number is shown in the top left corner, exposure and trigger times in the top right.

a separate program that accesses the USNO B star catalog (Monet et al. 2003), to generate tracking point and tracking star pairs that place the desired target field on the IFU fiber bundle.

3.4.4 In-Flight Target Acquisition and Pointing Procedure

An observation begins with the target coordinates being uploaded to the flight control computers. The gondola pointing system then orients the pivot and the siderostat mirror to the desired azimuth and elevation. The DTU sensor (Joergensen & Pickles 1998) takes control of the pointing. A command is issued for the optical guider to replace the DTU in the tracking loop, and to use the brightest star in its field at its current location as the tracking star and tracking point. The star-field in the FOV of the guider is then confirmed at the guider ground station using Astrometry.Net (Lang et al. 2010) and a specially written display program, written by Chris Martin with contributions from the author, that returns the necessary tracking point for any given star within the FOV that places the science target onto the IFU fiber bundle. The new tracking star and tracking point are designated. At this point, the instrument begins taking data. The guider is switched from full-CCD to ROI mode to improve tracking performance. It is periodically switched back to full chip mode to confirm pointing and adjust for the effects of natural field rotation associated with an alt-azimuth telescope mount. The guider mode as a function of time for an observation is shown in

Table 3.14. A highlight of the commands sent to the flight guider computer, and the messages transmitted back to the ground

Command	**Parameters**	**Description / Comments**
Switch Optical Sensor	—	Specifies which of the two optical sensors onboard the gondola is part of the pointing loop.
Switch Gondola Mode	—	Switches the gondola between the observing configuration and the autocollimation mode.
Acquire Star	—	Begins tracking on the brightest object in the field of view at the spot where it is located when the command is received. This command is essential in stabilizing pointing when the gondola is oscillating and the images of the stars move quickly on the guider CCD. This command was especially useful during the first flight, when it allowed FIREBall to guide on stars for short periods of time despite the loss of pivot control.
Adjust ROI	ROI coordinates	Changes the location and size of the ROI being used for guiding.
Adjust Times	Exposure and Trigger times	Changes the trigger and exposure times for the guider.
Adjust Tracking Point	New coordinates	Changes the location of the tracking point. This is usually used to adjust pointing for field rotation.
Change Tracking Star	New bounding box	Changes which star is to be used for tracking. Often sent in conjunction with a new tracking point.
Modify Display	New display parameters	Adjusts the display grayscale.
Move Focusing Stage	Number of steps	Moves the focusing stage a specified amount, or returns it to the predesignated zero position.
Toggle Focal Plane Pinholes	—	Toggles the focal plane pinhole illumination.
Toggle Dither	Dither ID	Toggles the execution of a specified dither pattern.
Track-Star Information	Star offset error, star size	Information sent to the ground station by the guider software.
Star-Field Information	up to 10 coordinates	Coordinates of up to 10 of the brightest objects in the field of view of the guider. Used to generate the ground-side display, and to find an astrometric solution.

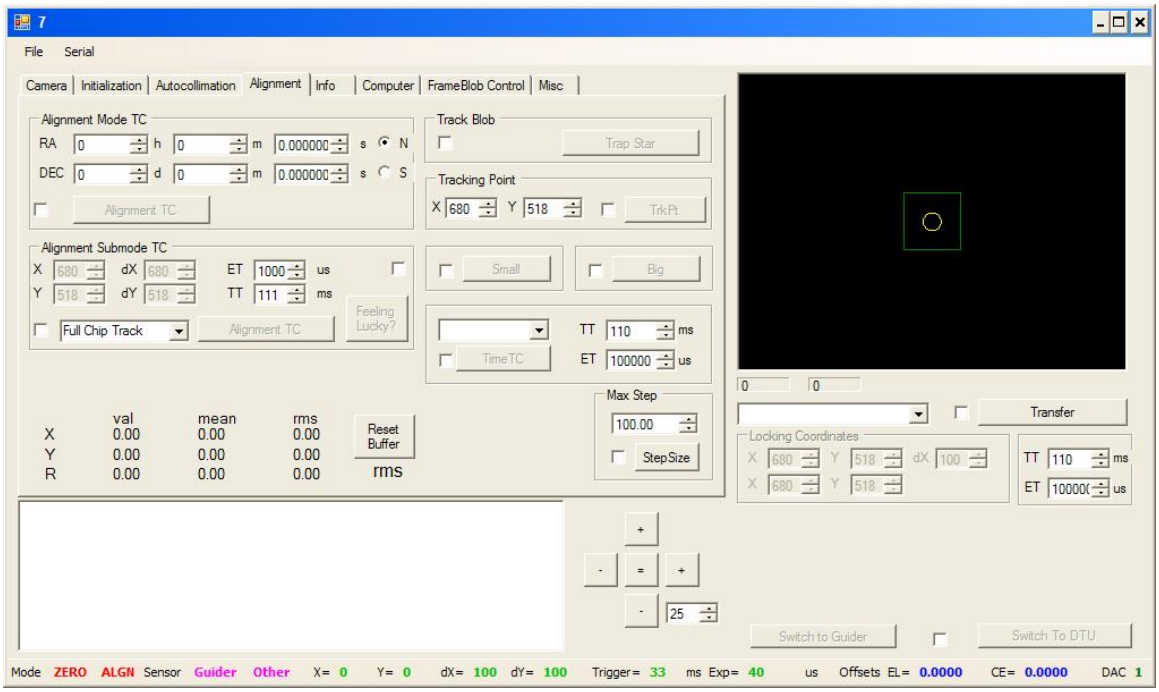

Figure 3.53. Guider ground station control window. The controls allow for changing the tracking point and tracking star, either by manually entering values into dialog boxes (which is used for refining pointing), or by clicking within the black rectangle representing the guider CCD. During the flight, the positions of the ten brightest stars in the field of view of the guider were displayed as circles in that box. Exposure and trigger times can be set, and control of the pointing can be transferred from the optical guider to the DTU. Controls in other tabs allow for adjustment of focus stage position, image display parameters, and camera settings. The software allows the operator to initiate dither patterns and adjust the source-finding algorithms. The status bar at the bottom of the window displays some of the housekeeping information that is sent down from the gondola.

Table 3.15. The structure of a serial message telemetry command. The message validity is checked by using the CRC and verifying the message length. The data values are checked to make sure they fall within specified physical limits.

Field	Bytes	Value	Comment
Sync. byte	1	0x55	Synchronization byte
Counter	2	varies	Message counter variable
Length	2	varies	Length of data in the message
Message ID	1	varies	Value identifies the kind of message
Message	varies	varies	The content of the message
CRC	1	varies	Cyclic redundancy check byte
Sync. byte	1	0xAA	Synchronization byte

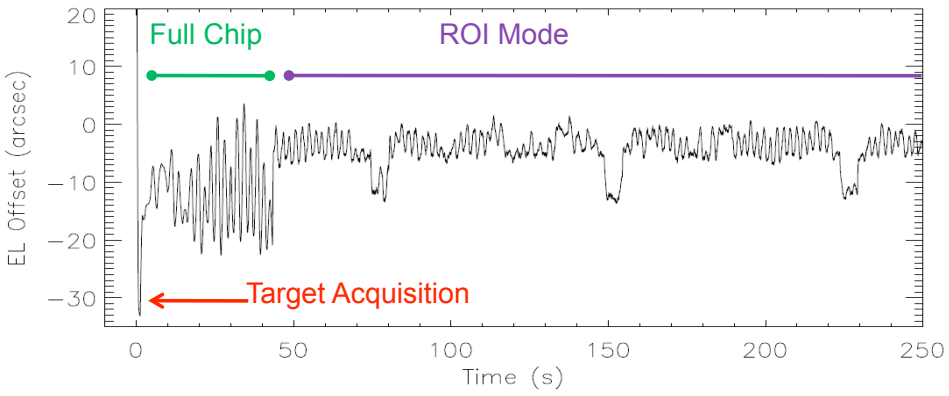

Figure 3.54. A curve showing the offset between a tracking star and a tracking point along the elevation axis. The guider starts off in full-CCD mode. The target star is acquired and brought within a couple of seconds to the desired tracking point. The pointing is verified and adjusted, if necessary. The guider is then switched to the ROI mode, where the instrument collects data.

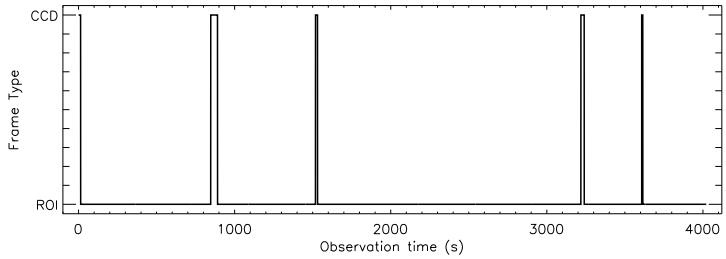

Figure 3.55. A graphical representation of the guider mode used during an on-target observation. The instrument starts in full CCD mode for field identification and target location correction. It is then switched to region of interest mode to improve the offset error delivery rate to the gondola hardware. The guider is periodically switched to the full CCD mode to verify pointing, and adjust if necessary.

figure 3.55, while the star-tracking point offset waveform at the start of an observations is shown in figure 3.54. During observations, the tracking system can implement a preprogrammed dither pattern (see section 3.4.3.4).

3.4.5 In-Flight Pointing Performance

The FIREBall telescope pointed without incident during the second flight. The guider computer records the offset between the tracking star and tracking point for every exposure taken during the flight. A sample waveform is shown in figure 3.56 The rms jitter in the pointing was below 3 arcseconds in the elevation axis and approximately 6 arcseconds in the cross-elevation axis; this performance is summarized in table 3.17. The pointing solution in ROI mode, delivered at 3 times the rate of the full-CCD mode, improves the tracking stability by a factor of two. The discrepancy

Table 3.16. Details of the FIREBall targets cross referenced with guider computer information used in reconstruction.

ID[a]	**Target**	**Target Coords.**[b]		**Track-star Coords.**[c]		**Track-star Pos.**[d]		**Framenumber**			**Star Catalog**	**USNOB**
	Name[e]	**RA**	**Dec**	**RA**	**Dec**	**x**	**y**	**Ref.**[f]	**Start**[g]	**Stop**[h]	**ID**[i]	**R1 Mag**[j]
2	TD1-16203	184.70826	75.160561	185.53814	75.110317	394.907	775.863	5977620	5976120	5977867	TYC4550-1460-1	10.7
2	TD1-16203	184.70826	75.160561	184.70826	75.160561	919.478	451.728	5977620	5977868	6035377	TD1 16203	5.4
3	D2ZLE1v1	252.76791	34.876111	252.78768	34.810639	636.147	548.552	6038980	6038636	6138859	TYC2597-915-1	9.6
3	D2ZLE1v1	252.76791	34.876111	252.78768	34.810639	659.791	552.384	6138920	6138860	6167170	TYC2597-915-1	9.6
4	PG1718+481	259.90938	48.070111	260.20092	48.054275	502.58	149.058	6182430	6182397	6186929	BD+48 2507	8.7
4	PG1718+481	259.90938	48.070111	259.8775	48.120828	949.389	616.396	6187040	6186930	6205379	USNOB1.0-3512-00721-1	11.3
4	PG1718+481	259.90938	48.070111	259.8775	48.120828	936.536	617.486	6205490	6205380	6222317	USNOB1.0-3512-00721-1	11.3
5	GLYA3	215.264	53.04	215.46046	53.148519	372.255	795.5	6230670	6229444	6246629	TYC3859-454-1	10.9
5	GLYA3	215.264	53.04	215.46046	53.148519	416.401	868.007	6246790	6246630	6264829	TYC3859-454-1	10.9
5	GLYA3	215.264	53.04	215.46046	53.148519	431.753	855.705	6264940	6264830	6275409	TYC3859-454-1	10.9
5	GLYA3	215.264	53.04	215.46046	53.148519	427.845	863.782	6275460	6275410	6278559	TYC3859-454-1	10.9
5	GLYA3	215.264	53.04	215.46046	53.148519	394.066	855.1	6278660	6278560	6284009	TYC3859-454-1	10.9
5	GLYA3	215.264	53.04	215.46046	53.148519	439.105	894.242	6284040	6284010	6286699	TYC3859-454-1	10.9
5	GLYA3	215.264	53.04	215.46046	53.148519	439.829	911.255	6286730	6286700	6293519	TYC3859-454-1	10.9
5	GLYA3	215.264	53.04	215.46046	53.148519	467.43	913.184	6293550	6293520	6302167	TYC3859-454-1	10.9
5	GLYA3	215.264	53.04	215.30944	52.967572	1024.18	743.87	6302510	6302168	6303699	USNOB1.0-3859-00701-1	11.2
5	GLYA3	215.264	53.04	215.30944	52.967572	977.514	718.771	6304520	6303700	6400079	USNOB1.0-3859-00701-1	11.2
5	GLYA3	215.264	53.04	215.30944	52.967572	1006.89	690.22	6400210	6400080	6455800	USNOB1.0-3859-00701-1	11.2
6	TD1-18930	241.20399	70.278383	241.20399	70.278383	795.551	627.025	6459740	6458363	6473058	TD1 18930	6.8
7	PG1718+481	259.90938	48.070111	259.83795	48.061878	844.918	493.73	6478610	6476650	6510029	TYC3512-642-1	8.9
7	PG1718+481	259.90938	48.070111	259.83795	48.061878	875.876	506.849	6510120	6510030	6527835	TYC3512-642-1	8.9
8	D2ZLE1v2	252.76791	34.876111	252.78768	34.810639	965.908	595.157	6530530	6530410	6555789	TYC2597-915-1	9.6
8	D2ZLE1v2	252.76791	34.876111	252.78768	34.810639	995.741	625.761	6556170	6555790	6575199	TYC2597-915-1	9.6
8	D2ZLE1v2	252.76791	34.876111	252.78768	34.810639	1005.58	623.839	6575310	6575200	6626439	TYC2597-915-1	9.6
8	D2ZLE1v2	252.76791	34.876111	252.78768	34.810639	970.531	589.531	6626620	6626440	6637789	TYC2597-915-1	9.6
8	D2ZLE1v2	252.76791	34.876111	252.78768	34.810639	1007.67	632.819	6637840	6637790	6650150	TYC2597-915-1	9.6

[a]Guider target field identifier
[b]Target field coordinates
[c]Tracking star coordinates
[d]Trackstar position on the guider CCD in the reference frame.
[e]Target name
[f]The number of the guider camera frame used as a reference for interpolating solutions between the start and the end frames.
[g]The start frame for an interpolation interval
[h]The end frame for an interpolation interval
[i]Tracking star catalog and identifier.
[j]The R1 magnitude of the tracking star reported by the USNO B 1.0 star catalog.

Target	ROI Mode				Full CCD Mode			
	Cross-Elevation		Elevation		Cross-Elevation		Elevation	
	Offset	RMS	Offset	RMS	Offset	RMS	Offset	RMS
DENEBOLA	-1.86	5.02	-3.93	1.90	-9.04	8.66	-9.12	6.04
TD1-16203	-0.73	4.65	-4.04	2.34	-1.66	13.67	-11.55	5.93
D2ZLE1v1	-0.92	5.45	-3.38	2.85	-2.95	11.12	-8.46	5.04
PG1718+481v1	-0.37	5.87	-3.69	2.89	1.57	11.61	-9.36	5.65
GLYA3	0.08	6.41	-4.49	2.89	2.12	15.08	-13.77	6.41
TD1-18930	0.77	5.96	-3.95	2.61	1.48	13.51	-12.22	5.64
PG1718+481v2	1.95	5.79	-4.37	2.63	7.97	12.15	-13.13	5.65
D2ZLE1v2	0.44	6.37	-4.25	3.10	-1.25	14.11	-11.91	8.07

Table 3.17. A summary of the FIREBall pointing stability. For each mode and axis the mean offset between the tracking point and star being used to guide is given, as is rms extent of the jitter around that mean. All numbers are given in arcseconds. The elevation axis outperforms the cross-elevation axis for both modes in stability by roughly a factor of two. The fine pointing ROI mode is also a factor of two more stable than the full-CCD mode. Non-zero offsets between the pointing star and tracking point are likely due to an imprecise zeroing or drifting offset added to the guider analog voltage sent to the gondola siderostat motion controller.

between the two axes is due to the cross-elevation drive relying on a screwjack that is heritage hardware from other CNES missions. The torque needed to actuate the FIREBall siderostat gimballed table is at the very edge of the rating for the custom motor. This is a mechanism that will likely be replaced for any future FIREBall mission, and it must be if an integrating CCD detector is to be used in lieu of a photon-counting microchannel plate. The offset waveforms can be Fourier transformed to glean insight into the nature of the residual oscillations and to improve the existing gondola rotation precompensation algorithms. The result of such a transformation is shown in figure 3.57, which highlights the observed residuals that were the chief contributors to the pointing jitter.

3.4.6 Postflight Pointing Reconstruction

A combination of in-flight pointing accurate to a few arcseconds, a photon-counting detector with high rate readout, and time-stamped guidance bookkeeping data allows for postflight pointing reconstruction. This process begins with finding a full astrometric solution to stored guider images that contain multiple stars. Astrometry.net software is used to identify these fields and generate a WCS solution, which includes a reference pixel (usually the centroid of the star being tracked on), reference coordinates ((α, δ) of that star), and a transformation matrix from guider pixel to celestial coordinates. Not every guider frame is recorded due to disk-space and processing-speed considerations; for those that are not, the tracking star centroid, and tracking point are recorded. The existing full astrometric solutions are interpolated based on this data, provided such solutions exist for nearby times on either side of the frame being solved. That is the case for almost all full-chip

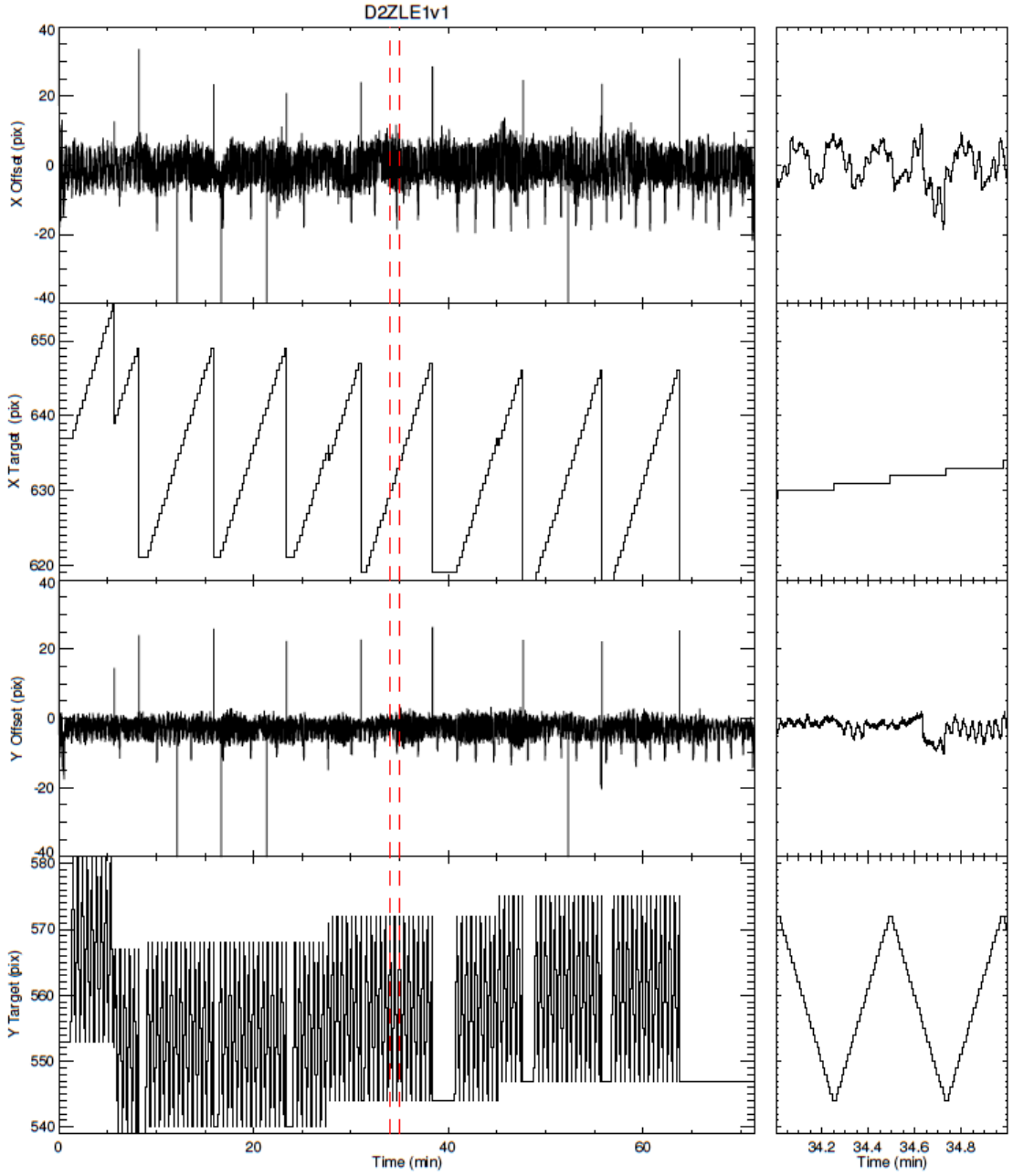

Figure 3.56. Pointing offset waveforms for the first visit to the D2ZLE1 field. The wider plots in the left column are for the full observation, the narrower boxes on the right for a subinterval marked with long-dashed red vertical lines. The top panel shows the offset between the tracking star and the tracking point along the telescope cross-elevation axis (tangent to the azimuthal direction); the panel immediately below it gives the cross-elevation coordinate of the designated tracking point. The remaining two panels show the same two quantities but for the elevation axis. The jagged nature of the tracking point coordinates is a manifestation of the use of the dithering algorithm.

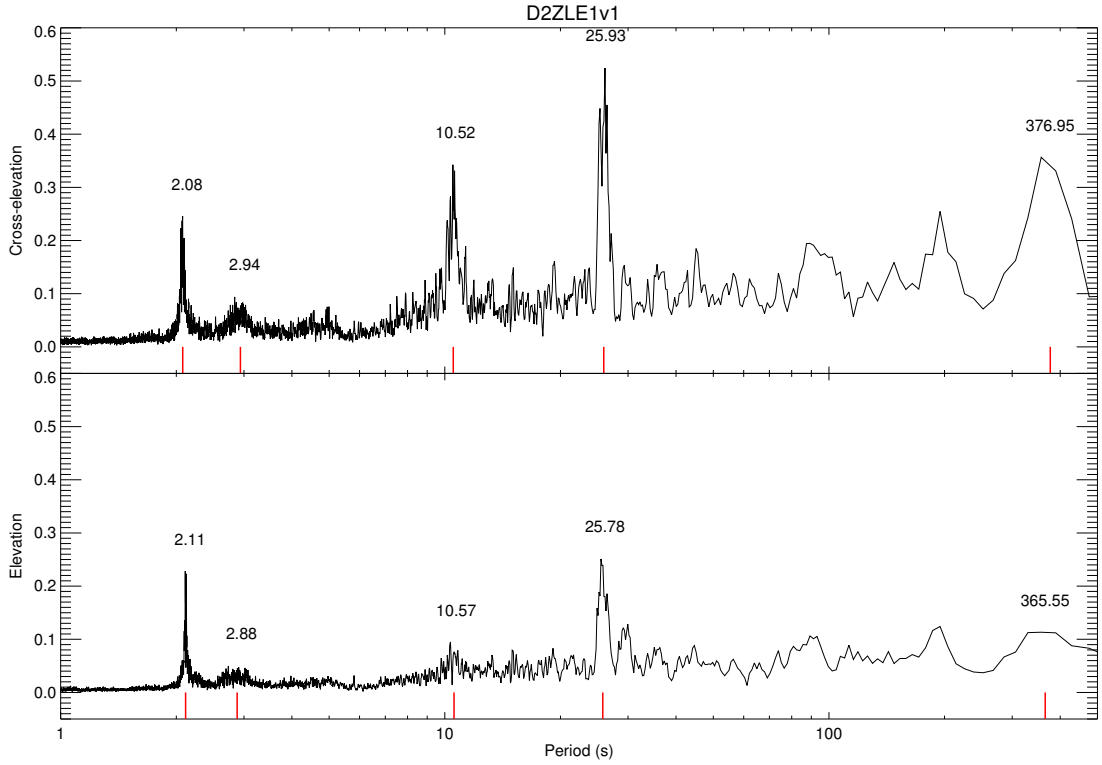

Figure 3.57. A fast Fourier transform of two residual tracking offset waveforms (such as those shown in figure 3.56). The residual power in the cross-elevation axis is larger than that in the elevation axis. This is consistent with the cross-elevation axis tracking being noisier than the elevation axis tracking (see table 3.17). Marked on the two plots are some of the more prominent peaks. The peaks at ∼2 s visible in both plots correspond to normal mode oscillations of the gondola around its center of mass. The bumps near ∼3 s are still under investigation. The sharp feature at ∼10.5 s is related to azimuthal oscillation of the gondola (twisting of the balloon train), which has much more impact on the cross-elevation pointing performance. Finally, the broad peak at ∼26 s is the pendular oscillation of the gondola suspended from the balloon. The large peak near 380 s is at roughly the right location to match the observed altitude oscillations, though as the waveforms being used are only 4300 s long, and the altitude oscillations are irregular, this peak is undersampled and the result is not conclusive.

frames. During science observations, when the guider is in region-of-interest mode, such full-chip solutions are much scarcer. In this instance, the offset between the tracking star and the target point is used as before to adjust the reference pixel of the WCS solution, but the natural field-rotation due to FIREBall being an alt-azimuth mounted telescope needs to be accounted for. This correction is included by multiplying the WCS solution `CD` matrix by a rotation matrix corresponding to the field rotation. The rotation matrix can be computed using gondola GPS information, and target star coordinates. This method yields good results, but does not take into account field rotation due to gondola perturbations. The rough stratospheric environment and gondola mechanisms affect the pointing stability and orientation of the gondola structure with respect to the pointing bore-sight. The observed field rotation can be recovered from stored ROI guider frames (5 per second), which for some fields include several fainter stars, in addition to the tracking star. Frame stacking, in conjunction with `SExtractor` (Bertin & Arnouts 1996) point-source extraction, leads to evaluation of the field rotation as a function of time. Figure 3.58 shows a typical, and an extreme instance of deviation of the field rotation from the nominal value. Attempts to model these field rotation deviations using gondola housekeeping data (siderostat angle, target coordinates, gondola orientation), so that the effects can be mitigated for fields lacking multiple stars in ROI mode, are ongoing. The impact of the typical $\sim$0.1 degree error in field angle is not significant. For all but one of the targets observed during the second FIREBall flight, the tracking star is under 400 CCD pixels away from the location of the fiber bundle. For the outstanding target, (GLYA3), this lever-arm is 500 pixels. The induced pointing errors are on the order of 1 arcsecond, with the exception of a visit to the DEEP2 field, where there appears to have been a major perturbation, where the natural field rotation approximation misses by the size of an IFU fiber. It is unclear what the cause for this effect was, other than that there is a corresponding sharp change in the tip angle of the siderostat mirror. Guider tracking was not affected by this transition.

The guider computer sends analog and serial messages to the detector computer that are folded into the detector data stream. These include timing and guider frame-number information. Consequently, each count recorded by the detector is associated with an IFU astrometric solution, and, once the fiber it originated from is recovered (see section 3.3.3.4), the fiber-size patch on the sky that it originated from is known. The residual pointing errors due to this step do not exceed 2 arcseconds. Figure 3.59 shows three of the principal FIREBall field reconstructions, while figures 3.60 and 3.61 show the reconstruction of two point sources observed by FIREBall.

3.5 FIREBall Target Selection

Given the short observation time, limited sky coverage available to the balloon telescope, and modest efficiency of the FIREBall instrument, the targets for the flight had to be selected carefully.

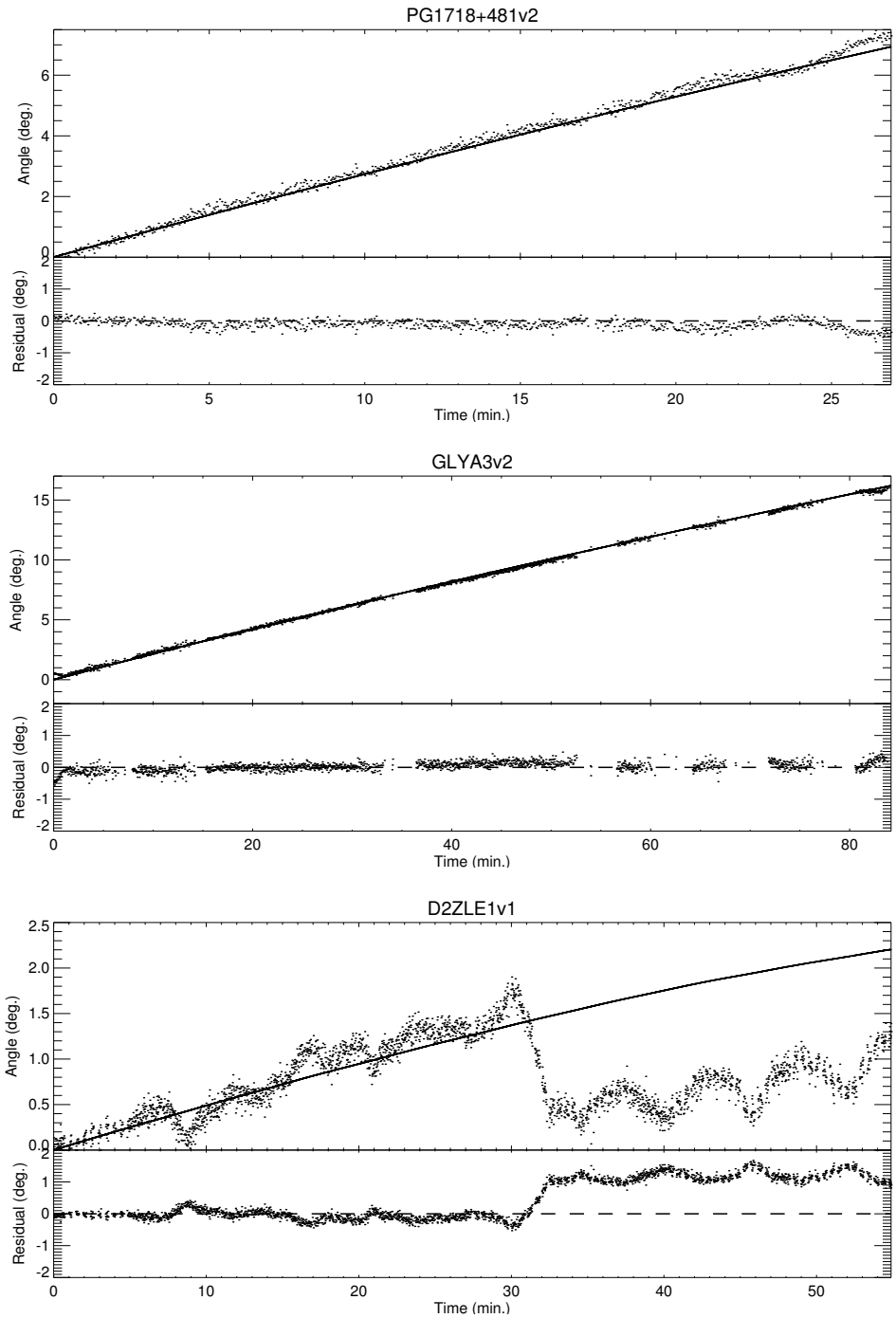

Figure 3.58. Comparison of the natural field rotation with observed field rotation for three of the targets observed during the 2009 FIREBall flight. Each plot consists of two panels. The top panels show the natural field rotation (solid line) and that observed and computed using a second star present in the ROI guider field of view (scattered points). The lower panels show the residuals. The computed curve is a good approximation the majority of the time. The cause of the large deviation during the D2ZLE1 observation is not fully understood, though it is likely due to a change in the orientation of the gondola.

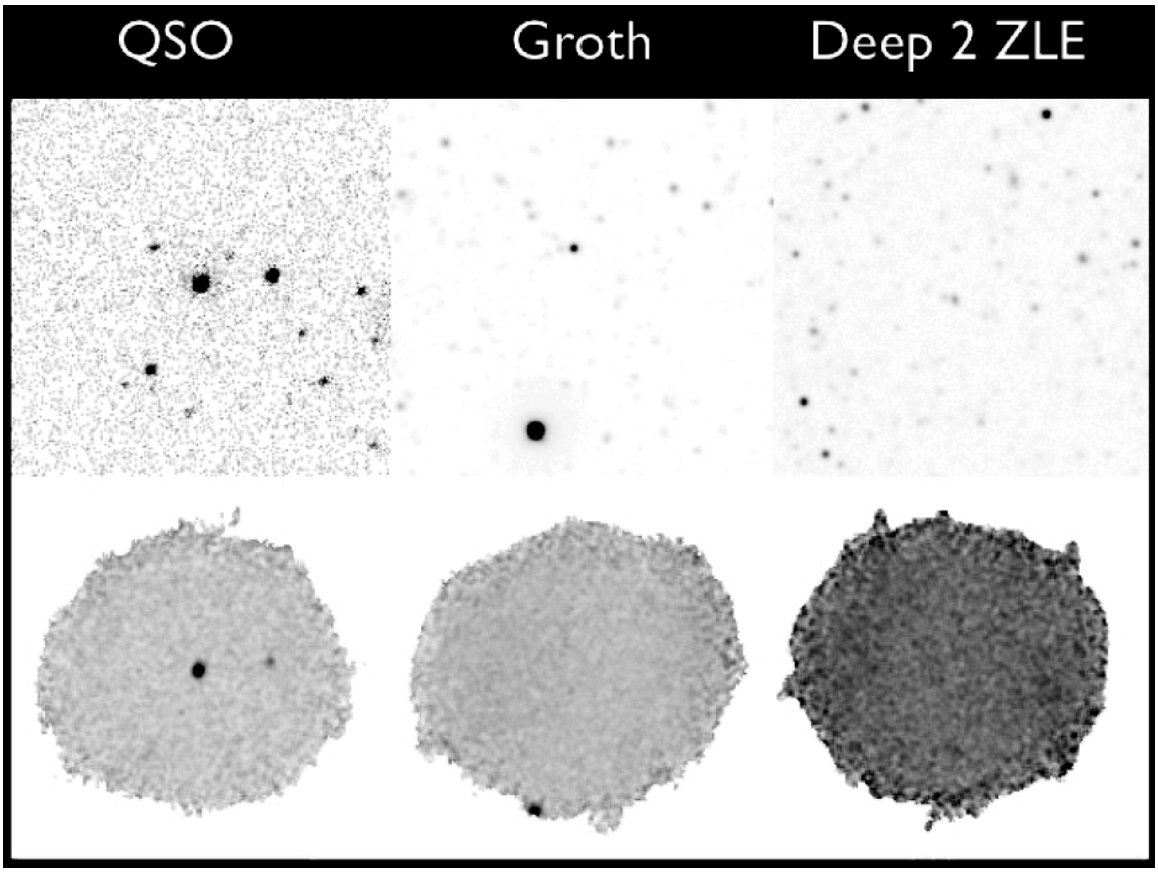

Figure 3.59. A comparison between the reconstructed FIREBall wavelength-collapsed data cubes (bottom row) and GALEX in-band imaging. The FIREBall data cube pixels are 1.5 arcseconds on a side to match the GALEX plate scale. Figure courtesy of D. Schiminovich.

A choice was made to observe several fields rather than to focus the entire flight on a single target. Although the latter strategy would have given the deepest exposure, the uncertainties in the expected levels of emission led the FIREBall team to select several targets with differing primary characteristics. These were a concentration of galaxies whose redshifts move the systemic Lyman α (1216 Å) emission into the FIREBall bandpass ($0.6 < z < 0.6$), a concentration of galaxies whose redshifts move the systemic O VI (1033 Å) emission into the instrument bandpass ($0.9 < z < 1.1$), and a QSO with multiple Lyman α and OVI (1033 Å) absorption systems within the wavelength range of the spectrograph. The first two fields were intended for the study of emission from the circumgalactic medium, and statistical approaches to IGM filament detection, and PLF study; the QSO field was targeted to characterize the emission from regions associated with the absorption systems via cross-correlation.

The candidate galaxy fields were selected from regions that have been extensively observed by other surveys and missions, including in-band imaging from GALEX (Martin et al. 2005). This

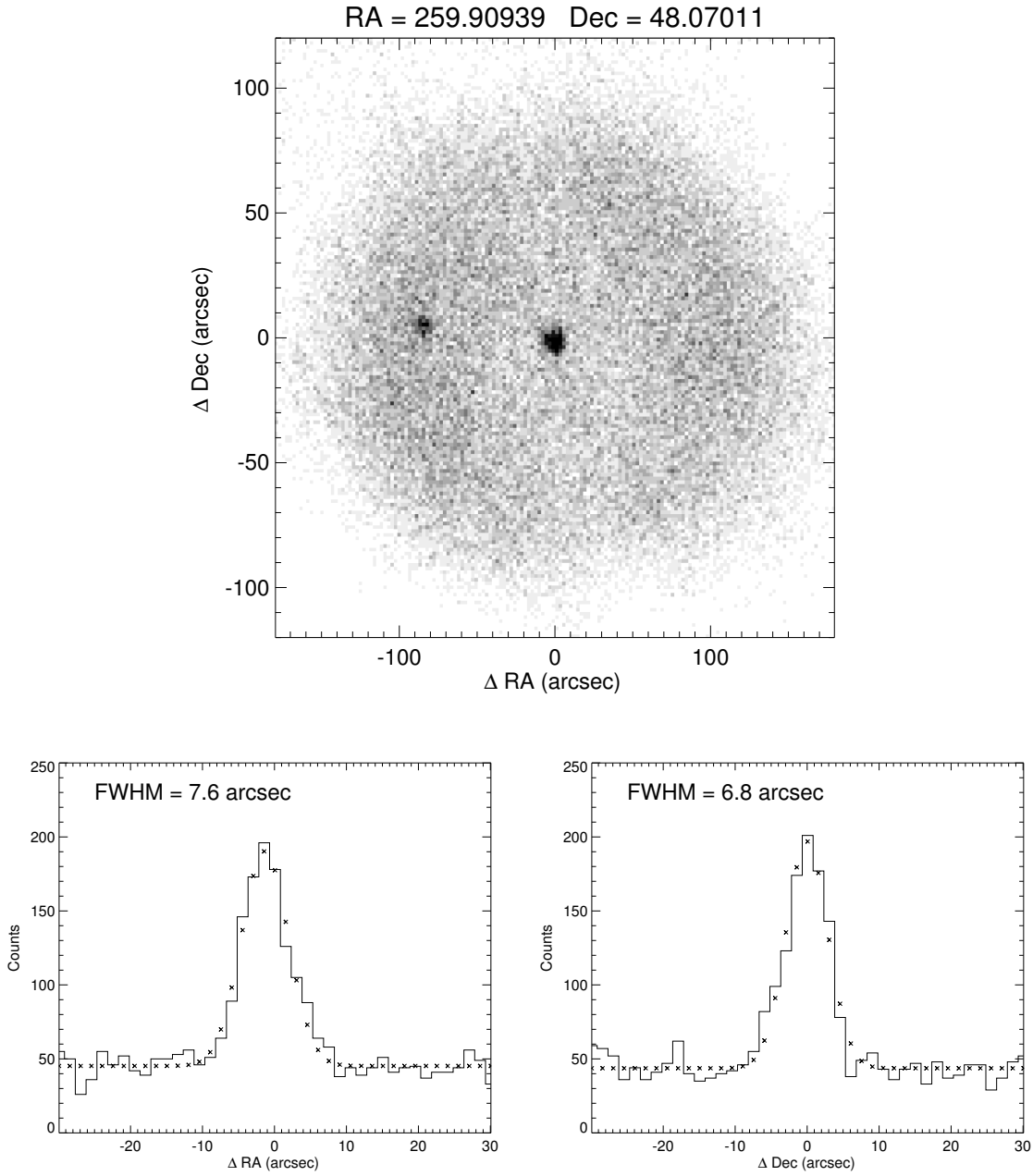

Figure 3.60. The top image shows the reconstructed collapsed spectrum of the PG1718+481 field, including the quasar point source and a star. The two bottom panels present the spot FWHM along the RA and Dec directions.

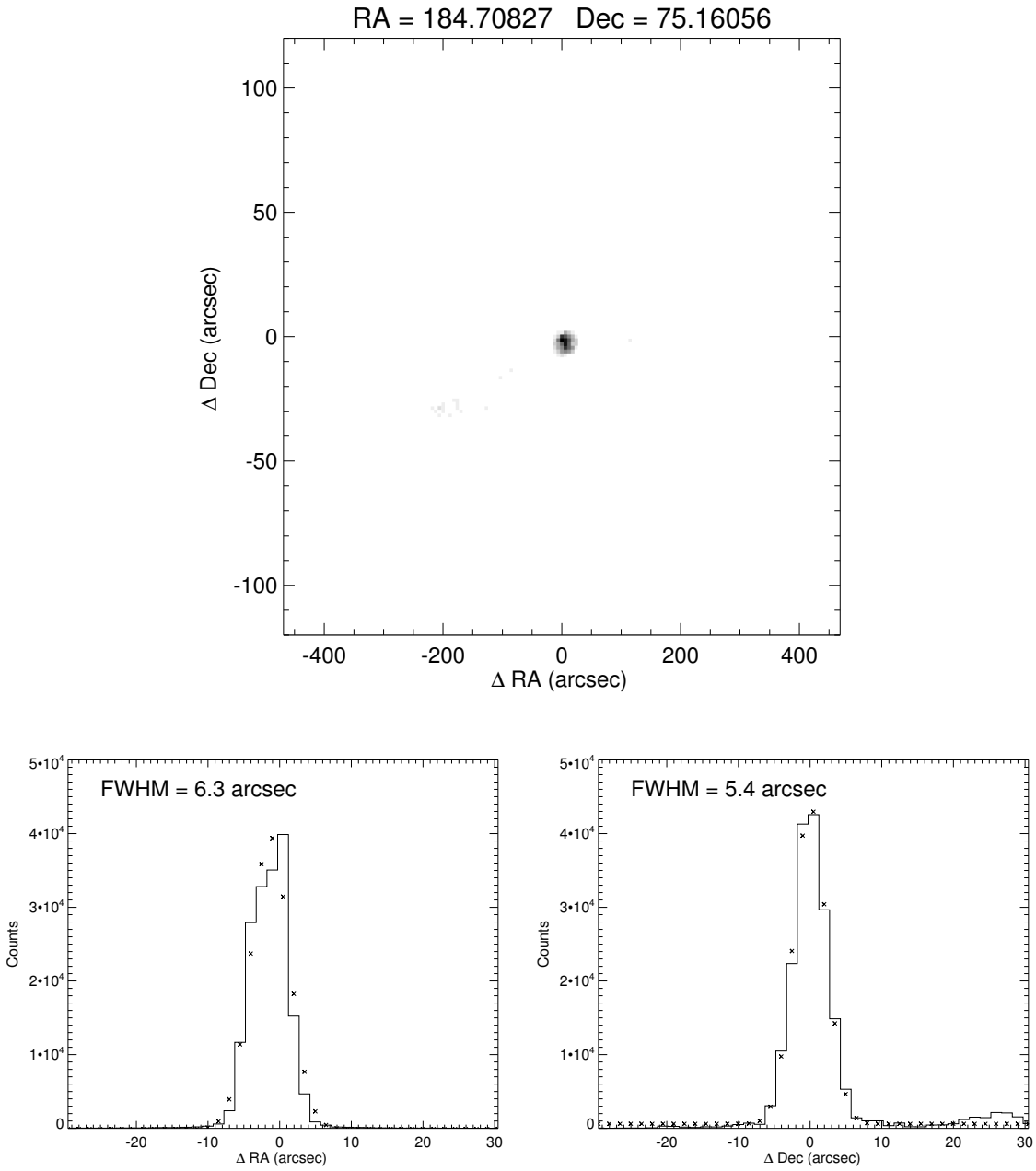

Figure 3.61. As figure 3.60, but for one of the calibration stars observed during the second FIREBall flight, TD1-16203. Note that the star FWHMs are slightly smaller than for the quasar. This is primarily due to two factors: shorter exposure time and the TD1 source being used as the tracking object, as opposed to the quasar, where an offset star was utilized.

coverage is necessary to rule out point-source contamination from any detected emission signatures, and cross-correlation with other data offers the best chance of detection.

This target field search was conducted within the Groth strip (Davis et al. 2007), and the DEEP 2 field 2 (Davis et al. 2003, 2007), both of which are accessible in the summer sky from Fort Sumner, New Mexico. Sloan Digital Sky Survey (Adelman-McCarthy et al. 2008) and DEEP2 galaxy redshift catalogs were used to find conglomerations of galaxies within narrow redshift ranges in fields slightly larger than FIREBall's 2 arcminute diameter. Galaxies at nearly the same systemic redshift were assumed to be parts of a single large-scale structure, and filamentary structure connecting them was inferred. Fields rich in these sources and expected structure were chosen for the flight. Figures 3.62 and 3.63 show the target diagrams for the two galaxy fields ultimately observed by FIREBall. The bulk of the work associated with target selection was done by David Schiminovich, Bruno Milliard, Celine Peroux, and Didier Vibert.

The QSO target was chosen by selecting objects from the SDSS DR5 (Richards et al. 2002; Schneider et al. 2007) with $m_v < 16$ that were observed with GALEX, and have HST/STIS or FOS spectra (Woodgate et al. 1998; Harms et al. 1979) with confirmed absorption systems within the FIREBall field of view. Two such QSOs were identified: PG1206+4557 ($z_{em} = 1.158$, $m_V = 15.79$, HST/FOS Burles & Tytler (1996)) and PG1718+481 ($z_{em} = 1.083$, $m_V = 15.33$, HST/STIS Jannuzi et al. (1998)). The first exhibits a highly saturated O VI absorption system at $z \approx 0.9266$ with equivalent widths EW > 2 Å for the two lines in the doublet. The second QSO has an absorption system of primary interest at $z \approx 1.0318$ with EW$\sim$0.4Å, with additional absorbers identified: LLS at $z \approx 0.7011$, O VI at $z \approx 1.0065$, OVI at $z \approx 1.0507$ with a missing OVIb component, and OVI at $z \approx 1.0548$ with a blended OVIa line.

Emission from the first source was expected to be stronger, though the second QSO has a higher resolution spectrum available. The choice as to which to target to observe was made for us by the 2009 summer weather conditions. Our early July flight ruled out PG1206+4557 as a viable target on observability grounds. The QSO target selection was led by the LAM members of the FIREBall collaboration: Bruno Milliard, Jean-Michel Deharveng, Stephan Frank, and Celine Peroux.

3.6 Conclusions and Future Work

This chapter has described the design, integration, and calibration of the FIREBall instrument. It laid out the target selection process, discussed data reduction, and initial data analysis. Due to the suboptimal balloon altitude during the second flight, the obtained data is not of ideal quality.

While the two flights demonstrated the functionality of the instrument, obtained data, and led to the understanding and development of data reduction tools, they highlighted some of the challenges

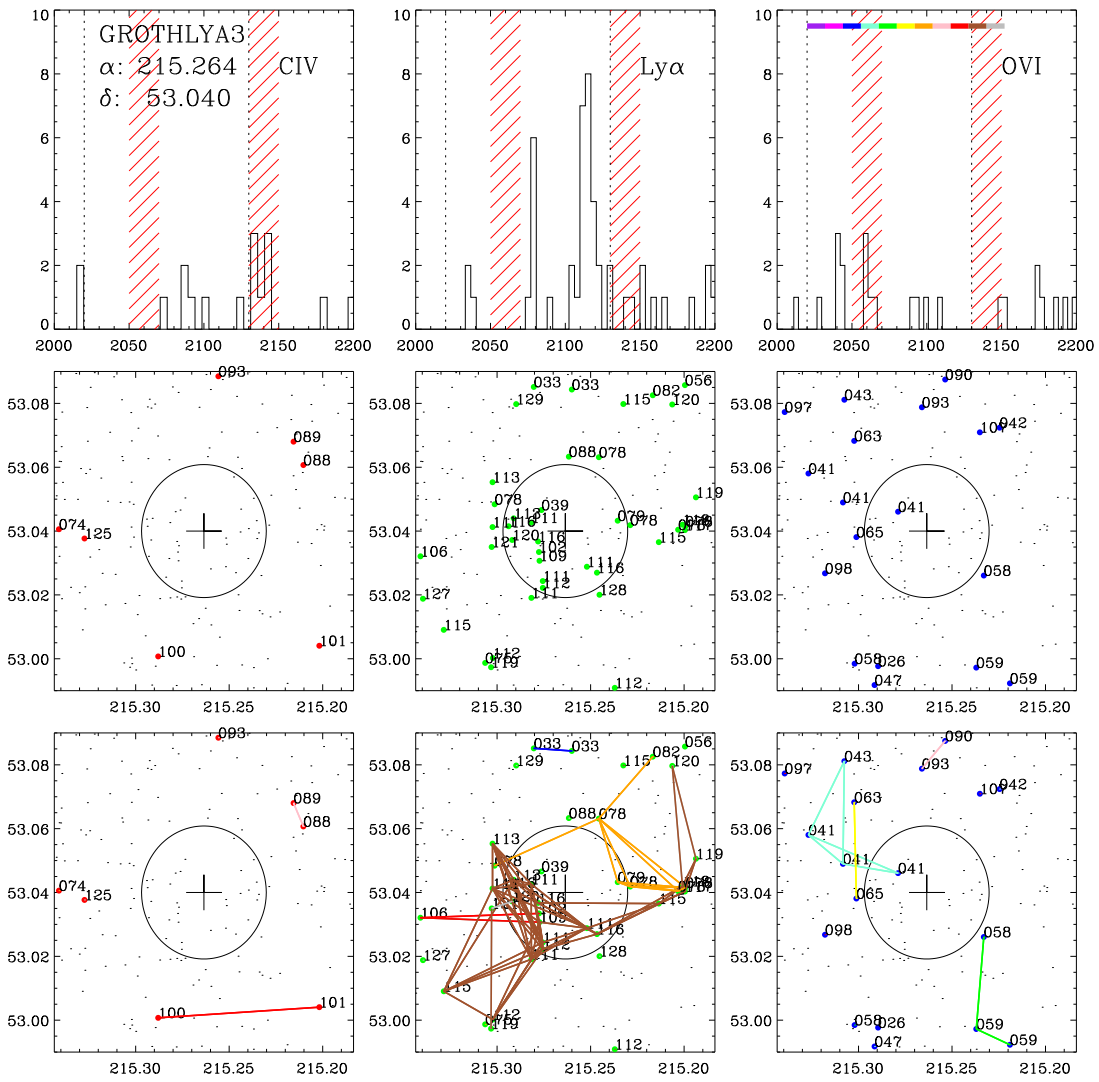

Figure 3.62. Diagrams showing the FIREBall in-band sources for the Groth Lyα field targeted during the flight. The three columns correspond to objects whose CIV (1548, 1550 Å), Lyα (1216 Å), and OVI (1033, 1038 Å) emission fall into the FIREBall bandpass, respectively. The top row shows the number of these sources binned by redshift, with parts of the spectrum obstructed by atmospheric NO emission lines hashed out. The vertical dashed lines mark out the nominal FIREBall bandpass. The plots in the middle row are centered on the field coordinates, the FIREBall field of view is shown as the central circle, and the galaxies marked with colored dots indicate those that fall within the requisite redshift range. There is a high concentration of galaxies with Lyα lines redshifted to around 2120Å, near the center of the instrument bandpass; this concentration was the principal driver behind the selection of this region. The bottom row shows the same set of galaxies linked into anticipated large-scale structure groups, indicating regions where excess CGM emission is expected. Figure courtesy David Schiminovich.

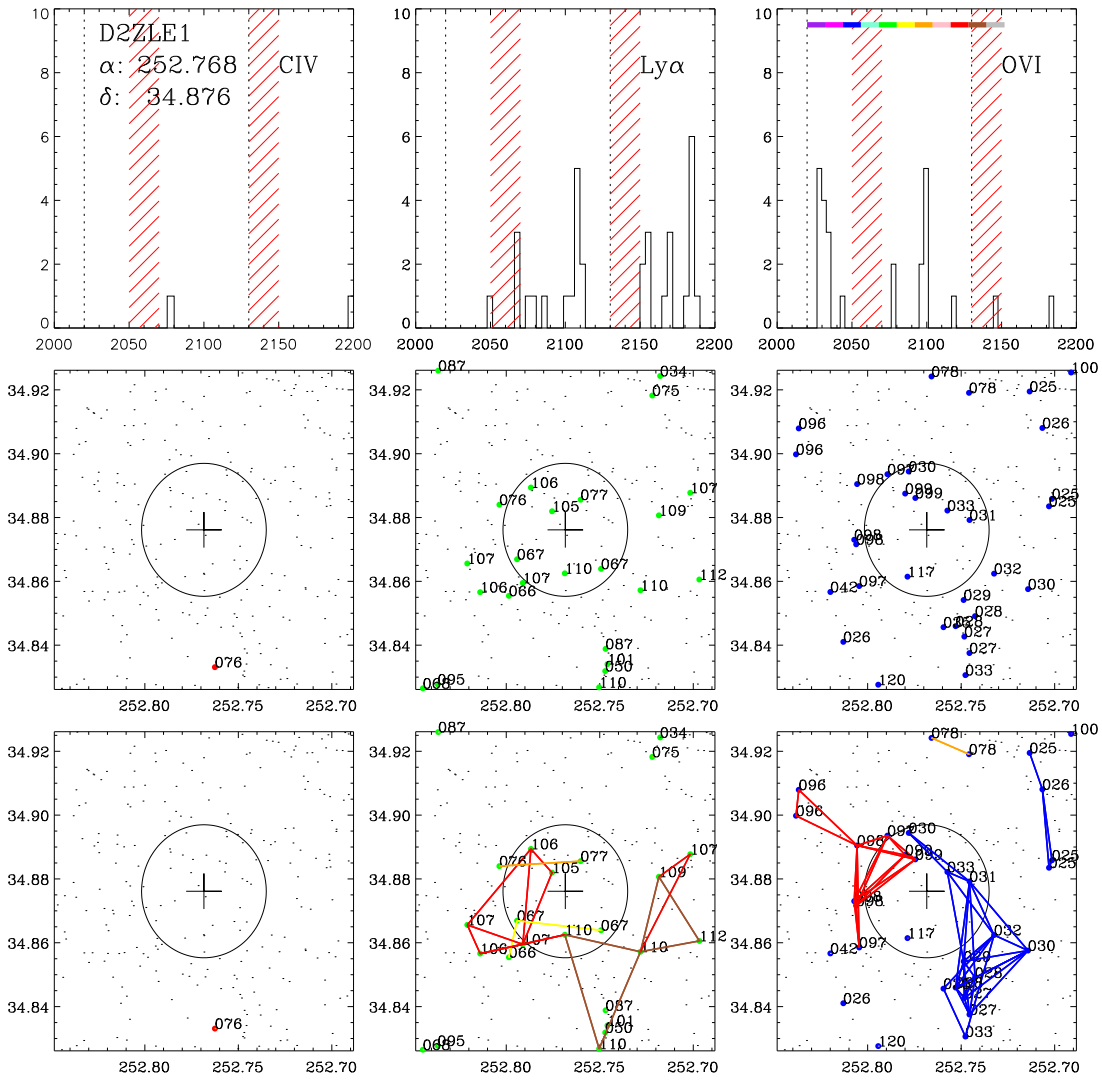

Figure 3.63. Diagrams showing the FIREBall in-band sources for the DEEP 2 ZLE field observed by FIREBall. The structure of the figure is the same as that of figure 3.62. This field was chosen for its increased concentration of galaxies whose OVI line is visible to FIREBall. Figure courtesy David Schiminovich.

that must be overcome to investigate the target science. The necessary tasks needed to meet these challenges are summarized in the following sections.

3.6.1 Flight 2 Data Analysis

Several steps remain to complete the analysis of the existing FIREBall data. The principal roadblock is the lack of a high quality detector dark image. Plans have been laid out to obtain this image during the second half of 2011. Once the data pipeline is in place, fully reduced and background-subtracted data cubes will be produced shortly thereafter. Interpretation of this data will follow, including likely upper bounds on the emission signals.

3.6.2 Emission Modeling, Target Selection, and Instrument Adjustment

It is unclear whether the structure formation and radiation models that were the driving force behind the design phases of FIREBall are truly representative of the intergalactic and circumgalactic medium emission. The algorithms used in these simulations have evolved, and some of the input physics is now better understood and modeled. As new ideas and updated computer simulations emerge, the format of the instrument may need to be adjusted to maximize the odds of detection and improve the instrument's ability to characterize the matter responsible for the radiation. Additionally, targets must be selected carefully to maximize scientific return. Given the limited integration time and effective area of a balloon experiment, the brightest regions of the IGM, likely the CGM, need to be targeted. These halos surround discrete galaxies, and a single contiguous IFU may not be the ideal way to sample this gas. Instead, a hybrid multiobject spectrograph IFU approach may be required, which involves a series of small bundles to be placed at the known locations of multiple galaxies that likely trace the same structure. This functional change would necessitate the introduction of a field derotator into the FIREBall telescope.

3.6.3 Instrument Improvement

The FIREBall instrument will need to be improved before the next flight. In addition to the target science driven alterations mentioned in the previous section, changes must be made to improve the instrument efficiency. The first of these is to replace the MCP detector with a UV sensitized δ-doped low-light-level CCD (Nikzad et al. 2011; Mackay et al. 2003) with specialized antireflection coatings (Hamden et al. 2011). The second is to aggressively lighten the payload — a loss of 1000 lb may lead to as much as a factor of 1.5 increase in throughput. While 1000 lb may be a tough ask, half of that is feasible. The third is to investigate the possibility of an afternoon launch. The first FIREBall flight, from Palestine, TX, was launched in the late afternoon and attained an altitude nearly 3 km higher than the second flight, which was launched from Ft. Sumner, NM., in the morning; a zero-pressure

balloon launched early in the day loses helium due to thermal effects pushing the gas outside the balloon. Telescope pointing will be improved by replacing the mechanism currently responsible for cross-elevation axis tracking. New tracking algorithms will need to be implemented to move from the pure photon-counting MCP detectors to the new CCDs; these will either need to make use of a new field derotator, or use the existing degrees of freedom (pivot, two axes of the siderostat) to counteract the effect of field rotation over the length of the exposures.

FIREBall has flown twice. The first flight demonstrated the functionality of the detector, tracking, and communication systems (despite azimuthal control failure). The instrument performed very well during the second flight. Pointing and data collection worked flawlessly; there were no thermal or communication issues. Unfortunately, the float altitude was several kilometers below the desired height, and the atmospheric throughput was a factor of 2 to 3 smaller than what the FIREBall team was hoping for. The quality of the resulting data is not what one would like. The existing instrument is a testbed for new detector and optical technologies, providing a step toward a possible satellite version of a UV-oriented integral field spectrograph.

Appendix A

Extended Source Sensitivity Limit Calculation

A.1 Overview

A key in designing an experiment is understanding the sensitivity limit of a design, given a set of instrument parameters. This appendix aims at exploring the parameter space relevant to detecting faint and diffuse emission. The parameters involved are listed in Table A.1. Ideally, an observation will include images of the target field and a background field. A subtraction is then performed to extract the signal of interest. In addition to the usual shot noise associated with collecting photoelectrons, detector read noise or background, as well as inaccuracy of subtraction, or change in the sky background will affect the ability to uncover the sought-after signal.

The on-target observation registers desired signal, the sky background, and the detector noise; off-target observation detect only the sky background and detector noise:

$$F_T = S + B + D; \qquad \sigma_T^2 = \sigma_S^2 + \sigma_B^2 + \sigma_D^2, \tag{A.1}$$

$$F_O = B' + D; \qquad \sigma_O^2 = \sigma_{B'}^2 + \sigma_D^2, \tag{A.2}$$

where

$$\sigma_S = \sqrt{S}, \tag{A.3}$$

$$\sigma_B = \sqrt{B}, \tag{A.4}$$

$$\sigma_{B'} = \sqrt{B + f^2 B^2}. \tag{A.5}$$

The error in the second sky background includes a possible change in the background level leading to a subtraction error. The nature of σ_D depends on the detector in question and will be discussed in a section below.

Symbol	Parameter Name	Units	Comments
A	Telescope area	cm^2	
η	Efficiency		System throughput efficiency, including the atmosphere, telescope, and instrument.
R	Spectral resolution		
Ω	Source extent	arcsec^2	Sky area subtended by the object being observed.
Λ	signal signature	Å	Expected spectral extent of the signal.
$d\lambda/dx$	dispersion	Å/mm	Linear dispersion on the detector.
T	Observation time	sec	Total time spent observing the science target.
t	Exposure time	sec	Length of a single exposure.
D	Detector background	$\mathrm{counts/s/cm}^2$	
I_S	Signal flux	$\frac{\mathrm{photons}}{\mathrm{s\,arcsec}^2\,\mathrm{cm}^2\,\mathring{\mathrm{A}}}$	
I_B	Background flux	$\frac{\mathrm{photons}}{\mathrm{s\,arcsec}^2\,\mathrm{cm}^2\,\mathring{\mathrm{A}}}$	
f	Subtraction error		The fraction of the sky background remaining after subtraction.
Σ	Minimum SNR		Minimum acceptable signal-to-noise ratio.

Table A.1. Parameters used in the calculation of the sensitivity of an instrument to diffuse emission.

The signal-to-noise ratio is

$$\mathrm{SNR} \equiv \frac{S}{\sqrt{S + 2B + f^2B^2 + 2\sigma_D^2}} \geq \Sigma. \tag{A.6}$$

This can be easily inverted for S:

$$S \geq \frac{1}{2}\left(\Sigma^2 + \sqrt{\Sigma^4 + 4\Sigma^2[2(B + \sigma_D^2) + f^2B^2]}\right). \tag{A.7}$$

One can investigate limiting cases, where the minimum detectable is dominated by either the detector noise or sky background. In either case the noise source is assumed to dominate the Σ terms.

In the case of a noisy detector:

$$S \geq \sqrt{2\Sigma^2\sigma_D^2}. \tag{A.8}$$

Using the scalings from the following sections, the minimum detectable flux scales as

$$I_S \propto \eta^{-1}\left(\frac{R}{T\Omega\Lambda}\right)^{\frac{1}{2}}. \tag{A.9}$$

Increasing spectral resolution has a negative impact on the instrument sensitivity, as the signal becomes more diluted on the detector. Improving efficiency, lengthening observation time, and observing larger sources all increase chances of detection.

When the detector is quiet and the sky is the dominant source of background, there are two limiting cases, depending on the ratio of the sky subtraction error to the sky background shot noise: $f^2B^2/2B$. When this ratio is much less than unity the sensitivity limit goes as

$$S \geq \sqrt{2\Sigma^2 B}, \tag{A.10}$$

$$I_S \propto \sqrt{I_B}\,(A\,\eta\,T\,\Omega\,\Lambda)^{-\frac{1}{2}}\,, \tag{A.11}$$

where the relations from the following sections were used to arrive at the second expression.

When the ratio is much greater than unity,

$$S \geq \Sigma\, fb, \tag{A.12}$$

$$I_S \propto f\, I_B. \tag{A.13}$$

The midpoint between the two cases occurs when

$$f^2B^2 \approx 2B, \tag{A.14}$$

$$f \approx \sqrt{\frac{2}{B}}. \tag{A.15}$$

A.2 Signal and Sky Background

The number of photoelectrons collected from the target and from the background are given by

$$S = I_S \times A\eta\,T\,\Omega\,\Lambda, \tag{A.16}$$

$$B = I_B \times A\eta\,T\,\Omega\,\Lambda. \tag{A.17}$$

These quantities need to be adjusted if the integral field unit is sparse, i.e., does not have full coverage of the field of view. That is the case with FIREBall, and an additional factor of u, the fiber packing efficiency, needs to be included in the above expressions. These quantities can be estimated for FIREBall and CWI.

$$S_{\rm FB} = 1.5\times10^3\left(\frac{I_S}{10^5\,\mathrm{CU}}\right)\left(\frac{\Omega}{7500\,\mathrm{arcsec}^2}\right)\left(\frac{T}{3\,\mathrm{hrs}}\right)\left(\frac{u}{0.5}\right)\left(\frac{\Lambda}{1\,\text{Å}}\right)\left(\frac{\eta}{0.03\,\%}\right)\mathrm{counts}, \tag{A.18}$$

$$B_{\rm FB} = 1.5\times10^1\left(\frac{I_B}{10^3\,\mathrm{CU}}\right)\left(\frac{\Omega}{7500\,\mathrm{arcsec}^2}\right)\left(\frac{T}{3\,\mathrm{hrs}}\right)\left(\frac{u}{0.5}\right)\left(\frac{\Lambda}{1\,\text{Å}}\right)\left(\frac{\eta}{0.03\,\%}\right)\mathrm{counts}, \tag{A.19}$$

where $1\,\mathrm{CU} = 1\,\mathrm{photon/s/cm^2/sr/Å}$. The estimate of the background level is based on data from the FOCA instrument (Milliard et al. 1994; Milliard 2010). The signal level, at $10^5\,\mathrm{CU}$, is roughly the flux that FIREBall is expected to be sensitive to.

$$S_{\mathrm{CWI}} = 1.5 \times 10^4 \left(\frac{I_S}{2 \times 10^2\,\mathrm{CU}}\right)\left(\frac{\Omega}{600\,\mathrm{arcsec}^2}\right)\left(\frac{T}{12\,\mathrm{hrs}}\right)\left(\frac{\Lambda}{1\,\text{Å}}\right)\left(\frac{\eta}{15\,\%}\right)\mathrm{photoelectrons}, \quad \text{(A.20)}$$

$$B_{\mathrm{CWI}} = 3.6 \times 10^6 \left(\frac{I_B}{5 \times 10^4\,\mathrm{CU}}\right)\left(\frac{\Omega}{600\,\mathrm{arcsec}^2}\right)\left(\frac{T}{12\,\mathrm{hrs}}\right)\left(\frac{\Lambda}{1\,\text{Å}}\right)\left(\frac{\eta}{15\,\%}\right)\mathrm{photoelectrons}. \quad \text{(A.21)}$$

As is shown in the next section, the sky background dominates the CWI signal-to-noise ratio. The break-even point between sky background shot noise and subtraction error occurs when $f \sim 10^{-3}$. When sky background subtraction is substantially less accurate than this, the minimum detectable flux is proportional to the background flux (in particular, for background at $I_B = 5 \times 10^4\,\mathrm{CU}$, which is approximately the sky brightness at $\lambda = 5000\,\text{Å}$). Requiring a signal-to-noise ratio of $\Sigma \approx 5$, assuming 1% sky subtraction accuracy, yields the sensitivity limit $I_S \approx 2500\,\mathrm{CU} \approx 2.4 \times 10^{-19}\,\mathrm{erg/s/cm^2/Å/arcsec^2}$ at 5000Å.

A.3 Detector Background

The type of detector background depends on the nature of the device and the area covered by the signal being sought. The principal types of detector noise affecting the two detectors used in CWI and FIREBall are noise proportional to time (counts per unit time, per unit area) and read noise (counts added by the hardware after exposure is finished). The latter can also be approximated as a rate.

A.3.1 CWI Detector Background

The CWI detector background comprises the CCD read noise and CCD dark current. The dark current, D_C, is statistically identical to sky background. The read noise, D_R, contribution to the observation depends on the number of exposures taken, T/t. Both scale with the detector area covered by the signal. The dark current is multiplied by the number of physical detector pixels, the read noise by the number of elements read out.

$$\sigma_D^2 = \left(T\frac{D_C}{p^2} + \frac{T}{t}\frac{D_R^2}{b^2p^2}\right)\left[\frac{\Omega}{s}\frac{F_C}{F_T}\left(\frac{F_T L}{\Theta}\right)^2\right]\left(\Lambda\frac{dx}{d\lambda}\right), \quad \text{(A.22)}$$

$$\frac{dx}{d\lambda} = \frac{sR}{\lambda}\frac{F_C}{F_T}, \quad \text{(A.23)}$$

where s is the spectrograph slit width, F_T and F_C are the telescope (collimator) and camera focal ratios, L is the telescope diameter, Θ the conversion factor from radians to arcseconds, p the physical

size of a pixel, and b the amount of binning. Rerranging some of the terms for clarity, this gives:

$$\sigma_D^2 = \left(D_C + \frac{D_R^2}{tb^2}\right)\left(\frac{F_C L}{\Theta p}\right)^2\left(\frac{TR\Omega\Lambda}{\lambda}\right). \tag{A.24}$$

The dark current for CWI was calculated to be $D_C = 1\,\mathrm{electron/pixel/hr}$. The read noise approximately 2.5 electrons per effective pixel. The pixels are $p = 15\,\mu m$ squares, and they are binned 2×2: $b = 2$. The focal ratio of the camera is $F_c = 2$, with the telescope diameter $L = 500\,\mathrm{cm}$. A typical exposure lasted 20 minutes, so $t = 1200\,\mathrm{s}$. Most of the observations to date have been at wavelengths around $\lambda = 5000\,\text{Å}$. The detector noise then scales as:

$$\sigma_{D_C}^2 = 7.5\times10^4\left(\frac{D_C}{1\,\mathrm{e/px/hr}}\right)\left(\frac{\Omega}{600\,\mathrm{arcsec}^2}\right)\left(\frac{T}{12\,\mathrm{hrs}}\right)\left(\frac{\Lambda}{1\,\text{Å}}\right)\left(\frac{R}{5000}\right)\mathrm{e}^-, \tag{A.25}$$

$$\sigma_{D_R}^2 = 3.5\times10^5\left(\frac{D_R}{2.5\,\mathrm{e}^-}\right)^2\left(\frac{b}{2\,\mathrm{px}}\right)^{-2}\left(\frac{t}{0.33\,\mathrm{hrs}}\right)^{-1}\left(\frac{\Omega}{600\,\mathrm{arcsec}^2}\right)\left(\frac{T}{12\,\mathrm{hrs}}\right)\left(\frac{\Lambda}{1\,\text{Å}}\right)\left(\frac{R}{5000}\right)\mathrm{e}^-. \tag{A.26}$$

The CWI detector background is not insignificant, but it is about an order of magnitude smaller than the sky background, and the signal-to-noise ratio is thus dominated by the sky.

A.3.2 FIREBall Detector Background

A single fiber covers an area Ω_F on the sky, and the fiber packing efficiency in the focal plane is u, meaning that a region of sky Ω is sampled by $N_F = u\Omega/\Omega_F$ fibers. Each fiber occupies a width x_F on the detector, and the length on the detector corresponding to the relevant wavelength range $\Lambda\frac{dx}{d\lambda}$. The detector background is, then

$$\sigma_D^2 = D_F T\left(\frac{x_F u\Omega}{\Omega_F}\right)\left(\Lambda\frac{dx}{d\lambda}\right), \tag{A.27}$$

$$\frac{dx}{d\lambda} = \frac{R\,d_F}{\lambda}, \tag{A.28}$$

where d_F is the diameter of a fiber. The detector background of the FIREBall microchannel plate device was measured in lab, and verified during flight, to be $D_F = 1\,\mathrm{count/s/cm}^2$. A single fiber covers approximately $\Omega_F \sim 50\,\mathrm{arcsec}^2$, and the fibers have a packing efficiency $u \approx 0.5$. The fiber diameter is $d_F = 100\,\mu\mathrm{m}$, and its image in the spatial direction is slightly larger, $x_F \approx 150\,\mu\mathrm{m}$. Observations are around $\lambda = 2100\text{Å}$. The FIREBall detector background is, approximately

$$\sigma_D^2 = 3\times10^2\left(\frac{D_F}{1\,\mathrm{ct\,s\,cm}^2}\right)\left(\frac{R}{5000}\right)\left(\frac{\Omega}{7500\,\mathrm{arcsec}^2}\right)\left(\frac{T}{3\,\mathrm{hrs}}\right)\left(\frac{u}{0.5}\right)\left(\frac{\Lambda}{1\,\text{Å}}\right)\mathrm{counts}. \tag{A.29}$$

The dominant source of noise for FIREBall is the detector.

Appendix B

Hale Telescope Focal Range

B.1 Introduction

During the design phase of CWI, there was some uncertainty as to the distance from the secondary to a datum surface on the 200" Hale Telescope. For most instruments, this is not a problem, as the location is sufficiently close to the nominal Cassegrain focus that the telescope can be easily focused to where it is required. The CWI design is such that the telescope needs to focus close to the lower end of the available range. Dan McKenna, Jeff Zolkower, Shahin Rahman, and I used a laser range finder newly acquired by Palomar to measure the location of the secondary. According to the manufacturer, the range finder measurements are accurate to within 1.5 mm, with the caveat that the instrument is typically used with a diffusing, rather than specular, surface. Data was taken on June 26, 2008. The temperature of the primary mirror cell was 20°C, the primary focus cage was at 17°C. The original version of this write-up was put together on July 1st, 2008 and updated in May 2011.

B.2 Configuration

This range finder was clamped in a vise and placed on the observatory floor with the cass-cage door removed. It was aligned along the optical axis of the telescope by eye. The device was shifted so that the return beam from the secondary did not come back directly onto the sensor; otherwise the device was saturated and would not produce an output. This shift/tilt does not introduce more than 1 mm of difference into the measurement.

The telescope was fitted with the F/16 secondary, and data points were taken for several primary cage encoder readings (Table B.1). To provide a datum surface, a 1/2" thick aluminum bar was clamped flush against the cass rotator ring. The range finder was then used to measure the distance to that bar. This measurement is also noted in Table B.1.

Finally, a caliper and ruler were used to measure the offset of the lower surface of the aluminum bar from the lower surface of the true cass ring (this is the ring shown in the construction drawing from Hal Petrie, (B.1). The remaining distances used in the calculation were taken from that same drawing.

Table B.1. Encoder reading for the primary focus cage and measured position of the secondary from the range finding device resting in a vise on the observatory floor. Also included is the distance from the device at that same place to a 1/2" thick bar spanning the bottom face of the Cassegrain rotator ring. The error in each measurement is no worse than 1.5 mm.

Primary Cage Encoder Reading	Distance Measurement (mm)
1.01	19263
2	19264
8	19270
15	19277
22	19284
29	19291
36	19298
43	19305
50	19312
70	19333
Bar Reading	4317

B.3 Results

The total thickness from the bottom surface of the aluminum bar to the bottom surface of the cass ring is 56.5 mm. Taking the measurement at 36 mm as the "central" location of the secondary, this gives the distance from the secondary to the lower cass ring as 14924.5 mm. The corresponding distance from the secondary to the primary vertex is 13763.4 mm. The value used in CWI design for this distance is 13768.0 mm, which is in reasonable agreement with the measured quantity. The error in our measurement should not exceed 3 mm, though this is a best-guess estimate of the error.

B.4 Discussion

This measurement does not gives either the curvature of the secondary, nor the focus location, and as such must rely on prior data to yield a useful conclusion about the location of the nominal focus. We do have one data point to work from, which is the location of the PALM3k focus as indicated

Table B.2. Other distances relevant to the measurement. Some of this data was taken at Palomar on June 26, 2008, the error on these is uncertain, but unlikely to total more than 3mm or so. Others values were taken from the Palomar 200" drawing.

Distance From	Distance To	(mm)	Notes
Aluminum bar	Cass Rotator	12.7	Clamped. ($\frac{1}{2}$")
Cass Rotator	Metal Ruler	10.7	Next surface is beveled. Ruler needed to be able to use the caliper.
Metal Ruler	Second Ring	1	See above
Second Ring	Cass Ring Lower Surface	32.1	—
Cass Ring	Mirror Cell	117.5	From Hale Drawing ($4\frac{5}{8}$")
Mirror Cell	—	612.8	Thickness. From Drawing ($24\frac{1}{8}$")
Gap	—	38.1	Between Mirror Cell and Mirror. From Drawing. ($1\frac{1}{2}$")
200" Mirror Rear	Mirror Vertex	498.5	From Drawing. ($19\frac{5}{8}$")

in the "as built" ZEMAX ray trace of the system[1]:
http://www.oir.caltech.edu/twiki_oir/bin/view/Palomar/HaleOptics.
The M2 to focus distance given by the file is 14997 mm. This puts the focus at ∼72.5 mm below the original cass ring, or ∼28.5 mm below the cass rotator ring. The night before our measurement, the cass encoder reading was 55 with an AO instrument in use. Taking the nominal values of the prime focus focal ratio and that of the Cass F/#, the shift in the position of the secondary corresponds to a factor of 22.6 larger shift in the focus position. $((\frac{F_{cass}}{F_{primary}})^2 = (\frac{15.7}{3.3})^2)$. The CWI focus is 900 mm behind the PALMAO focus, requiring that the secondary be shifted downward by 39.8 mm from the PALMAO location, to an encoder reading of roughly 15 mm. This indicates that the Hale can be focused far enough behind the primary mirror for the purposes of CWI. These measurements give no indication about the image quality at any point in the focus range; that measurement would likely require some on-sky engineering time.

[1] At the time when this report was originally written, in mid-2008, the ray trace was at http://www.oir.caltech.edu/twiki_oir/bin/view/Palomar/Reference/OpticalModels. That URL appears to have been lost. That was a model of the Hale telescope used for PALMAO and included several useful reference surfaces; the link in text is a simplified version of that model. This was also the model of the telescope used in the design of CWI. A ZEMAX generated prescription file of this model is attached at the end of this document.

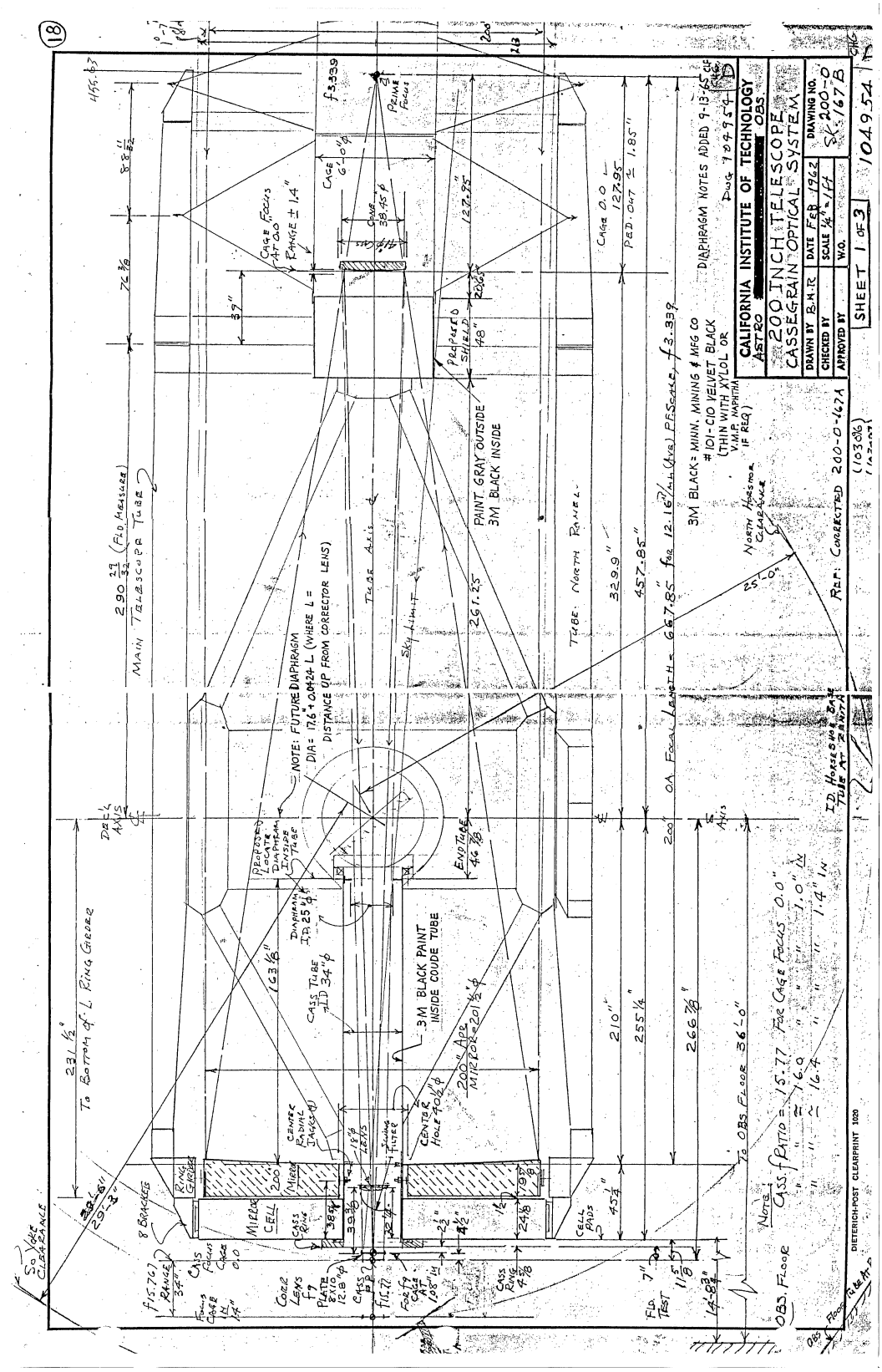

Figure B.1. A drawing of the Hale 200” telescope, kindly provided by Hal Petrie of Palomar Observatory.

B.5 Follow-up

The preceding paragraphs were written shortly after the distance measurements were made (mid 2008). At time of this update (May 2011), CWI had been built, commissioned, and seen several observing runs. The secondary-defocus surface thickness in the CWI `ZEMAX` model is $-17.33\,\mathrm{mm}$ when the telescope is in focus at the slicer. The instrument focuses well and close to the location found by our measurement and computed with `ZEMAX`. The secondary encoder reading for best focus has varied from 17 to 22 during our observing runs, depending on dome temperature. (There is a sign flip between the ray trace model and the encoder reading).

Appendix C

CWI Slicer Surface Data

Surface quality data and a reflective coating model for of a diamond-turned sample CWI slicer mirror surface provided by the image slicer manufacturer, Kugler.

PRECISION IN A NEW DIMENSION

Skizze

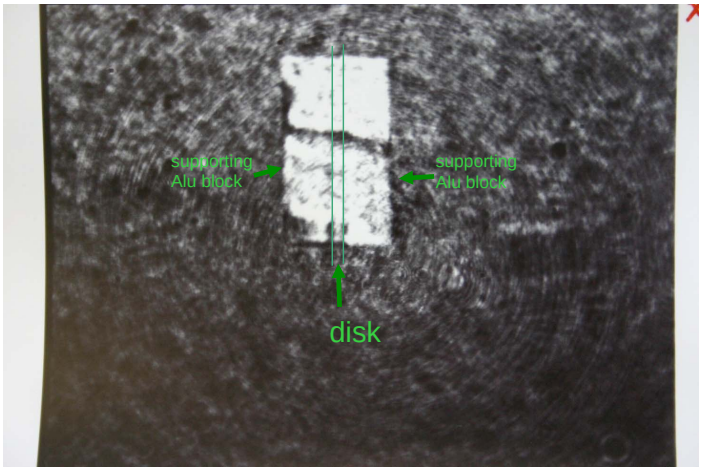

interferometric image:

disk tilted vertically by about 360 nm. Black line is horizontal. So no shape inaccuracies on the order of 150 nm (visual resolution). → Shape accuracy better than 150 nm.

KUGLER
PRECISION IN A NEW DIMENSION

Bernd Heitkamp, 12/05/08

1

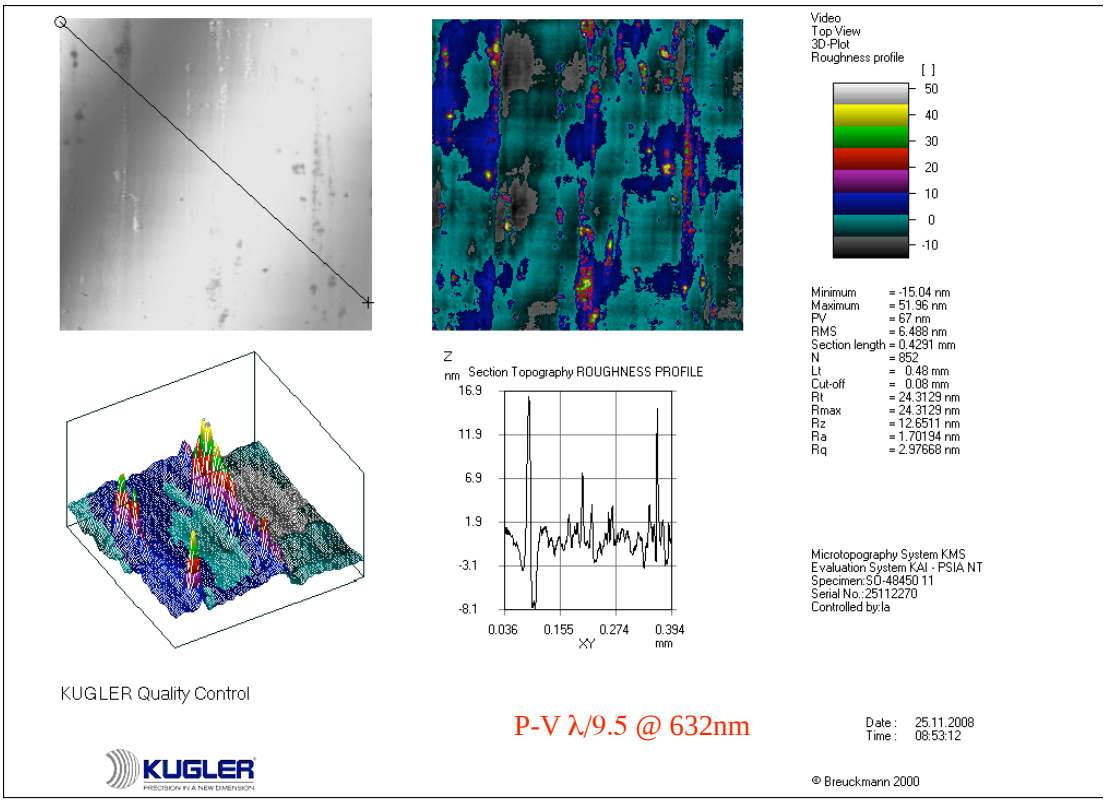

PRECISION IN A NEW DIMENSION

Skizze

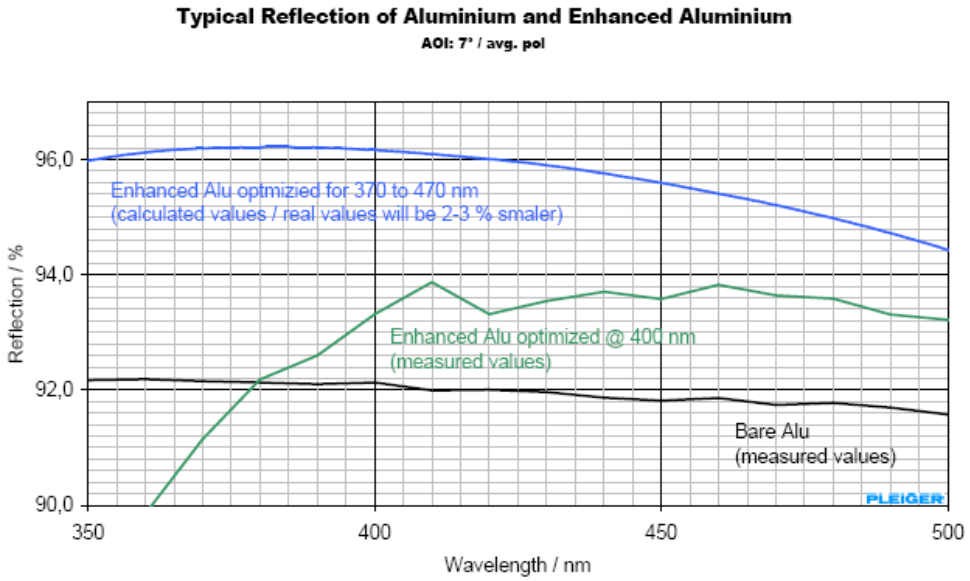

Bibliography

Acernese, F. & the VIRGO Scientific Collaboration. 2008, *Classical and Quantum Gravity*, 25, 184001 [ADS]

Ackerman, M. 1971, in Astrophysics and Space Science Library, Vol. 25, Mesospheric Models and Related Experiments, 149 [ADS]

Adelberger, K. L., Shapley, A. E., Steidel, C. C., Pettini, M., Erb, D. K., & Reddy, N. A. 2005, *Astrophys. J.*, 629, 636 [ADS]

Adelberger, K. L., Steidel, C. C., Kollmeier, J. A., & Reddy, N. A. 2006, *Astrophys. J.*, 637, 74 [ADS]

Adelman-McCarthy, J. K., Agüeros, M. A., Allam, S. S., Allende Prieto, C., Anderson, K. S. J., Anderson, S. F., Annis, J., Bahcall, N. A., Bailer-Jones, C. A. L., Baldry, I. K., Barentine, J. C., Bassett, B. A., Becker, A. C., Beers, T. C., Bell, E. F., Berlind, A. A., Bernardi, M., Blanton, M. R., Bochanski, J. J., Boroski, W. N., Brinchmann, J., Brinkmann, J., Brunner, R. J., Budavári, T., Carliles, S., Carr, M. A., Castander, F. J., Cinabro, D., Cool, R. J., Covey, K. R., Csabai, I., Cunha, C. E., Davenport, J. R. A., Dilday, B., Doi, M., Eisenstein, D. J., Evans, M. L., Fan, X., Finkbeiner, D. P., Friedman, S. D., Frieman, J. A., Fukugita, M., Gänsicke, B. T., Gates, E., Gillespie, B., Glazebrook, K., Gray, J., Grebel, E. K., Gunn, J. E., Gurbani, V. K., Hall, P. B., Harding, P., Harvanek, M., Hawley, S. L., Hayes, J., Heckman, T. M., Hendry, J. S., Hindsley, R. B., Hirata, C. M., Hogan, C. J., Hogg, D. W., Hyde, J. B., Ichikawa, S., Ivezić, Ž., Jester, S., Johnson, J. A., Jorgensen, A. M., Jurić, M., Kent, S. M., Kessler, R., Kleinman, S. J., Knapp, G. R., Kron, R. G., Krzesinski, J., Kuropatkin, N., Lamb, D. Q., Lampeitl, H., Lebedeva, S., Lee, Y. S., Leger, R. F., Lépine, S., Lima, M., Lin, H., Long, D. C., Loomis, C. P., Loveday, J., Lupton, R. H., Malanushenko, O., Malanushenko, V., Mandelbaum, R., Margon, B., Marriner, J. P., Martínez-Delgado, D., Matsubara, T., McGehee, P. M., McKay, T. A., Meiksin, A., Morrison, H. L., Munn, J. A., Nakajima, R., Neilsen, Jr., E. H., Newberg, H. J., Nichol, R. C.,

Nicinski, T., Nieto-Santisteban, M., Nitta, A., Okamura, S., Owen, R., Oyaizu, H., Padmanabhan, N., Pan, K., Park, C., Peoples, Jr., J., Pier, J. R., Pope, A. C., Purger, N., Raddick, M. J., Re Fiorentin, P., Richards, G. T., Richmond, M. W., Riess, A. G., Rix, H., Rockosi, C. M., Sako, M., Schlegel, D. J., Schneider, D. P., Schreiber, M. R., Schwope, A. D., Seljak, U., Sesar, B., Sheldon, E., Shimasaku, K., Sivarani, T., Smith, J. A., Snedden, S. A., Steinmetz, M., Strauss, M. A., SubbaRao, M., Suto, Y., Szalay, A. S., Szapudi, I., Szkody, P., Tegmark, M., Thakar, A. R., Tremonti, C. A., Tucker, D. L., Uomoto, A., Vanden Berk, D. E., Vandenberg, J., Vidrih, S., Vogeley, M. S., Voges, W., Vogt, N. P., Wadadekar, Y., Weinberg, D. H., West, A. A., White, S. D. M., Wilhite, B. C., Yanny, B., Yocum, D. R., York, D. G., Zehavi, I., & Zucker, D. B. 2008, *Astrophys. J. Suppl.*, 175, 297 [ADS]

Agafonova, I. I., Centurión, M., Levshakov, S. A., & Molaro, P. 2005, *Astron. & Astrophys.*, 441, 9 [ADS]

Agafonova, I. I., Levshakov, S. A., Reimers, D., Fechner, C., Tytler, D., Simcoe, R. A., & Songaila, A. 2007, *Astron. & Astrophys.*, 461, 893 [ADS]

Alcock, C. & Paczyński, B. 1979, *Nature*, 281, 358 [ADS]

Arns, J. A., Colburn, W. S., Barden, S. C., & Williams, J. B. 1999, in Bulletin of the American Astronomical Society, Vol. 31, Bulletin of the American Astronomical Society, 839 [ADS]

Auger Collaboration. 2004, *Nuclear Instruments and Methods in Physics Research Section A: Accelerators, Spectrometers, Detectors and Associated Equipment*, 523, 50 [LINK]

Bacon, R., Bauer, S., Boehm, P., Boudon, D., Brau-Nogué, S., Caillier, P., Capoani, L., Carollo, C. M., Champavert, N., Contini, T., Daguisé, E., Dallé, D., Delabre, B., Devriendt, J., Dreizler, S., Dubois, J., Dupieux, M., Dupin, J. P., Emsellem, E., Ferruit, P., Franx, M., Gallou, G., Gerssen, J., Guiderdoni, B., Hahn, T., Hofmann, D., Jarno, A., Kelz, A., Koehler, C., Kollatschny, W., Kosmalski, J., Laurent, F., Lilly, S. J., Lizon, J., Loupias, M., Lynn, S., Manescau, A., McDermid, R. M., Monstein, C., Nicklas, H., Parès, L., Pasquini, L., Pécontal-Rousset, A., Pécontal, E., Pello, R., Petit, C., Picat, J., Popow, E., Quirrenbach, A., Reiss, R., Renault, E., Roth, M., Schaye, J., Soucail, G., Steinmetz, M., Stroebele, S., Stuik, R., Weilbacher, P., Wozniak, H., & de Zeeuw, P. T. 2006, in Presented at the Society of Photo-Optical Instrumentation Engineers (SPIE) Conference, Vol. 6269, Society of Photo-Optical Instrumentation Engineers (SPIE) Conference Series [ADS]

Bacon, R., Copin, Y., Monnet, G., Miller, B. W., Allington-Smith, J. R., Bureau, M., Carollo, C. M., Davies, R. L., Emsellem, E., Kuntschner, H., Peletier, R. F., Verolme, E. K., & de Zeeuw, P. T. 2001, *Mon. Not. Roy. Astron. Soc.*, 326, 23 [ADS]

Bajtlik, S., Duncan, R. C., & Ostriker, J. P. 1988, *Astrophys. J.*, 327, 570 [ADS]

Ballinger, W. E., Peacock, J. A., & Heavens, A. F. 1996, *Mon. Not. Roy. Astron. Soc.*, 282, 877 [ADS]

Banday, A. J., Gorski, K. M., Bennett, C. L., Hinshaw, G., Kogut, A., Lineweaver, C., Smoot, G. F., & Tenorio, L. 1997, *Astrophys. J.*, 475, 393 [ADS]

Barden, S. C., Arns, J. A., Colburn, W. S., & Williams, J. B. 2002, in Society of Photo-Optical Instrumentation Engineers (SPIE) Conference Series, Vol. 4485, Society of Photo-Optical Instrumentation Engineers (SPIE) Conference Series, ed. A. M. Larar & M. G. Mlynczak, 429–438 [ADS]

Barden, S. C., Williams, J. B., Arns, J. A., & Colburn, W. S. 2000, in Astronomical Society of the Pacific Conference Series, Vol. 195, Imaging the Universe in Three Dimensions, ed. W. van Breugel & J. Bland-Hawthorn, 552 [ADS]

Barish, B. C. 1995, in American Institute of Physics Conference Series, Vol. 342, American Institute of Physics Conference Series, 479–486 [ADS]

Barkana, R. & Loeb, A. 2003, *Nature*, 421, 341 [ADS]

Basu-Zych, A. & Scharf, C. 2004, *Astrophys. J. Lett.*, 615, L85 [ADS]

Bechtold, J., Weymann, R. J., Lin, Z., & Malkan, M. A. 1987, *Astrophys. J.*, 315, 180 [ADS]

Becker, R. H., Fan, X., White, R. L., Strauss, M. A., Narayanan, V. K., Lupton, R. H., Gunn, J. E., Annis, J., Bahcall, N. A., Brinkmann, J., Connolly, A. J., Csabai, I., Czarapata, P. C., Doi, M., Heckman, T. M., Hennessy, G. S., Ivezić, Ž., Knapp, G. R., Lamb, D. Q., McKay, T. A., Munn, J. A., Nash, T., Nichol, R., Pier, J. R., Richards, G. T., Schneider, D. P., Stoughton, C., Szalay, A. S., Thakar, A. R., & York, D. G. 2001, *Astron. J.*, 122, 2850 [ADS]

Belz, J. 2009, *Nuclear Physics B - Proceedings Supplements*, 190, 5 , proceedings of the Cosmic Ray International Seminars [LINK]

Bennett, C. L., Banday, A. J., Gorski, K. M., Hinshaw, G., Jackson, P., Keegstra, P., Kogut, A., Smoot, G. F., Wilkinson, D. T., & Wright, E. L. 1996, *Astrophys. J. Lett.*, 464, L1+ [ADS]

Bennett, C. L., Bay, M., Halpern, M., Hinshaw, G., Jackson, C., Jarosik, N., Kogut, A., Limon, M., Meyer, S. S., Page, L., Spergel, D. N., Tucker, G. S., Wilkinson, D. T., Wollack, E., & Wright, E. L. 2003, *Astrophys. J.*, 583, 1 [ADS]

Bergeron, J. & Stasińska, G. 1986, *Astron. & Astrophys.*, 169, 1 [ADS]

Bershady, M. A. 2009, *ArXiv e-prints* [ADS]

Bertin, E. & Arnouts, S. 1996, *Astron. & Astrophys. Suppl. Ser.*, 117, 393 [ADS]

Bertone, S. & Schaye, J. 2010, *ArXiv e-prints* [ADS]

Bertone, S., Schaye, J., Booth, C. M., Dalla Vecchia, C., Theuns, T., & Wiersma, R. P. C. 2010a, *Mon. Not. Roy. Astron. Soc.*, 408, 1120 [ADS]

Bertone, S., Schaye, J., Dalla Vecchia, C., Booth, C. M., Theuns, T., & Wiersma, R. P. C. 2010b, *Mon. Not. Roy. Astron. Soc.*, 407, 544 [ADS]

Bertschinger, E. 1998, *Ann. Rev. Astron. Astrophys.*, 36, 599 [ADS]

Blake, C., Davis, T., Poole, G., Parkinson, D., Brough, S., Colless, M., Contreras, C., Couch, W., Croom, S., Drinkwater, M. J., Forster, K., Gilbank, D., Gladders, M., Glazebrook, K., Jelliffe, B., Jurek, R. J., Li, I., Madore, B., Martin, C., Pimbblet, K., Pracy, M., Sharp, R., Wisnioski, E., Woods, D., Wyder, T., & Yee, H. 2011, *ArXiv e-prints* [ADS]

Bond, J. R., Kofman, L., & Pogosyan, D. 1996, *Nature*, 380, 603 [ADS]

Bregman, J. N. 2007, *Ann. Rev. Astron. Astrophys.*, 45, 221 [ADS]

Bridge, C. R., Teplitz, H. I., Siana, B., Scarlata, C., Conselice, C. J., Ferguson, H. C., Brown, T. M., Salvato, M., Rudie, G. C., de Mello, D. F., Colbert, J., Gardner, J. P., Giavalisco, M., & Armus, L. 2010, *ArXiv e-prints* [ADS]

Bryan, G. L. 1999, *Comput. Sci. Eng., Vol. 1, No. 2, p. 46 - 53*, 1, 46 [ADS]

Bryan, G. L. 2008, in COSPAR, Plenary Meeting, Vol. 37, 37th COSPAR Scientific Assembly, 391 [ADS]

Bryan, G. L., Abel, T., & Norman, M. L. 2001, *ArXiv Astrophysics e-prints* [ADS]

Burgh, E. B., Bershady, M. A., Westfall, K. B., & Nordsieck, K. H. 2007, *Publ. Astron. Soc. Pac.*, 119, 1069 [ADS]

Burles, S., Nollett, K. M., & Turner, M. S. 2001, *Astrophys. J. Lett.*, 552, L1 [ADS]

Burles, S. & Tytler, D. 1996, *Astrophys. J.*, 460, 584 [ADS]

Calabretta, M. R. & Greisen, E. W. 2002, *Astron. & Astrophys.*, 395, 1077 [ADS]

Cantalupo, S., Porciani, C., Lilly, S. J., & Miniati, F. 2005, *Astrophys. J.*, 628, 61 [ADS]

Carrasco, E. & Parry, I. R. 1994, *Mon. Not. Roy. Astron. Soc.*, 271, 1 [ADS]

Carswell, R. F., Whelan, J. A. J., Smith, M. G., Boksenberg, A., & Tytler, D. 1982, *Mon. Not. Roy. Astron. Soc.*, 198, 91 [ADS]

Cen, R. 1992, *Astrophys. J. Suppl.*, 78, 341 [ADS]

Cen, R. & Fang, T. 2006, *Astrophys. J.*, 650, 573 [ADS]

Cen, R. & Ostriker, J. P. 1999, *Astrophys. J.*, 514, 1 [ADS]

Cen, R. & Ostriker, J. P. 2006, *Astrophys. J.*, 650, 560 [ADS]

Chaffee, Jr., F. H., Foltz, C. B., Bechtold, J., & Weymann, R. J. 1986, *Astrophys. J.*, 301, 116 [ADS]

Chen, H.-W., Prochaska, J. X., Bloom, J. S., & Thompson, I. B. 2005, *Astrophys. J. Lett.*, 634, L25 [ADS]

Chonko, J. C. 2006, PhD thesis, Columbia University, United States – New York [ADS]

Clowe, D., Bradač, M., Gonzalez, A. H., Markevitch, M., Randall, S. W., Jones, C., & Zaritsky, D. 2006, *Astrophys. J. Lett.*, 648, L109 [ADS]

Cohen, J. G., Oke, J. B., Carr, M., Harris, F. H., & Hamilton, D. 1988, in Astronomical Society of the Pacific Conference Series, Vol. 3, Fiber Optics in Astronomy, ed. S. C. Barden, 190–194 [ADS]

Couchman, H. M. P. & Rees, M. J. 1986, *Mon. Not. Roy. Astron. Soc.*, 221, 53 [ADS]

Cox, A. N. 2000, Allen's astrophysical quantities, ed. Cox, A. N. (New York: Springer) [ADS]

Croft, R. A. C. 2004, *Astrophys. J.*, 610, 642 [ADS]

Crotts, A. P. S. 1989, *Astrophys. J.*, 336, 550 [ADS]

Crotts, A. P. S. & Fang, Y. 1998, *Astrophys. J.*, 502, 16 [ADS]

Cuillandre, J. C., Fort, B., Picat, J. P., Soucail, J. P., Altieri, B., Beigbeder, F., Duplin, J. P., Pourthie, T., & Ratier, G. 1994, *Astron. & Astrophys.*, 281, 603 [ADS]

Daddi, E., Bournaud, F., Walter, F., Dannerbauer, H., Carilli, C. L., Dickinson, M., Elbaz, D., Morrison, G. E., Riechers, D., Onodera, M., Salmi, F., Krips, M., & Stern, D. 2010, *Astrophys. J.*, 713, 686 [ADS]

Dall'Aglio, A., Wisotzki, L., & Worseck, G. 2008, *Astron. & Astrophys.*, 491, 465 [ADS]

Danforth, C. W. & Shull, J. M. 2008, *Astrophys. J.*, 679, 194 [ADS]

Danforth, C. W., Stocke, J. T., & Shull, J. M. 2010, *Astrophys. J.*, 710, 613 [ADS]

Davis, M., Faber, S. M., Newman, J., Phillips, A. C., Ellis, R. S., Steidel, C. C., Conselice, C., Coil, A. L., Finkbeiner, D. P., Koo, D. C., Guhathakurta, P., Weiner, B., Schiavon, R., Willmer, C., Kaiser, N., Luppino, G. A., Wirth, G., Connolly, A., Eisenhardt, P., Cooper, M., & Gerke, B. 2003, in Society of Photo-Optical Instrumentation Engineers (SPIE) Conference Series, Vol. 4834, Society of Photo-Optical Instrumentation Engineers (SPIE) Conference Series, ed. P. Guhathakurta, 161–172 [ADS]

Davis, M., Guhathakurta, P., Konidaris, N. P., Newman, J. A., Ashby, M. L. N., Biggs, A. D., Barmby, P., Bundy, K., Chapman, S. C., Coil, A. L., Conselice, C. J., Cooper, M. C., Croton, D. J., Eisenhardt, P. R. M., Ellis, R. S., Faber, S. M., Fang, T., Fazio, G. G., Georgakakis, A., Gerke, B. F., Goss, W. M., Gwyn, S., Harker, J., Hopkins, A. M., Huang, J., Ivison, R. J., Kassin, S. A., Kirby, E. N., Koekemoer, A. M., Koo, D. C., Laird, E. S., Le Floc'h, E., Lin, L., Lotz, J. M., Marshall, P. J., Martin, D. C., Metevier, A. J., Moustakas, L. A., Nandra, K., Noeske, K. G., Papovich, C., Phillips, A. C., Rich, R. M., Rieke, G. H., Rigopoulou, D., Salim, S., Schiminovich, D., Simard, L., Smail, I., Small, T. A., Weiner, B. J., Willmer, C. N. A., Willner, S. P., Wilson, G., Wright, E. L., & Yan, R. 2007, *Astrophys. J. Lett.*, 660, L1 [ADS]

Dekel, A. & Birnboim, Y. 2006, *Mon. Not. Roy. Astron. Soc.*, 368, 2 [ADS]

Dekel, A., Birnboim, Y., Engel, G., Freundlich, J., Goerdt, T., Mumcuoglu, M., Neistein, E., Pichon, C., Teyssier, R., & Zinger, E. 2009, *Nature*, 457, 451 [ADS]

Dekker, H., D'Odorico, S., Kaufer, A., Delabre, B., & Kotzlowski, H. 2000, in Presented at the Society of Photo-Optical Instrumentation Engineers (SPIE) Conference, Vol. 4008, Society of Photo-Optical Instrumentation Engineers (SPIE) Conference Series, ed. M. Iye & A. F. Moorwood, 534–545 [ADS]

Dickson, L. D., Rallison, R. D., & Yung, B. H. 1994, *Appl. Opt.*, 33, 5378 [ADS]

Dijkstra, M. & Loeb, A. 2009, *Mon. Not. Roy. Astron. Soc.*, 400, 1109 [ADS]

Doroshkevich, A. G., Zel'Dovich, Y. B., & Novikov, I. D. 1967, *Sov. Astron.*, 11, 233 [ADS]

Efstathiou, G. 1992, *Mon. Not. Roy. Astron. Soc.*, 256, 43P [ADS]

Einstein, A. & de Sitter, W. 1932, *Proceedings of the National Academy of Science*, 18, 213 [ADS]

Epps, H. W. 1990, in Society of Photo-Optical Instrumentation Engineers (SPIE) Conference Series, Vol. 1235, Society of Photo-Optical Instrumentation Engineers (SPIE) Conference Series, ed. D. L. Crawford, 550–561 [ADS]

Faber, S. M., Phillips, A. C., Kibrick, R. I., Alcott, B., Allen, S. L., Burrous, J., Cantrall, T., Clarke, D., Coil, A. L., Cowley, D. J., Davis, M., Deich, W. T. S., Dietsch, K., Gilmore, D. K., Harper, C. A., Hilyard, D. F., Lewis, J. P., McVeigh, M., Newman, J., Osborne, J., Schiavon, R., Stover, R. J., Tucker, D., Wallace, V., Wei, M., Wirth, G., & Wright, C. A. 2003, in Presented at the Society of Photo-Optical Instrumentation Engineers (SPIE) Conference, Vol. 4841, Society of Photo-Optical Instrumentation Engineers (SPIE) Conference Series, ed. M. Iye & A. F. M. Moorwood, 1657–1669 [ADS]

Fan, X., Carilli, C. L., & Keating, B. 2006, *Ann. Rev. Astron. Astrophys.*, 44, 415 [ADS]

Fang, T., Buote, D. A., Humphrey, P. J., Canizares, C. R., Zappacosta, L., Maiolino, R., Tagliaferri, G., & Gastaldello, F. 2010, *Astrophys. J.*, 714, 1715 [ADS]

Fardal, M. A., Katz, N., Gardner, J. P., Hernquist, L., Weinberg, D. H., & Davé, R. 2001, *Astrophys. J.*, 562, 605 [ADS]

Feng, J. L. 2010, *Ann. Rev. Astron. Astrophys.*, 48, 495 [ADS]

Ferland, G. J., Korista, K. T., Verner, D. A., Ferguson, J. W., Kingdon, J. B., & Verner, E. M. 1998, *Publ. Astron. Soc. Pac.*, 110, 761 [ADS]

Fiore, F., Nicastro, F., Savaglio, S., Stella, L., & Vietri, M. 2000, *Astrophys. J. Lett.*, 544, L7 [ADS]

Fraternali, F. 2010, in American Institute of Physics Conference Series, Vol. 1240, American Institute of Physics Conference Series, ed. V. P. Debattista & C. C. Popescu, 135–145 [ADS]

Frederick, J. E. & Mentall, J. E. 1982, *Geophys. Res. Lett.*, 9, 461 [ADS]

Frieman, J. A., Turner, M. S., & Huterer, D. 2008, *Ann. Rev. Astron. Astrophys.*, 46, 385 [ADS]

Froning, C. S. & Green, J. C. 2009, *Astrophys. Space Sci.*, 320, 181 [ADS]

Fukugita, M. & Peebles, P. J. E. 2004, *Astrophys. J.*, 616, 643 [ADS]

Furlanetto, S. R., Schaye, J., Springel, V., & Hernquist, L. 2003, *Astrophys. J. Lett.*, 599, L1 [ADS]

Furlanetto, S. R., Schaye, J., Springel, V., & Hernquist, L. 2004, *Astrophys. J.*, 606, 221 [ADS]

Furlanetto, S. R., Schaye, J., Springel, V., & Hernquist, L. 2005, *Astrophys. J.*, 622, 7 [ADS]

Glazebrook, K., Blake, C., Couch, W., Forbes, D., Drinkwater, M., Jurek, R., Pimbblet, K., Madore, B., Martin, C., Small, T., Forster, K., Colless, M., Sharp, R., Croom, S., Woods, D., Pracy, M., Gilbank, D., Yee, H., & Gladders, M. 2007, in Astronomical Society of the Pacific Conference Series, Vol. 379, Cosmic Frontiers, ed. N. Metcalfe & T. Shanks, 72 [ADS]

Gnat, O. & Sternberg, A. 2007, *Astrophys. J. Suppl.*, 168, 213 [ADS]

Gould, A. & Weinberg, D. H. 1996, *Astrophys. J.*, 468, 462 [ADS]

Grange, R., Milliard, B., McLean, R., Martin, C., Deharveng, J. M., & Schiminovich, D. 2005, in Society of Photo-Optical Instrumentation Engineers (SPIE) Conference Series, Vol. 5898, Society of Photo-Optical Instrumentation Engineers (SPIE) Conference Series, ed. O. H. W. Siegmund, 308–312 [ADS]

Green, J. C. 2000, in Society of Photo-Optical Instrumentation Engineers (SPIE) Conference Series, Vol. 4013, Society of Photo-Optical Instrumentation Engineers (SPIE) Conference Series, ed. J. B. Breckinridge & P. Jakobsen, 352–359 [ADS]

Greenstein, J. L. & Sargent, A. I. 1974, *Astrophys. J. Suppl.*, 28, 157 [ADS]

Greisen, E. W., Calabretta, M. R., Valdes, F. G., & Allen, S. L. 2006, *Astron. & Astrophys.*, 446, 747 [ADS]

Gunn, J. E. & Peterson, B. A. 1965, *Astrophys. J.*, 142, 1633 [ADS]

Guth, A. H. 1981, *Phys. Rev. D*, 23, 347 [ADS]

Haardt, F. & Madau, P. 1996, *Astrophys. J.*, 461, 20 [ADS]

Haardt, F. & Madau, P. 2001, in Clusters of Galaxies and the High Redshift Universe Observed in X-rays, ed. D. M. Neumann & J. T. V. Tran [ADS]

Hamden, E. T., Greer, F., Hoenk, M. E., Blacksberg, J., Dickie, M. R., Nikzad, S., Martin, C. D., & Schiminovich, D. 2011, *ArXiv e-prints* [ADS]

Hamilton, D., Oke, J. B., Carr, M. A., Cromer, J., Harris, F. H., Cohen, J., Emery, E., & Blakee, L. 1993, *Publ. Astron. Soc. Pac.*, 105, 1308 [ADS]

Harms, R. J., Beaver, E., Burbidge, E. M., Angel, R., Bartko, F., Bloomquist, W., Flemming, J. C., Bohlin, R., Davidsen, A. F., & Ford, H. 1979, in Society of Photo-Optical Instrumentation Engineers (SPIE) Conference Series, Vol. 183, Society of Photo-Optical Instrumentation Engineers (SPIE) Conference Series, ed. C. L. Wyman, 74–87 [ADS]

Harrison, F. A., Boggs, S. E., Bolotnikov, A. E., Christensen, F. E., Cook, W. R., Craig, W. W., Hailey, C. J., Jimenez-Garate, M. A., Mao, P. H., Schindler, S. M., & Windt, D. L. 2000, in Presented at the Society of Photo-Optical Instrumentation Engineers (SPIE) Conference, Vol. 4012, Society of Photo-Optical Instrumentation Engineers (SPIE) Conference Series, ed. J. E. Truemper & B. Aschenbach, 693–699 [ADS]

Hayashino, T., Matsuda, Y., Tamura, H., Yamauchi, R., Yamada, T., Ajiki, M., Fujita, S. S., Murayama, T., Nagao, T., Ohta, K., Okamura, S., Ouchi, M., Shimasaku, K., Shioya, Y., & Taniguchi, Y. 2004, *Astron. J.*, 128, 2073 [ADS]

Hennawi, J. F., Prochaska, J. X., Burles, S., Strauss, M. A., Richards, G. T., Schlegel, D. J., Fan, X., Schneider, D. P., Zakamska, N. L., Oguri, M., Gunn, J. E., Lupton, R. H., & Brinkmann, J. 2006, *Astrophys. J.*, 651, 61 [ADS]

Hennawi, J. F., Prochaska, J. X., Kollmeier, J., & Zheng, Z. 2009, *Astrophys. J. Lett.*, 693, L49 [ADS]

Hopkins, A. M. 2007, in Astronomical Society of the Pacific Conference Series, Vol. 380, Deepest Astronomical Surveys, ed. J. Afonso, H. C. Ferguson, B. Mobasher, & R. Norris, 423 [ADS]

Hubble, E. 1929, *Proceedings of the National Academy of Science*, 15, 168 [ADS]

Hubrich, C. & Stuhl, F. 1980, *J. Photochem*, 12, 93

Huguenin, D. 1994, *Infrared Physics and Technology*, 35, 195 [ADS]

Hui, L., Stebbins, A., & Burles, S. 1999, *Astrophys. J. Lett.*, 511, L5 [ADS]

IceCube Collaboration. 2007, *Nuclear Physics B Proceedings Supplements*, 172, 13 [ADS]

Janknecht, E., Reimers, D., Lopez, S., & Tytler, D. 2006, *Astron. & Astrophys.*, 458, 427 [ADS]

Jannuzi, B. T., Bahcall, J. N., Bergeron, J., Boksenberg, A., Hartig, G. F., Kirhakos, S., Sargent, W. L. W., Savage, B. D., Schneider, D. P., Turnshek, D. A., Weymann, R. J., & Wolfe, A. M. 1998, *Astrophys. J. Suppl.*, 118, 1 [ADS]

Jelinsky, P. 2001, Detector to Instrument Interface Control Document, Tech. Rep. GAL-JPL-303-F, JPL

Joergensen, J. L. & Pickles, A. J. 1998, in Presented at the Society of Photo-Optical Instrumentation Engineers (SPIE) Conference, Vol. 3351, Society of Photo-Optical Instrumentation Engineers (SPIE) Conference Series, ed. H. Lewis, 51–61 [ADS]

Kaastra, J. S., Werner, N., Herder, J. W. A. d., Paerels, F. B. S., de Plaa, J., Rasmussen, A. P., & de Vries, C. P. 2006, *Astrophys. J.*, 652, 189 [ADS]

Kennicutt, Jr., R. C. 1998, *Ann. Rev. Astron. Astrophys.*, 36, 189 [ADS]

Kennicutt, Jr., R. C., Armus, L., Bendo, G., Calzetti, D., Dale, D. A., Draine, B. T., Engelbracht, C. W., Gordon, K. D., Grauer, A. D., Helou, G., Hollenbach, D. J., Jarrett, T. H., Kewley, L. J., Leitherer, C., Li, A., Malhotra, S., Regan, M. W., Rieke, G. H., Rieke, M. J., Roussel, H., Smith, J.-D. T., Thornley, M. D., & Walter, F. 2003, *Publ. Astron. Soc. Pac.*, 115, 928 [ADS]

Kereš, D., Katz, N., Davé, R., Fardal, M., & Weinberg, D. H. 2009a, *Mon. Not. Roy. Astron. Soc.*, 396, 2332 [ADS]

Kereš, D., Katz, N., Fardal, M., Davé, R., & Weinberg, D. H. 2009b, *Mon. Not. Roy. Astron. Soc.*, 395, 160 [ADS]

Kereš, D., Katz, N., Weinberg, D. H., & Davé, R. 2005, *Mon. Not. Roy. Astron. Soc.*, 363, 2 [ADS]

Kern, B. 2002, PhD thesis, CALIFORNIA INSTITUTE OF TECHNOLOGY [ADS]

Kim, Y. & Croft, R. A. C. 2007, *Mon. Not. Roy. Astron. Soc.*, 374, 535 [ADS]

Kirkman, D. & Tytler, D. 2008, *Mon. Not. Roy. Astron. Soc.*, 391, 1457 [ADS]

Kogelnik, H. 1969, *The Bell System Technical Journal*, 48, 2909 [ADS]

Kollmeier, J. A., Zheng, Z., Davé, R., Gould, A., Katz, N., Miralda-Escudé, J., & Weinberg, D. H. 2010, *Astrophys. J.*, 708, 1048 [ADS]

Komatsu, E., Smith, K. M., Dunkley, J., Bennett, C. L., Gold, B., Hinshaw, G., Jarosik, N., Larson, D., Nolta, M. R., Page, L., Spergel, D. N., Halpern, M., Hill, R. S., Kogut, A., Limon, M., Meyer, S. S., Odegard, N., Tucker, G. S., Weiland, J. L., Wollack, E., & Wright, E. L. 2011, *Astrophys. J. Suppl.*, 192, 18 [ADS]

Kuznetsov, I. G., Wilkinson, E., Content, D. A., Boucarut, R. A., & Madison, T. J. 2004, in Presented at the Society of Photo-Optical Instrumentation Engineers (SPIE) Conference, Vol. 5178, Society of Photo-Optical Instrumentation Engineers (SPIE) Conference Series, ed. M. A. Kahan, 267–277 [ADS]

Lang, D., Hogg, D. W., Mierle, K., Blanton, M., & Roweis, S. 2010, *Astron. J.*, 139, 1782 [ADS]

Laurent, F., Renault, E., Kosmalski, J., Adjali, L., Boudon, D., Bacon, R., Caillier, P., Remillieux, A., Salaun, Y., & Delabre, B. 2008, in Presented at the Society of Photo-Optical Instrumentation Engineers (SPIE) Conference, Vol. 7018, Society of Photo-Optical Instrumentation Engineers (SPIE) Conference Series [ADS]

Lee, A. T., Ade, P., Balbi, A., Bock, J., Borrill, J., Boscaleri, A., de Bernardis, P., Ferreira, P. G., Hanany, S., Hristov, V. V., Jaffe, A. H., Mauskopf, P. D., Netterfield, C. B., Pascale, E., Rabii, B., Richards, P. L., Smoot, G. F., Stompor, R., Winant, C. D., & Wu, J. H. P. 2001, *Astrophys. J. Lett.*, 561, L1 [ADS]

Leinert, C., Bowyer, S., Haikala, L. K., Hanner, M. S., Hauser, M. G., Levasseur-Regourd, A., Mann, I., Mattila, K., Reach, W. T., Schlosser, W., Staude, H. J., Toller, G. N., Weiland, J. L., Weinberg, J. L., & Witt, A. N. 1998, *Astron. & Astrophys. Suppl. Ser.*, 127, 1 [ADS]

Liske, J. & Williger, G. M. 2001, *Mon. Not. Roy. Astron. Soc.*, 328, 653 [ADS]

Loeb, A. & Barkana, R. 2001, *Ann. Rev. Astron. Astrophys.*, 39, 19 [ADS]

Lu, L. 1991, *Astrophys. J.*, 379, 99 [ADS]

Lynds, R. 1971, *Astrophys. J. Lett.*, 164, L73+ [ADS]

Mackay, C. D., Baldwin, J. E., & Tubbs, R. N. 2003, in Presented at the Society of Photo-Optical Instrumentation Engineers (SPIE) Conference, Vol. 4840, Society of Photo-Optical Instrumentation Engineers (SPIE) Conference Series, ed. J. R. P. Angel & R. Gilmozzi, 436–442 [ADS]

Madau, P., Ferguson, H. C., Dickinson, M. E., Giavalisco, M., Steidel, C. C., & Fruchter, A. 1996, *Mon. Not. Roy. Astron. Soc.*, 283, 1388 [ADS]

Marinacci, F., Binney, J., Fraternali, F., Nipoti, C., Ciotti, L., & Londrillo, P. 2010, *Mon. Not. Roy. Astron. Soc.*, 404, 1464 [ADS]

Marinoni, C. & Buzzi, A. 2010, *Nature*, 468, 539 [ADS]

Markwardt, C. B. 2009, in Astronomical Society of the Pacific Conference Series, Vol. 411, Astronomical Society of the Pacific Conference Series, ed. D. A. Bohlender, D. Durand, & P. Dowler, 251 [ADS]

Martin, D. C. 2009, rOSES Proposal, Submitted

—. 2010, private communication

Martin, D. C., Chang, D., Matuszewski, M., Rahman, S., Morrisey, P., Moore, A., & Steidel, C. C. 2011, *Nature*, submitted

Martin, D. C., Fanson, J., Schiminovich, D., Morrissey, P., Friedman, P. G., Barlow, T. A., Conrow, T., Grange, R., Jelinsky, P. N., Milliard, B., Siegmund, O. H. W., Bianchi, L., Byun, Y., Donas, J., Forster, K., Heckman, T. M., Lee, Y., Madore, B. F., Malina, R. F., Neff, S. G., Rich, R. M., Small, T., Surber, F., Szalay, A. S., Welsh, B., & Wyder, T. K. 2005, *Astrophys. J. Lett.*, 619, L1 [ADS]

Martin, D. C., Moore, A., Morrissey, P., Matuszewski, M., Rahman, S., Adkins, S., & Epps, H. 2010, in Presented at the Society of Photo-Optical Instrumentation Engineers (SPIE) Conference, Vol. 7735, Society of Photo-Optical Instrumentation Engineers (SPIE) Conference Series [ADS]

Mather, J. C., Cheng, E. S., Eplee, Jr., R. E., Isaacman, R. B., Meyer, S. S., Shafer, R. A., Weiss, R., Wright, E. L., Bennett, C. L., Boggess, N. W., Dwek, E., Gulkis, S., Hauser, M. G., Janssen, M., Kelsall, T., Lubin, P. M., Moseley, Jr., S. H., Murdock, T. L., Silverberg, R. F., Smoot, G. F., & Wilkinson, D. T. 1990, *Astrophys. J. Lett.*, 354, L37 [ADS]

Matsuda, Y., Yamada, T., Hayashino, T., Tamura, H., Yamauchi, R., Ajiki, M., Fujita, S. S., Murayama, T., Nagao, T., Ohta, K., Okamura, S., Ouchi, M., Shimasaku, K., Shioya, Y., & Taniguchi, Y. 2004, *Astron. J.*, 128, 569 [ADS]

Matsuda, Y., Yamada, T., Hayashino, T., Yamauchi, R., Nakamura, Y., Morimoto, N., Ouchi, M., Ono, Y., Kousai, K., Nakamura, E., Horie, M., Fujii, T., Umemura, M., & Mori, M. 2011, *Mon. Not. Roy. Astron. Soc.*, 410, L13 [ADS]

Matuszewski, M., Chang, D., Crabill, R. M., Martin, D. C., Moore, A. M., Morrissey, P., & Rahman, S. 2010, in Presented at the Society of Photo-Optical Instrumentation Engineers (SPIE) Conference, Vol. 7735, Society of Photo-Optical Instrumentation Engineers (SPIE) Conference Series [ADS]

Matuszewski, M. & Martin, D. C. in prep.

McDonald, P. & Miralda-Escudé, J. 1999, *Astrophys. J.*, 518, 24 [ADS]

Meiksin, A. A. 2009, *Reviews of Modern Physics*, 81, 1405 [ADS]

Ménard, B., Wild, V., Nestor, D., Quider, A., & Zibetti, S. 2009, *ArXiv e-prints* [ADS]

Milliard, B. 2010, Private Communication

Milliard, B., Donas, J., Laget, M., & Huguenin, D. 1994, in ESA Special Publication, Vol. 183, ESA Special Publication, ed. E. J. Rolfe, 253–257 [ADS]

Milliard, B., Martin, D. C., Schiminovich, D., Evrard, J., Matuszewski, M., Rahman, S., Tuttle, S., McLean, R., Deharveng, J.-M., Mirc, F., Grange, R., & Chave, R. 2010, in Presented at the Society of Photo-Optical Instrumentation Engineers (SPIE) Conference, Vol. 7732, Society of Photo-Optical Instrumentation Engineers (SPIE) Conference Series [ADS]

MINOS Collaboration. 2006, *Nuclear Physics B Proceedings Supplements*, 155, 162 [ADS]

Minzner, R. A., Reber, C. A., Jacchia, L. G., Huang, F. T., Cole, A. E., Kantor, A. J., Keneshea, T. J., Zimmerman, S. P., & Forbes, J. M. 1976, Defining constants, equations, and abbreviated tables of the 1975 US Standard Atmosphere, Tech. rep., US Government Printing Office [ADS]

Moharam, M. G. & Gaylord, T. K. 1983, *J. Opt. Soc. Am.*, 73, 1105 [LINK]

Molina, L. T. & Molina, M. J. 1986, *J. Geophys. Res.*, 91, 14501 [ADS]

Monet, D. G., Levine, S. E., Canzian, B., Ables, H. D., Bird, A. R., Dahn, C. C., Guetter, H. H., Harris, H. C., Henden, A. A., Leggett, S. K., Levison, H. F., Luginbuhl, C. B., Martini, J., Monet, A. K. B., Munn, J. A., Pier, J. R., Rhodes, A. R., Riepe, B., Sell, S., Stone, R. C., Vrba, F. J., Walker, R. L., Westerhout, G., Brucato, R. J., Reid, I. N., Schoening, W., Hartley, M., Read, M. A., & Tritton, S. B. 2003, *Astron. J.*, 125, 984 [ADS]

Moore, G. 1965, *Electronics Magazine*, 38

Moré, J. 1978, in Lecture Notes in Mathematics, Vol. 630, Numerical Analysis, ed. G. Watson (Springer Berlin / Heidelberg), 105–116, 10.1007/BFb0067700 [LINK]

Morrissey, P. 2004, "GALEX Detector Flight Operations Guide", gal-cit-329v6b edn., California Institute of Technology

Morrissey, P., Conrow, T., Barlow, T. A., Small, T., Seibert, M., Wyder, T. K., Budavári, T., Arnouts, S., Friedman, P. G., Forster, K., Martin, D. C., Neff, S. G., Schiminovich, D., Bianchi, L., Donas, J., Heckman, T. M., Lee, Y.-W., Madore, B. F., Milliard, B., Rich, R. M., Szalay, A. S., Welsh, B. Y., & Yi, S. K. 2007, *Astrophys. J. Suppl.*, 173, 682 [ADS]

Morton, D. C. 1991, *Astrophys. J. Suppl.*, 77, 119 [ADS]

Morton, D. C. 2000, *Astrophys. J. Suppl.*, 130, 403 [ADS]

Morton, D. C. 2003, *Astrophys. J. Suppl.*, 149, 205 [ADS]

Murdoch, H. S., Hunstead, R. W., Pettini, M., & Blades, J. C. 1986, in IAU Symposium, Vol. 119, Quasars, ed. G. Swarup & V. K. Kapahi, 563–566 [ADS]

Netterfield, C. B., Ade, P. A. R., Bock, J. J., Bond, J. R., Borrill, J., Boscaleri, A., Coble, K., Contaldi, C. R., Crill, B. P., de Bernardis, P., Farese, P., Ganga, K., Giacometti, M., Hivon, E., Hristov, V. V., Iacoangeli, A., Jaffe, A. H., Jones, W. C., Lange, A. E., Martinis, L., Masi, S., Mason, P., Mauskopf, P. D., Melchiorri, A., Montroy, T., Pascale, E., Piacentini, F., Pogosyan, D., Pongetti, F., Prunet, S., Romeo, G., Ruhl, J. E., & Scaramuzzi, F. 2002, *Astrophys. J.*, 571, 604 [ADS]

Neufeld, D. A. 1990, *Astrophys. J.*, 350, 216 [ADS]

Nicastro, F., Mathur, S., Elvis, M., Drake, J., Fiore, F., Fang, T., Fruscione, A., Krongold, Y., Marshall, H., & Williams, R. 2005, *Astrophys. J.*, 629, 700 [ADS]

Nikzad, S., Hoenk, M. E., Greer, F., Jones, T., Jacquot, B., Monacos, S., Blacksberg, J., Hamden, E., Schiminovich, D., Martin, C., & Morrissey, P. 2011, *ArXiv e-prints* [ADS]

Nilsson, K. K., Fynbo, J. P. U., Møller, P., Sommer-Larsen, J., & Ledoux, C. 2006, *Astron. & Astrophys.*, 452, L23 [ADS]

Norris, J., Peterson, B. A., & Hartwick, F. D. A. 1983, *Astrophys. J.*, 273, 450 [ADS]

O'Meara, J. M., Prochaska, J. X., Burles, S., Prochter, G., Bernstein, R. A., & Burgess, K. M. 2007, *Astrophys. J.*, 656, 666 [ADS]

O'Shea, B. W., Bryan, G. L., Bordner, J., Norman, M. L., Abel, T., Harkness, R., & Kritsuk, A. 2004, *ArXiv Astrophysics e-prints* [ADS]

O'Shea, B. W., Nagamine, K., Springel, V., Hernquist, L., & Norman, M. L. 2005, *Astrophys. J. Suppl.*, 160, 1 [ADS]

Owen, R. E., Siegmund, W. A., Limmongkol, S., & Hull, C. L. 1994, in Presented at the Society of Photo-Optical Instrumentation Engineers (SPIE) Conference, Vol. 2198, Society of Photo-Optical Instrumentation Engineers (SPIE) Conference Series, ed. D. L. Crawford & E. R. Craine, 110–114 [ADS]

Palmer, B. A. & Engleman, R. 1983, Atlas of the Thorium spectrum [ADS]

Palmer, C. & Loewen, E. 2005, Diffraction Grating Handbook, 6th edn. (Newport Corp.)

Peacock, J. A., The 2DF Galaxy Redshift Survey Team, Colless, M., Peacock, J., Baugh, C. M., Bland-Hawthorn, J., Bridges, T., Cannon, R., Cole, S., Collins, C., Couch, W., Cross, N., Dalton, G., Deeley, K., de Propris, R., Driver, S., Efstathiou, G., Ellis, R. S., Frenk, C. S., Glazebrook, K., Jackson, C., Lahav, O., Lewis, I., Lumsden, S., Maddox, S., Madgwick, D., Norberg, P., Percival, W., Peterson, B., Sutherland, W., & Taylor, K. 2001, in Deep Fields, ed. S. Cristiani, A. Renzini, & R. E. Williams, 221 [ADS]

Perlmutter, S., Gabi, S., Goldhaber, G., Goobar, A., Groom, D. E., Hook, I. M., Kim, A. G., Kim, M. Y., Lee, J. C., Pain, R., Pennypacker, C. R., Small, I. A., Ellis, R. S., McMahon, R. G., Boyle, B. J., Bunclark, P. S., Carter, D., Irwin, M. J., Glazebrook, K., Newberg, H. J. M., Filippenko, A. V., Matheson, T., Dopita, M., Couch, W. J., & The Supernova Cosmology Project. 1997, *Astrophys. J.*, 483, 565 [ADS]

Phillipps, S. 1994, *Mon. Not. Roy. Astron. Soc.*, 269, 1077 [ADS]

Pieri, M. M., Frank, S., Weinberg, D. H., Mathur, S., & York, D. G. 2010, *Astrophys. J. Lett.*, 724, L69 [ADS]

Popowski, P. A., Weinberg, D. H., Ryden, B. S., & Osmer, P. S. 1998, *Astrophys. J.*, 498, 11 [ADS]

Prince, T. 2009, in Astronomy, Vol. 2010, astro2010: The Astronomy and Astrophysics Decadal Survey, 238 [ADS]

Prochaska, J. X. & Tumlinson, J. 2009, in Astrophysics in the Next Decade, ed. Thronson, H. A., Stiavelli, M., & Tielens, A. (Springer), 419 [ADS]

Rahman, S. 2010, PhD thesis, California Institute of Technology

Ramsey, L. W. 1988, in Astronomical Society of the Pacific Conference Series, Vol. 3, Fiber Optics in Astronomy, ed. S. C. Barden, 26–39 [ADS]

Rasmussen, A. P., Kahn, S. M., Paerels, F., Herder, J. W. d., Kaastra, J., & de Vries, C. 2007, *Astrophys. J.*, 656, 129 [ADS]

Rauch, M. 1998, *Ann. Rev. Astron. Astrophys.*, 36, 267 [ADS]

Rauch, M., Haehnelt, M., Bunker, A., Becker, G., Marleau, F., Graham, J., Cristiani, S., Jarvis, M., Lacey, C., Morris, S., Peroux, C., Röttgering, H., & Theuns, T. 2008, *Astrophys. J.*, 681, 856 [ADS]

Rauch, M., Miralda-Escude, J., Sargent, W. L. W., Barlow, T. A., Weinberg, D. H., Hernquist, L., Katz, N., Cen, R., & Ostriker, J. P. 1997, *Astrophys. J.*, 489, 7 [ADS]

Reimers, D., Agafonova, I. I., Levshakov, S. A., Hagen, H., Fechner, C., Tytler, D., Kirkman, D., & Lopez, S. 2006, *Astron. & Astrophys.*, 449, 9 [ADS]

Reiprich, T. H. & Böhringer, H. 2002, *Astrophys. J.*, 567, 716 [ADS]

Richards, G. T., Fan, X., Newberg, H. J., Strauss, M. A., Vanden Berk, D. E., Schneider, D. P., Yanny, B., Boucher, A., Burles, S., Frieman, J. A., Gunn, J. E., Hall, P. B., Ivezić, Ž., Kent, S., Loveday, J., Lupton, R. H., Rockosi, C. M., Schlegel, D. J., Stoughton, C., SubbaRao, M., & York, D. G. 2002, *Astron. J.*, 123, 2945 [ADS]

Richter, P., Fang, T., & Bryan, G. L. 2006, *Astron. & Astrophys.*, 451, 767 [ADS]

Riess, A. G., Filippenko, A. V., Challis, P., Clocchiatti, A., Diercks, A., Garnavich, P. M., Gilliland, R. L., Hogan, C. J., Jha, S., Kirshner, R. P., Leibundgut, B., Phillips, M. M., Reiss, D., Schmidt, B. P., Schommer, R. A., Smith, R. C., Spyromilio, J., Stubbs, C., Suntzeff, N. B., & Tonry, J. 1998, *Astron. J.*, 116, 1009 [ADS]

Rossin, C., Grange, R., Milliard, B., Martin, L., Moreaux, G., Blanchard, P., Deharveng, J., Evrard, J., Martin, C., McLean, R., & Schiminovich, D. 2008, in Society of Photo-Optical Instrumentation Engineers (SPIE) Conference Series, Vol. 7018, Society of Photo-Optical Instrumentation Engineers (SPIE) Conference Series [ADS]

Rubin, V. C., Burstein, D., Ford, Jr., W. K., & Thonnard, N. 1985, *Astrophys. J.*, 289, 81 [ADS]

Sansonetti, J. E., Reader, J., Sansonetti, C. J., & Acquista, N. 1992, *National Institute of Standards and Technology Journal of Research*, 97, 1 [ADS]

Sargent, W. L. W., Young, P. J., Boksenberg, A., & Tytler, D. 1980, *Astrophys. J. Suppl.*, 42, 41 [ADS]

Schaye, J., Dalla Vecchia, C., Booth, C. M., Wiersma, R. P. C., Theuns, T., Haas, M. R., Bertone, S., Duffy, A. R., McCarthy, I. G., & van de Voort, F. 2010, *Mon. Not. Roy. Astron. Soc.*, 402, 1536 [ADS]

Schiminovich, D., Friedman, P. G., Martin, C., & Morrissey, P. F. 2001, *Astrophys. J. Lett.*, 563, L161 [ADS]

Schiminovich, D., Ilbert, O., Arnouts, S., Milliard, B., Tresse, L., Le Fèvre, O., Treyer, M., Wyder, T. K., Budavári, T., Zucca, E., Zamorani, G., Martin, D. C., Adami, C., Arnaboldi, M., Bardelli, S., Barlow, T., Bianchi, L., Bolzonella, M., Bottini, D., Byun, Y., Cappi, A., Contini, T., Charlot, S., Donas, J., Forster, K., Foucaud, S., Franzetti, P., Friedman, P. G., Garilli, B., Gavignaud, I., Guzzo, L., Heckman, T. M., Hoopes, C., Iovino, A., Jelinsky, P., Le Brun, V., Lee, Y., Maccagni, D., Madore, B. F., Malina, R., Marano, B., Marinoni, C., McCracken, H. J., Mazure, A., Meneux, B., Morrissey, P., Neff, S., Paltani, S., Pellò, R., Picat, J. P., Pollo, A., Pozzetti, L., Radovich, M., Rich, R. M., Scaramella, R., Scodeggio, M., Seibert, M., Siegmund, O., Small, T., Szalay, A. S., Vettolani, G., Welsh, B., Xu, C. K., & Zanichelli, A. 2005, *Astrophys. J. Lett.*, 619, L47 [ADS]

Schirber, M., Miralda-Escudé, J., & McDonald, P. 2004, *Astrophys. J.*, 610, 105 [ADS]

Schlegel, D. J., Finkbeiner, D. P., & Davis, M. 1998, *Astrophys. J.*, 500, 525 [ADS]

Schmoll, J., Roth, M. M., & Laux, U. 2003, *Publ. Astron. Soc. Pac.*, 115, 854 [ADS]

Schneider, D. P., Hall, P. B., Richards, G. T., Strauss, M. A., Vanden Berk, D. E., Anderson, S. F., Brandt, W. N., Fan, X., Jester, S., Gray, J., Gunn, J. E., SubbaRao, M. U., Thakar, A. R., Stoughton, C., Szalay, A. S., Yanny, B., York, D. G., Bahcall, N. A., Barentine, J., Blanton, M. R., Brewington, H., Brinkmann, J., Brunner, R. J., Castander, F. J., Csabai, I., Frieman, J. A., Fukugita, M., Harvanek, M., Hogg, D. W., Ivezić, Ž., Kent, S. M., Kleinman, S. J., Knapp, G. R., Kron, R. G., Krzesiński, J., Long, D. C., Lupton, R. H., Nitta, A., Pier, J. R., Saxe, D. H., Shen, Y., Snedden, S. A., Weinberg, D. H., & Wu, J. 2007, *Astron. J.*, 134, 102 [ADS]

Schroeder, D. J. 1987, Astronomical optics, 2nd ed. (Academic Press) [ADS]

Scott, J., Bechtold, J., Morita, M., Dobrzycki, A., & Kulkarni, V. P. 2002, *Astrophys. J.*, 571, 665 [ADS]

Seljak, U. & Zaldarriaga, M. 1996, *Astrophys. J.*, 469, 437 [ADS]

Selwyn, G., Podolske, J., & Johnston, H. S. 1977, *Geophys. Res. Lett.*, 4, 427 [ADS]

Sembach, K. R. & Tonry, J. L. 1996, *Astron. J.*, 112, 797 [ADS]

Serra, G., Giard, M., Bouchou, F., Dupac, X., Gabarrot, F., Meny, C., Ristorcelli, I., Lamarre, J. M., Bernard, J. P., Pajot, F., Stepnick, B., & Torre, J. P. 2002, *Advances in Space Research*, 30, 1297 [ADS]

Shapley, A. E., Steidel, C. C., Pettini, M., & Adelberger, K. L. 2003, *Astrophys. J.*, 588, 65 [ADS]

Shapley, A. E., Steidel, C. C., Pettini, M., Adelberger, K. L., & Erb, D. K. 2006, *Astrophys. J.*, 651, 688 [ADS]

Sheinis, A. I. 2006, in Presented at the Society of Photo-Optical Instrumentation Engineers (SPIE) Conference, Vol. 6269, Society of Photo-Optical Instrumentation Engineers (SPIE) Conference Series [ADS]

Shepherd, M. ????, "Palomar Autoguider", Palomar Observatory, California Institute of Technology [LINK]

Siegmund, O. H. W., Welsh, B. Y., Martin, C., Barlow, T., Bianchi, L., Byun, Y., Forster, K., Friedman, P. G., Jelinsky, P. N., Madore, B. F., Malina, R., Milliard, B., Morrissey, P. F., Neff, S. G., Rich, M. R., Schiminovich, D., Small, T., Szalay, A., & Wyder, T. K. 2004, in Presented at the Society of Photo-Optical Instrumentation Engineers (SPIE) Conference, Vol. 5488, Society of Photo-Optical Instrumentation Engineers (SPIE) Conference Series, ed. G. Hasinger & M. J. L. Turner, 13–24 [ADS]

Sigg, D. & the LIGO Scientific Collaboration. 2008, *Classical and Quantum Gravity*, 25, 114041 [ADS]

Simcoe, R. A., Sargent, W. L. W., & Rauch, M. 2002, *Astrophys. J.*, 578, 737 [ADS]

Simcoe, R. A., Sargent, W. L. W., & Rauch, M. 2004, *Astrophys. J.*, 606, 92 [ADS]

Simcoe, R. A., Sargent, W. L. W., Rauch, M., & Becker, G. 2006, *Astrophys. J.*, 637, 648 [ADS]

Smoot, G. & Murdin, P. 2002, in Encyclopedia of Astronomy and Astrophysics, ed. Murdin, P. [ADS]

Songaila, A., Hu, E. M., Cowie, L. L., & McMahon, R. G. 1999, *Astrophys. J. Lett.*, 525, L5 [ADS]

Springel, V. 2010, *Ann. Rev. Astron. Astrophys.*, 48, 391 [ADS]

Steidel, C. C. 2011, private communication

Steidel, C. C., Adelberger, K. L., Shapley, A. E., Pettini, M., Dickinson, M., & Giavalisco, M. 2000, *Astrophys. J.*, 532, 170 [ADS]

Steidel, C. C., Adelberger, K. L., Shapley, A. E., Pettini, M., Dickinson, M., & Giavalisco, M. 2003, *Astrophys. J.*, 592, 728 [ADS]

Steidel, C. C., Bogosavljević, M., Shapley, A. E., Kollmeier, J. A., Reddy, N. A., Erb, D. K., & Pettini, M. 2011, *ArXiv e-prints* [ADS]

Steidel, C. C., Erb, D. K., Shapley, A. E., Pettini, M., Reddy, N., Bogosavljević, M., Rudie, G. C., & Rakic, O. 2010, *Astrophys. J.*, 717, 289 [ADS]

Stocke, J. T., Danforth, C. W., Shull, J. M., Penton, S. V., & Giroux, M. L. 2007, *Astrophys. J.*, 671, 146 [ADS]

Sutherland, R. S. & Dopita, M. A. 1993, *Astrophys. J. Suppl.*, 88, 253, `http://adsabs.harvard.edu/abs/1993ApJS...88..253S`

Thatte, N., Tecza, M., Clarke, F., Goodsall, T., Lynn, J., Freeman, D., & Davies, R. L. 2006, in Presented at the Society of Photo-Optical Instrumentation Engineers (SPIE) Conference, Vol. 6269, Society of Photo-Optical Instrumentation Engineers (SPIE) Conference Series [ADS]

Thom, C. & Chen, H. 2008a, *Astrophys. J. Suppl.*, 179, 37 [ADS]

Thom, C. & Chen, H. 2008b, *Astrophys. J.*, 683, 22 [ADS]

Tripp, T. M., Sembach, K. R., Bowen, D. V., Savage, B. D., Jenkins, E. B., Lehner, N., & Richter, P. 2008, *Astrophys. J. Suppl.*, 177, 39 [ADS]

Turnshek, D. A., Bohlin, R. C., Williamson, II, R. L., Lupie, O. L., Koornneef, J., & Morgan, D. H. 1990, *Astron. J.*, 99, 1243 [ADS]

Tuttle, S. E. 2010, PhD thesis, Columbia University

Tuttle, S. E., Schiminovich, D., Grange, R., Rahman, S., Matuszewski, M., Milliard, B., Deharveng, J., & Martin, D. C. 2010, in Society of Photo-Optical Instrumentation Engineers (SPIE) Conference Series, Vol. 7732, Society of Photo-Optical Instrumentation Engineers (SPIE) Conference Series [ADS]

Tuttle, S. E., Schiminovich, D., Milliard, B., Grange, R., Martin, D. C., Rahman, S., Deharveng, J., McLean, R., Tajiri, G., & Matuszewski, M. 2008, in Society of Photo-Optical Instrumentation Engineers (SPIE) Conference Series, Vol. 7014, Society of Photo-Optical Instrumentation Engineers (SPIE) Conference Series [ADS]

Tytler, D., Kirkman, D., O'Meara, J. M., Suzuki, N., Orin, A., Lubin, D., Paschos, P., Jena, T., Lin, W., Norman, M. L., & Meiksin, A. 2004, *Astrophys. J.*, 617, 1 [ADS]

van Dokkum, P. G. 2001, *Publ. Astron. Soc. Pac.*, 113, 1420 [ADS]

Verhamme, A., Schaerer, D., & Maselli, A. 2006, *Astron. & Astrophys.*, 460, 397 [ADS]

Vogt, S. S., Allen, S. L., Bigelow, B. C., Bresee, L., Brown, B., Cantrall, T., Conrad, A., Couture, M., Delaney, C., Epps, H. W., Hilyard, D., Hilyard, D. F., Horn, E., Jern, N., Kanto, D., Keane, M. J., Kibrick, R. I., Lewis, J. W., Osborne, J., Pardeilhan, G. H., Pfister, T., Ricketts, T., Robinson, L. B., Stover, R. J., Tucker, D., Ward, J., & Wei, M. Z. 1994, in Presented at the Society of Photo-Optical Instrumentation Engineers (SPIE) Conference, Vol. 2198, Society of Photo-Optical Instrumentation Engineers (SPIE) Conference Series, ed. D. L. Crawford & E. R. Craine, 362 [ADS]

Vreeswijk, P. M., Ellison, S. L., Ledoux, C., Wijers, R. A. M. J., Fynbo, J. P. U., Møller, P., Henden, A., Hjorth, J., Masi, G., Rol, E., Jensen, B. L., Tanvir, N., Levan, A., Castro Cerón, J. M., Gorosabel, J., Castro-Tirado, A. J., Fruchter, A. S., Kouveliotou, C., Burud, I., Rhoads, J., Masetti, N., Palazzi, E., Pian, E., Pedersen, H., Kaper, L., Gilmore, A., Kilmartin, P., Buckle, J. V., Seigar, M. S., Hartmann, D. H., Lindsay, K., & van den Heuvel, E. P. J. 2004, *Astron. & Astrophys.*, 419, 927 [ADS]

Vreux, J. M. & Swings, J. P. 1977, *Astron. & Astrophys.*, 54, 451 [ADS]

Weiner, B. J., Coil, A. L., Prochaska, J. X., Newman, J. A., Cooper, M. C., Bundy, K., Conselice, C. J., Dutton, A. A., Faber, S. M., Koo, D. C., Lotz, J. M., Rieke, G. H., & Rubin, K. H. R. 2009, *Astrophys. J.*, 692, 187 [ADS]

Weitzel, L., Krabbe, A., Kroker, H., Thatte, N., Tacconi-Garman, L. E., Cameron, M., & Genzel, R. 1996, *Astron. & Astrophys. Suppl. Ser.*, 119, 531 [ADS]

Wells, D. C., Greisen, E. W., & Harten, R. H. 1981, *Astron. & Astrophys. Suppl. Ser.*, 44, 363 [ADS]

Werner, N., Finoguenov, A., Kaastra, J. S., Simionescu, A., Dietrich, J. P., Vink, J., & Böhringer, H. 2008, *Astron. & Astrophys.*, 482, L29 [ADS]

Weymann, R. 1965, *Physics of Fluids*, 8, 2112 [ADS]

Weymann, R. J., Williams, R. E., Peterson, B. M., & Turnshek, D. A. 1979, *Astrophys. J.*, 234, 33 [ADS]

Wilkinson, E., Morse, J., Ebbets, D., Green, J. C., & Andrews, J. 2002

Willmarth, D. W., Cheselka, M., Fitzpatrick, M., & Rippa, M. 2006, Photron Lamp Thorium Arhon Atlas, Tech. rep., NOAO, `http://www.noao.edu/kpno/specatlas/thar_photron/thar_photron.html`

Wolfe, A. M., Gawiser, E., & Prochaska, J. X. 2005, *Ann. Rev. Astron. Astrophys.*, 43, 861 [ADS]

Woodgate, B. E., Kimble, R. A., Bowers, C. W., Kraemer, S., Kaiser, M. E., Danks, A. C., Grady, J. F., Loiacono, J. J., Brumfield, M., Feinberg, L., Gull, T. R., Heap, S. R., Maran, S. P., Lindler, D., Hood, D., Meyer, W., Vanhouten, C., Argabright, V., Franka, S., Bybee, R., Dorn, D., Bottema, M., Woodruff, R., Michika, D., Sullivan, J., Hetlinger, J., Ludtke, C., Stocker, R., Delamere, A., Rose, D., Becker, I., Garner, H., Timothy, J. G., Blouke, M., Joseph, C. L., Hartig, G., Green, R. F., Jenkins, E. B., Linsky, J. L., Hutchings, J. B., Moos, H. W., Boggess, A., Roesler, F., & Weistrop, D. 1998, *Publ. Astron. Soc. Pac.*, 110, 1183 [ADS]

Wynne, C. G. 1993, *Mon. Not. Roy. Astron. Soc.*, 260, 307 [ADS]

Zwicky, F. 1933, *Helvetica Physica Acta*, 6, 110 [ADS]